Published in Journals: Batteries, Designs,
Energies, Sustainability and World Electric Vehicle Journal

Topic Reprint

Zero Carbon Vehicles and Power Generation

Edited by
Wenbin Yu and Guang Zeng

mdpi.com/topics

MDPI

Zero Carbon Vehicles and Power Generation

Zero Carbon Vehicles and Power Generation

Editors

Wenbin Yu
Guang Zeng

MDPI

Basel • Beijing • Wuhan • Barcelona • Belgrade • Novi Sad • Cluj • Manchester

Editors
Wenbin Yu
Shandong University
Jinan
China

Guang Zeng
SPIC Northeast Energy
Technology Co., Ltd.
Shenyang
China

Editorial Office
MDPI AG
Grosspeteranlage 5
4052 Basel, Switzerland

This is a reprint of articles from the Topic published online in the open access journals *Sustainability* (ISSN 2071-1050), *Energies* (ISSN 1996-1073), *World Electric Vehicle Journal* (ISSN 2032-6653), and *Designs* (ISSN 2411-9660) (available at: https://www.mdpi.com/topics/zero_carbon).

For citation purposes, cite each article independently as indicated on the article page online and as indicated below:

Lastname, A.A.; Lastname, B.B. Article Title. *Journal Name* **Year**, *Volume Number*, Page Range.

ISBN 978-3-7258-1943-0 (Hbk)
ISBN 978-3-7258-1944-7 (PDF)
doi.org/10.3390/books978-3-7258-1944-7

Contents

About the Editors

Wenbin Yu

Prof. Dr. Wenbin Yu is a full professor at the School of Energy and Power Engineering, Shandong University, China. He received his Ph.D degree from the State Key Laboratory of Engines, Tianjin University. From 2011 to 2013, he joined Great Wall Motor as their Chief Technical Expert. From 2013 to 2020, he joined the National University of Singapore as a Senior Research Fellow. In 2020, he joined the School of Energy and Power Engineering at Shandong University as a Professor.

Guang Zeng

Prof. Dr. Zeng has been a full professor at the SPIC Northeast Energy Technology Co., Ltd., since Jan. 2023, which is the support unit of the National Power Plant Combustion Engineering Technology Research Center. He received his Ph.D. from the Harbin Institute of Technology. From August 2008 to May 2016, he worked at the Northeast Electric Power Research Institute State Grid, China, as an Engineering Technologist. From June 2016 to March 2018, he joined the DSSP Power at Sinar Mas Group, Indonesia, as a Power Plant Technical Advisor. From April 2018 to January 2021, he joined the National University of Singapore as a Research Fellow. From January 2021 to January 2023, he joined the Institute of Engineering Thermophysics, Chinese Academy of Sciences, as a Research Professor. Currently, Prof. Dr. Zeng is a guest professor at the Shenyang Institute of Engineering. Furthermore, he is a postgraduate supervisor at the Harbin Institute of Technology, North China Electric Power University, and Shenyang Aerospace University.

sustainability

Editorial

Zero-Carbon Vehicles and Power Generation

Wenbin Yu [1,*] and Guang Zeng [2]

1 School of Energy and Power Engineering, Shandong University, Jinan 250061, China
2 SPIC Northeast Energy Technology Co., Ltd., Shenyang 110179, China; zengguang@spic.com.cn
* Correspondence: wbyu@sdu.edu.cn

Citation: Yu, W.; Zeng, G. Zero-Carbon Vehicles and Power Generation. *Sustainability* **2024**, *16*, 6447. https://doi.org/10.3390/su16156447

Received: 11 June 2024
Revised: 18 July 2024
Accepted: 22 July 2024
Published: 28 July 2024

In recent decades, traditional fossil fuels such as coal, oil, and natural gas have made the greatest contributions to the economic development of the industrial sector. However, the negative impact of fossil fuel-based energy has also resulted in the pollution of the natural environment, which presents a major threat to long-term growth and prosperity. In response to energy and environmental crises, zero-carbon vehicles and power generation technology are becoming hot topics, in both the industrial and academic communities. More experts and scholars have demonstrated significant and broad influence in their field, and the number of related technical papers is also rapidly increasing. Therefore, we are committed to providing a platform for high-quality papers on research topics including but not limited to the following: renewable energy vehicles, ammonia and hydrogen technologies in power systems, virtual vehicles, thermal power plant peak regulation technologies, etc. The Topic focuses on fundamental and applied research examining the specific impacts of automation on mobility, energy demand, and greenhouse gas emissions. Many up-to-date concepts in technologies designed to accelerate the race to carbon neutrality and sustainable development in vehicles and power systems are explored, discussed, and published as original research papers in this Topic, "Zero Carbon Vehicles and Power Generation".

Wu et al. [1] proposed a novel method characterizing the air backflow of the underhood, in order to improve the thermal efficiency of the air conditioning system (ACS) and reduce the energy consumption of Plug-in Hybrid Electric Vehicle (PHEV). Additionally, a 1D model for analyzing air backflow in the underhood was established and a Computational Fluid Dynamics (CFD) method for calculating air backflow rate and distribution was proposed. It was found that the decrease in the air backflow rate of the underhood helped to improve the refrigeration capacity of the ACS, and, when the backflow ratio cannot be reduced below 10%, the air backflow should be distributed as evenly as possible at the front end of the condenser.

Zhang et al. [2] introduced an analytical model of the voltage source converter (VSC) under the unbalanced condition through mathematical derivations, and the final model was a coupled Thevenin circuit. The proposed model allowed for the direct computation of non-characteristic third harmonics using harmonic power flow studies. The results showed that the VSC, under unbalanced conditions, emitted both positive-sequence and negative-sequence third harmonics, and that the positive-sequence third harmonic was much larger than the negative-sequence third harmonic. It also showed that the unbalanced level and the size of the dc-link capacitor were critical to the level of non-characteristic third harmonics.

Wu et al. [3] proposed and analyzed a multi-source microgrid economic dispatch model to reduce carbon emissions. The implemented carbon trading mechanism contributed to achieving carbon emissions control. Companies with surplus carbon emission quotas can increase their additional income by selling such quotas to reduce the total generation and operation cost of the power system. The low-carbon dispatch model enabled wind power, solar energy, electric vehicles, and other distributed power generation units to benefit from carbon trading and to reduce their operation costs while expanding the microgrid system, which ultimately reduced the total cost of the power system.

Guo et al. [4] established a system state equation based on the longitudinal dynamics equation of a vehicle, to deal with the factors influencing electric vehicles when driving under complex conditions. Combined with the improved Sage–Husa adaptive Kalman filter algorithm, a road slope estimation model was established. After the driving speed and rough slope observation were input into the slope estimation model, the accurate road slope estimation at the current time could be obtained. The road slope estimation method was compared with the original Sage–Husa adaptive Kalman filter road slope estimation method through three groups of road tests with different slope ranges, and the accuracy and stability advantages of the proposed algorithm in road conditions with large slopes were verified.

Jo and Kim [5] analyzed the aerodynamic interactions between platooning moving vehicles under different platooning conditions on a freeway. It was found that the effect of the vortex generated by the forward vehicle reduced the value of the stagnation pressure generated at the front of the rear vehicle, which effectively reduced drag on the driving vehicle.

Ji et al. [6] proposed a quantitative evaluation method of driving behavior, based on Naturalistic Driving Studies (NDS) data collected from shared electrical cars and online car-hiring services. In this study, data acquisition, the treatment method, and the data volume verification were analyzed to ensure the effectiveness of the dataset. The distribution characteristics of the main driving behavior parameters were studied. On this basis, the evaluation method was proposed and verified.

Tao et al. [7] presented a novel single-switch high-gain dc/dc converter with a ripple-free input current. The structure consisted of two cells: a coupled inductor cell and a switched capacitor cell. The coupled inductor cell in the proposed converter provided a ripple-free input current. The switched capacitor cell provided a high voltage gain. The converter had a simple control strategy due to the use of a single switch. Moreover, the output capacitor was charged and discharged continuously by a 180° phase shift to eliminate the output voltage ripple.

Ottesen et al. [8] explored consumer preferences for Electric Vehicles (EVs) in Kuwait, in terms of which factors are influential for the ‘early majority’ (i.e., a part of the general market vs. a niche one) that could influence their purchasing behavior in favor of EVs. A comprehensive and up-to-date picture of the preferences regarding this market was provided, while a variety of valuable promotional tactics were discussed, which may be implemented in conjunction with public incentives and policy changes in the State of Kuwait.

Mišić et al. [9] proposed special energy management for a mountain railway with optimal power distribution and minimum hydrogen consumption. A simulation model was created in a Matlab/Simulink environment for the optimization of hybridized power systems on trains, and it can be easily modified for the hybridization of any type of train. Optimization was performed using sequential quadratic programming (SQP). The results showed that this hybrid train topology had the ability to recover battery and supercapacitor state of charge (SOC) while meeting vehicle speed and propulsion power requirements.

Al-Shami et al. [10] described a novel approach for modeling, identifying, and controlling a running gas turbine power plant. A simplified nonlinear model structure composed of s-domain transfer functions and nonlinear blocks represented by rate limiters, saturations, and look-up tables was proposed. The model was used to design a multiple PI/PD control to regulate the gas turbine via the inlet guide vane and fuel vales, so as to raise and stabilize the compressor’s differential pressure or pressure ratio, as well as the raise the set-point of the temperature exhausted from the combustion turbine.

Asiamah et al. [11] developed a hierarchy for understanding the impacts of active and non-active transport modes on the environment and analyzed the adoption of active transportation between older and younger people. The review suggested that the only active transport modes with no or negligible carbon footprint are walking, running, and swimming, as they do not result in a product that adds to atmospheric greenhouse gasses.

Ma et al. [12] analyzed previous studies and current research on the current technical advances emerging for use in the assisted combustion of ammonia. It was highlighted that plasma-assisted combustion (PAC) was able to change classical ignition and extinction S-curves to monotonic stretching, which makes low-temperature ignition possible while resulting in moderate NOx emissions.

Li et al. [13] developed a new four-component jet fuel surrogate which could satisfactorily emulate the chemical and physical properties of real jet fuel, including the cetane number (CN), threshold sooting index (TSI), molecular weight (MW), a lower heating value (LHV), the ratio of hydrogen and carbon (H/C), and the liquid density, viscosity, and surface tension. Furthermore, a reduced and robust kinetic chemical mechanism (containing 124 species and 590 reactions) that could be directly employed in practical engine combustion simulations was also developed.

Banna et al. [14] used a quantitative descriptive method (with close-ended questions) to collect data from a sample of 227 Kuwaiti nationals who were representative of the owners of half a million internal combustion engine (ICE) cars, categorized as early majority consumers. The findings indicated that over 50 percent of the respondents would prefer to buy an EV in the subsequent three years, when certain criteria were satisfied, including government-controlled pricing policies and recharging point availability, high-speed roads, and free EV-dedicated parking spaces. Furthermore, over 40 percent of respondents stated that they would contemplate purchasing an electric vehicle if the price of gasoline or diesel increased by 19 to 50 percent. The findings also indicated that more than 40 percent of respondents believed that EVs are fire- and crash-safe, and roughly 50 percent of the respondents would be willing to pay between 6 and 20% more for an EV because they believed that EVs are eco-friendlier vehicles and are significantly faster than conventional petrol vehicles.

Nurdini et al. [15] used the open-source R language and the bibliometrix package to carry out a bibliometric analysis of data from 593 scientific publications, taken from Scopus, to investigate the research landscape of electric vehicle waste management. It was revealed that the research area of recycling electronic waste from electric vehicles is still experiencing annual growth that is accelerating rapidly. The findings also indicated that China stands out as the leading contributor to publications, with Tsinghua University being a prominent research institution in this field. In 2023, the most frequently occurring topic was “closed loop”, while “recycling” was the dominant keyword.

Hoth et al. [16] evaluated the solar energy potential of parking spaces in Berlin, considering challenges like building and tree shading using digital surface models and weather data for solar simulations. Utilizing open datasets and software, the analysis covered 48,827 parking spaces, revealing that vehicle-integrated photovoltaics (VIPV) could extend vehicle range from 7 to 14 km per day, equating to a median annual increase of 2527 km. The findings suggested possible median yearly cost savings of 164 euros from reduced grid charging, and this study introduced a method to pinpoint parking spaces that are most suitable for solar charging.

Chen et al. [17] comprehensively studied dynamic vehicle data contributing to traffic carbon emissions in terms of data sensitivity and uncertainty. The active subspace method could identify which input parameters were the most important through magnitudes of the input parameter weights, while exploring how the combination of inputs was related to the output of interest, without the expense of multiple simulations. It was concluded that the CO_2 emission factor was most sensitive to the vehicle specific power (VSP). The method has great potential to readily derive the relationship between the combination of inputs and outputs in a complex domain without the expense of multiple simulations. Also, the relationship between the input parameters (i.e., the active variables) and the CO_2 emission factor could be formulated using a quadratic function.

Zhang et al. [18] investigated the effects of bore taper, the starting height of the tapered profile, and ellipticity on the friction power and knocking energy of a piston ring cylinder bore (PRCB) system based on the full-scale test method, and the optimization of the design of the bore profile was carried out with the objectives of minimizing the system's friction power and the peak knocking kinetic energy.

Cardoso et al. [19] proposed an active, purely mechanical solution to the problem of irregular torque production in an alternative internal combustion engine. This solution used an actuator built on a camshaft and a spring, which stored and returned energy during the engine operating cycle, allowing torque production to be normalized, avoiding heavy flywheels.

Huang et al. [20] investigated the synergistic coupling process between the detonation and diesel cycles using gasoline as fuel. A numerical simulation model was constructed to analyze the detonation characteristics of a pulse detonation combustor (PDC), followed by experimental verification, which showed that the generation of detonation waves was influenced by flame and compression wave interactions. Increasing the airflow did not shorten the deflagration-to-detonation transition (DDT) time, whereas increasing the blockage ratio (BR) caused the DDT time to decrease and then increase. Large BRs affected the initiation speed of detonation in the tube, while small BRs impacted the DDT distance and peak pressure.

Liu et al. [21] combined the approaches of bench experiments and numerical simulations to investigate the influence of the injector nozzle diameter on the in-cylinder fuel–air mixture and combustion process, based on a combustion strategy characterized by a high-density and lean mixture. The research provided guidance and suggestions for the selection of an injector nozzle diameter in the development of advanced engine combustion systems.

The papers in this Topic reveal an exciting field, namely "zero carbon vehicles and power generation", which is critical to energy utilization and sustainable development. Pursuing work in this field requires professional knowledge in fields such as energy, fuel, automotives, and power generation. We are delighted to be invited to be the Editors for this "Topic". We have received strong support from professional researchers from many renowned universities and research institutions. We will continue to grow our strengths in order to make a greater contribution to carbon neutrality goals. We firmly believe that, through continuous collaboration among all researchers, these steps will help resolve global challenges and address energy sustainability at the source. We hope that this "Topic" will help bring the research community closer together. Finally, we would like to thank all authors, reviewers, and editors who contributed to this publication. We believe that the readers of all the journals involved in this Topic will find these scientific manuscripts interesting and useful for their future research efforts.

Author Contributions: Investigation, W.Y. and G.Z.; Writing—review and editing, W.Y. and G.Z. All authors have read and agreed to the published version of the manuscript.

Funding: This research received no external funding.

Conflicts of Interest: Author Guang Zeng was employed by the company SPIC Northeast Energy Technology Co., Ltd. The remaining authors declare that the research was conducted in the absence of any commercial or financial relationships that could be construed as a potential conflict of interest.

References

1. Wu, H.; Tang, X.; Xu, S.; Zhou, J. Research on Energy Saving of PHEV Air Conditioning System Based on Reducing Air Backflow in Underhood. *Energies* **2022**, *15*, 3183. [CrossRef]
2. Zhang, M.; Zhi, H.; Zhang, S.; Fan, R.; Li, R.; Wang, J. Modeling of Non-Characteristic Third Harmonics Produced by Voltage Source Converter under Unbalanced Condition. *Sustainability* **2022**, *14*, 6449. [CrossRef]
3. Wu, Y.; Lau, Y.-Y.; Wu, J.-A. Integration of Electric Vehicles into Microgrids: Policy Implication for the Industrial Application of Carbon Neutralisation in China. *World Electr. Veh. J.* **2022**, *13*, 96. [CrossRef]

4. Guo, J.; He, C.; Li, J.; Wei, H. Slope Estimation Method of Electric Vehicles Based on Improved Sage–Husa Adaptive Kalman Filter. *Energies* **2022**, *15*, 4126. [CrossRef]
5. Jo, J.; Kim, C.-H. Numerical Study on Aerodynamic Characteristics of Heavy-Duty Vehicles Platooning for Energy Savings and CO_2 Reduction. *Energies* **2022**, *15*, 4390. [CrossRef]
6. Ji, S.; Zhang, K.; Tian, G.; Yu, Z.; Lan, X.; Su, S.; Cheng, Y. Evaluation Method of Naturalistic Driving Behaviour for Shared-Electrical Car. *Energies* **2022**, *15*, 4625. [CrossRef]
7. Tao, R.; Yue, J.; Huang, Z.; An, R.; Li, Z.; Liu, J. A High-Gain DC Side Converter with a Ripple-Free Input Current for Offshore Wind Energy Systems. *Sustainability* **2022**, *14*, 11574. [CrossRef]
8. Ottesen, A.; Banna, S.; Alzougool, B. How to Cross the Chasm for the Electric Vehicle World's Laggards—A Case Study in Kuwait. *World Electr. Veh. J.* **2023**, *14*, 45. [CrossRef]
9. Mišić, M.; Stojkov, M.; Tomić, R.; Lovrić, M. Optimal Hybridization with Minimum Fuel Consumption of the Hybrid Fuel Cell Train. *Designs* **2023**, *7*, 45. [CrossRef]
10. Al-Shami, M.; Mohamed, O.; Abu Elhaija, W. Energy-Efficient Control of a Gas Turbine Power Generation System. *Designs* **2023**, *7*, 85. [CrossRef]
11. Asiamah, N.; Awuviry-Newton, K.; Nesser, W.; Alvarez, E.N. Carbon Footprints of Active and Non-Active Transport Modes: Hierarchy and Intergenerational Narrative Analyses. *Sustainability* **2023**, *15*, 12795. [CrossRef]
12. Ma, F.; Guo, L.; Li, Z.; Zeng, X.; Zheng, Z.; Li, W.; Zhao, F.; Yu, W. A Review of Current Advances in Ammonia Combustion from the Fundamentals to Applications in Internal Combustion Engines. *Energies* **2023**, *16*, 6304. [CrossRef]
13. Li, G.; Cui, B.; Zhang, C.; Chang, L.; Chen, L. Formulation of a Jet Fuel Surrogate and Its Kinetic Chemical Mechanism by Emulating Physical and Chemical Properties of Real Jet Fuel. *Sustainability* **2023**, *15*, 13792. [CrossRef]
14. Banna, S.; Ottesen, A.; Alzougool, B. Reasons Why Only Kuwaiti Citizens Drive Electric Vehicles despite Being Only a Quarter of the Population. *World Electr. Veh. J.* **2023**, *14*, 287. [CrossRef]
15. Nurdini, A.; Nurcahyo, R.; Prabuwono, A.S. Waste from Electric Vehicle: A Bibliometric Analysis from 1995 to 2023. *World Electr. Veh. J.* **2023**, *14*, 300. [CrossRef]
16. Hoth, P.; Heide, L.; Grahle, A.; Göhlich, D. Vehicle-Integrated Photovoltaics—A Case Study for Berlin. *World Electr. Veh. J.* **2024**, *15*, 113. [CrossRef]
17. Chen, J.; Yu, H.; Xu, H.; Lv, Q.; Zhu, Z.; Chen, H.; Zhao, F.; Yu, W. Investigation on Traffic Carbon Emission Factor Based on Sensitivity and Uncertainty Analysis. *Energies* **2024**, *17*, 1774. [CrossRef]
18. Zhang, J.; Wang, N.; Wang, J.; Wang, H.; Zhang, X.; Dai, H.; Lin, J. Low-Friction and -Knocking Diesel Engine Cylindrical-Tapered Bore Profile Design. *Energies* **2024**, *17*, 2042. [CrossRef]
19. Cardoso, D.S.; Fael, P.O.; Gaspar, P.D.; Espírito-Santo, A. An Innovative Mechanical Approach to Mitigating Torque Fluctuations in IC Engines during Idle Operation. *Designs* **2024**, *8*, 47. [CrossRef]
20. Huang, D.; Wang, J.; Shi, M.; Yang, P.; Wu, B. Combustion Mechanism of Gasoline Detonation Tube and Coupling of Engine Turbocharging Cycle. *Energies* **2024**, *17*, 2466. [CrossRef]
21. Liu, Y.; Su, W. The Influence of Injector Nozzle Diameter on High-Density and Lean Mixture Combustion in Heavy-Duty Diesel Engines. *Energies* **2024**, *17*, 2549. [CrossRef]

energies

Article

Research on Energy Saving of PHEV Air Conditioning System Based on Reducing Air Backflow in Underhood

Haibo Wu [1,2], Xingwang Tang [1], Sichuan Xu [1,*] and Jiangbin Zhou [2]

[1] School of Automotive Studies, Tongji University, Shanghai 200070, China; wuhaibo@csvw.com (H.W.); tangxingwang@tongji.edu.cn (X.T.)
[2] SAIC Volkswagen Automotive Co., Ltd., Shanghai 201800, China; zhoujiangbin@csvw.com
* Correspondence: scxu_tongji@163.com

Abstract: A novel method characterizing the air backflow of the underhood in order to improve the thermal efficiency of the air conditioning system (ACS) and reduce the energy consumption of PHEV is proposed in this paper. In addition, a 1D model for analyzing air backflow occurring in the underhood is established and a CFD method for calculating air backflow rate and distribution is proposed. It is found that the decrease in the air backflow rate of the underhood helps to improve the refrigeration capacity of the ACS, and when the backflow ratio cannot be reduced below 10%, the air backflow should be distributed as evenly as possible at the front end of the condenser. Moreover, in order to eliminate the impact of backflow on the underhood of PHEV, the gap between the radiator and the bracket is sealed and the gap around the air guide is reduced. Compared with the original structure, the backflow rate of the optimized structure is reduced from 32.7% to 9.3% and the cabin temperature can be reduced by 3–5 °C.

Keywords: PHEV; air conditioning system; air backflow; thermal management

Citation: Wu, H.; Tang, X.; Xu, S.; Zhou, J. Research on Energy Saving of PHEV Air Conditioning System Based on Reducing Air Backflow in Underhood. *Energies* **2022**, *15*, 3183. https://doi.org/10.3390/en15093183

Academic Editors: Wenbin Yu and Guang Zeng

Received: 30 March 2022
Accepted: 24 April 2022
Published: 27 April 2022

1. Introduction

With the proposal of "carbon peaking" and "carbon neutrality", a higher requirement for vehicle exhaust emissions is required. The shortage of non-renewable resources and the increasingly stringent pollutant emission regulations are driving vehicle manufacturers to lower fuel consumption and lower exhaust emissions [1–3]. Compared with traditional fuel vehicles, plug-in hybrid electric vehicles (PHEV) clearly reduce fuel consumption and CO_2 emissions [4,5]. The PHEV power sources rely on electric power generated by electric machines and mechanical power generated by internal combustion engines (ICEs) [6]. Due to the high efficiency of electric machines and the quick development of battery technology, the PHEV is a rational choice for a long period in terms of environmental issues and energy saving [7].

In the past decade, a lot of scholars have mainly focused on the energy management strategies in the research of energy saving for PHEV [8–11]. The author of [12] proposed a predictive energy management strategy (EMS) based on reinforcement learning for PHEV. The EMS combined the velocity prediction with the optimal power distribution between engine and electrical motor, which greatly improved the vehicle's fuel economy. The author of [13] obtained the optimized operating point of the engine based on the dynamic programming algorithm and proposed an improved rule-based energy management method. The results show that the energy management strategy can effectively reduce the fuel consumption per 100 km of the vehicle equipped with a diesel engine. 22.80 L/100 km. A PHEV-integrated optimization simulation platform based on Isight and MATLAB/Simulink software for bus is established in [14]. They proposed a multi-objective optimization and matching method and proved its effectiveness and superiority in fuel reduction and better performance. The optimization of the series fuel cell vehicle components by a single and a multi-objective genetic algorithm to improve the vehicle performance and the operational costs is also performed in [15]. A method for PHEV online energy management utilizing an evolutionary algorithm was developed in [16]. The results show that the proposed self-adaptive control strategy outperforms the conventional binary control strategy with an average of 10.7% fuel savings without considering charging opportunity and 31.5% fuel savings when considering charging opportunity. The author of [17] provided a comprehensive study regarding the PHEV's optimum powertrain design based on an interactive adaptive-weight genetic algorithm approach, which aims to simultaneously minimize the PHEV's fuel consumption, battery state of health, charging time, and costs.

Nowadays, in order to reduce the energy consumption of the PHEV, most research is limited to the energy management strategy. However, there is little research that pays attention to the energy-saving potential of the air conditioning system. As the core component of the PHEV, the air conditioning system needs to keep the cabin at a proper temperature. However, because it is also one of the most important energy-consuming components of PHEV, especially the compressor of the air conditioning system [18–20], a low-efficiency air conditioning system will bring great challenges to the endurance of the vehicle. The cooling load of an air conditioning system can cause an 18–37% reduction in the Urban Dynamometer Driving Schedule (UDDS) range depending on ambient conditions [21]. Therefore, in order to reduce the energy consumption of PHEV, it is vital to pay attention to the air conditioning system.

In this paper, in order to reduce energy consumption of PHEV, the efficiency of the air conditioning system is addressed. A detailed and quantitative analysis of the air backflow of the PHEV's underhood is carried out to improve the efficiency of the air conditioning system, so that the system energy consumption can be reduced. In fact, the air backflow phenomenon in the underhood of PHEV refers to when hot air from the underhood returns to the front-end cooling module, which increases the temperature of the windward air passing through the condenser, intercooler, low-temperature radiator, and electrical radiator, resulting in a decrease in the heat dissipation performance of the cooling module. Therefore, the air backflow in the underhood can cause the performance of the condenser to decrease, which in turn will affect the performance of the air conditioning system, resulting in increased energy consumption.

Based on the reviewed literature, optimizing the air backflow of the underhood is an effective way to improve the thermal efficiency of the air conditioning system and reduce the energy consumption of PHEV. Therefore, the contributions of this paper are threefold:

- A heat flux marking method is proposed to characterize the mechanism of air backflow and its distribution in the condenser, thereby quantifying the air backflow phenomenon in the underhood of PHEV.
- The performances of the air conditioning system, including the evaporator outlet temperature, cooling capacity, exhaust pressure of the compressor, and COP, are investigated under different ambient temperatures, air backflow ratios, and air backflow distribution.
- An optimization model of the underhood is proposed to eliminate the impact of air backflow on the air conditioning system of PHEV.

The rest of the paper is organized as follows. The research method, including the 1D model characterizing the effect of air backflow on the air conditioning system performances, the 3D model characterizing and quantifying the backflow phenomenon in the underhood of PHEV, and experimental test system verifying the air conditioning system performance, is presented in Section 2. The evaluation results, including the impact of the air backflow effect in the underhood of PHEV on the air conditioning system, mechanism analysis of air backflow phenomenon, and performance optimization, are reported in Section 3. Section 4 concludes the paper.

2. Research Method

2.1. Research Framework of the Air Backflow Effect in the Underhood

To quantify the backflow phenomenon in the underhood of PHEV and explore the impact of the air backflow in the underhood of PHEV on the air conditioning system, the research framework is constructed in this paper, as shown in Figure 1. The quantification and analysis of the air backflow phenomenon of the underhood of PHEV are realized based on the heat flux marking method demonstrated in this paper. The performances, including the evaporator outlet temperature, cooling capacity, exhaust pressure of compressor, and COP of ACS are investigated under different ambient temperatures, air backflow ratio, and backflow distribution based on one-dimensional simulation. Furthermore, the computational fluid dynamics (CFD) simulation of the underhood can characterize and reflect the air backflow flow field distribution and provide a basis for the structural parameter optimization of the underhood. Moreover, a real vehicle experiment is carried out in order to verify the performance of the air conditioning system after the underhood of PHEV is optimized.

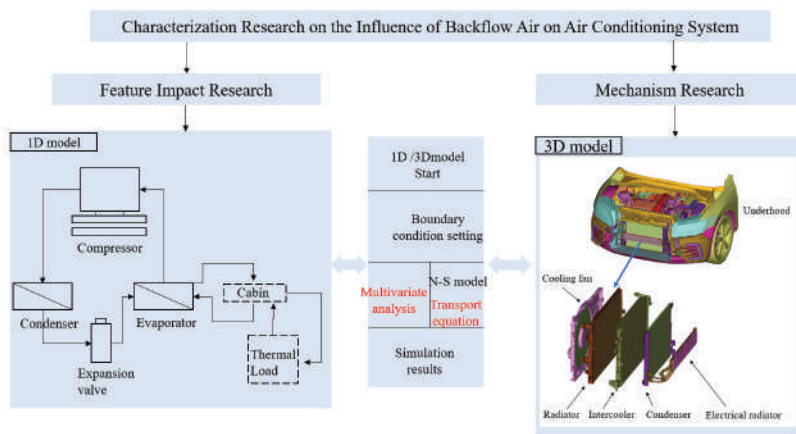

Figure 1. Research framework of the air backflow effect in the underhood of PHEV.

2.2. 1D Model

2.2.1. Compressor

A compressor is the core component of an air conditioning system;, so, the accuracy of its simulation model needs to be much higher than other components. Generally, a 1% error in the compressor simulation model will cause a 0.7% error in the air conditioning system approximately. In this paper, the compressor efficiency model is adopted and the physical model applied to the compressor efficiency model is shown in Equations (1)–(3) [22]:

$$m_{com} = \frac{\eta_v V_{th} r_{com}}{v_{suc}} \tag{1}$$

$$P_{comp} = m_{com} \left(h_{dis} - h_{suc}\right) / f_Q \tag{2}$$

$$h_{dis} = h_{suc} + \frac{h_{dis|s} - h_{suc}}{\eta_s} \tag{3}$$

where V_{th} is the displacement of the compressor, r_{com} is the rotary speed of the compressor, m_{com} is the mass flow of the compressor, η_v is the volumetric efficiency of the compressor, P_{comp} is the energy consumption of the compressor, h_{dis} is the exhaust enthalpy of the compressor, h_{suc} is the suction enthalpy of the compressor, η_s is the isentropic efficiency, $h_{dis|_s}$ is the exhaust enthalpy under the condition of isentropic compression, and f_Q is the heat loss of the compressor.

2.2.2. Condenser and Evaporator Model

In this paper, both the condenser and the evaporator of the ACS can be regarded as a model of the microchannel tube–fin heat exchanger; the working principle diagram of the heat exchanger is shown in Figure 2 [23]. The whole heat exchange process includes three parts: external convective heat exchange air–wall, heat conduction wall + fins, and internal convective heat exchange refrigerant–wall. In this model, the heat transfer correlation of the air side of the heat exchange can be expressed as follows [24]:

$$Nu = C_0 \times Re^N \times {Pr_t}^M \tag{4}$$

where Nu is the Nusselt number; Re is the Reynolds number; Pr_t is the Prandtl number; and M, N, and C_0 are the parameters that can be used to adjust the heat rejection performance of the heat exchanger.

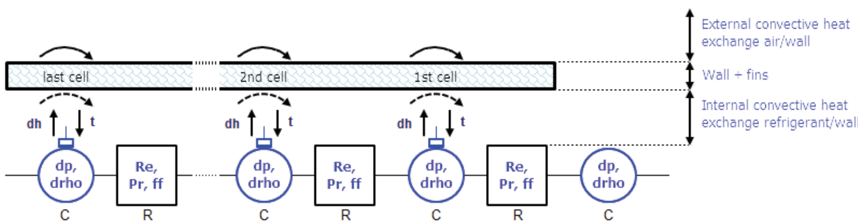

Figure 2. Diagram of discrete cell of the condenser component.

2.2.3. Expansion Valve

The expansion valve model is used in this paper to achieve different throttling effects by adjusting the opening degree of the expansion valve. The heat loss of the expansion valve is ignored in the model; so, the flow process of the refrigerant in the expansion valve is regarded as a constant enthalpy process. The mass flow rate is calculated as follows:

$$m_{exv} = \rho \times C_q \times A \times \sqrt{\frac{2 \times \Delta P}{\rho}} \tag{5}$$

$$\Delta P = P_i - P_O \tag{6}$$

where m_{exv} is the mass flow rate, kg/s; ρ is the density, kg/m^3; P_i is the inlet pressure, barA; P_O is the outlet pressure, barA; and C_q is the flow coefficient, which can be calculated by Formula (7):

$$C_q = C_{qmax} \times tanh\left(\frac{2 \times \lambda}{\lambda c}\right) \tag{7}$$

where C_{qmax} is the maximum flow coefficient; λ is the flow number; and λc is the critical flow number.

2.2.4. Fan and Radiator Model

The cooling fan is located at the front or rear of the radiator to increase the air flow through the radiator and improve the heat dissipation performance of the radiator. In this paper, the performance characteristic parameters of the fan are obtained based on the law of similarity, which mainly include the volumetric flow coefficient and pressure coefficient, and the calculation method is as follows [25]:

$$\phi = \frac{\dot{Q}}{A_{fan} \cdot V_{tip}} \tag{8}$$

$$\psi = \frac{\Delta P}{\frac{1}{2}\rho V_{tip}^2} \tag{9}$$

where ϕ is the volumetric flow coefficient; ψ is the pressure coefficient; $\dot{Q}$ is the volume flow of air; A_{fan} is the fan area; and V_{tip} is the linear velocity of the fan blade tip.

As for the radiator, the heat transfer and flow resistance of the cold side or hot side of the radiator can be calculated by the following formulas:

$$\Delta_p = \frac{1}{2} K \cdot \rho \cdot V_{\text{cool}}^2 \tag{10}$$

$$Q_{\text{rad}} = A_{\text{exch}} \cdot U \cdot (T_{\text{in}} - T_{\text{out}}) \tag{11}$$

where A_{exch} is the heat exchange area of heat exchanger; ρ is the air density; and K is the pressure loss coefficient.

2.3. 3D Models

2.3.1. Heat Exchanger

To characterize the backflow phenomenon in the underhood of PHEV, it is necessary to perform computational fluid analysis on the cooling module of the underhood. In the cooling module of the underhood, the condenser, intercooler and, radiator all belong to the heat exchanger. In this paper, the heat transfer model of the heat exchanger is established by *NTU* method, as follows [25]:

$$NTU = \frac{-\ln(1 - \varepsilon - \varepsilon C_r)}{(C_r + 1)} \tag{12}$$

where C_r is the heat capacity ratio and ε is the effectiveness.

The porous media model is adopted to characterize the pressure loss inside the heat exchanger; it also adopts the correction method of the standard momentum equation, which adds the momentum source term composed of viscous loss term and inertial to the momentum equations. The mathematical description is as follows [22]:

$$S_{\text{i}} = -\left(\sum_{\text{j}=1}^{3} D_{\text{ij}} \mu u_{\text{j}} + \sum_{\text{j}=1}^{3} C_{\text{ij}} \frac{1}{2} \rho |u| u_{\text{j}} \right) \tag{13}$$

where S_{i} is the source term in the momentum equation, $|u|$ is the velocity scalar, u is the velocity vector, μ is the aerodynamic viscosity, and D and C is the given matrix.

D and C are defined as diagonal matrices, and the formula can be expressed as follows:

$$S_{\text{i}} = -\left(\frac{\mu}{\beta} u_{\text{i}} + \eta \frac{1}{2} \rho |u| u_{\text{i}} \right) \tag{14}$$

where $\frac{1}{\beta}$ is the viscous resistance coefficient, and η is the inertial resistance coefficient.

The simplified momentum equation of porous media can be expressed in the form of pressure loss and source term as follows:

$$\Delta P = -\left(\frac{\mu \Delta n}{D} u_{\text{i}} + C_1 \frac{1}{2} \rho |u| \Delta n u_{\text{i}} \right) \tag{15}$$

The characteristic parameters of the heat exchangers are demonstrated in Table 1:

Table 1. The viscous resistance coefficient and inertial resistance coefficient of heat exchangers.

Heat Exchanger	Viscous Resistance Coefficient (m^{-2})	Inertial Resistance Coefficient (m^{-1})
Radiator	1192.5	160.1
Intercooler	813.6	74.5
Condenser	851.8	126.9
Electrical radiator	808.2	114.3

2.3.2. Meshing of the PHEV Underhood

The 3D solid model of the PHEV underhood, including the condenser, radiator, and other components, is shown in Figure 3a. In order to avoid the interference of the airflow disturbance in the limited space on the model accuracy, a rectangular air domain (10 L × 10 W × 6 H) is added, as shown in Figure 3b.

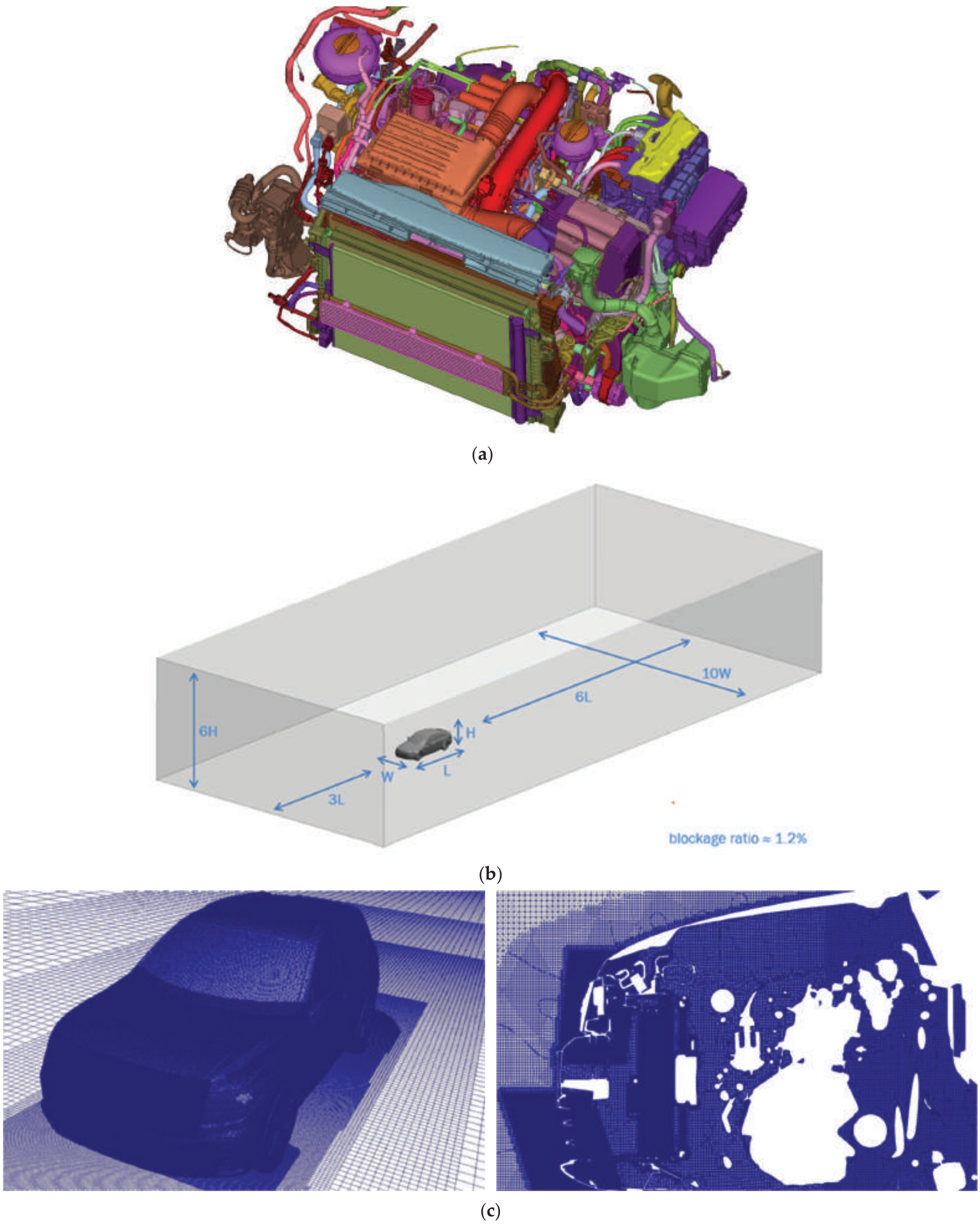

Figure 3. The 3D model of the underhood for PHEV. (**a**) A 3D solid model of the underhood; (**b**) the CFD calculation domain of the underhood for PHEV; (**c**) the mesh of the underhood for PHEV.

In view of the fact that the air backflow of the underhood is determined in this paper, the front half of the car body surface is also meshed to ensure that the flow details are captured. The mesh model with 80 million mesh is shown in Figure 3c.

2.3.3. Boundary Condition

The air backflow flow field distribution is investigated based on the CFD method. Some boundary conditions should be determined:

(1) RANS steady-state model is used for steady flow in this model;
(2) Pressure outlet and velocity inlet are selected for outlet and inlet boundary conditions, respectively;
(3) The condenser, intercooler, radiator, and electrical radiator are calculated based on the porous media model;
(4) The cooling fan is simulated based on the multiple reference frame (MRF) method.

2.4. Experimental Test System

In order to verify the effect of air backflow of the underhood on the cooling capacity of the air conditioning system for PHEV, a system bench experiment is established. The measurement points of the temperature sensor in the cabin are shown in Figure 4, and the cabin temperature value is obtained by calculating the average temperature of multiple measurement points.

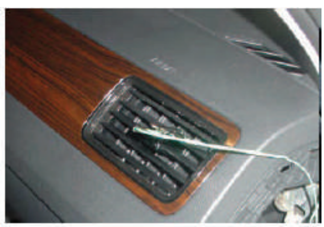

(**a**)

(**b**)

(**c**)

(**d**)

(**e**)

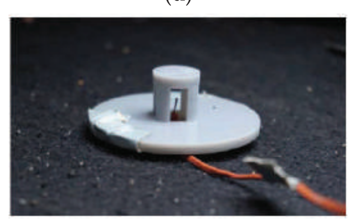

(**f**)

Figure 4. The measurement points of temperature sensor in the cabin. (**a**) Side air outlet; (**b**) Middle air outlet; (**c**) Front seat passenger; (**d**) Rear seat passenger; (**e**) Dashboard area; (**f**) Cabin bottom.

In order to ensure more accurate simulation results in the 1D/3D calculation, the relevant key parameters of the condenser, evaporator, and other radiators are obtained through the enthalpy difference experiment. The laboratory is shown in Figure 5.

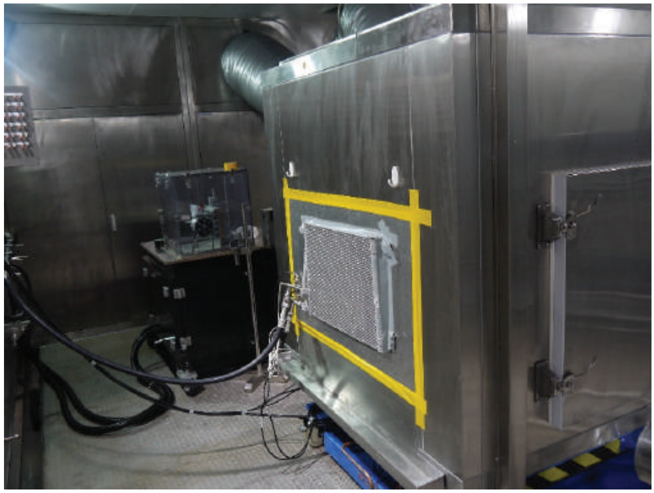

Figure 5. The heat exchanger performance test platform.

2.5. Heat Flux Marking Method

In order to solve the problem that the air backflow phenomenon of the underhood cannot be judged based on a streamline method, a heat flux marking method is proposed based on the mechanism and distribution of air backflow in the heat exchanger. The air flow passing the heat exchanger will be marked. In order to monitor the backflow air, a monitoring surface will be set at the front end of the heat exchanger. The schematic diagram is shown in Figure 6.

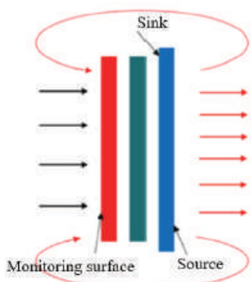

Figure 6. Schematic diagram of air backflow calculation method.

In this paper, in order to quantify the distribution of heated air and calculate the backflow rate, the scalar γ is used to express the proportion of the volume of hot air, referring to the momentum transport equation. The calculation method is as follows:

$$\frac{\partial \gamma}{\partial t} + u_j \frac{\partial \gamma}{\partial x_i} = \nu \frac{\partial^2 \gamma}{\partial x_j \partial x_j} - \nu_t \frac{\partial \gamma}{\partial x_j} \tag{16}$$

When the air backflow phenomenon is characterized based on the CFD method, the N-S equation for the entire fluid domain needs to be solved first. Then, the transport equation should be solved after the flow field is in a stable state. Finally, the distribution of hot air in the entire fluid domain can be obtained after the calculation converges.

3. Results and Discussion

In order to systematically analyze the air backflow phenomenon of the underhood of PHEV in this paper, the influence of the air backflow rate on the air conditioning system is explored under different ambient temperatures and backflow distribution. Furthermore, to eliminate the impact of air backflow of the underhood and improve the performance of the thermal management system, the underhood of PHEV is optimized in this paper.

3.1. Effect of Backflow Rate under Different Ambient Temperatures

In this section, the influence of air backflow rate on the air conditioning system is explored under different ambient temperatures. Figure 7 shows that under ambient temperatures of 30 °C, 35 °C, and 40 °C, as the backflow rate increases from 0% to 30%, the air conditioning system performance parameters, including evaporator outlet temperature, evaporator heat exchange, compressor discharge pressure, and COP, are changed accordingly.

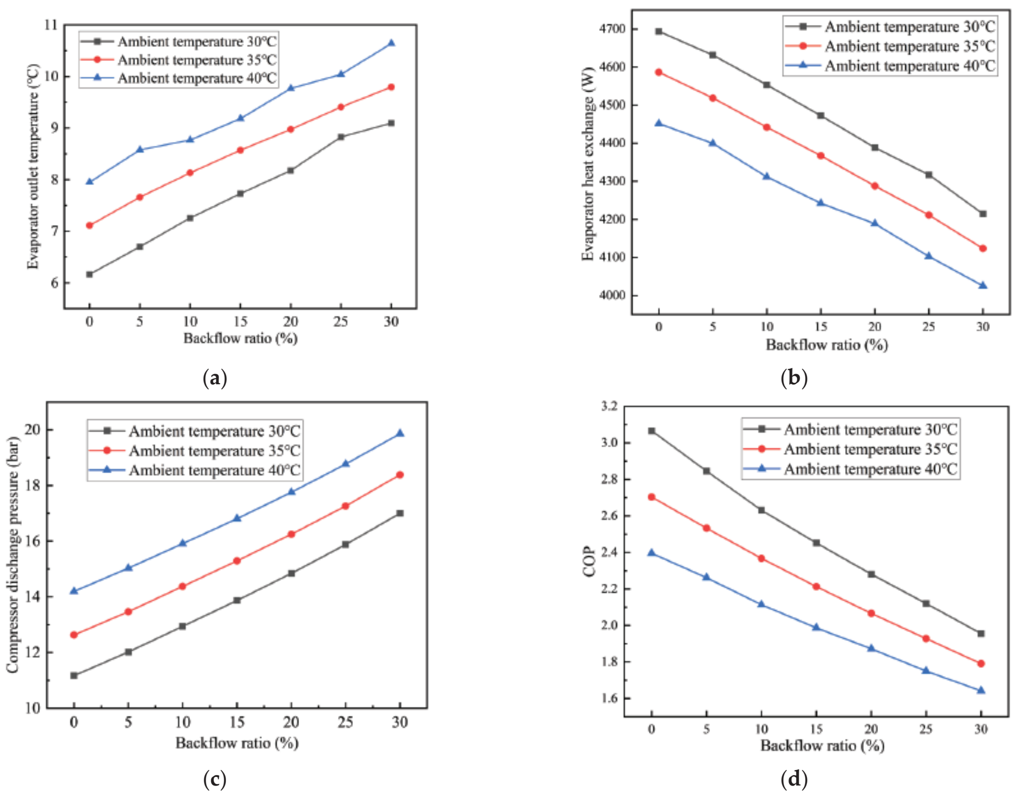

Figure 7. Influences of backflow rate on air conditioning performances under different ambient temperatures. (**a**) Evaporator outlet temperature; (**b**) evaporator heat rejection; (**c**) compressor discharge pressure; and (**d**) COP.

As shown in Figure 7, as the air backflow rate of the underhood is increased from 0% to 30%, the heat exchange performance and energy efficiency of the system is reduced. Specifically, when ambient temperature is 30 °C, the heat exchange of evaporator is reduced from 4693 to 4214 W and the reduction rate is 10.2%, at the same time, while the system COP is reduced from 3.07 to 1.96 and the reduction rate is 36.16%. Thus, more than a 35% improvement of COP could be achieved solely by eliminating air backflow of the underhood of PHEV, which indicates that the decline of the air backflow rate of the underhood enhances the cooling capacity in the air conditioning system. In fact, when the air backflow rate is enhanced, the oncoming air temperature of the condenser will be increased and the heat exchange capacity of the condenser will be decreased, enhancing the condensing pressure and the condensing temperature, thus increasing the discharge pressure of the compressor, as shown in Figure 2(C). Furthermore, when the compressor speed remains unchanged, the suction pressure of the compressor will increase, and the evaporation pressure and evaporation temperature will increase accordingly; thus, the cooling capacity will increase. Moreover, the increase in the suction pressure will cause the compressor power consumption to increase, and the system COP will decrease.

3.2. Effect of Air Backflow Rate under the Different Air Backflow Distribution

In fact, the air backflow phenomenon of the underhood occurs in different local areas of the condenser; thus, the influence of different air backflow distribution on the air conditioning system is analyzed in this section. In view of the fact that the distribution ratio of the cooling tube of the condenser analyzed in this paper is 27:13:7:5, the air backflow distribution form is set according to 27:13:7:5 (uniform distribution), 1:1:1:1, and 1:1:2:2. Figure 8 shows that under different backflow distribution, the air backflow rate has an effect on the performance of the air conditioning system.

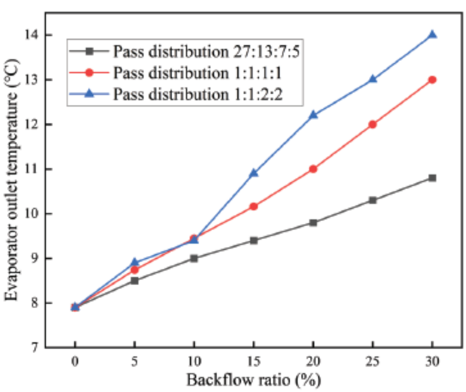

(**a**)

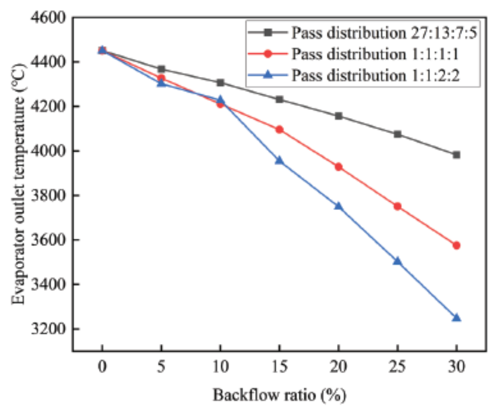

(**b**)

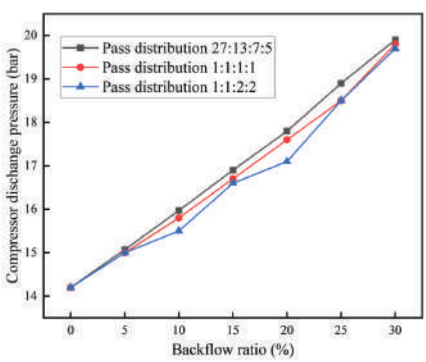

(**c**)

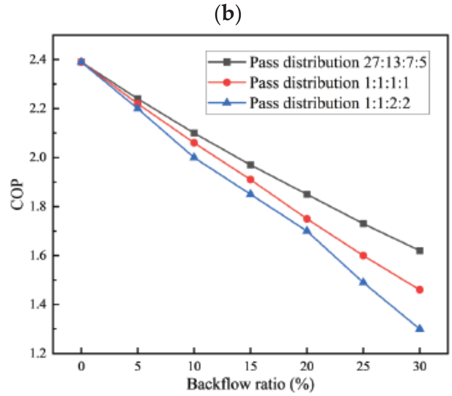

(**d**)

Figure 8. Influences of the backflow rate on air conditioning performances under different ambient temperatures. (**a**) Evaporator exit temperature; (**b**) evaporator heat rejection; (**c**) discharge pressure; and (**d**) COP.

As shown in Figure 8, when the air backflow rate is lower than 10%, the air backflow distribution has almost no effect on the performance of air conditioning system. However, when the air backflow rate is higher than 10%, compared to the air backflow concentrated under the condenser (Pass distribution 27:13:7:5) when air backflow is evenly distributed on the surface of the condenser, the cooling capacity of the air conditioning system will be higher and the system efficiency will improve. Specifically, compared to the air backflow concentrated under the condenser, when the air backflow rate is 30% and air backflow is evenly distributed on the surface of the condenser, the heat exchange performance increases from 3248 to 3983 W and the growth rate is 22.6%; at the same time, the system COP increases from 1.3 to 1.62 and the reduction rate is 24.6%, which indicates that the air backflow should be distributed as evenly as possible at the front end of the condenser.

3.3. Mechanism Analysis of Backflow Phenomenon

The analysis in the above section exhibits that the air backflow rate and air backflow distribution of the underhood have a great impact on the performance of the air conditioning system. In order to avoid the impact of air backflow on the air conditioning system of PHEV, the mechanism that causes the backflow phenomenon is analyzed in this section; thus, the performance of the air conditioning system can be optimized in the subsequent section.

The air backflow phenomenon of the underhood is analyzed and the distribution of air backflow on the surface of the condenser is shown in Figure 9.

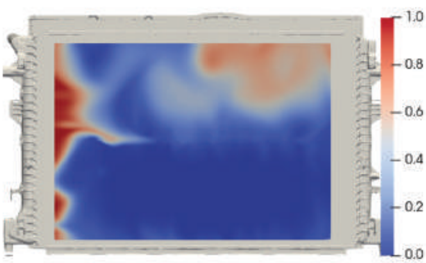

(**a**)

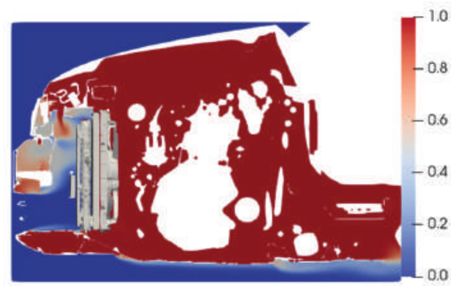

(**b**)

Figure 9. Backflow air distribution of original structure. (**a**) Backflow air distribution front view; (**b**) backflow air distribution side view.

Figure 9 shows that the distribution of the backflow hot air on the surface of the condenser is mainly concentrated on the left and upper right corners of the condenser. In order to trace the source of backflow hot air, as shown in Figure 9b, most of the backflow hot air is generated by the gap between the radiator and the bracket and the gap between the air guide parts.

3.4. Mechanism Analysis of Air Backflow Phenomenon

In order to eliminate the impact of air backflow on the air conditioning system, a cooling module of the underhood for PHEV is optimized in this section. The optimized structure is shown in the Figure 10. As shown in red in Figure 10, the gap between the radiator and the bracket is sealed and the gap around the air guide is reduced.

Figure 11 shows the optimized results of the PHEV underhood, and that the air backflow phenomenon in the left area is significantly improved and that there only is some backflow hot air around some pores that cannot be sealed.

In order to quantitatively analyze the backflow phenomenon of the optimized structure, the air backflow rate and the mass flow of backflow air are calculated based on the heat flux regression method, and the results are shown in Table 2.

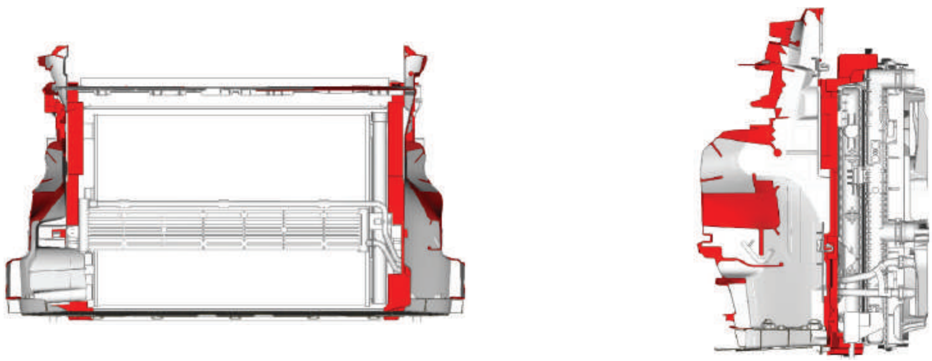

(**a**) (**b**)

Figure 10. Optimized cooling module of PHEV. (**a**) Optimized structure front view; (**b**) optimized structure side view.

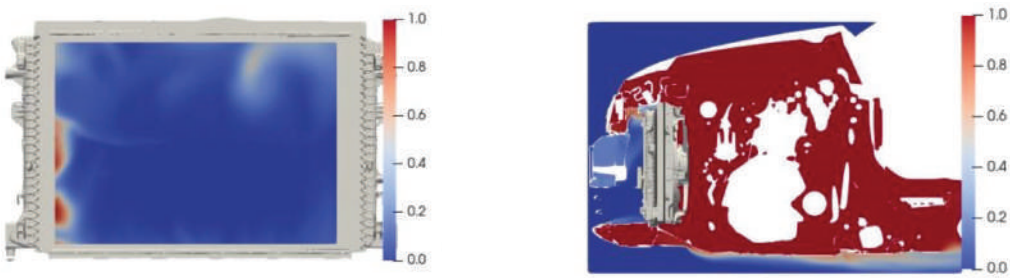

(**a**) (**b**)

Figure 11. Backflow air distribution of optimized structure. (**a**) Optimized structure front view; (**b**) optimized structure side view.

Table 2. Comparison of the backflow rate of the optimized cooling module and the original structure.

	Air Mass Flow (kg/s)	Backflow Ratio (%)	Backflow Air Mass Flow (kg/s)
Original Structure	0.518	32.7	0.169
Optimized structure	0.518	9.3	0.048

As shown in Table 2, compared with the original structure, the backflow rate of the optimized structure is reduced from 32.7% to 9.3%, the backflow air in the left area is significantly reduced, and the backflow air mass flow is reduced from 0.169 kg/s to 0.048 kg/s. The reduction rate is 36.16% and the backflow situation of underhood cooling module is significantly improved.

In order to verify results of the optimization, the performance of the air conditioning system installed with the original cooling module and the optimized cooling structure is tested in a real vehicle under driving conditions of 32 km/h. The performance results of the air conditioning system are shown in Figure 12.

As shown in Figure 12, when the air backflow phenomenon is weakened, the cooling capacity of the air conditioning system is significantly better. Compared with the original underhood cooling structure, the cabin temperature can be reduced by 3–5 °C.

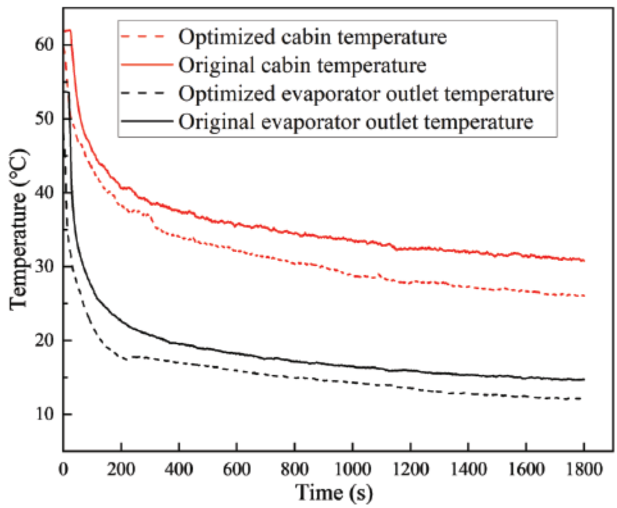

Figure 12. HVAC performances after reflux optimization.

4. Conclusions

The air backflow phenomenon of the PHEV underhood is quantitatively investigated in this paper and the relevant conclusions are as follows:

(1) The heat flux marking method proposed in this paper can accurately quantify the backflow phenomenon in the underhood of PHEV based on the momentum transport equation.
(2) The decrease in the air backflow rate of the underhood helps to improve the refrigeration capacity of the air conditioning system, thereby increasing the COP of the system
(3) When the air backflow ratio cannot be reduced below 10%, the air backflow should be distributed as evenly as possible at the front end of the condenser.
(4) In order to eliminate the impact of air backflow on the PHEV underhood, the gap between the radiator and the bracket is sealed and the gap around the air guide is reduced. Compared with the original structure, the air backflow rate of the optimized structure is reduced from 32.7% to 9.3% and the cabin temperature can be reduced by 3–5 °C.

In order to further investigate the effect of backflow phenomenon of the underhood on air conditioning system, digital twin technology should be considered in the future so that backflow phenomenon can be investigated in an all-round way without a large number of time-consuming and high-cost experiments and simulations.

Author Contributions: Funding acquisition, S.X.; investigation, H.W. and X.T.; methodology, H.W.; project administration, S.X.; visualization, J.Z.; writing—original draft, H.W.; writing—review and editing, X.T. All authors have read and agreed to the published version of the manuscript.

Funding: The authors wish to acknowledge for the financial support from the National Natural Science Foundation of China Grant No. 21776221, for the work reported in this paper.

Institutional Review Board Statement: Not applicable.

Informed Consent Statement: Not applicable.

Data Availability Statement: Not applicable.

Conflicts of Interest: The authors declare that they have no known competing financial interests or personal relationships that could have appeared to influence the work reported in this paper.

Nomenclature

PHEV	plug-in hybrid electric vehicles
ACS	air conditioning system
ICE	internal combustion engine
UDDS	urban dynamometer driving schedule
CFD	computational fluid dynamics
EMS	energy management strategy
COP	coefficient of performance
BTMS	battery thermal management system
MTMS	motor thermal management system
Acronyms	
V_{th}	displacement of the compressor
m_{com}	mass flow of the compressor
P_{comp}	energy consumption of the compressor
h_{suc}	suction enthalpy of the compressor
$h_{dis\|_s}$	exhaust enthalpy under the condition of isentropic compression
ρ	density
η	inertial resistance coefficient
γ	volume proportion of the hot air
ϕ	volumetric flow coefficient
Nu	Nusselt number
Pr_t	Prandtl number
V_{tip}	linear velocity of the fan blade tip
r_{com}	rotary speed of the compressor
η_v	volumetric efficiency of the compressor
h_{dis}	exhaust enthalpy of the compressor
η_s	isentropic efficiency
f_Q	heat loss of compressor
u	velocity vector
$\frac{1}{\beta}$	viscous resistance coefficient
C_r	heat capacity ratio
Re	Reynold number
$\dot{Q}$	volume flow of air
A_{fan}	Fan Area

References

1. Solmaz, H.; Ardebili, S.; Calam, A.; Yılmaz, E.; İpci, D. Prediction of Performance and Exhaust Emissions of a CI Engine Fueled with Multi-Wall Carbon Nanotube Doped Biodiesel-Diesel Blends Using Response Surface Method. *Energy* **2021**, *227*, 120518. [CrossRef]
2. Geng, L.; Xiao, Y.; Li, S.; Chen, H.; Chen, X. Effects of injection timing and rail pressure on particulate size-number distribution of a common rail DI engine fueled with fischer-tropsch diesel synthesized from coal. *J. Energy Inst.* **2021**, *95*, 219–230. [CrossRef]
3. Liu, J.; Wu, P.; Sun, P.; Ji, Q.; Zhang, Q.; Wang, P. Effects of iron-based fuel borne catalyst addition on combustion, in-cylinder soot distribution and exhaust emission characteristics in a common-rail diesel engine. *Fuel* **2021**, *290*, 120096. [CrossRef]
4. Zhang, Y.; Yuan, X.; Duan, L.; Xu, Y.; Lan, F. Environmental temperature effects on the energy flow of plug-in hybrid electric vehicles. *J. Power Sources* **2021**, *506*, 230231. [CrossRef]
5. Mahmoodi-k, M.; Montazeri, M.; Madanipour, V. Simultaneous multi-objective optimization of a PHEV power management system and component sizing in real world traffic condition. *Energy* **2021**, *233*, 121111. [CrossRef]
6. Aljehane, N.; Mansour, R. Optimal allocation of renewable energy source and charging station for PHEVs. *Sustain. Energy Technol. Assess.* **2021**, *49*, 101669. [CrossRef]
7. Böhme, T.; Frank, B. *Hybrid Systems, Optimal Control and Hybrid Vehicles*; Springer: Berlin/Heidelberg, Germany, 2017.
8. Hemmati, S.; Doshi, N.; Hanover, D.; Morgan, C.; Shahbakhti, M. Integrated cabin heating and powertrain thermal energy management for a connected hybrid electric vehicle. *Appl. Energy* **2021**, *283*, 116353. [CrossRef]
9. Liu, J.; Chen, Y.; Li, W.; Shang, F.; Zhan, J. Hybrid-Trip-Model-Based Energy Management of a PHEV with Computation-Optimized Dynamic Programming. *IEEE Trans. Veh. Technol.* **2018**, *67*, 338–353. [CrossRef]
10. Fan Li Zhang, Y.; Dou, H.; Zou, R. Design of an integrated energy management strategy for a plug-in hybrid electric bus. *J. Power Sources* **2019**, *448*, 227391. [CrossRef]

11. Chen, Z.; Xiong, R.; Cao, J. Particle swarm optimization-based optimal power management of plug-in hybrid electric vehicles considering uncertain driving conditions. *Energy* **2016**, *96*, 197–208. [CrossRef]
12. Liu, T.; Hu, X.; Li, S.; Cao, D. Reinforcement Learning Optimized Look-Ahead Energy Management of a Parallel Hybrid Electric Vehicle. *IEEE Trans. Mechatron.* **2017**, *22*, 1497–1507. [CrossRef]
13. Peng, J.; He, H.; Xiong, R. Rule based energy management strategy for a series-parallel plug-in hybrid electric bus optimized by dynamic programming. *Appl. Energy* **2017**, *185*, 1633–1643. [CrossRef]
14. Song, P.; Lei, Y.; Fu, Y. Multi-objective optimization and matching of power source for PHEV based on genetic algorithm. *Energies* **2020**, *13*, 1127. [CrossRef]
15. Ribau, J.; Sousa, J.; Silva, C. *Multi-Objective Optimization of Fuel Cell Hybrid Vehicle Powertrain Design—Cost and Energy*; SAE Technical Paper; SAE: Detroit, MI, USA, 2013. [CrossRef]
16. Qi, X.; Wu, G.; Boriboonsomsin, K.; Barth, M.J. Development and evaluation of an evolutionary algorithm-based online energy management system for plug-in hybrid electric vehicles. *IEEE Trans. Intell. Transp. Syst.* **2017**, *18*, 2181–2191. [CrossRef]
17. Silva, S.; Eckert, J.; Silva, F.; Silva, L.; Dedini, F. Multi-objective optimization design and control of plug-in hybrid electric vehicle powertrain for minimization of energy consumption, exhaust emissions and battery degradation. *Energy Convers. Manag.* **2021**, *234*, 113909. [CrossRef]
18. Pan, L.; Liu, C.; Zhang, Z.; Wang, T.; Shi, J.; Chen, J. Energy-saving effect of utilizing recirculated air in electric vehicle air conditioning system. *Int. J. Refrig.* **2019**, *12*, 122–129. [CrossRef]
19. Zhang, Z.; Liu, C.; Chen, X.; Zhang, C.; Chen, J. Annual energy consumption of electric vehicle air conditioning in China. *Appl. Therm. Eng.* **2017**, *125*, 567–574. [CrossRef]
20. Oh, M.; Ahn, J.; Kim, D.; Jang, D.; Kim, Y. Thermal comfort and energy saving in a vehicle compartment using a localized air-conditioning system. *Appl. Energy* **2014**, *133*, 14–21. [CrossRef]
21. Jeffers, M.; Chaney, L.; Rugh, J. *Climate Control Load Reduction Strategies for Electric Drive Vehicles in Warm Weather*; SAE Technical Paper; SAE: Detroit, MI, USA, 2015. [CrossRef]
22. Liu, Y.; Gao, Q.; Zhang, T.; Cui, C.; Jin, S. Exploration of interactive thermal influence characteristics of power and air conditioning system based on 1D/3D coupling calculation in electric vehicle underhood. *Appl. Therm. Eng.* **2020**, *167*, 114717. [CrossRef]
23. Hofstadtera, R.; Jorge, A.; Kozek, M. Energy optimal control of thermal comfort in trams. *Appl. Therm. Eng.* **2018**, *143*, 812–821. [CrossRef]
24. Collier, J.; Thome, J. *Convective Boiling and Condensation*, 3rd ed.; Oxford University Press: Oxford, UK.
25. Shen, M.; Gao, Q. System simulation on refrigerant-based battery thermal management technology for electric vehicles. *Energy Convers. Manag.* **2020**, *203*, 112176. [CrossRef]

sustainability

MDPI

Article

Modeling of Non-Characteristic Third Harmonics Produced by Voltage Source Converter under Unbalanced Condition

Min Zhang *, Huiqiang Zhi, Shifeng Zhang, Rui Fan, Ran Li and Jinhao Wang

State Grid Shanxi Electric Power Research Institute, Taiyuan 030024, China; ypub75@163.com (H.Z.); sgwd53@163.com (S.Z.); ctwf99@163.com (R.F.); lydq47@163.com (R.L.); hkzd90@163.com (J.W.)
* Correspondence: ffwy26@163.com

Abstract: A three-phase three-wire voltage source converter (VSC) can produce third harmonics when it is operated under an unbalanced condition. It is essential to understand the mechanism of the production of this third harmonic and to assess its impact on power systems. Therefore, this paper presents an analytical model of the VSC under the unbalanced condition through mathematical derivations, and the final model is a coupled Thevenin circuit. The proposed model allows for direct computation of the non-characteristic third harmonics through harmonic power flow studies. The results show that VSC under unbalanced conditions emits both positive-sequence and negative-sequence third harmonics, and that the positive-sequence third harmonic is much larger than the negative-sequence third harmonic. It also shows that the unbalanced level and the size of the dc-link capacitor are critical to the level of non-characteristic third harmonics. The correctness of the proposed model and its application on noncharacteristic third harmonic evaluations have been verified using EMT simulations.

Keywords: voltage source converter; unbalanced condition; non-characteristic third harmonic; harmonic modeling

Citation: Zhang, M.; Zhi, H.; Zhang, S.; Fan, R.; Li, R.; Wang, J. Modeling of Non-Characteristic Third Harmonics Produced by Voltage Source Converter under Unbalanced Condition. *Sustainability* **2022**, *14*, 6449. https://doi.org/10.3390/su14116449

Academic Editor: Guang Zeng

Received: 25 April 2022
Accepted: 17 May 2022
Published: 25 May 2022

1. Introduction

In this context, this paper presents an analytical model of the VSC under unbalanced conditions for the direct computation of the non-characteristic third harmonics through rigorous mathematical derivations. The new model reveals the mechanism of the generation of third harmonics and the characteristics of third harmonics. The new model shows that a Thevenin circuit can represent the VSC for both the positive-sequence and negative-sequence third harmonics. In addition, there are coupling effects between the positive-sequence and negative-sequence third harmonics. The model also shows that the positive-sequence third harmonic is much larger than the negative-sequence third harmonic. The computation of the source and the impedance of the developed Thevenin model requires positive-sequence and negative-sequence fundamental frequency voltage and current on the ac side of the VSC, which can be obtained through load flow studies.

Power electronic devices have experienced a dramatic increase in modern power systems due to the initiative of renewable energies such as wind power generation and photovoltaic (PV) [1], and other applications such as flexible AC transmission system (FACTS) and high voltage DC (HVDC) transmission [2,3]. In recent years, the voltage source converter (VSC) has become the most popular basis of power electronic devices due to its advantages of bidirectional power flow and independent control of active and reactive power [4]. With the massive integration of these VSC devices, there is a concern about their harmonic impact on power systems [5–7]. Under the normal condition, VSC devices only produce very-high-frequency harmonics, which is produced by the PWM switching, but such harmonics can generally be impeded by a passive filter in front of the VSC [8,9]. However, VSC devices can generate low-order non-characteristic third harmonics under the unbalanced condition, which is a power quality concern of power systems. Such a phenomenon occurs because the unbalanced fundamental frequency voltage and current on the ac side of the VSC can induce second harmonic ripples in the dc-link voltage of the VSC through the switching process [9]. These second harmonic ripples in the dc-link voltage, in turn, will lead to a third harmonic voltage on the ac side of the VSC, again through the switching process. As a result, under the unbalanced condition, the VSC becomes a voltage source at the third harmonic. Therefore, it is essential to understand the mechanism of the production of the third harmonic voltage, especially in the distribution system, which can be unbalanced since single-phase loads are dominant [10]. A computation method of the third harmonics under the unbalanced conditions is also needed to assess their impacts.

To date, there are numerous papers presenting the studies of the VSC under unbalanced conditions, but most of these works focus on the control strategies that can suppress the unbalanced condition-induced third harmonics [11–14]. These papers have shown that the unbalanced fundamental frequency voltage and current will lead to double-frequency power oscillation on the ac side of the VSC. As a result, the dc side experiences second harmonic voltage, which can lead to third harmonics on the ac side of the VSC. Based on this finding, the control schemes that can be used to suppress the second harmonic on the dc-link are designed in [12,13]. However, these papers do not provide an analytical algorithm to compute the second harmonic on the dc side or the third harmonic on the ac side. A few other works are proposed specifically for assessing VSC's third harmonic emission under unbalanced conditions [15–17]. In [15], the switching function of the VSC and the harmonic interaction between the ac side and dc side of the VSC are analyzed to obtain the model that can be used to compute the third harmonic distortion. Nevertheless, the impact of the third harmonic on the switching function is not included in this method. Thus, the result could be inaccurate. In [16], the oscillation between the dc side and ac side of the VSC is analyzed based on the ac/dc power interaction, which reveals the mechanism of the production of the third harmonic, but the final analytical method of the uncharacteristic third harmonics is not presented. The reference [17] further provides a method for assessing the third harmonic distortions using the power interaction between the ac side and dc side of the VSC. However, the proposed model omits the effect of the control loop so that the model is not accurate. Moreover, this method is not able to fully show the differences between the positive-sequence and negative-sequence third harmonics and the coupling effect between these two kinds of third harmonics. References [18,19] propose a method that can be used to reveal the harmonic characteristics of the VSC by analyzing the control and AC/DC interaction, but the non-characteristic third harmonics are not analyzed. In summary, a full model that reveals the characteristics of third harmonics produced by VSC is still desired.

This paper presents an analytical model of the VSC under unbalanced conditions for the direct computation of the non-characteristic third harmonics through rigorous mathematical derivations. The development of the new model reveals the mechanism of the generation of third harmonics and their characteristics. The new model shows that a Thevenin circuit can represent the VSC at both the positive-sequence and negative-sequence third harmonics. In addition, there are coupling effects between the positive-sequence and negative-sequence third harmonics. The model also shows that the positive-sequence third harmonic is much larger than the negative-sequence third harmonic. The computation of the source and the impedance of the developed Thevenin model requires a positive-sequence and negative-sequence fundamental frequency voltage and current on the ac side of the VSC, which can be obtained through load flow studies.

The rest of this paper is organized as follows. Section 2 explains the mechanism of generating the non-characteristic third harmonics by the VSC under unbalanced conditions. Section 3 presents the development of the model of VSC under unbalanced conditions for a non-characteristic third harmonic. The proposed model is validated via time-domain simulations in Section 4. Section 5 shows some discussions on the proposed model.

2. Mechanism of the Production of Noncharacteristic Third Harmonics

A typical VSC system is illustrated in Figure 1a, and the control strategy of this VSC is presented in Figure 1b. As one can see, a two-loop control scheme is used, and the outer control loop is used to generate the reference current for the inner current control. The current is controlled using a PI regulator. A capacitor contains the dc-link voltage of the VSC. An inductor L_f is connected at the front end of the VSC to filter out the switching harmonics.

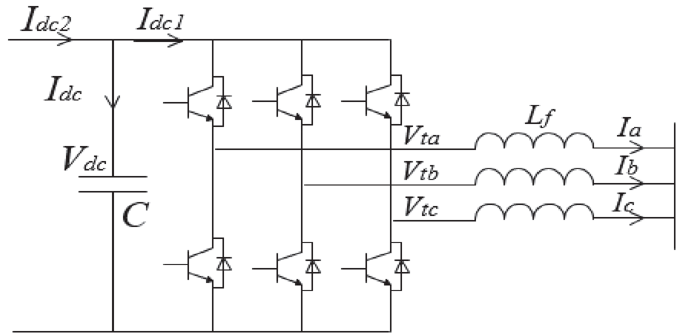

(**a**)

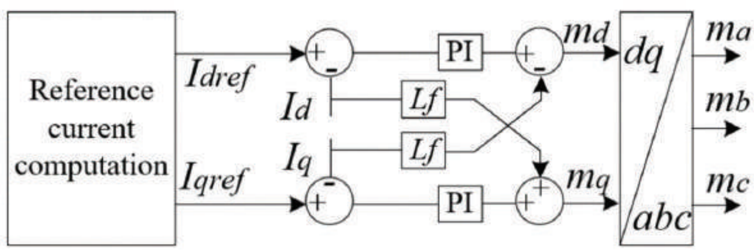

(**b**)

Figure 1. The VSC for unbalanced condition illustration. (**a**) VSC. (**b**) Control of the VSC.

Under the unbalanced operational condition, there are positive-sequence and negative-sequence fundamental frequency voltage and current on the AC side of the VSC, and the three-phase current can be expressed as

$$\begin{aligned} I_a(t) &= I_{1+}\cos(\omega_1 t + \delta_{1+}) + I_{1-}\cos(\omega_1 t + \delta_{1-}) \\ I_b(t) &= I_{1+}\cos(\omega_1 t + \delta_{1+} - 120^\circ) + I_{1-}\cos(\omega_1 t + \delta_{1-} + 120^\circ) \\ I_c(t) &= I_{1+}\cos(\omega_1 t + \delta_{1+} + 120^\circ) + I_{1-}\cos(\omega_1 t + \delta_{1-} - 120^\circ) \end{aligned} \tag{1}$$

It is noted that the modulation signal is a result of the inner current control, so the modulation signal contains the same types of components as those in the current. Thus, the three-phase modulation signals can be expressed as

$$\begin{aligned} m_a(t) &= m_{1+}\cos(\omega_1 t + \theta_{1+}) + m_{1-}\cos(\omega_1 t + \theta_{1-}) \\ m_b(t) &= m_{1+}\cos(\omega_1 t + \theta_{1+} - 120^\circ) + m_{1-}\cos(\omega_1 t + \theta_{1-} + 120^\circ) \\ m_c(t) &= m_{1+}\cos(\omega_1 t + \theta_{1+} + 120^\circ) + m_{1-}\cos(\omega_1 t + \theta_{1-} - 120^\circ) \end{aligned} \tag{2}$$

Since we focus on the study of the third harmonic, the high-frequency harmonics in the switching function can be omitted. Consequently, the modulation signal can be used to represent the switching function of the VSC. As a result, based on (1) and (2), the current on the DC side can be computed as

$$\begin{aligned} I_{dc}(t) &= m_a(t)I_a(t) + m_b(t)I_b(t) + m_c(t)I_c(t) \\ &= \tfrac{3}{2}m_{1+}I_{1+}\cos(\theta_{1+} - \delta_{1+}) + \tfrac{3}{2}m_{1-}I_{1-}\cos(\theta_{1-} - \delta_{1-}) \\ &+ \tfrac{3}{2}m_{1+}I_{1-}\cos(2\omega_1 t + \theta_{1+} + \delta_{1-}) + \tfrac{3}{2}m_{1-}I_{1+}\cos(2\omega_1 t + \theta_{1-} + \delta_{1+}) \end{aligned} \tag{3}$$

According to the above DC side current, the voltage on the DC-link capacitor can be written as

$$\begin{aligned} V_{dc}(t) &= \tfrac{1}{C}\int_0^t i_{dc}(t)dt + V_{dc}(0) \\ &= V_{dc0} + \frac{3}{4C\omega_1}m_{1+}I_{1-}\cos(2\omega_1 t + \theta_{1+} + \delta_{1-} - \tfrac{\pi}{2}) \\ &+ \frac{3}{4C\omega_1}m_{1-}I_{1+}\cos(2\omega_1 t + \theta_{1-} + \delta_{1+} - \tfrac{\pi}{2}) \end{aligned} \tag{4}$$

where V_{dc0} is the steady-state dc-link voltage. It can be seen that, due to the unbalanced condition, there are second harmonic ripples in the dc-link voltage. It is noteworthy that the expression in (4) is obtained on the basis that all dc-side harmonic currents pass through the dc-link capacitor. In practice, there will be a load (or source) on the other side of the dc-link that has an equivalent impedance Z_{load}, and the harmonic components in I_{dc} will be distributed between the load and dc-link capacitor (I_{dc1} and I_{dc2} in Figure 1a), that is, all of the harmonic components in (4) will be multiplied by $Z_{load}/(Z_{load} + Z_C)$. For simplification but not losing generality, Z_{load} is assumed to be very large so it can be ignored. The DC-link voltage in (4) is converted to AC voltage through the switching process, obtaining the expressions of the three-phase voltages, which are expressed in (5)~(7).

As one can see from (5)~(7), there are third harmonic components in the three-phase voltage of the VSC. In addition, it is found that the third harmonic voltages contain both positive-sequence or negative-sequence components, which are different from the conventional zero-sequence third harmonic. It can also be noted that the third harmonic is in the form of a voltage that is only affected by the positive-sequence and negative-sequence fundamental frequency components.

$$\begin{aligned} V_{ta}(t) &= m_a(t)V_{dc}(t) \\ &= \{m_{1+}\cos(\omega_1 t + \theta_{1+}) + m_{1-}\cos(\omega_1 t + \theta_{1-})\}V_{dc0} + \tfrac{3}{8\omega_1 C}m_{1+}{}^2 I_{1-}\cos(\omega_1 t + \delta_{1-} - \tfrac{\pi}{2}) + \tfrac{3}{8\omega_1 C}m_{1+}m_{1-}I_{1-}\cos(\omega_1 t + \theta_{1+} - \theta_{1-} + \delta_{1-} - \tfrac{\pi}{2}) \\ &+ \tfrac{3}{8\omega_1 C}m_{1-}m_{1+}I_{1+}\cos(\omega_1 t + \theta_{1-} - \theta_{1+} + \delta_{1+} - \tfrac{\pi}{2}) + \tfrac{3}{8\omega_1 C}m_{1-}{}^2 I_{1+}\cos(\omega_1 t + \delta_{1+} - \tfrac{\pi}{2}) + \tfrac{3}{8\omega_1 C}m_{1+}{}^2 I_{1-}\cos(3\omega_1 t + 2\theta_{1+} + \delta_{1-} - \tfrac{\pi}{2}) \\ &+ \tfrac{3}{8\omega_1 C}m_{1+}m_{1-}I_{1-}\cos(3\omega_1 t + \theta_{1+} + \theta_{1-} + \delta_{1-} - \tfrac{\pi}{2}) + \tfrac{3}{8\omega_1 C}m_{1-}m_{1+}I_{1+}\cos(3\omega_1 t + \theta_{1-} + \theta_{1+} + \delta_{1+} - \tfrac{\pi}{2}) + \tfrac{3}{8\omega_1 C}m_{1-}{}^2 I_{1+}\cos(3\omega_1 t + 2\theta_{1-} + \delta_{1+} - \tfrac{\pi}{2}) \end{aligned} \tag{5}$$

$$\begin{aligned} V_{tb}(t) &= m_b(t)V_{dc}(t) \\ &= \{m_{1+}\cos(\omega_1 t + \theta_{1+} - 120^\circ) + m_{1-}\cos(\omega_1 t + \theta_{1-} + 120^\circ)\}V_{dc0} + \tfrac{3}{8\omega_1 C}m_{1+}{}^2 I_{1-}\cos(3\omega_1 t + 2\theta_{1+} + \delta_{1-} - \tfrac{\pi}{2} - 120^\circ) \\ &+ \tfrac{3}{8\omega_1 C}m_{1+}{}^2 I_{1-}\cos(\omega_1 t + \delta_{1-} - \tfrac{\pi}{2} + 120^\circ) + \tfrac{3}{8\omega_1 C}m_{1+}m_{1-}I_{1-}\cos(3\omega_1 t + \theta_{1+} + \theta_{1-} + \delta_{1-} - \tfrac{\pi}{2} + 120^\circ) \\ &+ \tfrac{3m}{8\omega_1 C}m_{1+}m_{1-}I_{1-}\cos(\omega_1 t + \theta_{1+} - \theta_{1-} + \delta_{1-} - \tfrac{\pi}{2} - 120^\circ) + \tfrac{3}{8\omega_1 C}m_{1-}m_{1+}I_{1+}\cos(3\omega_1 t + \theta_{1-} + \theta_{1+} + \delta_{1+} - \tfrac{\pi}{2} - 120^\circ) \\ &+ \tfrac{3}{8\omega_1 C}m_{1-}m_{1+}I_{1+}\cos(\omega_1 t + \theta_{1-} - \theta_{1+} + \delta_{1+} - \tfrac{\pi}{2} + 120^\circ) + \tfrac{3}{8\omega_1 C}m_{1-}{}^2 I_{1+}\cos(3\omega_1 t + 2\theta_{1-} + \delta_{1+} - \tfrac{\pi}{2} + 120^\circ) + \tfrac{3}{8\omega_1 C}m_{1-}{}^2 I_{1+}\cos(\omega_1 t + \delta_{1+} - \tfrac{\pi}{2} - 120^\circ) \end{aligned} \tag{6}$$

$$\begin{aligned} V_{tc}(t) &= m_c(t)V_{dc}(t) \\ &= \{m_{1+}\cos(\omega_1 t + \theta_{1+} - 120^\circ) + m_{1-}\cos(\omega_1 t + \theta_{1-} + 120^\circ)\}V_{dc0} + \tfrac{3}{8\omega_1 C}m_{1+}{}^2 I_{1-}\cos(3\omega_1 t + 2\theta_{1+} + \delta_{1-} - \tfrac{\pi}{2} + 120^\circ) \\ &+ \tfrac{3}{8\omega_1 C}m_{1+}{}^2 I_{1-}\cos(\omega_1 t + \delta_{1-} - \tfrac{\pi}{2} - 120^\circ) + \tfrac{3}{8\omega_1 C}m_{1+}m_{1-}I_{1-}\cos(3\omega_1 t + \theta_{1+} + \theta_{1-} + \delta_{1-} - \tfrac{\pi}{2} - 120^\circ) \\ &+ \tfrac{3}{8\omega_1 C}m_{1+}m_{1-}I_{1-}\cos(\omega_1 t + \theta_{1+} - \theta_{1-} + \delta_{1-} - \tfrac{\pi}{2} + 120^\circ) + \tfrac{3}{8\omega_1 C}m_{1-}m_{1+}I_{1+}\cos(3\omega_1 t + \theta_{1-} + \theta_{1+} + \delta_{1+} - \tfrac{\pi}{2} + 120^\circ) \\ &+ \tfrac{3}{8\omega_1 C}m_{1-}m_{1+}I_{1+}\cos(\omega_1 t + \theta_{1-} - \theta_{1+} + \delta_{1+} - \tfrac{\pi}{2} - 120^\circ) + \tfrac{3}{8\omega_1 C}m_{1-}{}^2 I_{1+}\cos(3\omega_1 t + 2\theta_{1-} + \delta_{1+} - \tfrac{\pi}{2} - 120^\circ) + \tfrac{3}{8\omega_1 C}m_{1-}{}^2 I_{1+}\cos(\omega_1 t + \delta_{1+} - \tfrac{\pi}{2} + 120^\circ) \end{aligned} \tag{7}$$

3. Modeling VSC under Unbalanced Condition

The above analysis has shown that an unbalanced condition can introduce a third harmonic voltage for the VSC. Such a third harmonic voltage will further introduce a third harmonic current in the interconnected grid. As a result of the current feedback control strategy, the third harmonic current would lead to an additional third harmonic voltage on the ac side of the VSC via the control section. As a result, the third harmonic voltage of the VSC shall be computed as shown in Figure 2. As can be seen, there are two parts to be included. The first is the third harmonic voltage caused by the fundamental frequency voltage and current, and the second is the distribution of this third harmonic voltage. To compute the final voltage, it is necessary to include the third harmonic on the ac side of the

VSC, and, as a result, the steady-state current and modulation signal can be expressed as (8) and (9).

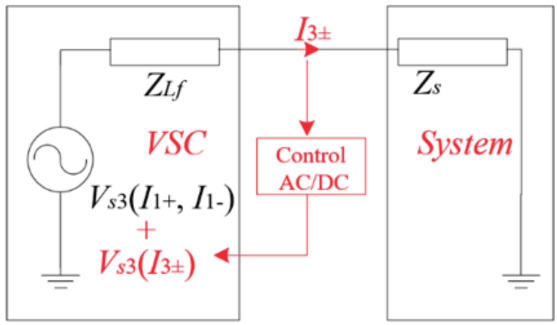

Figure 2. Illustration of modeling of the third harmonic.

$$\begin{aligned}
&I_a(t) = I_{1+}\cos(\omega_1 t + \delta_{1+}) + I_{1-}\cos(\omega_1 t + \delta_{1-}) \\
&+I_{3+}\cos(3\omega_1 t + \delta_{3+}) + I_{3-}\cos(3\omega_1 t + \delta_{3-}) \\
&I_b(t) = I_{1+}\cos(\omega_1 t + \delta_{1+} - 120^\circ) + I_{1-}\cos(\omega_1 t + \delta_{1-} + 120^\circ) \\
&+I_{3+}\cos(3\omega_1 t + \delta_{3+} - 120^\circ) + I_{3-}\cos(3\omega_1 t + \delta_{3-} + 120^\circ) \\
&I_c(t) = I_{1+}\cos(\omega_1 t + \delta_{1+} + 120^\circ) + I_{1-}\cos(\omega_1 t + \delta_{1-} - 120^\circ) \\
&+I_{3+}\cos(3\omega_1 t + \delta_{3+} + 120^\circ) + I_{3-}\cos(3\omega_1 t + \delta_{3-} - 120^\circ)
\end{aligned} \tag{8}$$

$$\begin{aligned}
&m_a = m_{1+}\cos(\omega_1 t + \theta_{1+}) + m_{1-}\cos(\omega_1 t + \theta_{1-}) \\
&+m_{3+}\cos(3\omega_1 t + \theta_{3+}) + m_{3-}\cos(3\omega_1 t + \theta_{3-}) \\
&m_b = m_{1+}\cos(\omega_1 t + \theta_{1+} - 120^\circ) + m_{1-}\cos(\omega_1 t + \theta_{1-} + 120^\circ) \\
&+m_{3+}\cos(3\omega_1 t + \theta_{3+} - 120^\circ) + m_{3-}\cos(3\omega_1 t + \theta_{3-} + 120^\circ) \\
&m_c = m_1\cos(\omega_1 t + \theta_{1+} + 120^\circ) + m_{1-}\cos(\omega_1 t + \theta_{1-} - 120^\circ) \\
&+m_{3+}\cos(3\omega_1 t + \theta_{3+} + 120^\circ) + m_{3-}\cos(3\omega_1 t + \theta_{3-} - 120^\circ)
\end{aligned} \tag{9}$$

The equations in (8) and (9) can be used to obtain the current on the DC side, which is given as (10):

$$\begin{aligned}
&I_{dc}(t) = m_a(t)I_a(t) + m_b(t)I_b(t) + m_c(t)I_c(t) \\
&= \frac{3}{2}\left\{\begin{array}{l}
m_{1+}I_{1+}\cos(\theta_{1+} - \delta_{1+}) + m_{1+}I_{1-}\cos(2\omega_1 t + \theta_{1+} + \delta_{1-}) \\
+m_{1+}I_{3+}\cos(2\omega_1 t + \delta_{3+} - \theta_{1+}) + m_{1+}I_{3-}\cos(4\omega_1 t + \delta_{3-} + \theta_{1+}) \\
+m_{1-}I_{1+}\cos(2\omega_1 t + \theta_{1-} + \delta_{1+}) + m_{1-}I_{1-}\cos(\theta_{1-} - \delta_{1-}) \\
+m_{1-}I_{3+}\cos(4\omega_1 t + \delta_{3+} + \theta_{1-}) + m_{1-}I_{3-}\cos(2\omega_1 t + \delta_{3-} - \theta_{1-}) \\
+m_{3+}I_{1+}\cos(2\omega_1 t + \theta_{3+} - \delta_{1+}) + m_{3+}I_{1-}\cos(4\omega_1 t + \theta_{3+} + \delta_{1-}) \\
+m_{3+}I_{3+}\cos(\theta_{3+} - \delta_{3+}) + m_{3+}I_{3-}\cos(6\omega_1 t + \theta_{3+} + \delta_{3-}) \\
+m_{3-}I_{1+}\cos(4\omega_1 t + \theta_{3-} + \delta_{1+}) + m_{3-}I_{1-}\cos(2\omega_1 t + \theta_{3-} - \delta_{1-}) \\
+m_{3-}I_{3+}\cos(6\omega_1 t + \delta_{3+} + \theta_{3-}) + m_{3-}{I_{3-}}^2\cos(\theta_{3-} - \delta_{3-})
\end{array}\right\}
\end{aligned} \tag{10}$$

Accordingly, the DC-link voltage can be computed as

$$\begin{aligned}
&V_{dc}(t) = \frac{1}{C}\int_0^t i_{dc}dt + V_{dc0} = V_{dc0} + \\
&\left\{\begin{array}{l}
\frac{3}{4C\omega_1}m_{1+}I_{1-}\cos(2\omega_1 t + \theta_{1+} + \delta_{1-} - \frac{\pi}{2}) + \frac{3}{4C\omega_1}m_{1+}I_{3+}\cos(2\omega_1 t + \delta_{3+} - \theta_{1+} - \frac{\pi}{2}) \\
+\frac{3}{8C\omega_1}m_{1+}I_{3-}\cos(4\omega_1 t + \delta_{3-} + \theta_{1+} - \frac{\pi}{2}) + \frac{3}{4C\omega_1}m_{1-}I_{1+}\cos(2\omega_1 t + \theta_{1-} + \delta_{1+} - \frac{\pi}{2}) \\
+\frac{3}{8C\omega_1}m_{1-}I_{3+}\cos(4\omega_1 t + \delta_{3+} + \theta_{1-} - \frac{\pi}{2}) + \frac{3}{4C\omega_1}m_{1-}I_{3-}\cos(2\omega_1 t + \delta_{3-} - \theta_{1-} - \frac{\pi}{2}) \\
+\frac{3}{4C\omega_1}m_{3+}I_{1+}\cos(2\omega_1 t + \theta_{3+} - \delta_{1+} - \frac{\pi}{2}) + \frac{3}{8C\omega_1}m_{3+}I_{1-}\cos(4\omega_1 t + \theta_{3+} + \delta_{1-}) \\
+\frac{3}{12C\omega_1}m_{3+}I_{3-}\cos(6\omega_1 t + \theta_{3+} + \delta_{3-}) + \frac{3}{8C\omega_1}m_{3-}I_{1+}\cos(4\omega_1 t + \theta_{3-} + \delta_{1+}) \\
+\frac{3}{4C\omega_1}m_{3-}I_{1-}\cos(2\omega_1 t + \theta_{3-} - \delta_{1-}) + \frac{3}{12C\omega_1}m_{3-}I_{3+}\cos(6\omega_1 t + \delta_{3+} + \theta_{3-})
\end{array}\right\}
\end{aligned} \tag{11}$$

The above dc-link voltage is converted to the ac-side voltage by the switching function, and the phase-A voltage is given as

$$
\begin{aligned}
&V_a(t) = m_a(t)\cdot V_{dc}(t) \\
&= \frac{1}{2}\left\{ \begin{array}{l} (m_{1+}\cos(\omega_1 t+\theta_{1+}) + m_{1-}\cos(\omega_1 t+\theta_{1-}) \\ +H_1(j2\omega_1)I_{3+}\cos(3\omega_1 t+\delta_{3+}) + H_1(j4\omega_1)I_{3-}\cos(3\omega_1 t+\delta_{3-})) \end{array} \right\} \\
&\cdot\left\{ \begin{array}{l} V_{dc0} + \frac{3m_{1+}I_{1-}}{4C\omega_1}\cos(2\omega_1 t+\theta_{1+}+\delta_{1-}-\frac{\pi}{2}) + \frac{3m_{1+}I_{3+}}{4C\omega_1}\cos(2\omega_1 t+\delta_{3+}-\theta_{1+}-\frac{\pi}{2}) \\ +\frac{3}{8C\omega_1}m_{1+}I_{3-}\cos(4\omega_1 t+\delta_{3-}+\theta_{1+}-\frac{\pi}{2}) + \frac{3}{4C\omega_1}m_{1-}I_{1+}\cos(2\omega_1 t+\theta_{1-}+\delta_{1+}-\frac{\pi}{2}) \\ +\frac{3}{8C\omega_1}m_{1-}I_{3+}\cos(4\omega_1 t+\delta_{3+}+\theta_{1-}-\frac{\pi}{2}) + \frac{3}{4C\omega_1}m_{1-}I_{3-}\cos(2\omega_1 t+\delta_{3-}-\theta_{1-}-\frac{\pi}{2}) \\ +\frac{3}{4C\omega_1}m_{3+}I_{1+}\cos(2\omega_1 t+\theta_{3+}-\delta_{1+}-\frac{\pi}{2}) + \frac{3}{8C\omega_1}m_{3+}I_{1-}\cos(4\omega_1 t+\theta_{3+}+\delta_{1-}) \\ +\frac{3}{12C\omega_1}m_{3+}I_{3-}\cos(6\omega_1 t+\theta_{3+}+\delta_{3-}) + \frac{3}{8C\omega_1}m_{3-}I_{1+}\cos(4\omega_1 t+\theta_{3-}+\delta_{1+}) \\ +\frac{3}{4C\omega_1}m_{3-}I_{1-}\cos(2\omega_1 t+\theta_{3-}-\delta_{1-}) + \frac{3}{12C\omega_1}m_{3-}I_{3+}\cos(6\omega_1 t+\delta_{3+}+\theta_{3-}) \end{array} \right\}
\end{aligned} \tag{12}
$$

and the phase-B and phase-C voltages can be computed similarly. As one can see, there will be numerous types of components in the ac voltage. Since we are only interested in the third harmonic components, the third harmonic components in (12) are extracted as in (13).

$$
\begin{aligned}
&V_{ta3}(t)=\tfrac{1}{2}\{m_{3+}\cos(3\omega_1 t+\theta_{3+})+m_{3-}\cos(3\omega_1 t+\theta_{3-})\}V_{dc0}+\tfrac{3m_{1+}^2 I_{1-}}{16C\omega_1}\cos(3\omega_1 t+2\theta_{1+}+\delta_{1-}-\tfrac{\pi}{2})+\tfrac{3m_{1+}I_{1-}}{16C\omega_1}\cos(3\omega_1 t+\theta_{1+}+\theta_{1-}+\delta_{1-}-\tfrac{\pi}{2}) \\
&+\tfrac{3m_{1+}^2 I_{3+}}{16C\omega_1}\cos(3\omega_1 t+\delta_{3+}-\tfrac{\pi}{2})+\tfrac{3m_{1+}m_{1-}I_{3+}}{16C\omega_1}\cos(3\omega_1 t+\delta_{3+}-\theta_{1+}+\theta_{1-}-\tfrac{\pi}{2})+\tfrac{3m_{1+}^2 I_{3-}}{32C\omega_1}\cos(3\omega_1 t+\delta_{3-}-\tfrac{\pi}{2})+\tfrac{3m_{1-}m_{1+}I_{3-}}{32C\omega_1}\cos(3\omega_1 t+\delta_{3-}+\theta_{1+}-\theta_{1-}-\tfrac{\pi}{2}) \\
&\tfrac{3m_{1+}m_{1-}I_{1+}}{16C\omega_1}\cos(3\omega_1 t+\theta_{1-}+\theta_{1+}+\delta_{1+}-\tfrac{\pi}{2})+\tfrac{3m_{1-}^2 I_{1+}}{16C\omega_1}\cos(3\omega_1 t+2\theta_{1-}+\delta_{1+}-\tfrac{\pi}{2})+\tfrac{3m_{1+}m_{1-}I_{3+}}{32C\omega_1}\cos(3\omega_1 t+\delta_{3+}+\theta_{1-}-\theta_{1+}-\tfrac{\pi}{2})+\tfrac{3m_{1-}^2 I_{3+}}{32C\omega_1}\cos(3\omega_1 t+\delta_{3+}-\tfrac{\pi}{2}) \\
&+\tfrac{3m_{1+}m_{1-}I_{3-}}{16C\omega_1}\cos(3\omega_1 t+\delta_{3-}-\theta_{1-}+\theta_{1+}-\tfrac{\pi}{2})+\tfrac{3m_{1-}^2 I_{3-}}{16C\omega_1}\cos(3\omega_1 t+\delta_{3-}-\tfrac{\pi}{2})+\tfrac{3m_{1+}m_{3+}I_{1+}}{16C\omega_1}\cos(3\omega_1 t+\theta_{3+}+\theta_{1+}-\delta_{1+}-\tfrac{\pi}{2})+\tfrac{3m_{1-}m_{3+}I_{1+}}{16C\omega_1}\cos(3\omega_1 t+\theta_{3+}+\theta_{1-}-\delta_{1+}-\tfrac{\pi}{2}) \\
&+\tfrac{3m_{1+}m_{3+}I_{1-}}{32C\omega_1}\cos(3\omega_1 t+\theta_{3+}+\delta_{1-}-\theta_{1+})+\tfrac{3m_{1-}m_{3+}I_{1-}}{32C\omega_1}\cos(3\omega_1 t+\theta_{3+}+\delta_{1-}-\theta_{1-})+\tfrac{3m_{1+}m_{3-}I_{1+}}{32C\omega_1}\cos(3\omega_1 t+\theta_{3-}+\delta_{1+}-\theta_{1+})+\tfrac{3m_{1-}m_{3-}I_{1+}}{32C\omega_1}\cos(3\omega_1 t+\theta_{3-}+\delta_{1+}-\theta_{1-}) \\
&+\tfrac{3m_{1+}m_{3-}I_{1-}}{16C\omega_1}\cos(3\omega_1 t+\theta_{3-}-\delta_{1-}+\theta_{1+})+\tfrac{3m_{1-}m_{3-}I_{1-}}{16C\omega_1}\cos(3\omega_1 t+\theta_{3-}-\delta_{1-}+\theta_{1-})
\end{aligned} \tag{13}
$$

The expression in (13) shows that the AC-side voltage of the converter contains third harmonic components, which means that the converter acts as a source at the third harmonic. Specifically, we can see that the terms of the third harmonic voltage in (13) can be categorized into two types. The first type is the terms that are determined by fundamental frequency components ($m_{\pm 1}$ and $I_{\pm 1}$). The second type is the terms that are affected by external third harmonic components ($m_{\pm 3}$ and $I_{\pm 3}$). The first type of third harmonic voltage is an independent voltage source and the second type of third harmonic voltage exhibits an impedance nature. Therefore, (13) indicates that the VSC can be represented as a Thevenin circuit at the third harmonic. In the following, the detailed Thevenin circuit will be presented.

In (13), it is noted that the third harmonic components in the modulation signal can be related to the third harmonic current on the ac side of the VSC by (14):

$$m_{3\pm} = H(s \mp j\omega_1)(I_{ref3} - I_{3\pm}) \tag{14}$$

It is noted that the outer control loop of the VSC generally has a very limited bandwidth (e.g., 100 Hz), so the reference current that is generated by the outer control loop can be considered as harmonic-free (i.e., I_{ref} = 0). Substituting (14) into (13) leads to an equation that contains the third harmonic voltage and current, which gives the following model

$$\begin{bmatrix} V_{t3+} \\ V_{t3-} \end{bmatrix} = \begin{bmatrix} V_{st3+} \\ V_{st3-} \end{bmatrix} + \begin{bmatrix} Z_{3+} & Z_{3+,3-} \\ Z_{3-,3+} & Z_{3-} \end{bmatrix} \begin{bmatrix} I_{3+} \\ I_{3-} \end{bmatrix} \tag{15}$$

where

$$
\begin{aligned}
V_{st3+}(t) &= \frac{3}{16C\omega_1}k_2 m_{1+}^2 I_{1-}\cos(3\omega_1 t + 2\theta_{1+} + \delta_{1-} - \tfrac{\pi}{2}) \\
&+ \frac{3}{16C\omega_1}k_2 m_{1+}m_{1-}I_{1+}\cos(3\omega_1 t + \theta_{1-} + \theta_{1+} + \delta_{1+} - \tfrac{\pi}{2})
\end{aligned} \tag{16}
$$

$$
\begin{aligned}
V_{st3-}(t) &= \frac{3}{16C\omega_1}k_2 m_{1-}m_{1+}I_{1-}\cos(3\omega_1 t + \theta_{1+} + \theta_{1-} + \delta_{1-} - \tfrac{\pi}{2}) \\
&+ \frac{3}{16C\omega_1}k_2 m_{1-}^2 I_{1+}\cos(3\omega_1 t + \theta_{1-} + \theta_{1-} + \delta_{1+} - \tfrac{\pi}{2})
\end{aligned} \tag{17}
$$

$$
\begin{aligned}
Z_{3+} &= \tfrac{1}{2}H_1(j2\omega_1)V_{dc0} + \frac{-j3}{16C\omega_1}k_2 {m_{1+}}^2 + \frac{-j3}{32C\omega_1}k_4 {m_{1-}}^2 \\
&+ \frac{-j3}{16C\omega_1}k_2 H(j2\omega_1)I_{1+}m_{1+}e^{j(\theta_{1+}-\delta_{1+})} \\
&+ \frac{-j3}{32C\omega_1}k_4 H(j2\omega_1)m_{1-}I_{1-}e^{j(\delta_{1-}-\theta_{1-})}
\end{aligned} \tag{18}
$$

$$\begin{aligned} Z_{3-} = {} & \tfrac{1}{2} H_1(j4\omega_1)V_{dc0} + \tfrac{-j3}{32C\omega_1} k_4 {m_{1+}}^2 + \tfrac{-j3}{16C\omega_1} k_2 {m_{1-}}^2 \\ & + \tfrac{-j3}{32C\omega_1} k_4 H(j4\omega_1) I_{1+} m_{1+} e^{j(-\theta_{1+}+\delta_{1+})} \\ & + \tfrac{-j3}{16C\omega_1} k_2 H(j4\omega_1) m_{1-} I_{1-} e^{j(-\delta_{1-}+\theta_{1-})} \end{aligned} \tag{19}$$

$$\begin{aligned} Z_{3-,3+} = {} & \tfrac{-j3}{16C\omega_1} k_2 m_{1+} m_{1-} I_{3+} e^{j(\theta_{1-}-\theta_{1+})} + \tfrac{-j3}{32C\omega_1} k_4 m_{1+} m_{1-} e^{j(\theta_{1-}-\theta_{1+})} \\ & + \tfrac{-j3}{16C\omega_1} k_2 H(j2\omega_1) I_{1+} m_{1-} e^{j(\theta_{1-}-\delta_{1+})} \\ & + \tfrac{-j3}{32C\omega_1} k_4 H(j2\omega_1) m_{1+} I_{1-} e^{j(\delta_{1-}-\theta_{1+})} \end{aligned} \tag{20}$$

$$\begin{aligned} Z_{3+,3-} = {} & \tfrac{-j3}{32C\omega_1} k_4 m_{1+} m_{1-} e^{j(-\theta_{1-}+\theta_{1+})} + \tfrac{-j3}{16C\omega_1} k_2 m_{1-} m_{1+} e^{j(-\theta_{1-}+\theta_{1+})} \\ & + \tfrac{3}{32C\omega_1} k_4 H(j4\omega_1) m_{1-} I_{1+} e^{j(\delta_{1+}-\theta_{1+})} \\ & + \tfrac{-j3}{16C\omega_1} k_2 H(j4\omega_1) m_{1+} I_{1-} e^{j(-\delta_{1-}+\theta_{1+})} \end{aligned} \tag{21}$$

The above final model gives the following key findings:

- A Thevenin circuit can represent the VSC at both the positive-sequence and negative-sequence third harmonics, and the analytical expression of the Thevenin circuit can be established.
- There is a coupling effect between the positive-sequence third harmonic and negative-sequence third harmonic. The coupling effect mainly originates from the interaction between positive-sequence fundamental frequency components and negative-sequence third harmonic components and vice versa.
- The source of the Thevenin circuit is determined only by the positive-sequence and negative-sequence fundamental frequency components, whereas the impedances are determined by both the inner PI regulator and the fundamental frequency voltage and current.

According to the above results, the fundamental frequency components are needed to complete the developed model. For this purpose, the load flow methods regarding the unbalanced power systems with VSC devices are needed. At present, numerous works have been conducted on this aspect [20–23]. These methods can be used to compute the positive-sequence and negative-sequence fundamental frequency voltage and current. The procedure to obtain the final model of the VSC can be summarized as the flow chart in Figure 3.

Compared with other existing models, the proposed model for third harmonic computation has the following advantages:

- The mechanism of the production of the non-characteristic third harmonics are fully revealed so that the contributions of the different components to the non-characteristic third harmonics emission can be easily analyzed. Accordingly, the control scheme that can suppress the third harmonic emission can be designed.
- The computation of the proposed model is very easy as the analytical expression of the proposed model is given. Compared with other methods, it is more straightforward for users.
- The proposed model can be integrated into the existing harmonic power flow tools. As a result, the non-characteristic third harmonic can be computed along with other harmonic components, which can be easily adopted by the users.

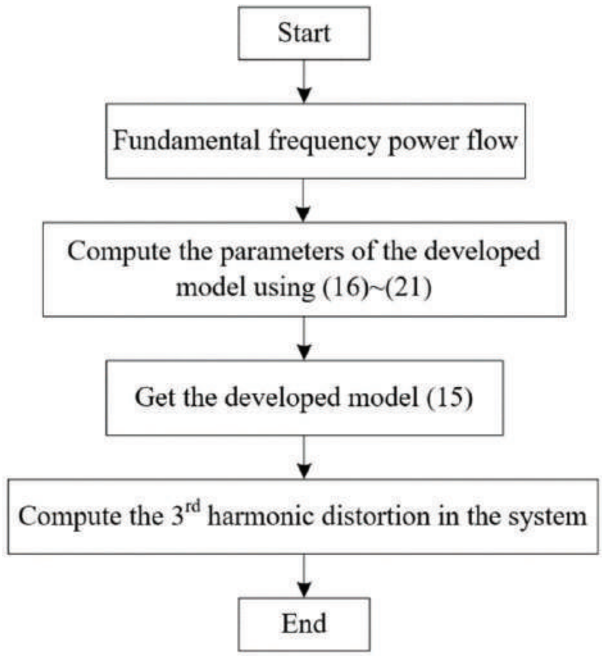

Figure 3. Procedure to compute the noncharacteristic third harmonics under the unbalanced condition.

4. Verification of the Proposed Model by Time-Domain Simulations

In this section, the developed model of VSC under unbalanced conditions is verified via time-domain simulations in the VSC system of Figure 4 in MATLAB/Simulink. The VSC has the same control strategy as that in Figure 1. The system parameters are listed in Table 1 [24,25]. The unbalanced condition is created by adding a negative-sequence fundamental frequency voltage in the AC source (V_s in Figure 4). Therefore, the ac voltage source can be expressed as

$$V_{sa}(t) = V_{s+}\cos(\omega_1 t + \phi_{s+}) + V_{s-}\cos(\omega_1 t + \phi_{s-}) \tag{22}$$

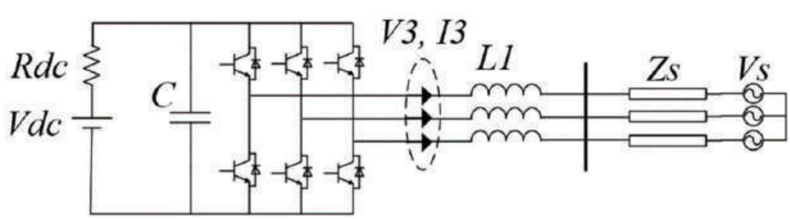

Figure 4. The VSC for unbalanced condition illustration.

Table 1. System parameters.

Parameter	Value	Parameter	Value
f_{switch}	3 kHz	Vs	200 V
L_1	5 mL	Ls	10 mL
Kp	0.023	Ki	43.15
C	50 µF	Vdc	600 V
R_{dc}	60 Ω	Nominal P	1 kW

For illustration, the unbalanced level of the system is defined as

$$l = \frac{V_{s-}}{V_{s+}} \times 100\% \tag{23}$$

The basic strategy to verify the proposed model is summarized as follows:

- Implement the simulation system in MATLAB/Simulink, then set different unbalanced levels to run the simulations. The simulation results give the third harmonic distortion levels.
- Based on the parameters of the simulation system and the unbalanced levels, the Thevenin circuit can be computed.
- Once the Thevenin circuit is obtained, the third harmonic distortion levels in the system can be computed for different unbalanced levels.
- The calculated third harmonic distortion levels are compared with the results obtained from the time-domain simulations in step (1). If these two types of results match well, then it verifies the correctness of the proposed model at third harmonics.

The developed third harmonic model is tested under an unbalanced level of 5%, 15%, 25%, and 35%. The simulated waveforms of the AC-side voltage and current of the VSC are presented in Figure 5. The waveforms of the VSC's voltage and current can be used to compute the third harmonic voltage and current using FFT, and the IHDs of the third harmonics for different unbalanced levels are shown in Figure 6. It can be seen that a larger unbalanced level leads to larger third harmonics. When the unbalanced level is only 5%, the IHD of the positive-sequence third harmonic current is around 2%, while it increases to 11% when the unbalanced level rises to 35%. Additionally, one can also see that the positive-sequence third harmonic is much higher than the negative-sequence third harmonic. The reason is that, according to Equations (16)~(21), the positive-sequence third harmonic is more relevant with the positive-sequence fundamental frequency components, whereas the negative-sequence third harmonic is more relevant with the negative-sequence fundamental frequency components. As a result of the large positive-sequence third harmonic current, the coupling between the negative-sequence third harmonic and positive-sequence third harmonic current cannot be ignored.

It has been mentioned previously that, to obtain the developed model, the positive-sequence and negative-sequence fundamental frequency voltage and current are needed. In the following, the calculated positive-sequence and negative-sequence voltage and current are compared with the simulation results first, and then these values are used to compute the developed model.

4.1. Computation of the Fundamental Frequency Components

The positive-sequence and negative-sequence fundamental frequency voltage and current can be obtained through load flow studies. However, it is noted from the derived model that both the positive-sequence and negative-sequence fundamental frequency components in the modulation signal are needed to compute the developed model. Due to the control and switching process features, the positive-sequence and negative-sequence fundamental-frequency components in the modulation signal can be computed using Equations (24) and (25), respectively.

$$m_{1+} = V_{1+}/V_{dc0} \tag{24}$$

$$m_{1-} = H(2j\omega_1)I_{1-} \tag{25}$$

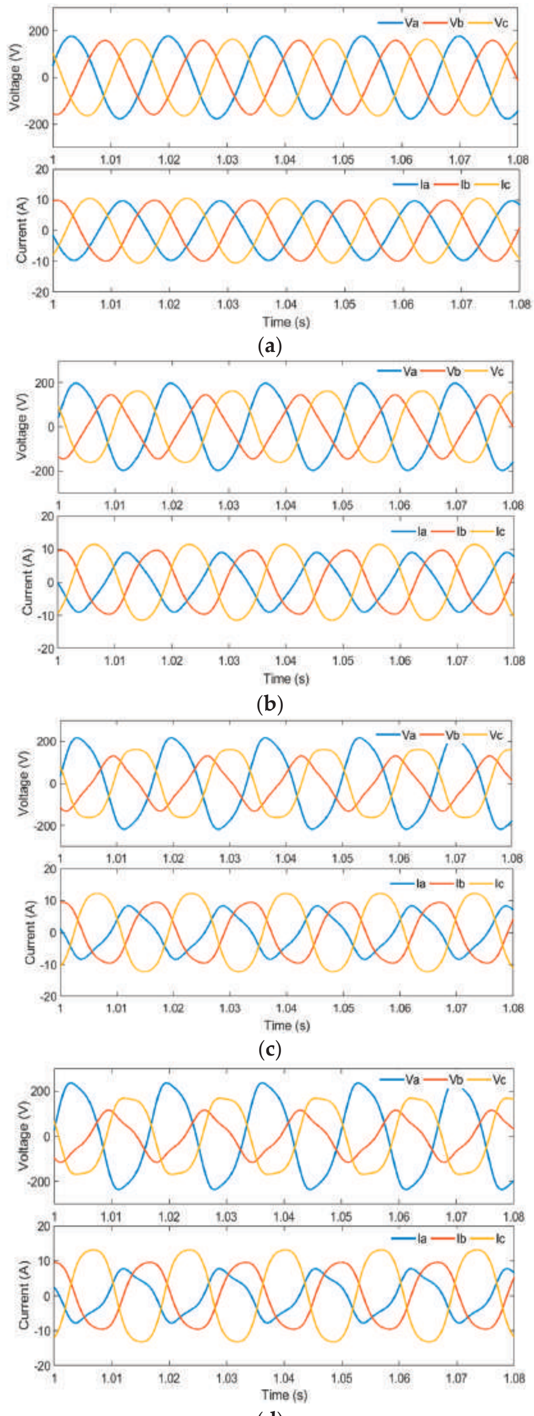

Figure 5. Voltage and current waveforms on the ac side of the VSC under different unbalanced levels. (**a**) l = 5%. (**b**) l = 15%. (**c**) l = 25%. (**d**) l = 5%.

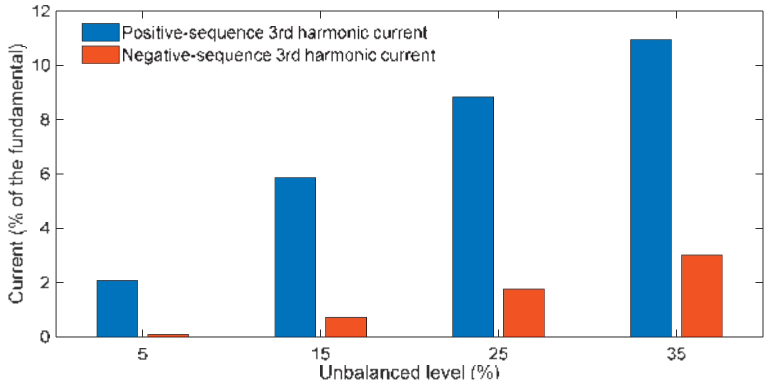

Figure 6. IHDs of the third harmonic on the ac side of the VSC.

For the studied four cases, the calculated ac-side positive-sequence fundamental frequency voltage and negative-sequence fundamental frequency current and modulation signals regarding various unbalanced levels are compared in Tables 2 and 3. It can be seen that the calculated fundamental frequency components under various unbalanced conditions match well with the simulated results. Based on the obtained positive-sequence voltage and the negative-sequence current, the corresponding modulation signal can be computed using (24) and (25).

Table 2. Results of the positive-sequence fundamental frequency voltage.

Unbalanced Level (l)	Simulated V_{t1+}	Calculated V_{t1+}
5%	$0.9815\angle-70.9336°$	$0.982\angle-70.9159°$
15%	$0.982\angle-70.8655°$	$0.982\angle-70.9159°$
25%	$0.9829\angle-70.7298°$	$0.982\angle-70.9159°$
35%	$0.9842\angle-70.5274°$	$0.982\angle-70.9159°$

Table 3. Results of the positive-sequence fundamental frequency current.

Unbalanced Level (l)	Simulated I_{1-}	Calculated I_{1-}
5%	$-0.0137 - 0.0419i$	$-0.0137 - 0.0420i$
15%	$-0.0387 - 0.1233i$	$-0.0410 - 0.1259i$
25%	$-0.0586 - 0.1989i$	$-0.0540 - 0.1998i$
35%	$-0.0739 - 0.2677i$	$-0.0756 - 0.2797i$

4.2. Verification of the Proposed Model

According to the obtained fundamental frequency components above, the parameters of the developed model in (15) can be computed, and the parameters of this model for different unbalanced levels are listed in Table 4. It can be seen that, since the positive-sequence third harmonic current is much larger than the negative-sequence third harmonic current, the coupling between the negative-sequence third harmonic voltage and the positive-sequence third harmonic current is more important. According to the calculated parameters, the third harmonic current can be computed using the following equation:

$$\begin{bmatrix} V_{s3+} \\ V_{s3-} \end{bmatrix} = \begin{bmatrix} Z_{3+} & Z_{3+,3-} \\ Z_{3-,3+} & Z_{3-} \end{bmatrix} \begin{bmatrix} I_{3+} \\ I_{3-} \end{bmatrix} + \begin{bmatrix} Z_{L1} + Z_{Ls} & 0 \\ 0 & Z_{L1} + Z_{Ls} \end{bmatrix} \begin{bmatrix} I_{3+} \\ I_{3-} \end{bmatrix} \tag{26}$$

and the third harmonic voltage on the ac side of the VSC can be computed as

$$\begin{bmatrix} V_{t3+} \\ V_{t3-} \end{bmatrix} = \begin{bmatrix} V_{st3+} \\ V_{st3-} \end{bmatrix} + \begin{bmatrix} Z_{3+} & Z_{3+,3-} \\ Z_{3-,3+} & Z_{3-} \end{bmatrix} \begin{bmatrix} I_{3+} \\ I_{3-} \end{bmatrix} \tag{27}$$

Table 4. Computed impedance and source.

l	Z_{3+}	Z_{3-}	$Z_{3+,3-}$	$Z_{3-,3+}$	V_{3t+}	V_{3t-}
5%	7.73 − 14.86i	6.44 − 7.87i	0.13 − 0.12i	0.03 − 0.22i	−1.58 + 0.50i	−0.06 + 0.09i
15%	7.84 − 15.26i	6.56 − 8.1i	0.37 − 0.35i	0.11 − 0.64i	−4.48 + 1.3i	−0.57 + 0.75i
25%	8.13 − 16.1i	6.84 − 8.55i	0.55 − 0.55i	0.21 − 0.98i	−6.82 + 1.76i	−1.53 + 1.79i
35%	8.07 − 16.3i	6.78 − 8.62i	0.69 − 0.71i	0.33 − 1.25i	−8.6 + 1.93i	−2.86 + 2.97i

The comparison results between the calculated harmonic voltage and current on the ac side of the VSC for the four studied cases are listed in Tables 5 and 6. One can see that both the calculated positive-sequence and negative-sequence third harmonic voltages match well with the simulated results, which verifies the correctness of the proposed model. In the calculations, the coupling between the positive-sequence and negative sequence third harmonics is included. This is very important for the computation for the negative-sequence third harmonics due to the large positive-sequence third harmonic current.

Table 5. Test results of the developed model for voltage.

Unbalanced Level (l)	Positive-Sequence Third Harmonic Voltage Using Time-Domain Simulations	Positive-Sequence Third Harmonic Voltage Using Proposed Model
5%	0.1742 − 0.113i	0.1745 − 0.1106i
15%	0.5131 − 0.284i	0.5141 − 0.2761i
25%	0.8169 − 0.3377i	0.8187 − 0.3189i
35%	1.058 − 0.2822i	1.0573 − 0.2508i
Unbalanced Level (l)	**Negative-Sequence Third Harmonic Voltage Using Time-Domain Simulations**	**Negative-Sequence Third Harmonic Voltage Using Proposed Model**
5%	0.0008 − 0.0086i	0.0008 − 0.0086i
15%	0.0088 − 0.071i	0.0088 − 0.071i
25%	0.0278 − 0.1733i	0.0286 − 0.1736i
35%	0.0574 − 0.2959i	0.0589 − 0.2956i

Table 6. Test results of the developed model for current.

Unbalanced Level (l)	Positive-Sequence Third Harmonic Voltage Using Time-Domain Simulations	Positive-Sequence Third Harmonic Voltage Using Proposed Model
5%	−1.9172 − 2.9548i	−1.9124 − 2.9669i
15%	−4.8182 − 8.7052i	−4.7920 − 8.7518i
25%	−5.7287 − 13.8587i	−5.6458 − 14.1981i
35%	−4.7867 − 17.9513i	−4.6459 − 17.5674i
Unbalanced Level (l)	**Negative-Sequence Third Harmonic Voltage Using Time-Domain Simulations**	**Negative-Sequence Third Harmonic Voltage Using Proposed Model**
5%	−0.1456 − 0.0139i	−0.1466 − 0.0136i
15%	−1.2053 − 0.1488i	−1.2154 − 0.1488i
25%	−2.9408 − 0.4724i	−2.9901 − 0.5058i
35%	−5.0207 − 0.9740i	−5.0250 − 0.9508i

4.3. Impact of the Dc-Link Capacitor

According to the derivations in Sections 2 and 3, the value of the DC-side capacitor plays an important role in the developed model. For the same unbalanced level, the larger the DC-side capacitor, the smaller the third harmonic. This can be verified by the simulation results in Figure 7, which are based on an unbalanced level of 25%. As one can see, when the DC-side capacitor is increased to 100 μF, the third harmonic voltage and current are significantly decreased. The results can also be supported by the harmonic voltage of the dc side, which is shown in Figure 8. It is found that the harmonic ripples (mainly second harmonics) in the dc-link voltage for a dc-link capacitor of 100 µF are much smaller than those for a dc-link capacitor of 50 µF. In summary, increasing the DC-link capacitor's value can resist the generation of the uncharacteristic third harmonic.

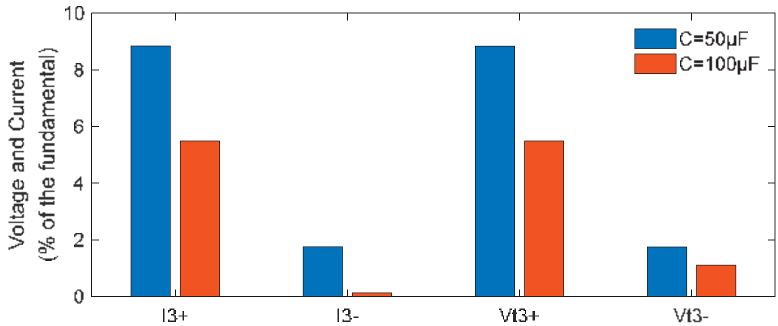

Figure 7. Impact of the size of the dc-link capacitor.

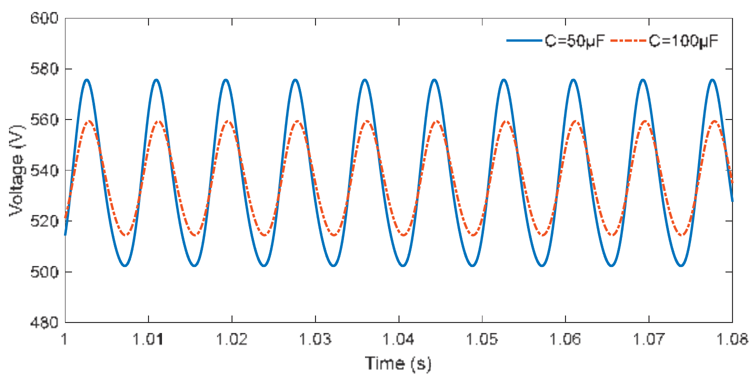

Figure 8. Waveforms of the dc-link voltage for different dc-link capacitors.

5. Discussion

The above results have shown the correctness of the developed model, but it has to be pointed out that the new model can only be developed with the accurate information of the positive-sequence and negative-sequence fundamental frequency voltage and current. If these parameters cannot be provided, then the model cannot be accurately developed. It is noteworthy that the positive-sequence third harmonic distortion is much larger than the negative-sequence third harmonic. Therefore, for the evaluation of the harmonic impact, the level of the positive-sequence third harmonic is sufficient. Moreover, since the negative-sequence harmonic is quite small, its coupling effect to the positive-sequence voltage can be ignored as well. As a result, for the evaluation of the non-characteristic third harmonics, the model can be practically simplified as a Thevenin circuit, and the computation can be simplified accordingly.

The proposed model is able to show the effect of different components on the Thevenin circuit, and, thus, an optimal parameter design can be achieved to reduce the third harmonic distortion. Additionally, the proposed model can help to implement the control schemes for suppressing the third harmonic distortion caused by the VSC under unbalanced conditions.

6. Conclusions

An analytical model of VSC for calculating the non-characteristic third harmonics generated by the VSC operated under unbalanced conditions has been developed. The model is a coupled Thevenin circuit, which can be used to compute the noncharacteristic third harmonics. The correctness and effectiveness of the proposed model for computing noncharacteristic third harmonics have been verified by EMT simulations. Based on the proposed model, the findings regarding the noncharacteristic third harmonic caused by the VSC can be summarized as follows:

- The VSC generates both positive-sequence and negative-sequence third harmonics under unbalanced conditions. The VSC can be modeled as a coupled Thevenin circuit at third harmonics. The source of the Thevenin circuit is determined by the fundamental frequency voltage and current. The impedances are determined by the control parameters and the fundamental frequency components.
- The positive-sequence third harmonic distortion is much larger than the negative-sequence third distortion. As a result, only computing the positive-sequence third harmonic is sufficient to evaluate the impact of the VSC's third harmonic emission under unbalanced condition.
- The larger unbalanced levels and smaller size of the dc-link capacitor introduce a larger third harmonic current.

Author Contributions: Methodology, M.Z. and H.Z.; validation, M.Z. and H.Z.; writing, M.Z. and H.Z.; funding acquisition, H.Z. and R.F.; resources, M.Z. and S.Z.; data curation, M.Z., R.L. and J.W. All authors have read and agreed to the published version of the manuscript.

Funding: This work is supported by State Grid Shanxi Electric Power Company Science and Technology Project Research: Research and application of fusion perception and data mining technology of distribution network power quality based on smart IOT (52053020000X).

Institutional Review Board Statement: Not applicable.

Informed Consent Statement: Not applicable.

Data Availability Statement: The data are available upon request from the corresponding author.

Conflicts of Interest: The authors declare no conflict of interest.

Nomenclature

$V_{(.)}$	Voltage
$I_{(.)}$	Current
$m_{(.)}$	Modulation signal
ω	Angular frequency
$(.)_a$	Quantities for phase A
$(.)_b$	Quantities for phase B
$(.)_c$	Quantities for phase C
$(.)_{1+}$	Quantities at positive-sequence fundamental frequency
$(.)_{1-}$	Quantities at negative-sequence fundamental frequency
$(.)_{3+}$	Quantities at positive-sequence third harmonic
$(.)_{3-}$	Quantities at negative-sequence fundamental frequency
δ	Angle of current
θ	Angle of modulation signal
$(.)_{dc}$	Quantities on the dc side
C	DC-link capacitor
L_f	Front-end passive filter
H_1(s)	Transfer function of VSC's inner control loop
i	The imaginary part of the plural

References

1. Carrasco, J.M.; Franquelo, L.G.; Bialasiewicz, J.T.; Galvan, E.; Portillo, R.; Prats, M.M.; Leon, J.I.; Moreno-Alfonso, N. Power-electronic systems for the grid integration of renewable energy sources: A survey. *IEEE Trans. Ind. Electron.* **2006**, *53*, 1002–1016. [CrossRef]
2. Segundo-Ramirez, J.; Medina, A. Modeling of FACTS Devices Based on SPWM VSCs. *IEEE Trans. Power Del.* **2009**, *24*, 1815–1823. [CrossRef]
3. Pan, E.; Yue, B.; Li, X.; Zhao, Z.; Zhu, Q. Integration technology and practice for long-distance offshore wind power in China. *Energy Convers. Econ.* **2020**, *1*, 4–19. [CrossRef]
4. Arazi, M.; Payman, A.; Camara, M.B.; Dakyo, B. Bidirectional Interface Resonant Converter for Wide Voltage Range Storage Applications. *Sustainability* **2022**, *14*, 377. [CrossRef]
5. Sirjani, R. Optimal Capacitor Placement in Wind Farms by Considering Harmonics Using Discrete Lightning Search Algorithm. *Sustainability* **2017**, *9*, 1669. [CrossRef]
6. Rao, S.N.V.B.; Kumar, Y.V.P.; Pradeep, D.J.; Reddy, C.P.; Flah, A.; Kraiem, H.; Al-Asad, J.F. Power Quality Improvement in Renewable-Energy-Based Microgrid Clusters Using Fuzzy Space Vector PWM Controlled Inverter. *Sustainability* **2022**, *14*, 4663. [CrossRef]
7. Iqbal, M.N.; Kütt, L.; Daniel, K.; Asad, B.; Ghahfarokhi, P.S. Estimation of Harmonic Emission of Electric Vehicles and Their Impact on Low Voltage Residential Network. *Sustainability* **2021**, *13*, 8551. [CrossRef]
8. Blasko, V.; Kaura, V. A new mathematical model and control of a three-phase AC-DC voltage source converter. *IEEE Trans. Power Electron.* **1997**, *12*, 116–123. [CrossRef]
9. Torquato, R.; Hax, G.R.T.; Freitas, W.; Nassif, A. Impact Assessment of High-Frequency Distortions Produced by PV Inverters. *IEEE Trans. Power Del.* **2021**, *36*, 2978–2987. [CrossRef]
10. Yazdani, A.; Iravani, R. A unified dynamic model and control for the voltage-sourced converter under unbalanced grid conditions. *IEEE Trans. Power Del.* **2006**, *21*, 1620–1629. [CrossRef]
11. Kamh, M.Z.; Iravani, R. Unbalanced Model and Power-Flow Analysis of Microgrids and Active Distribution Systems. *IEEE Trans. Power Del.* **2010**, *25*, 2851–2858. [CrossRef]
12. Karimi, H.; Karimi-Ghartemani, M.; Sheshyekani, K. Robust Control of Three-Phase Voltage Source Converters under Unbalanced Grid Conditions. *IEEE Trans. Power Electron.* **2019**, *34*, 11278–11289. [CrossRef]
13. Merritt, N.R.; Chakraborty, C.; Bajpai, P. New Voltage Control Strategies for VSC-Based DG Units in an Unbalanced Microgrid. *IEEE Trans. Sustain. Energy* **2017**, *8*, 1127–1139. [CrossRef]
14. Hwang, J.G.; Lehn, P.W.; Winkelnkemper, M. Control of grid connected AC-DC converters with minimized DC link capacitance under unbalanced grid voltage condition. In Proceedings of the 2007 European Conference on Power Electronics and Applications, Aalborg, Denmark, 2–5 September 2007; pp. 1–10.
15. Lo, Y.H.; Chen, Y.C.; Lian, K.L.; Karimi, H.; Wang, C.Z. An Iterative Control Method for Voltage Source Converters to Eliminate Uncharacteristic Harmonics Under Unbalanced Grid Voltages for High-Power Applications. *IEEE Trans. Sustain. Energy* **2019**, *10*, 1419–1429. [CrossRef]
16. Zhong, Q.; Lin, L.X.; Wang, G.; Zhang, Y.; Wu, Z.G. Harmonic analysis model for voltage source converter under unbalanced conditions. *IET Gener. Transm. Distrib.* **2015**, *9*, 12–21. [CrossRef]
17. Nascimento, C.F.; Watanabe, E.H.; Dietrich, A.B.; Dias, R.F.S.; Diene, O. Non-Characteristic Harmonics and DC Side Capacitor Calculation in VSC Connected to a Distribution System with Unbalanced Voltage. In Proceedings of the 2015 IEEE 24th International Symposium on Industrial Electronics (ISIE), Buzios, Brazil, 3–5 June 2015; pp. 349–354.
18. Nascimento, C.F.; Watanabe, E.H.; Diene, O.; Dietrich, A.B.; Goedtel, A.; Gyselinck, J.J.C.; Dias, R.F.S. Analysis of Noncharacteristic Harmonics Generated by Voltage-Source Converters Operating under Unbalanced Voltage. *IEEE Trans. Power Del.* **2017**, *32*, 951–961. [CrossRef]
19. Gao, B.; Wang, Y.; Xu, W. Modeling Voltage Source Converters for Harmonic Power Flow Studies. *IEEE Trans. Power Del.* **2021**, *36*, 3426–3437. [CrossRef]
20. Gao, B.; Wang, Y.; Xu, W. An Improved Model of Voltage Source Converters for Power System Harmonic Studies. *IEEE Trans. Power Del.* **2021**. *early access*. [CrossRef]
21. Khushalani, S.; Solanki, J.M.; Schulz, N.N. Development of three-phase unbalanced power flow using PV and PQ models for distributed generation and study of the impact of DG models. *IEEE Trans. Power Syst.* **2007**, *22*, 1019–1025. [CrossRef]
22. AlHajri, M.F.; El-Hawary, M.E. Exploiting the Radial Distribution Structure in Developing a Fast and Flexible Radial Power Flow for Unbalanced Three-Phase Networks. *IEEE Trans. Power Del.* **2010**, *25*, 378–389. [CrossRef]
23. Wang, Y.; Zhang, N.; Li, H.; Yang, J.W.; Kang, C.Q. Linear Three-Phase Power Flow for Unbalanced Active Distribution Networks with PV Nodes. *CSEE J. Power Energy Syst.* **2017**, *3*, 321–324. [CrossRef]
24. Yazdani, A.; Iravani, R. *Voltage-Sourced Converter in Power Systems: Modelling, Control, and Application*; Wiley: New York, NY, USA, 2010.
25. Liserre, M.; Blaabjerg, F.; Dell'Aquila, A. Step-by-step design procedure for a grid-connected three-phase PWM voltage source converter. *Int. J. Electron.* **2004**, *91*, 445–460. [CrossRef]

World Electric Vehicle Journal

Article

Integration of Electric Vehicles into Microgrids: Policy Implication for the Industrial Application of Carbon Neutralisation in China

Yang (Andrew) Wu [1,*], Yui-Yip Lau [2] and Ju-Ai Wu [3]

[1] Division of Science, Engineering and Health Studies, College of Professional and Continuing Education, Hong Kong Polytechnic University, Hong Kong SAR, China
[2] Division of Business and Hospitality Management, College of Professional and Continuing Education, Hong Kong Polytechnic University, Hong Kong SAR, China; yuiyip.lau@cpce-polyu.edu.hk
[3] College of Automation & College of Artificial Intelligence, Nanjing University of Posts and Telecommunication, Nanjing 210023, China; wujuai@njupt.edu.cn
* Correspondence: andrew.wu@cpce-polyu.edu.hk

Abstract: With the dynamic development of renewable energies, energy storage devices, and electric vehicles, microgrids have been playing an increasingly vital role in smart power grids. Under the recent development of carbon neutralisation, microgrid systems containing multiple clean energy sources have become significant modules for energy conservation and emission reduction. Considering technological and environmental elements, we investigated the economic operation of microgrids with the integration of electric vehicles. In this paper, carbon trading mechanisms and operation scheduling strategies are analysed in the simulation models. Then, transaction costs and power balance are discussed. Industrial applications and policy implications are also presented.

Keywords: electric vehicle; carbon neutralisation; microgrid; energy storage; economic operation; carbon trading

Citation: Wu, Y.; Lau, Y.-Y.; Wu, J.-A. Integration of Electric Vehicles into Microgrids: Policy Implication for the Industrial Application of Carbon Neutralisation in China. *World Electr. Veh. J.* **2022**, *13*, 96. https://doi.org/10.3390/wevj13060096

Academic Editors: Wenbin Yu and Guang Zeng

Received: 4 April 2022
Accepted: 23 May 2022
Published: 26 May 2022

1. Introduction

The exploitation of fossil energy has shifted humanity's focus from agriculture to industrialisation. Industrialisation has driven the tremendous advancement of civilisation for over two centuries. The predicted total volume of CO_2 created by fossil fuels is estimated to be 2.2 trillion tons [1]. In recent years, fossil fuel-based energy utilisation models have resulted in serious carbon emissions and global warming. Greta Thunberg, a Swedish teenage girl and a world-renowned environmental activist, warned at the 2020 Davos Forum to "stop investing in fossil fuels immediately, or explain to your children why you did not protect them from the climate chaos you create" [2]. In the past decade, the power industry has actively promoted energy conservation and emission reduction. However, due to economic costs and load constraints, wind and solar curtailment persists [3–6]. With recent policy incentives, carbon neutralisation and the vigorous development of electric vehicles and renewable energies have become inevitable trends in the power industry [7–9]. As a comprehensive integrated technology combining multiple types of renewable energies, the microgrid can increase the utilisation of wind power and solar energy, reducing carbon emissions [10,11]. Renewable energy sources, such as wind power and solar energy, are unstable and intermittent due to unpredictable weather conditions (e.g., heatwaves, tropical cyclone, storms) during generation. Thus, applying these valuable electric energies continuously and stably is difficult [12]. Ultimately, it is imperative to contribute to energy conservation and carbon neutralisation.

Since 1906, the average global temperature has increased by 1.1 °C [1]. To effectively address the adverse effects of global warming on human society, the 2015 United Nations Framework Convention on Climate Change (UNFCCC) was held in Paris, France. The consensus of keeping global warming under 2 °C was reached. Countries worldwide have further clarified their scope of greenhouse gas emission reduction. Different from the 1997 Kyoto Protocol, the Paris Agreement allowed each party to clarify their submission on greenhouse gas emission reductions through a bottom-up approach based on their emission reduction responsibilities and capabilities, which were defined as Nationally Determined Contributions (NDCs) targets [13]. In China, President Xi Jinping has emphasised the importance of environmental protection and ecological civilisation since the 18th National Congress of the Communist Party of China [14]. This mechanism can avoid problems of selection and formulation of emission reduction responsibility allocation options among countries.

The carbon trading mechanism allows trading entities to adjust their carbon emission rights through trading and exchange within a certain range to achieve regional carbon reduction at the lowest cost. However, compared with the carbon tax, the policy setting and design process of the carbon trading mechanism are more sophisticated and complicated. Setting the appropriate amount of regionally total carbon emission rights and determining the coverage and allocation of appropriate initial carbon emission rights for various industrial sectors are extremely challenging for policy makers.

Carbon trading mechanisms have provided economic incentives for market players to reduce carbon emissions and promote the utilisation of renewable energies and electric vehicles [15]. The introduction of carbon trading mechanisms no longer defines carbon as emission costs, but additional economic gains through carbon trading [16]. Regulation has been deployed to encourage the power industry to transform its energy structure and to improve technological innovation, achieving an environmentally economic operation model. Ref. [17] considered the economic impact of carbon emission allowances on scheduling strategies. Ref. [18] established a mathematical model for calculating carbon transaction costs based on carbon emission intervals. Ref. [19] constructed an optimal dispatch model for large-scale solar farms accessing smart grids under carbon trading mechanisms, which examined the low-carbon performance of the proposed system, especially in the post-COVID-19 era. The microgrid provides an efficient approach to facilitate the high penetration of renewable energies and electric vehicles into the power grid [20–22], serving as an important link in energy saving and emission reduction. The rapid growth of electric vehicles has essentially affected the development of microgrids in the smart power system [23], which can further stimulate the achievement of carbon neutralisation [24]. The dynamic increase in carbon emissions in China can be neutralised with the promotion and penetration of electric vehicles [25].

We investigated the economic operation of microgrids with the integration of electric vehicles and renewable energies, including wind power and solar energy. In this paper, a microgrid optimal dispatch model is constructed. Carbon trading mechanisms and operation scheduling strategies are analysed through the simulation models. Transaction costs in economic dispatch and power balance are discussed. The related constraints of balance are designed to reduce the carbon emissions of the microgrid system, increase the utilisation of renewable energies, and promote carbon neutralisation in the power industry. Industrial and policy implications are provided in the conclusion.

The remainder of this paper is structured as follows. Section 2 presents the research methodology. Section 3 presents a robust low-carbon economic dispatch model. Sections 4 and 5 provide industrial applications and policy implications in carbon neutralisation, respectively. Section 6 summarises and discusses future research directions.

2. Research Methodology

Electric vehicles have been playing an increasingly vital role in the smart grid and power system technology, owing to updated charging technology, financial subsidies, and low cruise costs. With the expansion of the scale of using electric vehicles, the operational model of the microgrid must be modified accordingly. Electric vehicles have adjustable charging and discharging properties, and they have a dual role when they are connected to the grid: they can be used as a load to charge and as a power source to supply power to the microgrid. Therefore, research to incorporate electric vehicles into the microgrid to optimise the allocation of microgrid resources can improve the economic and stable operation of the microgrid, which will further enhance the dynamic performance of the main power grid. In this paper, we propose a microgrid economic dispatch model containing electric vehicles, wind power, solar energy, and energy storage devices. In addition, carbon neutralisation and carbon emission costs are added to the model as constraints. A standard structure of a microgrid connected to the main grid containing wind power, solar energy, electric vehicles, and energy storage devices is shown in Figure 1.

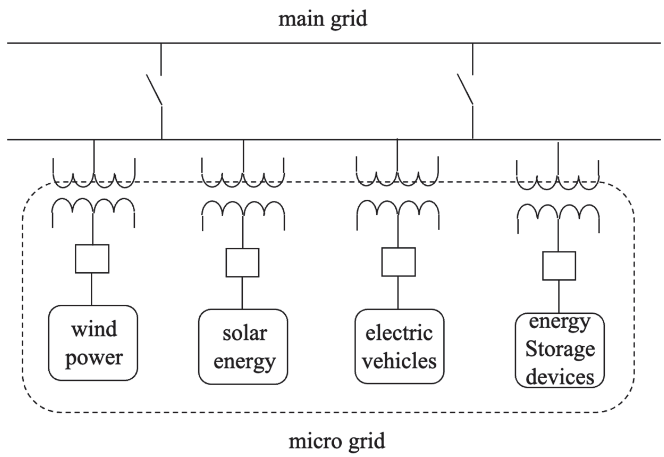

Figure 1. Sample structure of a microgrid connected to a main electric grid.

3. Low-Carbon Dispatch Model

The microgrid system is connected to the main grid and comprises electric vehicles, wind power, photovoltaic power generation, and storage batteries. If the electricity purchased by the microgrid from the main grid is generated by thermal power units, the microgrid's free carbon emission quota is:

$$C_m = \mu \sum_{t=1}^{T} \left(P_w \cdot t + P_s \cdot t + P_{ev} \cdot t - P_g \cdot t \right). \tag{1}$$

where:

C_m is the carbon emission quota of the microgrid;

μ is the co-efficiency as regulated by related authorities;

t is the time duration of the operation;

P_w is the electric power generated by the wind turbines;

P_s is the electric power generated from solar energy;

P_{ev} is the electric power charged by or used by electric vehicles connected to the microgrids, which can be positive or negative; and

P_g is the electric power purchased from the main grid.

Carbon emissions are lower than quotas, resulting in carbon emission benefits. Low carbon emissions can generate substantial carbon trading benefits and may even offset the increase in costs caused by gas turbine power generation from the main grid. This fully mobilises energy saving and emission reduction in the power generation industry.

To prevent excessive charging and discharging of the energy storage devices, charging constraints are introduced to fulfil upper and lower limits:

$$0 \leq P_b \leq P_{b,max}. \tag{2}$$

where:

P_b is the electric power saved in the energy storage devices; and

$P_{b,max}$ is the maximum charging capacity of the energy storage devices.

The trading data disclosed by the two leading carbon trading pilot centres in China, i.e., the Beijing Trading Centre and the Guangzhou Trading Centre, reveal a significant gap between the carbon trading patterns of northern and southern China, although the annual cumulative carbon emission rights and trading turnovers are close to each other, both being approximately 26 million tons at around USD 170 million [26,27], as shown in Figure 2.

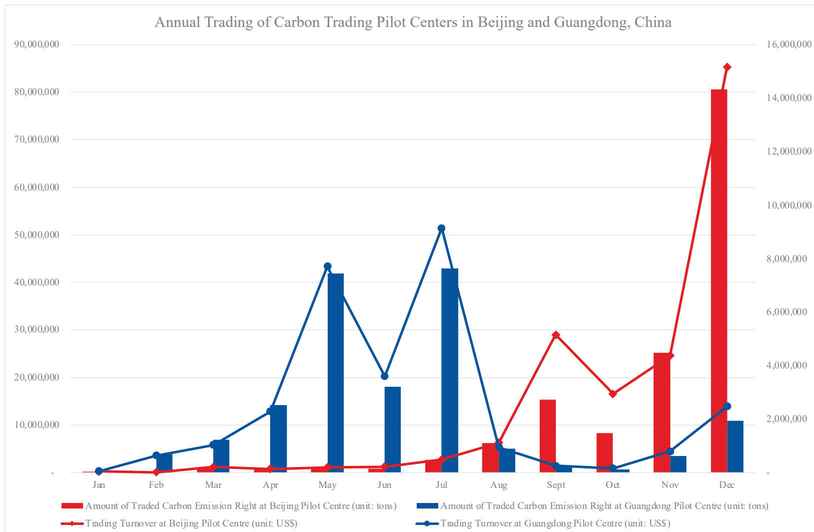

Figure 2. Annual turnover of carbon trading pilot centres in China in 2021.

The peak trading season in Guangzhou is summer, mainly May to July; meanwhile, the peak trading season in Beijing is mainly November and December. The reason is due to different details on policy execution and settlement regimes. Market players in Guangzhou must face the mid-term inspection of carbon emissions, which is an important policy incentive for the market players with high carbon emission to increase their trading for sufficient emission right in the summer. Meanwhile, the market players in Beijing have only a year-end examination of their carbon emissions, and thus tend to wait until the year's end to complete their carbon trading. In addition to the different settlement regimes, another major reason is the different patterns of energy consumption between northern and southern China due to different weather conditions.

The above-mentioned pilot centres are only at the regional level, and can only provide a carbon trading platform for enterprises within their administrative regions. In July 2021, a national-level trading platform was launched in Shanghai under a trial mode. More information is to be released in the near future. With the official launch of the national carbon emission rights trading market, government authorities can utilise the market and pricing mechanism to regulate the use of carbon emission rights. When the carbon trading price is overly high, the carbon emission quota allocated to the industrial manufacturer may be reduced. Meanwhile, the pressure on the manufacturer to reduce emissions increases will drive the enterprise to spend more money to purchase carbon emission rights, which is not conducive to its production and operation. Therefore, an appropriate adjustment in the carbon trading price may not only reduce the emission reduction pressure of emission enterprises, but also effectively increase the manufactory output and broaden the eligible industrial sectors of the carbon quota mechanism.

4. Industrial Applications

By the end of 2020, the cumulative installed capacity of power generation from renewable energies reached 535,000 MW in China, a year-on-year increase of 29.4%, accounting for 24.3% of the total installed capacity. The newly installed capacity of renewable energy power generation in 2020 reached 120,000 MW, accounting for 63% of the total installed capacity of renewable energies in the whole nation [28]. Furthermore, the national power generation from renewable energies achieved 10% of the total power generation, highlighting a considerable improvement in renewable energy utilisation.

Under the guidance of the development goals of the electric power system, the future development of the new energy industry has shown a trend of deploying more renewable energies and electric vehicles. Distributed power generation, microgrids, and integration with electric vehicles have gained considerable importance in the industry. The widespread use of microgrids has intensified the demand for flexible adjustment resources, such as energy storage devices.

The shift from centralised generation to distributed generation has attracted the interest of academics, policy makers, and industrial engineers, thereby accelerating the development of microgrid systems. Energy storage devices are among the essential factors to facilitate such a trend. In addition to distributed renewable energy resources, such as roof-top wind turbines and solar panels, fuel cells are considered a clean and flexible option for promising energy resources in microgrid application [29]. Flow batteries have also been revived recently, especially for large-scale energy storage systems in microgrids, due to their low cost and eco-friendly materials, even with favourable design flexibility [30].

In recent years, electric vehicle sales have grown rapidly due to the incentive financial subsidy policy. The government's subsidy policy has greatly stimulated enthusiasm to invest in the electric vehicle industry. Domestic sales rose sharply with the implementation of the subsidy policy. Due to policy relaxation and tax benefits, electric vehicle manufacturers have also increased. The driving range and the safety of the power battery are constantly improving. Power battery technology is constantly advancing. Power semiconductor technology, intelligent drive technology, and power component integration technology have improved to increase power density, reduce losses, and ensure reliability. The main domestic charging method is AC slow charging, supplemented by DC fast charging. Convenience will be an important concern in the future. Microgrid power generation is in a low-carbon mode, interacting power transmission with the main grid. The sum of the total power generation in the microgrid is equal to the total load value in the microgrid, which satisfies the balance of supply and demand. When the load is low, the microgrid sells electricity to the main grid, the battery is charged, and the output of wind power and solar energy drops. When the load peaks, the output of wind power and solar energy increases, and the battery discharges to the main grid.

The electric vehicle industry policy aims to promote the development of the new automobile industry. Ref. [31] predicted electric vehicle sales in the next few years, as shown in Figure 3. In the implementation process, policy formulation has faced challenges from various aspects, including technical, financial, and environmental issues. Related policies and their implementation have encountered a lack of references. Therefore, policy formulation must be further improved. The competent authority shall formulate long-term policy plans considering standardisation and stability. The transition period of the policy should be well connected to ensure continuity and predictability, which will gradually form legal documents.

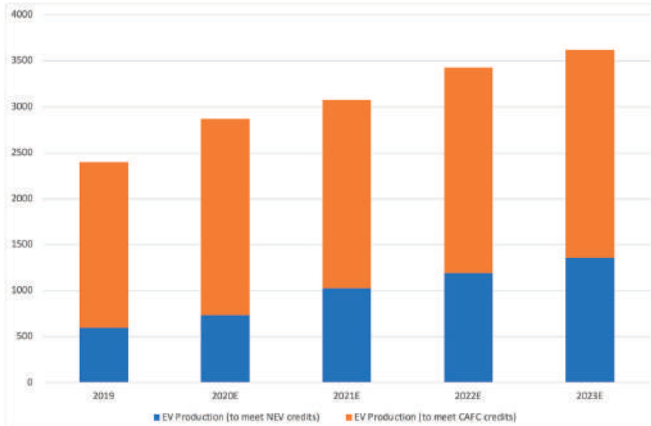

Figure 3. Predicted increase in EV production in China (unit: thousand).

To accommodate the flexibility of the microgrid system, energy storage devices of electric vehicles should be light with the potential to possess high energy density. The application of lithium batteries in recent years has been proven to be a feasible solution. The integration of lithium batteries in electric vehicles can significantly reduce carbon emissions and road-side air pollution [32].

Generation units of renewable energies are small in capacity, large in number, scattered in locations, and diverse in characteristics. Power electronic equipment adopts discrete control based on fast switching, which makes a fundamental change in the control mode of the distributed microgrid power system and has continuous adjustment and control capabilities.

The form of the power system has transformed from the traditional large power grid to the complementary symbiosis of the large power grid and the microgrids. The power system must not only satisfy the access and consumption of centralised new energy but also support the access and withdrawal of distributed power generation. Wind power and solar energy will become the installed capacity of electricity supply as well as bear the responsibility for the safe and stable operation of the power system.

China has launched carbon emission trading pilot schemes in eight regions, actively exploring the trading mechanism and future direction of the carbon trading market. In 2011, China first opened carbon emission rights in seven regions, Beijing, Tianjin, Shanghai, Chongqing, Hubei, Guangzhou, and Shenzhen. In 2017, Fujian joined as the eighth pilot region. Each pilot region followed a similar carbon emission measurement approach; however, the coverage for industrial sectors varied [33]. The development in those eight pilot regions built a solid foundation for the national carbon trading platform in the next stage.

The carbon trading pilot centre in Beijing is the most representative of the eight centres to reflect the carbon emission and trading situation in northern China. Meanwhile, the carbon trading pilot centre in Guangzhou is the most representative of the situation in southern China.

The essential purpose of running an enterprise is for production and sales. The reason why companies with emission pressure are willing to reduce emissions is that excess carbon emission rights exist that can be traded in the carbon trading market for profit. Therefore, related government authorities should encourage enterprises to invest in research and develop emission reduction technologies to reduce the operational and environmental costs of emission reduction. Furthermore, guidelines for consumers to buy low-carbon products will also boost market demand and increase production and sales revenue for enterprises.

5. Policy Implications

The power production structure has undergone profound changes. The primary energy supply for the new power system will shift from stable and controllable conventional energy sources, such as coal, gas, and water, to new energy, such as wind power and solar energy. The technical foundation of the power system has undergone significant changes. The synchronous operation of the AC power system of the new energy unit is driven by the physical characteristics of the steering control algorithm. This is a time to construct a carbon emission management system and a supervision system for low-carbon and green energy development [1]. Moreover, the policy support for industry–university research cooperation and policy support for new and in-depth collaboration between industry, academia, and research led by energy automobile companies must be strengthened. The support and incentives for technology innovation will provide a platform to encourage knowledge transfer and the transformation of scientific and technological achievements related to the automobile and power industry, which will encourage cooperation and integration amongst enterprises and research institutes, including collaborative technology development and industrialisation. The government may introduce various innovation and technology funds to support academic institutions and firms to purchase equipment and recruit research personnel.

Regarding subsidies and tax policies, direct subsidies should be gradually reduced, and low-interest loans and other financial policy support should be increased. The policy scope should consider the whole business chain of the electric vehicle industry. Subsidy policy can be returned to consumers to expand consumer demand. The requirements for products have driven automobile companies to invest in research and development. Subsidies and tax policies have also strengthened review and supervision, thereby increasing the execution power on regulations and laws. Other supporting policies, such as purchase discounts and exemption from traffic restrictions, will also improve the advantages and consumers' willingness to drive electric vehicles.

In addition to the global economic crisis and other factors, issues persist, such as the setting of the total amount of carbon emission rights, the determination of industry coverage, and the allocation of initial carbon emission rights in the design process of the carbon trading mechanism, which have become obstacles to the construction process of carbon trading markets in various countries and have affected the carbon trading mechanism. Government authorities can consider formulating the guidance price of carbon emission rights based on the emission reduction target and the industrial average emission reduction cost. The decision-making behaviours of automobile manufacturers under the carbon trading mechanism include energy intensity, carbon credit evaluation decisions, production decisions, automobile pricing decisions, and carbon credit accounting and trading considering energy intensity. In addition, car manufacturers can interact with car users when selling cars.

Given that information on China's carbon market has not been fully disclosed, investors' decisions based on known information are sophisticated, which exacerbates the randomness of investment decisions and expected yield from carbon trading in the market [34,35]. Therefore, the transparent information disclosure system in the carbon trading market must be improved. The current pricing mechanism in carbon trading pilot centres cannot fully reflect market information. Thus, market pricing efficiency must be improved. Furthermore, establishing appropriate mechanisms to prevent insider trading is essential for controlling market risks. In addition, an adjustment mechanism to effectively prevent abnormal price fluctuations and a risk prevention and control mechanism to prevent market manipulation should be established to form an effective price formation that reflects factors such as supply and demand, emission reduction costs, and so on.

To stimulate carbon trading activities in the pilot centres, government authorities can consider guiding relevant enterprises to increase their willingness to trade spontaneously in the carbon market by providing financial incentives and stimulation mechanisms. On the one hand, penalties for companies that fail to comply with the carbon emission targets should be implemented; on the other hand, more tax incentives and green credits to companies that actively participate in carbon trading and achieve the carbon emission targets should be provided. Such a stimulative mechanism can enhance the enthusiasm of companies to seek profit through active trading activities or to reduce carbon emissions.

Furthermore, the electric vehicle industry faces a challenge of long-term capital occupation and substantial initial financial investment. Based on the experiences of the conventional automobile industry, corporate investment and financing can appropriately reduce financing costs. Financing channels, such as corporate loans and bonds, must be broadened, and banks, financial intermediaries, and credit guarantee centres must be encouraged to provide priority services for electric automobile companies, moderately relax conditions, lower interest rates, and introduce foreign capital. Concurrently, a risk prevention and control mechanism should be implemented.

6. Conclusions and Future Work

In this paper, we proposed and analysed a multi-source microgrid economic dispatch model to reduce carbon emissions. The implemented carbon trading mechanism contributes to achieving carbon emissions control. Companies with surplus carbon emission quotas can increase their additional income by selling such quotas to reduce the total generation and operation cost of the power system. The low-carbon dispatch model enables wind power, solar energy, electric vehicles, and other distributed power generation units to benefit from carbon trading and to reduce the operation costs while expanding the microgrid system, which ultimately reduces the total cost of the power system.

The cost of distributed generation from renewable energies in microgrids is relatively higher than that of conventional generation. When the power generation exceeds a certain range, the system can sacrifice a certain economy to increase the penetration rate of new energy, thereby reducing the carbon emissions of the system and improving the environmental protection of the system.

The issuance and implementation of industrial policies on electric vehicles have become important factors that promote rapid development. With the advent of the post-subsidy era, the electric vehicle industry continues to face challenges related to core technologies and structures. Therefore, industrial policies must be continuously improved to promote the healthy and rapid development of the industry.

With the continuous introduction of new carbon trading-related financial products in China, the volatility of the carbon trading market may be affected by emerging factors. Future research must entail a comprehensive analysis and volatility assessment of the incentives for carbon trading volatility. Furthermore, automobile users are not included in the current emission reduction framework in China. To achieve carbon neutralisation, automobile users, such as the general public who drive EVs, should also be included.

Future study must incorporate related economic and microgrid management indicators into our mathematical model to enrich simulation scenarios with consideration of climate values. As such, it may contribute to the interdisciplinary research direction in the future. Moreover, future research must develop a climate-resilient infrastructure on how to minimise the vulnerabilities or risks influenced by climate change and improve climate resilience [36,37].

Author Contributions: Conceptualisation, methodology, and writing—original draft preparation, Y.W.; validation, formal analysis, and writing—review and editing, Y.-Y.L.; data curation and visualisation, J.-A.W.; funding and project administration, Y.W. All authors have read and agreed to the published version of the manuscript.

Funding: This research was funded by the Research Grant Council of Hong Kong SAR, project reference number UGC/IIDS24/E01/20; the PolyU CPCE Research Fund, project reference number SEHS-2019-169(J); and the PolyU CPCE Research Fund, project reference number SEHS-2021-228(J).

Institutional Review Board Statement: Not applicable.

Informed Consent Statement: Not applicable.

Data Availability Statement: Not applicable.

Conflicts of Interest: The authors declare no conflict of interest.

References

1. Li, Q. The view of technological innovation in coal industry under the vision of carbon neutralisation. *Int. J. Coal Sci. Technol.* **2021**, *8*, 1197–1207. [CrossRef]
2. Sengupta, S. Greta Thunberg's Message at Davos Forum: Our House Is Still on Fire. *The New York Times*, 21 January 2020. Available online: https://www.nytimes.com/2020/01/21/climate/greta-thunberg-davos.html(accessed on 30 March 2022).
3. Jiang, Y.; Deng, Z.; You, S. Size optimization and economic analysis of a coupled wind-hydrogen system with curtailment decisions. *Int. J. Hydrog. Energy* **2019**, *44*, 19658–19666. [CrossRef]
4. Davison-Kernan, R.; Liu, X.; McLoone, S.; Fox, B. Quantification of wind curtailment on a medium-sized power system and mitigation using municipal water pumping load. *Renew. Sustain. Energy Rev.* **2019**, *112*, 499–507. [CrossRef]
5. Canbulat, S.; Balci, K.; Canbulat, O.; Bayram, I.S. Techno-Economic Analysis of On-Site Energy Storage Units to Mitigate Wind Energy Curtailment: A Case Study in Scotland. *Energies* **2021**, *14*, 1691. [CrossRef]
6. Boddapati, V.; Nandikatti, A.S.R.; Daniel, S.A. Techno-economic performance assessment and the effect of power evacuation curtailment of a 50 MWp grid-interactive solar power park. *Energy Sustain. Dev.* **2021**, *62*, 16–28. [CrossRef]
7. Li, Y.; Mohammed, S.Q.; Nariman, G.S.; Aljojo, N.; Rezvani, A.; Dadfar, S. Energy Management of Microgrid Considering Renewable Energy Sources and Electric Vehicles Using the Backtracking Search Optimization Algorithm. *J. Energy Resour. Technol.* **2020**, *142*, 052103. [CrossRef]
8. Eseye, A.T.; Lehtonen, M.; Tukia, T.; Uimonen, S.; Millar, R.J. Optimal Energy Trading for Renewable Energy Integrated Building Microgrids Containing Electric Vehicles and Energy Storage Batteries. *IEEE Access* **2019**, *7*, 106092–106101. [CrossRef]
9. Abubakrab, H.; Mohamed, T.H.; Hussein, M.M.; Guerrero, J.M.; Agundis-Tinajero, G. Adaptive frequency regulation strategy in multi-area microgrids including renewable energy and electric vehicles supported by virtual inertia. *Int. J. Electr. Power Energy Syst.* **2021**, *129*, 106814. [CrossRef]
10. Iacobucci, R.; McLellan, B.; Tezuka, T. The Synergies of Shared Autonomous Electric Vehicles with Renewable Energy in a Virtual Power Plant and Microgrid. *Energies* **2018**, *11*, 2016. [CrossRef]
11. Elkadeem, M.R.; Wong, S.; Azmy, A.M.; Atiya, E.G.; Ullah, Z.; Sharshir, S.W. A systematic decision-making approach for planning and assessment of hybrid renewable energy-based microgrid with techno-economic optimization: A case study on an urban community in Egypt. *Sustain. Cities Soc.* **2020**, *54*, 102013. [CrossRef]
12. Sun, C.; Zhang, H. Review of the Development of First-Generation Redox Flow Batteries: Iron-Chromium System. *ChemSusChem* **2022**, *15*, e202101798. [CrossRef]
13. Van den Berg, N.J.; van Soest, H.L.; Hof, A.F.; den Elzen, M.G.J.; van Vuuen, D.P.; Chen, W.; Drouet, L.; Emmerling, J.; Fujimori, S.; Hohne, N.; et al. Implications of various effort-sharing approaches for national carbon budgets and emission pathways. *Clim. Chang.* **2020**, *162*, 1805–1822. [CrossRef]
14. Wang, Y.; Guo, C.; Chen, X.; Jia, L.; Guo, X.; Chen, R.; Zheng, M.; Chen, Z.; Wang, H. Carbon peak and carbon neutrality in China: Goals, implementation path and prospects. *China Geol.* **2021**, *4*, 720–746. [CrossRef]
15. Wu, C.; Guo, S.; Liu, Y.; Song, T.E.; Han, H. A model predictive control approach in microgrid considering multi-uncertainty of electric vehicles. *Renew. Energy* **2021**, *163*, 1385–1396. [CrossRef]
16. Shi, R.; Zhang, P.; Zhang, J.; Niu, L.; Han, X. Multidispatch for Microgrid including Renewable Energy and Electric Vehicles with Robust Optimization Algorithm. *Energies* **2020**, *13*, 2813. [CrossRef]
17. Liu, C.; Abdulkareem, S.S.; Rezvani, A.; Samad, S.; Aljojo, N.; Foong, L.K.; Nishihara, K. Stochastic scheduling of a renewable-based microgrid in the presence of electric vehicles using modified harmony search algorithm with control policies. *Sustain. Cities Soc.* **2020**, *59*, 102183. [CrossRef]
18. Shang, T.; Yangg, L.; Liu, P.; Shang, K.; Zhang, Y. Financing mode of energy performance contracting projects with carbon emissions reduction potential and carbon emissions ratings. *Energy Policy* **2020**, *144*, 111632. [CrossRef]
19. Tian, J.; Yu, L.; Xue, R.; Zhuang, S.; Shan, Y. Global low-carbon energy transition in the post-COVID-19 era. *Appl. Energy* **2022**, *307*, 118205. [CrossRef]
20. Noorollahi, Y.; Golshanfard, A.; Aligholian, A.; Mohammadi-ivatloo, B.; Nielsen, S.; Hajinezhad, A. Sustainable Energy System Planning for an Industrial Zone by Integrating Electric Vehicles as Energy Storage. *J. Energy Storage* **2020**, *30*, 101553. [CrossRef]
21. Sayed, K.; Abo-Khalil, A.G.; Alghamdi, A.S. Optimum Resilient Operation and Control DC Microgrid Based Electric Vehicles Charging Station Powered by Renewable Energy Sources. *Energies* **2019**, *12*, 4240. [CrossRef]
22. Hao, Y.; Dong, L.; Liang, J.; Liao, X.; Wang, L.; Shi, L. Power forecasting-based coordination dispatch of PV power generation and electric vehicles charging in microgrid. *Renew. Energy* **2020**, *155*, 1191–1210. [CrossRef]
23. Wang, M.; Wang, Y.; Chen, L.; Yang, Y.; Li, X. Carbon emission of energy consumption of the electric vehicle development scenario. *Environ. Sci. Pollut. Res.* **2021**, *28*, 42401–42413. [CrossRef] [PubMed]
24. Ghosh, A. Possibilities and Challenges for the Inclusion of the Electric Vehicle (EV) to Reduce the Carbon Footprint in the Transport Sector: A Review. *Energies* **2020**, *13*, 2602. [CrossRef]

25. Lin, B.; Wu, W. The impact of electric vehicle penetration: A recursive dynamic CGE analysis of China. *Energy Econ.* **2021**, *94*, 105086. [CrossRef]
26. Beijing Environment Exchange. Monthly Report of Carbon Trading at Beijing Environment Exchange. 2022. Available online: https://www.bjets.com.cn/ (accessed on 30 March 2022).
27. Guangzhou Emission Exchange. Weekly Report of Carbon Trading at Guangzhou Emission Exchange. 2022. Available online: http://www.cnemission.com/ (accessed on 30 March 2022).
28. Energy Bureau of Chinese Central Government. Continuous Optimization of Energy Structure in the First Three Quarters of 2021. In *Press Release of Chinese Central Government*; Energy Bureau of Chinese Central Government: Beijing, China, 2021.
29. Akinyele, D.; Olabode, E.; Amole, A. Review of Fuel Cell Technologies and Applications for Sustainable Microgrid Systems. *Inventions* **2020**, *5*, 42. [CrossRef]
30. Zhang, H.; Sun, C. Cost-effective iron-based aqueous redox flow batteries for large-scale energy storage application: A review. *J. Power Sources* **2021**, *493*, 229445. [CrossRef]
31. Wu, Y.A.; Ng, A.W.; Yu, Z.; Huang, J.; Meng, K.; Dong, Z.Y. A review of evolutionary policy incentives for sustainable development of electric vehicles in China: Strategic implications. *Energy Policy* **2021**, *148*, 111983. [CrossRef]
32. Speirs, J.; Contestabile, M.; Houari, Y.; Gross, R. The future of Lithium availability for electric vehicle batteries. *Renew. Sustain. Energy Rev.* **2014**, *35*, 183–193. [CrossRef]
33. Wu, Y.; Wang, P.; Liu, X.; Chen, J.; Song, M. Analysis of regional carbon allocation and carbon trading based on net primary productivity in China. *China Econ. Rev.* **2020**, *60*, 101401. [CrossRef]
34. Jia, Z.; Lin, B. Rethinking the choice of carbon tax and carbon trading in China. *Technol. Forecast. Soc. Change* **2020**, *159*, 120187. [CrossRef]
35. Lau, Y.Y.; Wu, A.W.; Mak, W.Y. A way forward for electric vehicle in Greater Bay Area: Challenges and opportunities for the 21st century. *Vehicles* **2022**, *4*, 420–432. [CrossRef]
36. Yang, Z.; Ng, A.K.Y.; Lee, P.T.W.; Wang, T.; Qu, Z.; Rodrigues, V.S.; Pettit, S.; Harris, I.; Zhang, D.; Lau, Y.Y. Risk and cost evaluation of port adaptation measures to climate change impacts. *Transp. Res. Part D Transp. Environ.* **2018**, *61*, 444–458. [CrossRef]
37. Ng, A.K.Y.; Zhang, H.; Afenyo, M.; Becker, A.; Cahoon, S.; Chen, S.L.; Esteban, M.; Ferrari, C.; Lau, Y.Y.; Lee, P.T.W.; et al. Port decision maker perceptions on the effectiveness of climate adaptation actions. *Coast. Manag.* **2018**, *46*, 148–175. [CrossRef]

energies

Article

Slope Estimation Method of Electric Vehicles Based on Improved Sage–Husa Adaptive Kalman Filter

Jiawei Guo [1,2], Chao He [1,2], Jiaqiang Li [1,2,*] and Heng Wei [1,3]

1 School of Machinery and Transportation, Southwest Forestry University, Kunming 650224, China; williamgjw@swfu.edu.cn (J.G.); chao.he@swfu.edu.cn (C.H.); henrywei1@whut.edu.cn (H.W.)
2 Key Laboratory of Vehicle Emission and Safety on Plateau Mountain, Yunnan Provincial Department of Education, Kunming 650224, China
3 Hubei Key Laboratory of Advanced Technology for Automotive Components, Wuhan University of Technology, Wuhan 430070, China
* Correspondence: lijiaqiang@swfu.edu.cn

Abstract: In order to deal with many influence factors of electric vehicles in driving under complex conditions, this paper establishes the system state equation based on the longitudinal dynamics equation of vehicle. Combined with the improved Sage–Husa adaptive Kalman filter algorithm, the road slope estimation model is established. After the driving speed and rough slope observation are input into the slope estimation model, the accurate road slope estimation at the current time can be obtained. The road slope estimation method is compared with the original Sage–Husa adaptive Kalman filter road slope estimation method through three groups of road tests in different slope ranges, and the accuracy and stability advantages of the proposed algorithm in road conditions with large slopes are verified.

Keywords: road slope estimation; adaptive Kalman filter; electric car

Citation: Guo, J.; He, C.; Li, J.; Wei, H. Slope Estimation Method of Electric Vehicles Based on Improved Sage–Husa Adaptive Kalman Filter. *Energies* **2022**, *15*, 4126. https://doi.org/10.3390/en15114126

Academic Editors: Wenbin Yu, Guang Zeng and Tek Tjing Lie

Received: 10 April 2022
Accepted: 1 June 2022
Published: 3 June 2022

1. Introduction

Accurate road slope prediction method is of vital importance in the field of autonomous driving. The system collects parameters through algorithms, predicts the slope at the next moment in advance, and prepares to control the vehicle power system at the next moment, so as to improve the control ability of automatic transmission of vehicles, optimize the power and economy of vehicles, and reduce energy consumption while running smoothly. The parameters of the vehicle the system collects include torque, vehicle speed, acceleration, slope, etc. Among all the parameters, accurate slope information acquisition and prediction has a very special research significance for intelligent vehicle driving; details are shown below.

Figure 1 explains the basic principle of unmanned driving—all behaviors of human drivers in driving can be planned into three steps: environmental perception, decision and planning, control and execution. Environmental perception is the first and most important part. For example, human drivers collect the road condition information of the current vehicle through hearing and vision, and make decisions about the following driving behavior according to this information. Autonomous driving systems also need to collect road information before planning power systems, so high-precision collection algorithms are very important. In addition, the parameter of road slope is a very important part of the longitudinal dynamics equation of the vehicle. Both rolling friction and slope resistance are related to the road slope of the vehicle at the current moment, which to some extent determines the advantages and disadvantages of the adjustment of the dynamic performance of the vehicle in the automatic driving link.

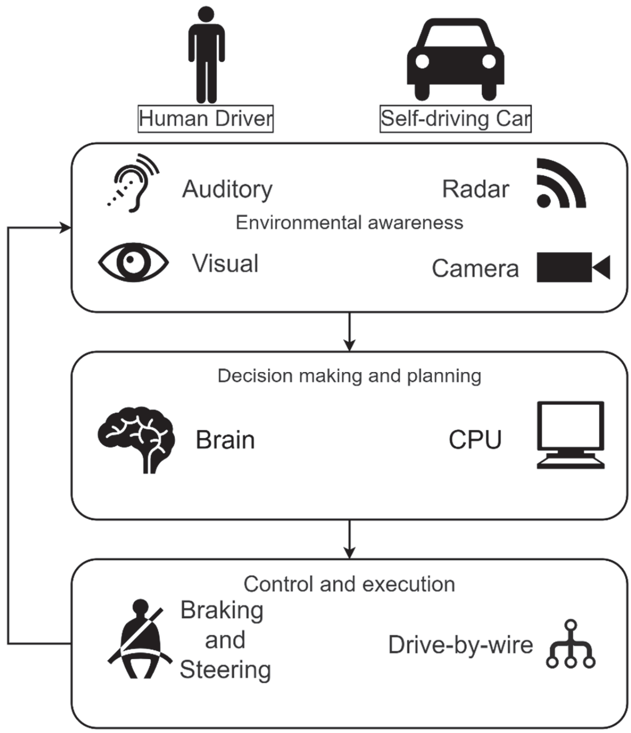

Figure 1. Concept of autonomous driving.

From the perspective of the long-term development of automatic driving, accurate slope prediction is the necessary guarantee for automatic driving technology to step into level 4 and level 5. Level 5 autonomous driving technology requires the vehicle to be able to navigate unknown roads and environments. Therefore, scholars all over the world have done a lot of research on slope prediction and have achieved some results.

In the past 5 years, most of the research on slope estimation algorithms has been based on longitudinal dynamics of vehicles. Some scholars designed a series of slope estimation methods using unscented Kalman filter, such as Dual Unscented Kalman Filter (DUKF) and Quaternion Unscented Kalman Filter (QUKF) [1–4]. A few scholars used extended Kalman filter to construct slope estimation methods and achieved some results [5,6]. The least square method was also used to construct slope estimation algorithms [7–9]. Jiang et al. proposed a two-stage estimation method for vehicle mass and road slope under longitudinal moving condition of mini fuel cell vehicle (FCV) [10]. Hu et al. established the longitudinal kinematics model of vehicles, using the recursive least squares method with adaptive forgetting factors and extended Kalman filter algorithm to estimate the vehicle mass and road grade, respectively [11]. Rodríguez et al. presented a novel accurate estimator based on errorEKF and UKF for vehicle dynamics [12]. Bian et al. presented a MPC based vehicular following control algorithm with road grade prediction [13]. Feng et al. proposed a slope estimation algorithm based on multi-model and multi-data fusion [14].

To sum up, the accuracy of slope prediction is closely related to autonomous driving technology. At the same time, slope estimation is an important cornerstone of the development of autonomous driving technology. Previous literatures have achieved certain results in slope prediction with good prediction accuracy, but there are still gaps in some aspects. The accuracy of the basic Kalman filter has struggled to meet the current requirements of automatic driving. The extended Kalman Filter (EKF) uses Taylor Expansion to construct approximate linear function by obtaining the slope of nonlinear function. The nonlinear system is approximated to linear system by means of ignoring the higher-order term, which inevitably introduces linear error and even leads to the divergence of filter. Thus, the accuracy of slope estimation is reduced. Unscented Kalman filter (UKF) is more accurate than EKF, and its accuracy is equivalent to second-order Taylor expansion, but the speed is slower. A large amount of calculation will require a longer calculation time, so whether it can be applied to the dynamic slope estimation of vehicles remains to be discussed. If the technical choice is to use hardware means to speed up the calculation, the cost of hardware is also higher.

In many Kalman filter algorithms, adaptive Kalman filter plays a very important role. Adaptive Kalman filter uses the measured data to filter and continuously judge whether the system dynamic changes by filtering itself. The model parameters and noise statistics are estimated and modified to improve the filter design and reduce the actual error of the filter. It automatically scales the system noise covariance matrix Q. It is considered that the algorithm has fewer tuning parameters and better robustness than the scaling state covariance matrix algorithm [15]. Therefore, scholars have done a lot of research on it. They combined adaptive steps with extended Kalman filter, untraced Kalman filter and other algorithms to derive a series of adaptive Kalman filters, and have made considerable achievements in various fields [16–23]. Due to the addition of adaptive steps, the accuracy of AEKF and AUKF algorithm is improved and the convergence speed is accelerated compared with the original algorithm. However, considering the complexity of calculation of UKF and EKF, on the premise of the same data sets and the same hardware devices, AKF's calculation speed is higher than AEKF's, and AEKF's calculation speed is higher than AUKF's. Adaptive Kalman filter has also made some contributions to slope estimation. Liao et al. proposed a road slope estimation method based on AEKF [24]. The method was based on the longitudinal dynamics equation of vehicle, and the state space system was discretized. Then, the innovation-based adaptive tuning part was designed to estimate time-varying process noise covariance and measurement noise covariance. Finally, the proposed method was verified by simulation on Carsim platform, and the result was better than the existing EKF algorithm. Sun et al. proposed a road slope estimation method based on AUKF [25]. By increasing the initial noise of the mass prediction model and designing the adaptive shrinkage coefficient to dynamically adjust the covariance matrix of the prediction error, the method realized the rapid and accurate joint estimation of vehicle mass and road slope under the condition of small acceleration. This adaptive step shortened the convergence time of UKF algorithm to some extent, but the convergence time was still about 10 s.

In this paper, an improved road grade estimation method based on Sage–Husa adaptive Kalman filter is proposed. In the method, the model is established based on the longitudinal dynamics of vehicles. The missing quantity in Sage–Husa algorithm is supplemented in the adaptive covariance matrix Q, and the updating of prediction noise q and observation noise r is cancelled. The effect of initial noise variance in Sage–Husa algorithm is retained to some extent, and the proportion of fixed noise variance can be controlled. At the same time, this method eliminates the deviation caused by approximate mathematical expectation in the process of recursive accumulation, thus further improving the accuracy of the algorithm, and maintaining the accuracy and stability of the method in a long time. In this paper, the test data measured by real vehicle is substituted into the slope algorithm proposed in this paper to calculate, and multiple groups of filtering results are obtained. By comparing the prediction results with the reference values, RMSE and MAE are used to evaluate the slope prediction effect, and the accuracy of the slope prediction algorithm is better. Compared with the traditional adaptive Kalman filtering algorithm, the accuracy of the improved algorithm is significantly improved, and the accuracy can be maintained for a long time. Compared with previous slope prediction algorithms, this algorithm has some advantages in accuracy and convergence time.

2. Modeling

2.1. Modeling Based on Electric Vehicle Longitudinal Dynamics

As shown in Figure 2 above, the longitudinal dynamics equation of an electric vehicle can be expressed as:

$$F_t = F_f + F_i + F_w + F_g + F_{err} \tag{1}$$

where F_t is the driving force. According to the characteristics of electric vehicles.

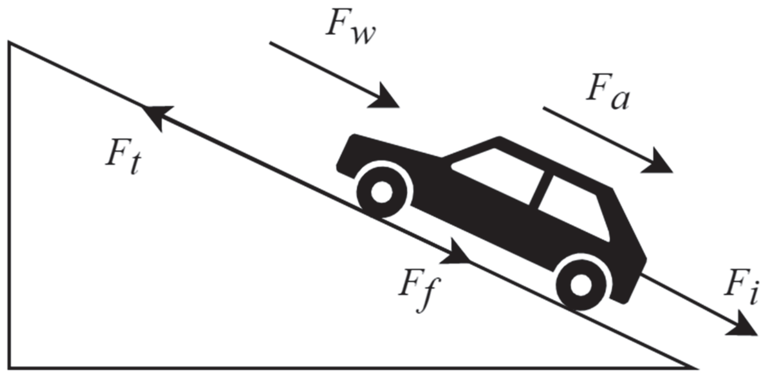

Figure 2. Diagram of electric vehicle longitudinal dynamics.

The driving force can be expressed as:

$$F_t = \frac{T_{tq} i_0 \eta}{r} \tag{2}$$

where T_{tq} is the motor torque, i_0 is the transmission ratio of the main reducer, η is the mechanical efficiency of the transmission system, and r is the rolling radius of the wheel, which is the default wheel radius when the tire pressure is sufficient.

The rolling resistance F_f can be expressed as:

$$F_f = mgf \cos \alpha \tag{3}$$

where m is the vehicle mass, g is the gravitational acceleration, f is the rolling resistance coefficient, and α is the road slope angle where the vehicle is located. It is generally considered that the road slope angle is small, $\cos \alpha \approx 1$.

The acceleration resistance F_i can be expressed as:

$$F_i = \frac{\delta m du}{dt} \tag{4}$$

where δ is the conversion coefficient of vehicle rotating mass, which defaults to 1 in some common algorithms. However, in actual driving conditions, δ is usually distributed between 1.1 and 1.4, and the default value of 1 will affect the accuracy of the prediction equation to a certain extent.

The air resistance F_w can be expressed as:

$$F_w = \frac{C_D A \rho u^2}{2} \tag{5}$$

where C_D is the air resistance coefficient, A is the windward area, ρ is the air density, u is the vehicle speed.

The ramp resistance F_g, the component of gravity on the slope, can be expressed as:

$$F_g = mg\ sin\ \alpha \tag{6}$$

The system error F_{err} is caused by uncertain environment disturbance in longitudinal dynamics [26].

To sum up, the longitudinal dynamics equation of an electric vehicle can be rewritten as [27]:

$$\frac{T_{tq} i_0 \eta}{r} = mgf + \frac{\delta m du}{dt} + \frac{C_D A \rho u^2}{2} + mgi \tag{7}$$

The windward area A of BAIC EX360 electric vehicle used in this paper is 2.77 square meters. The air resistance coefficient C_D generally takes an empirical value, and this paper sets C_D as 0.3.

2.2. Prediction Equation and Observation Equation

In this paper, appropriate state variables are selected, namely, speed u and road slope i, because they are easy to read. The state variable x can be expressed as:

$$x = \begin{bmatrix} u \\ i \end{bmatrix} \tag{8}$$

Generally, the slope of urban roads changes gently and the driving speed is low, so the differential equation of speed and slope can be obtained:

$$\begin{bmatrix} \dot{u} \\ \dot{i} \end{bmatrix} = \begin{bmatrix} \frac{T_{tq} i_0 \eta}{\delta m r} - \frac{fg}{\delta} - \frac{gi}{\delta} - \frac{C_D A \rho u^2}{2\delta m} \\ 0 \end{bmatrix} \tag{9}$$

Under urban road conditions, the vehicle speed is usually within 30 km/h, and the maximum is no more than 50 km/h. In the differential equation above, $\frac{T_{tq} i_0 \eta}{\delta m r}$ is usually small enough to be ignored.

Based on the arithmetic relation of velocity and acceleration and the longitudinal dynamic equation of electric vehicle above, the equation of state can be set as:

$$u_k = u_{k-1} + \dot{u}\Delta t \tag{10}$$

$$\begin{bmatrix} \dot{u}_{k|k-1} \\ i_{k|k-1} \end{bmatrix} = \begin{bmatrix} 1 & g\Delta t \\ 0 & 1 \end{bmatrix} \begin{bmatrix} u_{k-1} \\ i_{k-1} \end{bmatrix} + \begin{bmatrix} \frac{\Delta t}{\delta m} \left(\frac{T_{tq} i_0 \eta}{r} - fmg \right) \\ 0 \end{bmatrix} + q \tag{11}$$

In the above formula, $\dot{u}_{k|k-1}$ and $i_{k|k-1}$ represent the prior results, that is, the values at time k without Kalman filtering. Additionally, q is the noise vector of the prediction equation.

In the real vehicle test, the speed parameter u_k can be easily measured. Therefore, this paper first takes the speed u_k as the observed value and the observation equation can be expressed as:

$$Z_k = Hx_{k|k-1} + r \tag{12}$$

In the observation equation, $H = \begin{bmatrix} 1 & 0 \\ 0 & 1 \end{bmatrix}$, indicating that both velocity and slope have been observed. Because of the immeasurable noise in the actual experiment and the substitution of empirical values in some data of the prediction equation, the error of the prediction equation cannot be ignored. Therefore, a low-precision slope observation is added in this paper. r represents the measurement noise vector.

3. Adaptive Kalman Filtering

3.1. Flow Chart of Basic Kalman Filter

As shown in Figure 3, the application process of Kalman filter is divided into prediction and update. Kalman filter is a state optimal estimation algorithm. It calculates the priori estimate $x_{k|k-1}$ at time k by substituting the optimal estimate x_{k-1} at time $k-1$ into the prediction equation, compares $x_{k|k-1}$ with the measured value Z_k at time k, assigns weights to $x_{k|k-1}$ and Z_k by Kalman gain, and finally obtains the optimal estimate x_k at time k. After that, Kalman filter recursively computes the optimal estimate at the next time.

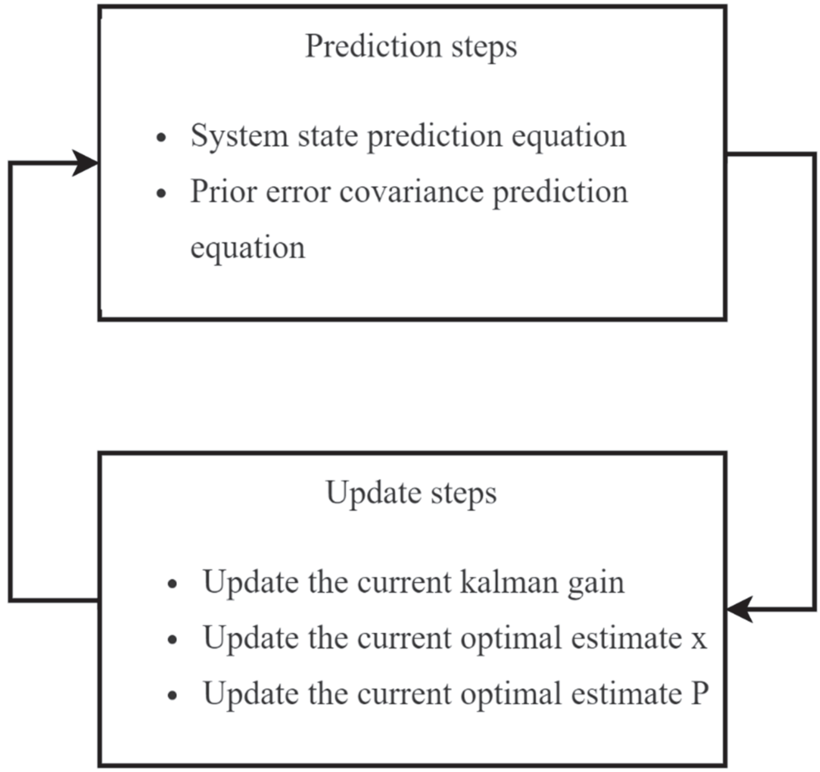

Figure 3. Flow chart of Kalman filter.

3.2. Prediction Equations

The prediction equation of the system can be expressed as:

$$x_{k|k-1} = Fx_{k-1} + B_{k-1} + q \tag{13}$$

Among them, $F = \begin{bmatrix} 1 & g\Delta t \\ 0 & 1 \end{bmatrix}$, $B_{k-1} = \begin{bmatrix} \frac{\Delta t}{\delta m}\left(\frac{T_{tq} i_0 \eta}{r} - fmg\right) \\ 0 \end{bmatrix}$.

The prediction equation of the prior error covariance can be expressed as:

$$P_{k|k-1} = FP_{k-1}F^T + Q \tag{14}$$

where P is the variance of the state estimate and represents the measure of the uncertainty in the predicted state, which comes from process error and the error of the estimate. Q is the covariance matrix of prediction noise q.

3.3. The Update Equation

The update of Kalman gain can be expressed as:

$$K_g = P_{k|k-1}H^T\left(HP_{k|k-1}H^T + R\right)^{-} \tag{15}$$

where K_g is Kalman gain and represents the weight relationship between predicted value and measured value. R is the covariance of the observed value and represents the uncertainty of the observed state. The smaller the value is, the more accurate the observation is.

The update of the optimal estimate of x_k can be expressed as:

$$x_k = x_{k|k-1} + K_g \left(Z_k - H x_{k|k-1} \right) \tag{16}$$

The update of the optimal estimate P_k can be expressed as:

$$P_k = \left(I - K_g H \right) P_{k|k-1} \tag{17}$$

where I represents the identity matrix, whose order is equal to the number of elements of the state variable.

3.4. Sage–Husa Adaptive Kalman Filter

Adaptive Kalman filter updates q_k, Q_k, r_k and R_k on the basis of Kalman filter.

A weighting coefficient d_k is given, d_k can be expressed as:

$$d_k = (1-b)\left(1-b^{k+1}\right)^{-} \tag{18}$$

where d_k is usually between 0.95 and 0.99. The weighting coefficient is used to enhance the effect of recent data and update noise.

The update formula is as follows:

$$\begin{aligned}
\varepsilon_k &= Z_k - H x_{k|k-1} - r_{k-1} \\
q_k &= (1-d_k) q_{k-1} + d_k (x_k - F x_{k-1}) \\
Q_k &= (1-d_k) Q_{k-1} + d_k \left(K_g \varepsilon_k \varepsilon_k^T K_g^T + P_k - F x_{k-1} F^T \right) \\
r_k &= (1-d_k) r_{k-1} + d_k \left(Z_k - H x_{k|k-1} \right) \\
R_k &= (1-d_k) R_{k-1} + d_k \left(\varepsilon_k \varepsilon_k^T - H P_{k|k-1} H^T \right)
\end{aligned} \tag{19}$$

3.5. Improved Sage–Husa Adaptive Kalman Filter

Wei et al. from Northwestern Polytechnical University studied Sage–Husa adaptive Kalman filter and found that the contribution of Q_0, the initial value of the covariance matrix, to Q_k would decrease sharply with the increase of k in the operation process, and would soon approach zero. When some systems need fixed noise with proportion, the applicability of traditional Sage–Husa adaptive Kalman filter will be reduced. The traditional Sage–Husa adaptive Kalman filter adopts the method of average information allocation for q_k, Q_k, r_k and R_k, and the proportion of initial value to contribution is only $1/k$. At the same time, Wei et al. found in their calculation that the deviation of q_k and r_k would affect the coordination relationship between R_k and Q_k, leading to the increase of subsequent deviation [15].

In view of the above situation, this paper improved the algorithm by canceling the calculation of q_k and r_k, and setting the forgetting factors b_1 and b_2 respectively. The traditional Sage–Husa Kalman filter formula is rewritten as follows:

$$\begin{aligned}
d_{k1} &= (1-b_1)\left(1-b_1^{k+1}\right)^{-} \\
d_{k2} &= (1-b_2)\left(1-b_2^{k+1}\right)^{-} \\
R_k &= (1-d_{1k}) R_{k-1} + d_{1k} \left(\varepsilon_k \varepsilon_k^T - H P_{k|k-1} H^T \right) \\
Q_k &= (1-d_{2k}) Q_{k-1} + d_{2k} \Big(K_g \varepsilon_k \varepsilon_k^T K_g^T + P_k - F x_{k-1} F^T - 2 K_g R_k K_g^T \\
&\quad - 2 K_g H P_{k|k-1} H^T K_g^T + P_{k|k-1} H^T K_g^T + K_g H P_{k|k-1} \Big)
\end{aligned} \tag{20}$$

Combined with the above and Figure 4, it can be concluded that, compared with the previous algorithm, the calculation of q_k and r_k is cancelled, and the original forgetting factor b is replaced. Instead, two forgetting factors b_1 and b_2 are set for the update of R_k and Q_k respectively. Meanwhile the system noise Q_k is rederived by a series of approximate processing in the steps.

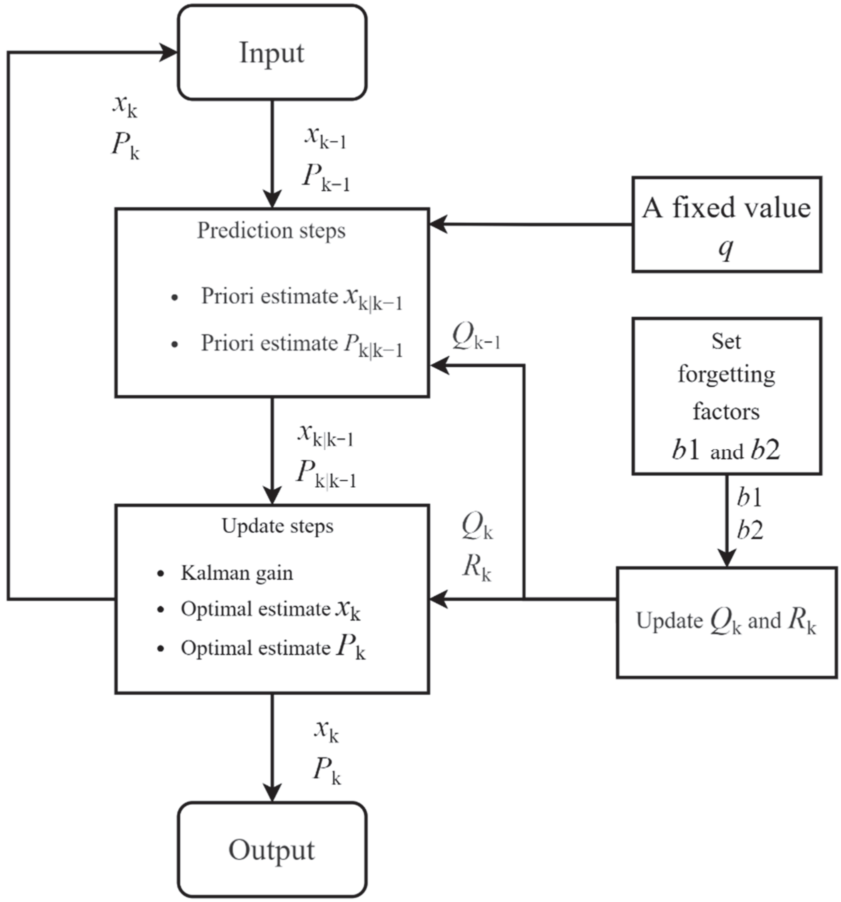

Figure 4. Flow chart of improved adaptive Kalman filter.

4. Experiment

4.1. Experiment Plan

In order to verify the effectiveness of the improved Sage–Husa adaptive Kalman filter for road slope estimation, a large number of vehicle tests were carried out. The driving data of multiple groups of roads with different slopes in and around southwest Forestry University in Kunming city, Yunnan Province were collected in the experiment, and the most representative groups of data were selected to verify the scheme.

4.2. Experiment Equipment and Parameters

The equipment used in the test includes BAIC New Energy EX-360 electric vehicle, on-board OBD, SD card, low-cost gyroscope, high-precision IMU and GPS. InVIEW is used as data processing and analysis software. Matlab is used to build algorithms model and produce results by inputting test data into the algorithm model.

Among them, the low-precision gyroscope is used to assist the algorithm proposed in this paper, that is, to provide rough observation value for the subsequent system to input the observation value into the algorithm. The high-precision IMU and GPS are used to provide an experimental slope value with a very small error, which can be used as a reference value for the real slope. The IMU used in this experiment is shown in Figure 5.

Figure 5. IMU of high accuracy.

Some vehicle parameters and model parameters are shown in Tables 1 and 2.

Table 1. Test vehicle parameters.

Parameter	VALUE
Vehicle type	BAIC EX360
Maximum motor power	80 kW
Maximum motor torque	230 N·m
Transmission type	fixed gear ratio
Curb weight	1480 kg
Size	4110 mm × 1750 mm × 1543 mm
Transmission efficiency	97%
Tire type	205/50 R16

Table 2. Prediction model parameters.

Parameter	VALUE
r	0.3 m
m	1715 kg
δ	1.1

The tire rolling radius r is the approximate tire rolling radius based on tire specification 205/50 R16 and taking into account the bearing time and sufficient tire pressure. Actual curb weight m includes the quality of the car itself, the instruments and the testers. The rotational mass conversion coefficient δ of the test vehicle is derived from the empirical value of the rotational mass of the car.

4.3. Experiment Section

According to the slope classification of geomorphic detail map application of geomorphic survey and Geomorphic Mapping Commission of international Geographical Union, the slope grade is defined as 0°~0.5° plain, 0.5°~2° micro slope, 2°~5° gentle slope and 5°~15° slope. In this paper, the angle value is converted into slope value, and the data of the three groups of sections in the test are classified according to the division basis, which are micro-slope model, gentle slope model R1 and gentle slope model R2. These sections are shown in Figure 6 below.

(**a**)

(**b**)

(**c**)

Figure 6. GPS images of the test sections. (**a**) Micro slope model, (**b**) Gentle slope model R1, (**c**) Gentle slope model R2.

Micro slope model: the road with a low slope, with a slope of 1 to 5%. The starting point of the road section is at the gate of the Second canteen of Southwest Forestry University, and it moves forward to the school gymnasium, then runs along the slope to the Engineering

Building, and stops in the middle of the slope. The slope of this section is mostly in the range of micro-slope, so this paper regards it as a micro-slope model.

Gentle slope model R1: the road with a moderate slope, with a slope of 2 to 6%, which is located on the west side of building 19 student dormitory of Southwest Forestry University. The slope of this section is mostly in the interval of gentle slope, so this paper regards it as a gentle slope model.

Gentle slope model R2: the road with a moderate slope, with a slope of 5 to 8%. This road is a long slope from gate No. 1 to gate No. 2 of Southwest Forestry University. The slope of this section is mostly in the interval of gentle slope, so this paper regards it as a gentle slope model.

4.4. Error Analysis

In order to evaluate the accuracy of this algorithm, Root Mean Square Error (RMSE) and Mean Absolute Error (MAE) are introduced. The errors of the data obtained by the common adaptive Kalman filter algorithm and the improved Sage–Husa adaptive Kalman filter algorithm are calculated with the real data respectively, and the size of the error index is analyzed.

RMSE and MAE are expressed as follows:

$$\mathrm{RMSE} = \sqrt{\mathrm{MSE}} = \sqrt{\frac{SSE}{n}} = \sqrt{\frac{1}{n}\sum_{i=1}^{n}(y_i - \hat{y}_i)^2} \tag{21}$$

$$\mathrm{MAE} = \frac{1}{n}\sum_{i=1}^{n}|y_i - \hat{y}_i| \tag{22}$$

In this paper, AKF1 represents the initial adaptive Kalman filter algorithm, and AKF2 represents the improved adaptive Kalman filter algorithm. The black solid line is used to represent the reference measured road slope value, the blue solid line is used to draw the data results of the original adaptive Kalman filter algorithm, and the red solid line is used to draw the data results of the improved adaptive Kalman filter algorithm. In order to compare the two algorithms more clearly, some regions in the Figure 7 are enlarged and displayed on the right side of the original line chart. The RMSE and MAE of the algorithm results are drawn into tables, as shown in Figure 8.

As can be seen from Figures 7 and 8, the convergence speed of the two algorithms is fast. By longitudinal comparison of the two slope estimation methods under the three models, RMSE and MAE values of the original adaptive Kalman filter slope algorithm increase significantly with the increase of slope, RMSE value increases from 0.048 to 0.081%, MAE value increases from 0.035 to 0.064%, and the changes are particularly obvious. However, the RMSE and MAE values of the improved adaptive Kalman filter slope algorithm change only from 0.038 to 0.040%, and MAE from 0.029 to 0.030%. It can be concluded that the improved adaptive Kalman filter slope algorithm can better adapt to the road conditions in various slope ranges and has strong stability.

The two algorithms in the same slope range were compared horizontally. After the algorithm ran for a period of time, the accuracy of the original adaptive Kalman filter slope algorithm began to decline significantly, and errors that could not be ignored appeared. As shown in Figure 7, in the micro-slope model, the value of the original adaptive Kalman filter slope algorithm began to float significantly above the actual measured value near the moment of 24 s. In the gentle slope model R1, the error of the algorithm is more obvious when it starts near 26 s. In the gentle slope model R2, the error of the original adaptive Kalman filter slope algorithm cannot be ignored after 25 s, completely deviating from the real value. The improved adaptive Kalman filter slope algorithm can keep the data in accordance with the actual measured values in the three slope models, and will not lose the accuracy after running for a period of time.

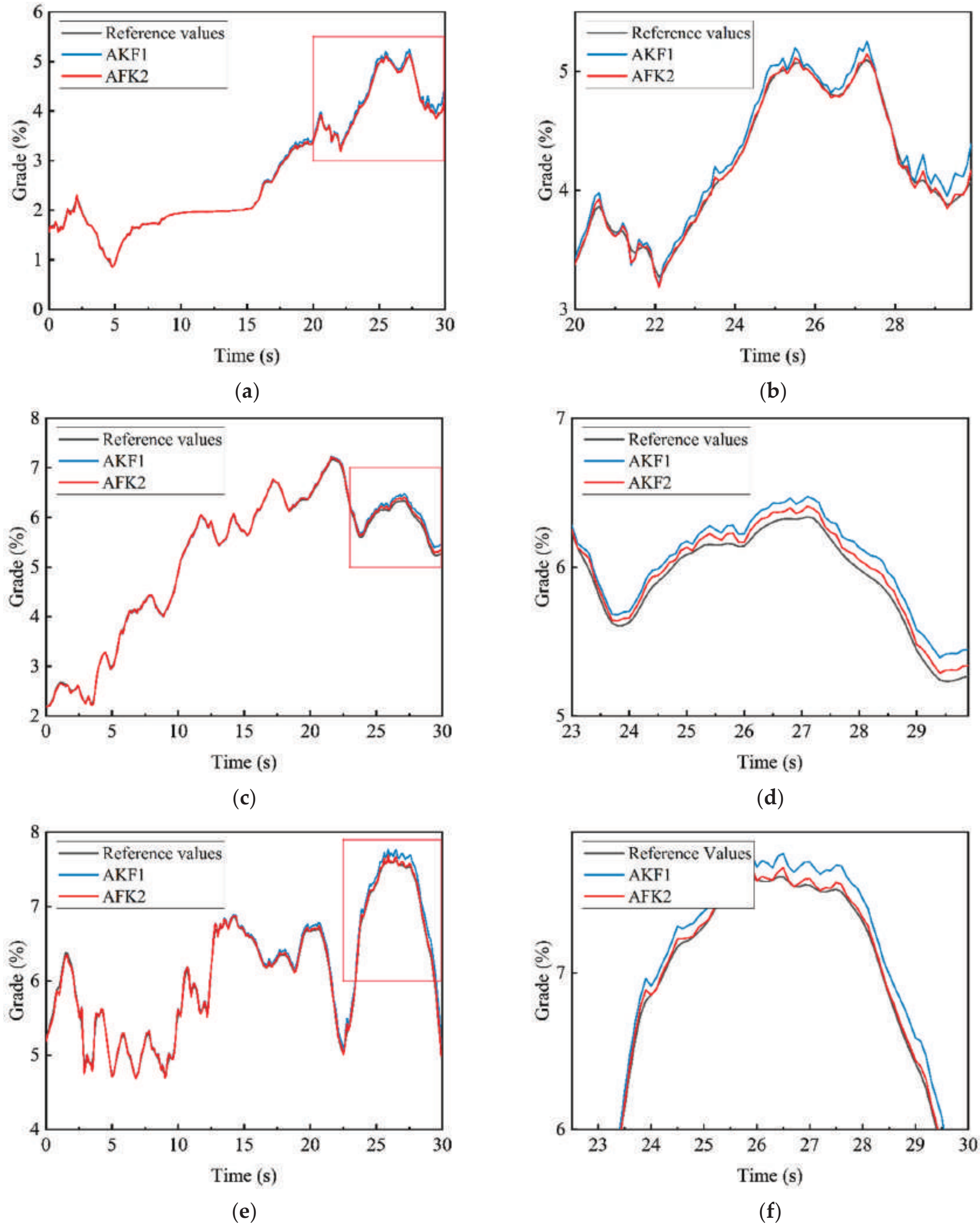

Figure 7. Contrast diagram of test effect. (**a**) Micro slope model, (**b**) part of micro slope model, (**c**) gentle slope model R1, (**d**) part of gentle slope model R1, (**e**) gentle slope model R2, (**f**) part of gentle slope model R2.

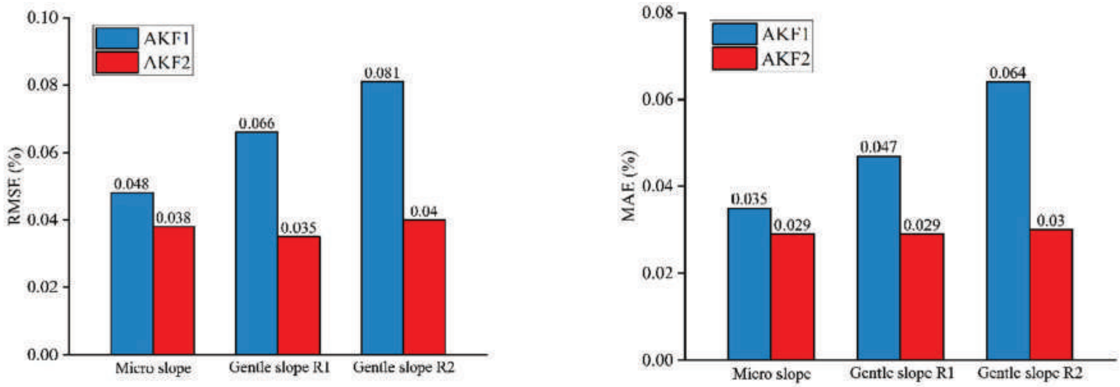

(**a**) (**b**)

Figure 8. Comparison diagram of RMSE and MAE for two algorithms. (**a**) Comparison diagram of RMSE, (**b**) comparison diagram of MAE.

As shown in Figure 9, this paper also presents three groups of 100 s filtering results. In order to display the effect clearly, the original adaptive Kalman filter result is represented by the blue solid line, and the improved adaptive Kalman filter result is represented by the red dotted line. The filtering effect of the first few seconds is shown in the attached figure on the right. It can be seen that the error of the original adaptive Kalman filter gradually becomes obvious after a period of time. The results of the improved adaptive Kalman filter still fit the real value after a long time. From what has been discussed above, the gap between the two algorithms is greatly obvious. The RMSE value of the 100s filtering value of the slope prediction algorithm proposed in this paper increases to some extent compared with the RMSE value of the filtering value of the previous 30 s, but the result is still satisfactory.

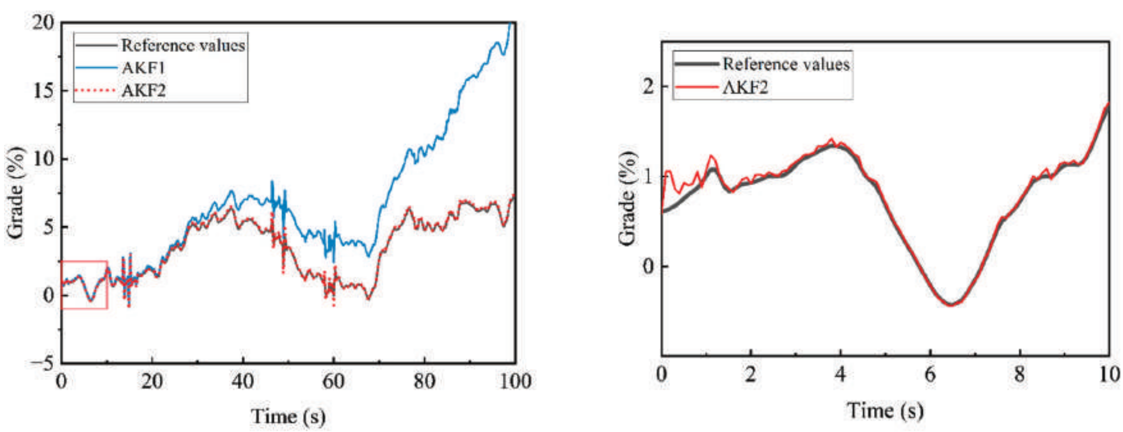

(**a**) (**b**)

Figure 9. *Cont.*

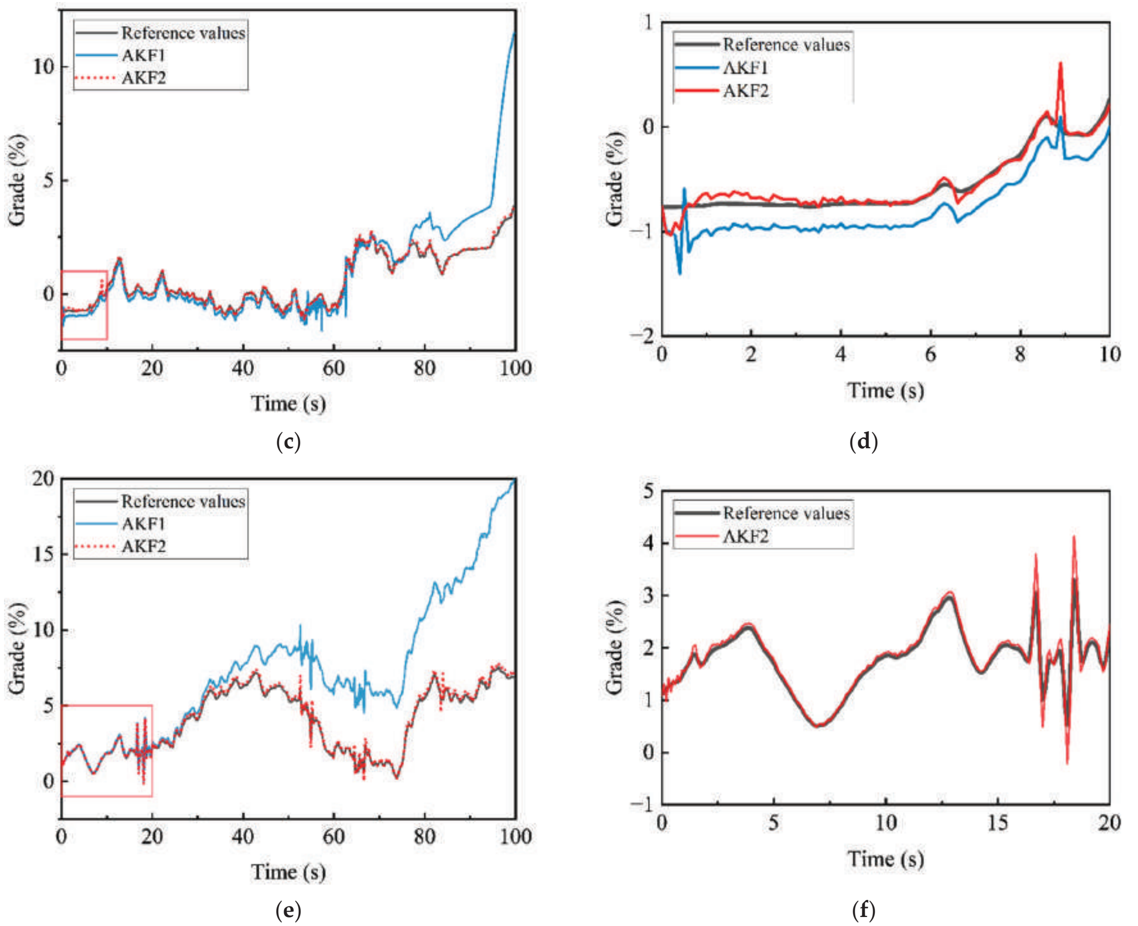

Figure 9. Contrast diagram of long-term test effect. (**a**) Micro slope model, (**b**) part of micro slope model, (**c**) gentle slope model R1, (**d**) part of gentle slope model R1, (**e**) gentle slope model R2, (**f**) part of gentle slope model R2.

Through the study and calculation of Wei et al., it is speculated that the reason for the increase of the time error may be that the recursive formula of q_k and r_k in the original Sage–Husa adaptive Kalman filter algorithm is the approximation of the system equation and the measurement equation. In the process of recursive accumulation, the deviation caused by the expectation of approximate mathematics may sometimes be large. However, the deviation of q_k and r_k will affect the coordination relationship between Q_k and R_k, leading to the increase of subsequent deviation, thus affecting the accuracy of estimation. Taking the gentle slope model R1 as an example, the prediction equation and observation equation of the two algorithms are consistent, so the initial set values of q_k, r_k, R_k and Q_k are consistent. In the subsequent update, the two algorithms adopt different processing methods. The improved adaptive Kalman filter algorithm eliminates the calculation of q_k and r_k, uses the variance P of state estimation to approximate Q_{k-1}, and uses correlation substitution, so less information is discarded.

As shown in the Table 3 below, compared with the QUKF algorithm proposed by He et al., according to RMSE standards, the algorithm proposed in this paper has higher accuracy under certain conditions and uses longer scene time [1].

Table 3. Algorithm RMSE comparison.

Algorithm		AKF2		QUKF	
Experiment	Test 1	Test 2	Test 3	Test 1	Test 2
RMSE	1.3%	0.8%	1.9%	7.8%	7.8%

Compared with the DUKF algorithm proposed by Jin et al., the algorithm proposed in this paper has a faster convergence speed [2]. It can be seen from Figure 9 that the convergence time of the algorithm in this paper is less than 4 s, compared with the convergence time of the DUKF algorithm of about 7 s. Within the scope of adaptive Kalman filter, the convergence speed of the algorithm proposed in this paper is faster than the AEKF algorithm proposed by Liao et al. and the AUKF algorithm proposed by Sun et al. [24,25]. In the experiment of AEKF slope estimation method proposed by Liao et al., the distance was taken as abscissa and the slope was taken as ordinate to output filtered images. It can be seen from the literature that the algorithm converges when the driving distance is about 100 m, and the convergence speed is slow. The convergence time of the AUKF algorithm proposed by Sun et al. is about 10 s, which is longer than the convergence time of the slope estimation method proposed in this paper. Therefore, this algorithm has obvious advantages in the starting stage of electric vehicles. In the starting process of pure electric vehicle, the system directly controls the motor output torque to make the vehicle start normally. When electric vehicles start, if the output torque does not adapt to the starting slope, too much output torque may lead to vehicle running forward in small slope, while too little output torque may lead to vehicle sliding behind or insufficient starting power in large slope. Therefore, the slope algorithm proposed in this paper can improve the smoothness at the start time of EV autonomous driving.

5. Conclusions

(1) In this paper, the improved adaptive Kalman filtering algorithm draws on the valuable experience of predecessors and changes the traditional adaptive Kalman filtering algorithm. It removes the calculation of q_k and r_k, which may lead to a sharp increase in the subsequent deviation, and reasonably improves the update of Q_k and R_k by using double forgetting factors b_1 and b_2.

(2) The algorithm proposed in this paper has a wide range of application. Under the experimental data of multiple 30 s micro slope model and gentle slope model, RMSE can always be maintained within 0.04%, MAE can always be maintained within 0.03%, and short-term effect is relatively good. The RMSE and MAE can always be kept within 0.19% and 0.15%, respectively, under the demonstration of multiple groups of 100 s gentle slope model test data. Generally speaking, the algorithm is applicable to a wide range of slope and has a good general effect.

(3) After a comprehensive comparison of the results of the two algorithms above, it can be found that, compared with the results of the original adaptive Kalman filter slope estimation method, the RMSE and MAE of the improved algorithm are significantly reduced. The RMSE of the micro slope model is reduced by 0.01%, which is 20.8% lower than the original algorithm. The MAE of the micro-slope model is reduced by 0.006%, which is 17.1% lower than the original algorithm. The RMSE of the gentle slope model R1 is reduced by 0.031%, which is 47% lower than the original algorithm. The MAE of the gentle slope model R1 is reduced by 0.018%, which is 38.3% lower than the original algorithm. The RMSE of the gentle slope model R2 is reduced by 0.041%, which is 50.6% lower than the original algorithm. The MAE of the gentle slope model R2 is reduced by 0.034%, which is 53.1% lower than the original algorithm. The error of the 100 s filtering result of the algorithm proposed in this paper increases to some extent compared with the previous 30 s filtering result. However, the error is still reasonable. In conclusion, the improved adaptive Kalman filter slope estimation method is superior.

Author Contributions: Conceptualization, J.G.; methodology, J.G.; data curation, J.G.; funding acquisition, C.H.; software, H.W.; supervision, C.H. and J.L.; writing—review and editing, J.G. and C.H. All authors have read and agreed to the published version of the manuscript.

Funding: This research was funded by National Natural Science Foundation of China grant number 51968065 and Yunnan Provincial high level talent support project grant number YNWR-QNBJ-2018-066, YNQR-CYRC-2019-001.

Data Availability Statement: Not applicable.

Conflicts of Interest: The authors declare no conflict of interest.

References

1. He, W.; Xi, J. A Quaternion Unscented Kalman Filter for Road Grade Estimation. In Proceedings of the 2020 IEEE Intelligent Vehicles Symposium (IV), Las Vegas, NV, USA, 19 October–13 November 2020; pp. 1635–1640.
2. Jin, X.; Yang, J.; Li, Y.; Zhu, B.; Wang, J.; Yin, G. Online estimation of inertial parameter for lightweight electric vehicle using dual unscented Kalman filter approach. *IET Intell. Transp. Syst.* **2020**, *14*, 412–422. [CrossRef]
3. Boada, B.L.; Boada, M.J.L.; Zhang, H. Sensor fusion based on a dual kalman filter for estimation of road irregularities and vehicle mass under static and dynamic conditions. *IEEE/ASME Trans. Mechatron.* **2019**, *24*, 1075–1086. [CrossRef]
4. Pei, X.; Chen, Z.; Yang, B.; Chu, D. Estimation of states and parameters of multi-axle distributed electric vehicle based on dual unscented Kalman filter. *Sci. Prog.* **2020**, *103*, 0036850419880083. [CrossRef] [PubMed]
5. Sun, Y.; Li, L.; Yan, B.; Yang, C.; Tang, G. A hybrid algorithm combining EKF and RLS in synchronous estimation of road grade and vehicle′ mass for a hybrid electric bus. *Mech. Syst. Signal Process.* **2016**, *68*, 416–430. [CrossRef]
6. Büyükköprü, M.; Uzunsoy, E. Reliability of Extended Kalman Filtering Technic on Vehicle Mass Estimation. *J. Innov. Sci. Eng.* **2021**, *5*, 1–11. [CrossRef]
7. Li, X.; Ma, J.; Zhao, X.; Wang, L. Intelligent Two-Step Estimation Approach for Vehicle Mass and Road Grade. *IEEE Access* **2020**, *8*, 218853–218862. [CrossRef]
8. Karoshi, P.; Ager, M.; Schabauer, M.; Lex, C. Robust and numerically efficient estimation of vehicle mass and road grade. In *Advanced Microsystems for Automotive Applications 2017*; Springer: Berlin/Heidelberg, Germany, 2018; pp. 87–100.
9. Zhang, Y.; Zhang, Y.; Ai, Z.; Feng, Y.; Hu, Z. A cross iteration estimator with base vector for estimation of electric mining haul truck's mass and road grade. *IEEE Trans. Ind. Inform.* **2018**, *14*, 4138–4148. [CrossRef]
10. Jiang, S.; Wang, C.; Zhang, C.; Bai, H.; Xu, L. Adaptive estimation of road slope and vehicle mass of fuel cell vehicle. *ETransportation* **2019**, *2*, 100023. [CrossRef]
11. Hu, M.; Gao, W.; Zeng, Y.; Li, H.; Yu, Z. Vehicle mass and road grade estimation based on adaptive forgetting factor RLS and EKF algorithm. In Proceedings of the 2020 5th International Conference on Power and Renewable Energy (ICPRE), Shanghai, China, 12–14 September 2020; pp. 342–346.
12. Rodríguez, A.J.; Sanjurjo, E.; Pastorino, R.; Naya, M.Á. State, parameter and input observers based on multibody models and Kalman filters for vehicle dynamics. *Mech. Syst. Signal Process.* **2021**, *155*, 107544. [CrossRef]
13. Bian, J.; Qiu, B.; Liu, Y.; Su, H. Adaptive Cruise Control for Electric Bus based on Model Predictive Control with Road Grade Prediction. In Proceedings of the VEHITS 2018, Funchal, Portugal, 16–18 May 2018; pp. 217–224.
14. Feng, J.; Qin, D.; Liu, Y.; You, Y. Real-time estimation of road slope based on multiple models and multiple data fusion. *Measurement* **2021**, *181*, 109609. [CrossRef]
15. Wei, W.; Qin, Y.Y.; Zhang, X.D.; Zhang, Y.C. Amelioration of the Sage-Husa algorithm. *J. Chin. Inert. Technol.* **2012**, *6*, 678–686. [CrossRef]
16. Narasimhappa, M.; Mahindrakar, A.D.; Guizilini, V.C.; Terra, M.H.; Sabat, S.L. MEMS-based IMU drift minimization: Sage Husa adaptive robust Kalman filtering. *IEEE Sens. J.* **2019**, *20*, 250–260. [CrossRef]
17. Liu, R.; Liu, F.; Liu, C.; Zhang, P. Modified sage-husa adaptive Kalman filter-based SINS/DVL integrated navigation system for AUV. *J. Sens.* **2021**, *2021*, 9992041. [CrossRef]
18. Song, K.; Wang, Y.; Hu, X.; Cao, J. Online Prediction of Vehicular Fuel Cell Residual Lifetime Based on Adaptive Extended Kalman Filter. *Energies* **2020**, *13*, 6244. [CrossRef]
19. Yan, W.; Ding, Q.; Chen, J.; Liu, Y.; Cheng, S.S. Needle Tip Tracking in 2D Ultrasound Based on Improved Compressive Tracking and Adaptive Kalman Filter. *IEEE Robot. Autom. Lett.* **2021**, *6*, 3224–3231. [CrossRef]
20. Huang, X.; Chen, G.; Liu, Z. Sage Husa Adaptive Integrated Navigation Algorithm Based on Variable Fading Factor. In Proceedings of the 2020 International Conference on Computer Network, Electronic and Automation (ICCNEA), Xi'an, China, 25–27 September 2020; pp. 378–383.
21. Zhang, F.; Yin, L.; Kang, J. Enhancing Stability and Robustness of State-of-Charge Estimation for Lithium-Ion Batteries by Using Improved Adaptive Kalman Filter Algorithms. *Energies* **2021**, *14*, 6284. [CrossRef]
22. Luo, Z.; Fu, Z.; Xu, Q. An Adaptive Multi-Dimensional Vehicle Driving State Observer Based on Modified Sage–Husa UKF Algorithm. *Sensors* **2020**, *20*, 6889. [CrossRef]

23. Xu, S.; Zhou, H.; Wang, J.; He, Z.; Wang, D. SINS/CNS/GNSS integrated navigation based on an improved federated Sage–Husa adaptive filter. *Sensors* **2019**, *19*, 3812. [CrossRef]
24. Liao, X.; Huang, Q.; Sun, D.; Liu, W.; Han, W. Real-time road slope estimation based on adaptive extended Kalman filter algorithm with in-vehicle data. In Proceedings of the 2017 29th Chinese Control and Decision Conference (CCDC), Chongqing, China, 28–30 May 2017; pp. 6889–6894.
25. Sun, E.; Yin, Y.; Xin, Z.; Li, S.; He, J.; Kong, Z.; Liu, X. Adaptive joint estimates of vehicle mass and road grades for small acceleration driving scenarios. *J. Tsinghua Univ. Sci. Technol.* **2022**, *62*, 125–132.
26. Lin, N.; Zong, C.; Shi, S. The method of mass estimation considering system error in vehicle longitudinal dynamics. *Energies* **2018**, *12*, 52. [CrossRef]
27. Wei, H.; He, C.; Li, J.; Zhao, L. Online estimation of driving range for battery electric vehicles based on SOC-segmented actual driving cycle. *J. Energy Storage* **2022**, *49*, 104091. [CrossRef]

energies

Article

Numerical Study on Aerodynamic Characteristics of Heavy-Duty Vehicles Platooning for Energy Savings and CO_2 Reduction

Junik Jo [1] and Chul-Ho Kim [2,*]

1 Department of Automotive Engineering, Graduate School, Seoul National University of Science & Technology, Seoul 01811, Korea; junik.jo@seoultech.ac.kr
2 Department of Mechanical & Automotive Engineering, Seoul National University of Science & Technology, Seoul 01811, Korea
* Correspondence: hokim@seoultech.ac.kr

Abstract: This study aims to analyze the aerodynamic interaction between moving vehicles platooning with the change in the platooning conditions on a freeway. The effect of the vortex generated by the forward vehicle reduces the value of the stagnation pressure generated at the front of the rear vehicle, which effectively reduces drag on the driving vehicle. To elucidate this, a total of four vehicles were applied to platooning at a speed of 100 km/h by altering the gap distance of heavy-duty vehicles (HDVs) such as 0.5 Length (L), 1 L, 1.5 L, 2.0 L, and 2.5 L under the conditions of 1 L equal to 13.16 m. The stagnation pressure at the front of the following vehicle (FV) was reduced, and quantitative analysis of drag force generated at each leading vehicle (LV) and following vehicle that is platooning exhibited a reduction of about 51%, 56%, and 52%, respectively, when compared to the single moving HDV. This is considered as a reduction in engine power for the driving vehicle. Taken together, these results are effective in improving fuel efficiency and reducing CO_2, a representative greenhouse gas, and predicting fuel and CO_2 reduction based on HDV annual mileage according to the highway conditions and logistics.

Keywords: aerodynamic drag; CFD (computational fluid dynamics); platooning; CO_2 reduction; GHG (greenhouse gas)

Citation: Jo, J.; Kim, C.-H. Numerical Study on Aerodynamic Characteristics of Heavy-Duty Vehicles Platooning for Energy Savings and CO_2 Reduction. *Energies* **2022**, *15*, 4390. https://doi.org/10.3390/en15124390

Academic Editors: Wenbin Yu and Guang Zeng

Received: 9 May 2022
Accepted: 13 June 2022
Published: 16 June 2022

1. Introduction

Greenhouse gas reduction has emerged as one of the biggest global problems. The six primary greenhouse gases are CO_2, CH_4, N_2O, HFCs, PFCs, and SF_6, which cause the greenhouse effect. Among them, CO_2 was increased by 80% in annual emissions from 1970 to 2004. To reduce greenhouse gas (GHG) emissions, the world government has established decarbonization policies, and automobiles are moving away from internal combustion engines in line with policies. However, due to logistics on the road it would take a long time to change internal combustion engine vehicles to eco-friendly vehicles. Previous studies have examined actively utilizing aerodynamic characteristics to improve the fuel efficiency of internal combustion engines. Representatively, recent studies were performed on mounting an airfoil-shaped spoiler at the tail end of a vehicle [1], mounting a vortex generator [2], attempting to change the rear design of the vehicle [3], mounting an air duct [4], and securing the seal of the side window of the vehicle [5]. In particular, research and development applying aerodynamic characteristics such as a roof fairing system is representative [6]. Recently, as autonomous driving such as V2X (Vehicle-to-Everything) became an issue, European countries tried to solve the problem of air resistance that occurs during driving rather than reducing air resistance by changing the vehicle's exterior. For example, in 2011, the SARTRE project [7], an empirical study conducted for GHG reduction using the aerodynamic characteristics, occurred during platooning of the freight vehicles. However, the technology for controlling the distance between vehicles was not developed at that time, so the project could only confirm the possibility of

GHG reduction through platooning. Therefore, the SARTRE project, an empirical study, researched controlling the distance between vehicles by lowering the freight vehicle to 6 m, thereby confirming the possibility of improving fuel economy and reducing GHG. Those effects lead to the reduction in logistics costs [8]. In addition, the Korean government leads the Truck Platooning Project of Korea (TROOP) [9], an empirical study for platooning large freight vehicles. This project has been conducted to control the distance between vehicles at about 15 m. Based on V2X for the safety of autonomous vehicles, diversified platooning safety research is underway, such as distance control of ACC (Adaptive Cruise Control) [10], platooning for CACC (Cooperative Adaptive Cruise Control) [11,12], analysis of acceleration driving of lead vehicles during platooning [13], and emergency braking control [14]. Previous studies demonstrated that platooning driving might contribute to an eco-friendly road environment by reducing air resistance. Therefore, the objective of this study is to understand the variation in aerodynamic characteristics of each model vehicle in platooning by analyzing the change in pressure and drag force of each vehicle in platooning.

2. Description of the Model Vehicle with Its Numerical Grid

In this study, we chose the SCANIA R-series heavy-duty vehicle with a 13.0 liter diesel engine with its maximum brake power, 500 hp. This model vehicle has been used for on-road tests for aerodynamic performance analysis of vehicle platooning in previous empirical studies, due to occupying a large position in the transportation and logistics market worldwide [15,16]. The simplified model vehicle was used for this numerical study, and the solid model with the geometric dimensions 13.16 m × 2.495 m × 3.725 m (Length × Width × Heigth) is given in Figure 1.

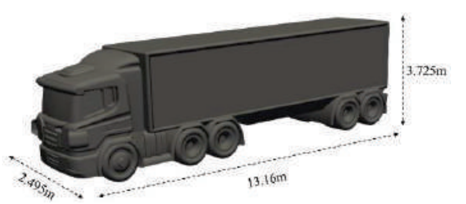

Figure 1. A perspective view of the simplified model vehicle with its dimensions.

2.1. Numerical Domain and Its Conditions

The numerical domain size was defined as shown in Figure 2. Especially, 8 L was given at the rear side of the last model vehicle for stable convergence on the simulation result.

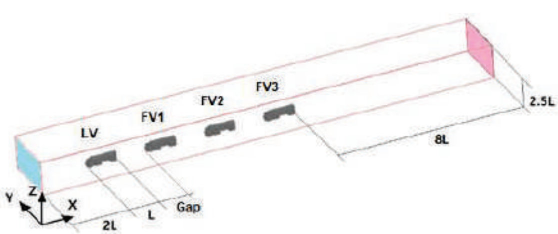

Figure 2. Numerical domain with the model heavy-duty vehicles platooning.

The airflow field was assumed as a 3-dimensional steady incompressible and turbulent flow field for the numerical calculation. The details of the initial and boundary conditions are given in Table 1. The inlet was defined as the velocity boundary with the plugged flow condition, and the outlet was assumed as fully developed and defined as the pressure boundary with the ambient condition. The moving boundary was set to the ground with the same speed as the inlets.

Table 1. Boundary and initial conditions on the control volume.

Boundary Surface	Boundary and Initial Conditions
Inlet	Velocity boundary: 100 km/h
Outlet	Pressure boundary: ambient pressure, 1 atm
Sides and top	Open boundary: symmetric conditions
Ground	Moving boundary condition: 100 km/h
Model surface	No-slip wall

2.2. Numerical Grid of the Physical Model

The CAD-to-CFD method [17] in conjunction with the orthogonal grid was used for the discretization of the physical domain in this study. First, the 3D CAD program, Pro-Engineers, was used as solid model of the vehicle and it was transferred into the numerical domain to generate the hexagonal meshes in the Cartesian coordinate system.

Figure 3 shows a typical grid in the numerical domain with four model vehicles keeping their distance (1 L) in between. For the optimum grid in the domain, the grid convergence test was conducted by thorough grid dependence evaluation with different iterations and very nicely converged with the cut-off error of the residual fraction of the main properties less than 0.01%. The optimum grid size was decided to be (658 × 99 × 87), and the total number of the grid was 5,667,354.

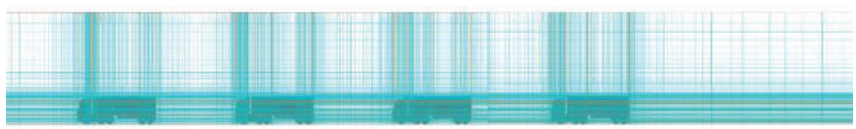

Figure 3. A typical numerical grid with the four model vehicles in platooning (658 × 99 × 87).

3. Numerical Scheme and Its Condition

The general-purpose FVM (finite volume method) CFD code, PHOENICS (ver.2020), was used for a numerical calculation of the turbulent incompressible flow field. The 3-dimensional Naiver–Stokes equations were solved with the KECHEN turbulent model (Chen–Kim κ-ε model), a modified standard κ-ε turbulent model that had good agreement with experimental data [18]. The turbulent no-slip condition near the solid boundary was modeled by logarithmic law.

The airflow field for the analysis was defined as follows:

- Quasi-3D flow.
- Turbulent flow.
- Incompressible flow.
- Steady flow.

3.1. Governing Equations

The governing equation for the steady, incompressible, and turbulent flow fields is given below:

(1) Continuity equation:

$$\frac{\partial U_i}{\partial x_i} + \frac{\partial U_j}{\partial y_i} + \frac{\partial U_k}{\partial z_i} = 0 \tag{1}$$

(2) Momentum equation:

$$\frac{\partial U_i}{\partial t} + \frac{\partial}{\partial x_j}(U_i U_i) = -\frac{1}{\rho}\frac{\partial P}{\partial x_i} + \frac{\partial U}{\partial x_j}\left[v\left(\frac{\partial U_i}{\partial x_j} + \frac{\partial U_j}{\partial x_i}\right) - \overline{u_i u_j}\right] - g_i \tag{2}$$

where $-\overline{u_i u_j} = v_t\left(\frac{\partial U_i}{\partial x_j} + \frac{\partial U_j}{\partial x_i}\right) - \frac{2}{3}k\delta_{ij}$.

(3) κ-ε turbulent energy model (KECHEN);

- Turbulent kinetic energy equation:

$$\frac{\partial}{\partial x_i}(U_j k) = \frac{\partial}{\partial x_i}\left[\left(v + \frac{v_t}{\sigma_k}\right)\frac{\partial \varepsilon}{\partial x_j}\right] + G - \varepsilon \tag{3}$$

where $G = -\overline{u_i u_j}\frac{\partial U_i}{\partial x_j}$, $v_t = C_\mu \frac{k^2}{\varepsilon}$.

- Energy dissipation equation:

$$\frac{\partial}{\partial x_i}(U_j \varepsilon) = \frac{\partial}{\partial x_i}\left[\left(v + \frac{v_t}{\sigma_\varepsilon}\right)\frac{\partial \varepsilon}{\partial x_j}\right] + \frac{\varepsilon}{k}(C_{\varepsilon 1} G - C_{\varepsilon 2}\varepsilon) \tag{4}$$

where $(C_\mu = 0.09,\ C_{\varepsilon 1} = 1.15,\ C_{\varepsilon 2} = 1.92,\ \sigma_k = 1.0,\ \sigma_\varepsilon = 1.0)$.

v_t is turbulent kinematic viscosities, σ_k, σ_ϵ Prandtl number connected to the diffusivity of K and ε to eddy viscosity [18].

3.2. Aerodynamic Pressure Drag

The drag force (F_D) and drag coefficient (C_D) of the model vehicle are calculated using the following equations.

- Drag force (F_D)

$$F_D = C_D \cdot \frac{1}{2} \cdot \rho_{air} \cdot A_y \cdot V_{HDV}^2 \tag{5}$$

where A_y is the projected area of the model vehicle in the longitudinal direction.

- Drag coefficient (C_D)

$$C_D = \frac{2F_D}{\rho_{air} \cdot A_y \cdot V_{HDV}^2} \tag{6}$$

3.3. Fuel Savings and CO_2 Reduction

3.3.1. Traction Power Saved on Each Model Vehicle Platooning

The reduction in the tractive power of each model vehicle platooning compared to the single moving vehicle (SV) can be calculated by Equation (7) [19].

- Tactive power saved,

$$PW_{sav} = \left(F_{D_{Single}} - F_{D_{platoon}}\right) \times V_{HDV} \tag{7}$$

where:

PW_{sav}: tractive power saved [kW].
$F_{D_{Single}}$: drag force of a single vehicle moving (SV) [kN].
$F_{D_{platoon}}$: drag force of each vehicle platooning (or FV1, 2, 3) [kN].
V_{HDV}: velocity of the model vehicle [m/s].

3.3.2. Fuel Saved on Each Model Vehicle Platooning Compared to SV

The mass flow rate of the fuel saved by the aerodynamic reduction can be calculated with the power saved as follows:

- Fuel mass and volume flow rate,

$$\dot{m}_{fuel} = PW_{sav} / \left(Q_{LHV} \times \eta_{engine}\right) \tag{8}$$

$$\dot{Q}_{fuel} = \dot{m}_{fuel} / \rho_{fuel} \tag{9}$$

- Fuel consumption (fc, km/liter) of a vehicle by aerodynamic resistance,

$$fc = \frac{V_{HDV}}{\dot{Q}_{fuel}}(km/h) \tag{10}$$

where, Q_{LHV}, ρ_{fuel} are the lower heating value and density of diesel fuel, η_{engine} is the brake thermal efficiency of the diesel engine. The values are given in Table 2.

Table 2. Property of the diesel fuel and IC engine thermal efficiency [20–22].

Q_{LHV} MJ/kg	ρ_{fuel} kg/m^3	η_{engine} [%]
42	815	0.40

3.3.3. Reduction in Carbon Dioxide

The reduction in CO_2 emission is calculated by the equation given below [23]

$$CO_2 \text{ emissions} = \sum(AL \cdot CL \cdot OF)_i \cdot 44/12 \tag{11}$$

where,
CO_2 emissions: incineration of fossil liquid waste, [Gg].
AL_i: the amount of incinerated fossil liquid waste type i, [Gg].
CL_i: carbon content of fossil liquid waste type i, (fraction).
OF_i: oxidation factor for fossil liquid waste type i, (fraction).
44/12: conversion factor from C to CO_2.

4. Results and Discussion

4.1. Aerodynamics Characteristics of the Model Vehicles in Platooning

The C_D of the leading vehicle (LV) is 0.6 at 0.5 L condition, which is 15% lower than the single vehicle moving (SV) (Table 3). It is due to the rear pressure recovery because of the higher stagnation pressure formed on the frontal surface of the following vehicle (FV1). However, the C_D of LV does not change much under the different distance conditions. However, FV1, FV2, and FV3 have a serious reduction in C_D, and the average reduction compared to SV is about 44% which is similar to the results reported in the previous study [24].

Figure 4 shows the variation in C_D of each model vehicle in platooning with the change in gap. The LV in platooning has the highest drag coefficient in all gaps but the averaged C_D (Figure 4) is still lower than the SVs (0.71). The drag decreases continuously as the distance between the model vehicles is shortened.

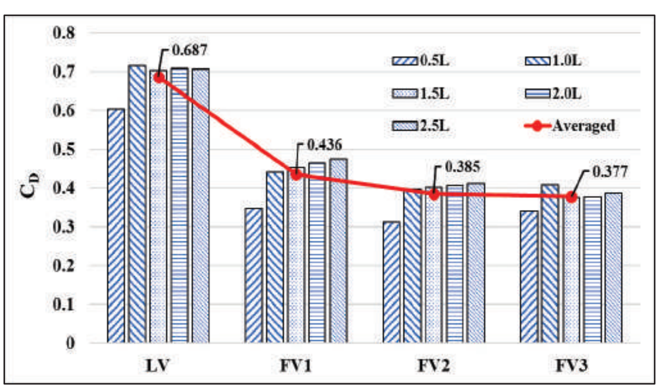

Figure 4. Variation in drag coefficient (C_D) of each model vehicle in platooning with the change in the gap.

Table 3. Variation in drag coefficient of the model vehicle with the gap and the position.

Gap		C_D	C_D Reduction Rate [%]
Single Moving Vehicle (SV)		0.710	-
0.5 L	LV	0.604	15%
	FV1	0.347	51%
	FV2	0.311	56%
	FV3	0.340	52%
1.0 L	LV	0.710	0%
	FV1	0.440	38%
	FV2	0.396	44%
	FV3	0.409	42%
1.5 L	LV	0.704	1%
	FV1	0.453	36%
	FV2	0.402	43%
	FV3	0.374	47%
2.0 L	LV	0.709	0%
	FV1	0.464	35%
	FV2	0.406	43%
	FV3	0.376	47%
2.5 L	LV	0.707	0%
	FV1	0.474	33%
	FV2	0.411	42%
	FV3	0.386	46%

Figure 5 shows the averaged reduction in C_D of each vehicle platooning compared to the SV. As shown, the front leading vehicle has only 3.3% less drag than the SV and the drag drops significantly from the 2nd vehicle (FV1) and the reduction reaches 46.9% on the last-placed vehicle (FV3) (Figure 5).

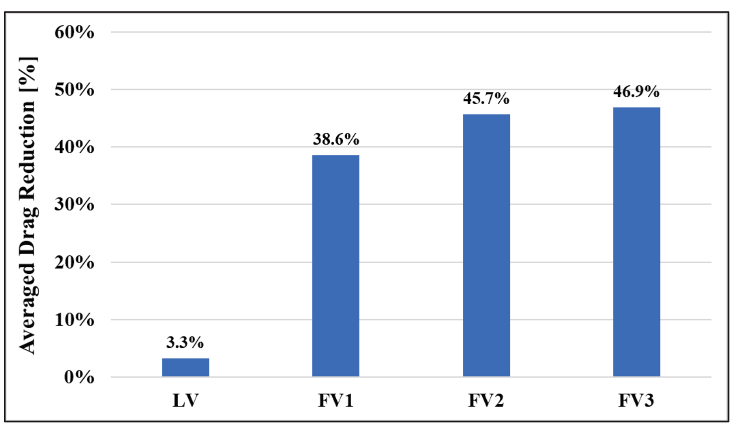

Figure 5. Reduction in the averaged C_D of each vehicle in platooning compared to SV.

Figure 6 shows the static pressure distribution around the vehicles platooning and it indicates that the stagnation pressure is highest at the front surface of the LV and gradually decreases for the following vehicles because the incoming air velocity decreases due to the circulation flow at the front region of each following vehicle. Table 3 shows that LV has 15% lower drag than the SV under the 0.5 L condition. It is due to the higher station pressure formed on the frontal region of FV1 which recovers the rear pressure of the LV. Additionally, the effect disappears as the gap distance increases.

Figure 6. Comparison of the static pressure distribution with the change in the gap at 100 km/h.

The drag force on a moving vehicle generates air resistance due to the pressure difference between the front and rear sides of the vehicle. When two vehicles are moving in parallel, a serious vortex is generated at the rear side of the front vehicle as shown in Figure 7. This complicated flow phenomenon decreases the stagnation pressure on the front side of the following vehicle and decreases air resistance on it.

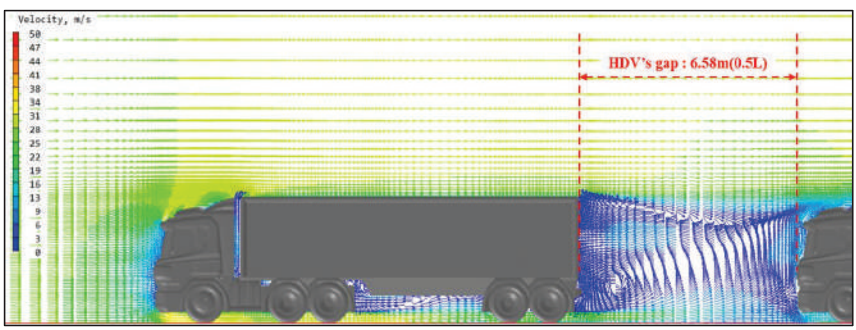

Figure 7. Vortex generated in between LV and FV1 at 0.5 L and 100 km/h in speed.

It is caused by the lower stagnation pressure formed on the frontal face of each model vehicle in platooning (Figure 6) and the lower turbulent kinetic energy formed at the rear side of each model vehicle (Figure 7).

Figure 8 shows the turbulent kinetic energy distribution between the model vehicles with the different gaps. As the gap is shorter, the kinetic energy formed between the vehicles is higher and it is the reason for the lower static pressure formed in the gap, and it contributes to the lower stagnation pressure formed on the frontal face of the following vehicles.

4.2. Fuel Efficiency and GHG Emission Improvement in the Model Vehicles

According to the research reports from the EU FT7 (SARTRE project, 2016), it was found that close distance between the vehicles in platooning improves the fuel efficiency for all vehicles [24]. In the case of a 6 m gap, which is half-length of the model HDV, the LV saved 8% of fuel compared to SV and up to 16% for the following FV [25]. We also predicted fuel consumption and GHG reduction in this study.

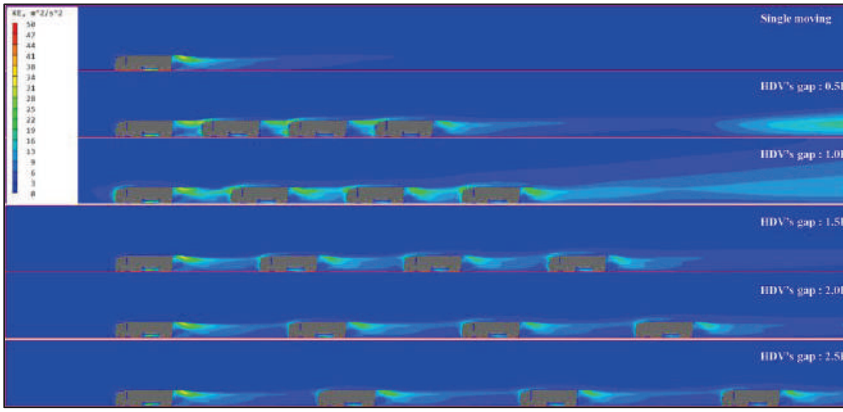

Figure 8. Comparison of the turbulent kinetic energy distribution with the change in the gap at 100 km/h.

Figure 9 shows the tractive power saved by the vehicles platooning compared to the single moving vehicle (SV). For the leading vehicle (LV), the power energy was not saved much compared to SV but from the 2nd vehicle (FV1, FV2, FV3) the tractive power distinctively decreased. The power saved on the model vehicles platooning versus SV was calculated with Equation (7).

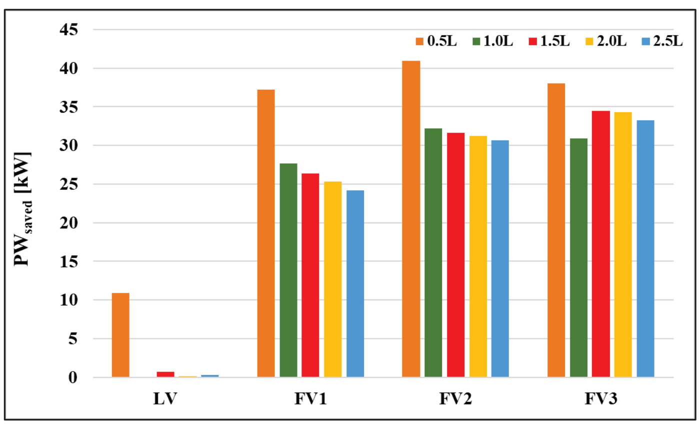

Figure 9. Tractive power (PW_{saved}) saved on the vehicles platooning compared to SV at 100 km/h.

LV saved approximately 10 kW of power at the 0.5 L gap condition. Under 1.0 L~2.5 L gap conditions, a relatively narrower gap does result in a better traction power reduction than SV, and the power saved increases as the location of the model vehicle is far from the leading position. When the HDV's gap is 0.5 L, the averaged traction power saved for FV1, FV2, and FV3 is 38 kW compared to the SV. Additionally, the FVs kept an average of 30 kW of power under the condition of the 1.0 L~2.5 L gap.

The fuel savings for each model vehicle platooning compared to SV was calculated with Equations (8)–(10).

The fuel consumption of SV by aerodynamic resistance was calculated as 5.2 km/liter at 100 km/h from Equation (10). When a single vehicle was moving, the fuel efficiency of FV1, FV2, and FV3 can be predicted as shown in Table 4. As a result, among simulation cases, the possibility of increasing the fuel efficiency of FV 1, 2, and 3 to 10 km/L is also confirmed under the 0.5 L conditions with maximum aerodynamic effects (100 km/h cruising driving condition).

Table 4. Fuel mileage of each model vehicle platooning compared to the single moving vehicle (SV).

Vehicle's Gap	Fuel Mileage [km/Liter]				
	Single Moving	LV	FV1	FV2	FV3
0.5 L	5.2	6.1	10.7	11.9	10.9
1.0 L		5.2	8.4	9.3	9.0
1.5 L		5.2	8.2	9.2	9.9
2.0 L		5.2	8.0	9.1	9.8
2.5 L		5.2	7.8	9.0	9.6

According to KOTI (The Korea Transport Institute) report. 2021, Vol.62, the average daily driving distance of a loaded HDV was about 300 km/day in Korea for 2020 [26]. The averaged cruising speed of the HDV on a highway is 100 km/h; thus, the daily drive time is 3 h.

Based on HDV's gap of 0.5 L, LV kept 2100 liter per year compared to SV. The saved result of an average of 7435 liter of FVs is shown in Figure 10. CO_2 reduction is calculated through Equation (11), resulting in LV saved by 5.3 tons per year and FVs saved by an average about 18.8 tons per year compared to the SV (Figure 11).

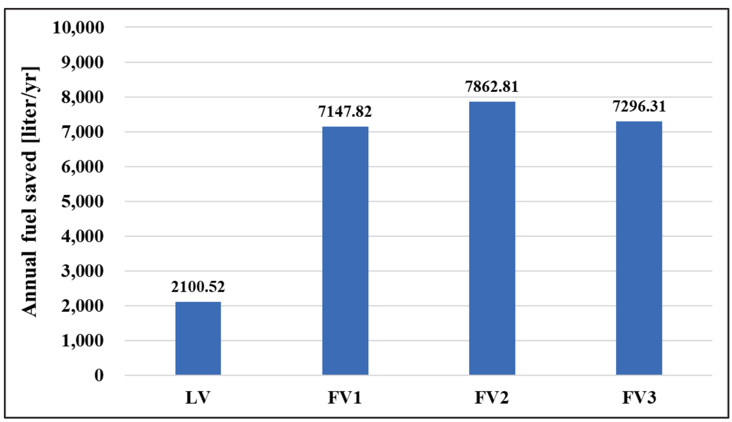

Figure 10. Annual fuel saving on the model vehicles platooning compared to the single moving vehicle (SV) at a 0.5 L gap.

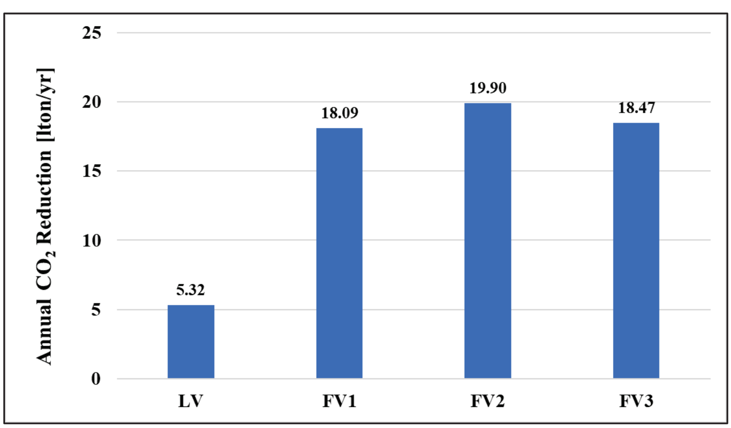

Figure 11. Annual CO_2 reduction in platooning vehicle driving compared to the single moving vehicle (SV) at a 0.5 L gap.

Thus, reducing drag force from the platoon can reduce the power required by the engine, resulting in reduced fuel consumption and GHG. Furthermore, aerodynamic drag is proportional to the square of vehicle speed, so high speed platooning could be more effective in saving energy.

5. Conclusions

This numerical study aimed to understand the aerodynamic effect of the heavy-duty vehicles platooning with the change in the platooning conditions; the gap between the model vehicles and the platooning position of the model vehicle. With the platooning condition change, aerodynamic resistance was analyzed to have the possibility of GHG emission reductions and fuel efficiency improvement. This study only considered steady driving conditions on a level road with no side wind. In addition, the aerodynamic characteristics of the vehicle were theoretically analyzed to determine the energy saving of the vehicle. Further study is needed to analyze the real driving state. From the research, the following were found:

i. The stagnation pressure of FV is reduced due to the rear vortex generated by the front leading vehicle. This is the main cause of the drag reduction on the FV. In this study, the drag of FVs was reduced over 50% compared to SV at the gap (0.5 L) (Table 3).
ii. The shorter the gap between the model vehicles platooning, the smaller C_D of FV, which indicates the shorter the gap distance, the more significant the influence of vortex on the FV. As the gap between the model vehicles widens, the rear vortex of the LV gradually decreases and the static pressure recovers to the ambient pressure. It is the reason for increasing the stagnation pressure of FV causing to C_D increase.
iii. Platoon driving has very positive effect not only to the fuel savings but also on the GHG reduction. Thus, the platoon driving mode of heavy-duty vehicles would seriously contribute to the logistics industry, economically and environmentally.
iv. This study hypothesized the driving conditions of autonomous vehicles based on V2X and suggested that the aerodynamic effect can be maximized when an appropriate platoon gap is set in vehicle-to-vehicle distance control. However, this study aimed to confirm the possibility of reducing GHG according to the platooning concept.
v. This study performed a theoretical analysis using the FVM numerical simulation method. Platooning simulations were performed under the steady driving condition on a level road with no side wind to determine the fuel economy effect so this study might be used for reference. In future research, we will undertake the aerodynamic driving stability research on vehicle platooning. In the study, the weight of the vehicle with the road condition such as the friction coefficient and slippery factor of the road and the side wind, the gyration radius of the road with the tilted angle, etc., should be the important parameters to evaluate the road-load power for the study.

Author Contributions: Conceptualization, J.J. and C.-H.K.; methodology, J.J. and C.-H.K.; software, J.J.; validation, C.-H.K.; writing—original draft preparation, J.J. and C.-H.K.; writing—review and editing, J.J.; visualization, J.J.; supervision, C.-H.K.; project administration, C.-H.K. All authors have read and agreed to the published version of the manuscript.

Funding: This research received no external funding.

Institutional Review Board Statement: Not applicable.

Informed Consent Statement: Not applicable.

Data Availability Statement: The data presented in this study are available on request from the corresponding author.

Acknowledgments: This research is sponsored by the foundation of research and industry of Seoul National University of Science and Technology.

Conflicts of Interest: The authors declare no conflict of interest.

References

1. Buljac, A.; Džijan, I.; Korade, I.; Krizmanić, S.; Kozmar, H. Automobile aerodynamics influenced by airfoil-shaped rear wing. *Int. J. Automot. Technol.* **2016**, *17*, 377–385. [CrossRef]
2. Cihan, B. Numerical drag reduction of a ground vehicle by NACA2415 airfoil structured vortex generator and spoiler. *Int. J. Automot. Technol.* **2019**, *20*, 943–948. [CrossRef]
3. Song, K.S.; Kang, S.O.; Jun, S.O.; Park, H.I.; Kee, J.D.; Kim, K.H.; Lee, D.H. Aerodynamic design optimization of rear body shapes of a sedan for drag reduction. *Int. J. Automot. Technol.* **2012**, *13*, 905–914. [CrossRef]
4. Huluka, A.W.; Kim, C.H. A Numerical Analysis on Ducted Ahmed Model as a New Approach to Improve Aerodynamic Performance of Electric Vehicle. *Int. J. Automot. Technol.* **2021**, *22*, 291–299. [CrossRef]
5. Zhu, W.F.; Jiang, X.H.; Chen, X.; Lin, P.J. Automotive window seal design considering external aerodynamic load and surrogate constraint modeling. *Int. J. Automot. Technol.* **2016**, *17*, 853–864. [CrossRef]
6. Banks, J. Turbulence Modeling in PHOENICS. 2007. Available online: http://www.cham.co.uk/phoenics/d_polis/d_enc/turmod/enc_t342.htm (accessed on 13 June 2021).
7. Davila, A.; Nombela, M. *Sartre-Safe Road Trains for the Environment Reducing Fuel Consumption through Lower Aerodynamic Drag Coefficient*; SAE Technical Paper 2011-36-0060; SAE International: Warrendale, PA, USA, 2011.
8. Sun, X.; Yin, Y. Behaviorally stable vehicle platooning for energy savings. *Trans. Res. Part C Emerg. Technol.* **2019**, *99*, 37–52. [CrossRef]
9. Ministry of Land, Infrastructure and Transport. *Development of Operation Technology for V2X Truck Platooning. Land Infrastructure and Transport R&D Report*; 20TLRP-B147674-03; Ministry of Land, Infrastructure and Transport: Sejong, Korea, 2018.
10. Shin, K.; Choi, J.; Huh, K. Adaptive cruise controller design without the transitional strategy. *Int. J. Automot. Technol.* **2020**, *21*, 675–683. [CrossRef]
11. Emirler, M.T.; Guvenc, L.; Guvenc, B.A. Design and evaluation of robust cooperative adaptive cruise control systems in parameter space. *Int. J. Automot. Technol.* **2018**, *19*, 359–367. [CrossRef]
12. Saleem, A.; Al Maashri, A.; Al-Rahbi, M.A.; Awadallah, M.; Bourdoucen, H. Cooperative cruise controller for homogeneous and heterogeneous vehicle platoon system. *Int. J. Automot. Technol.* **2019**, *20*, 1131–1143. [CrossRef]
13. Wi, H.; Park, H.; Hong, D. Model predictive longitudinal control for heavy-duty vehicle platoon using lead vehicle pedal information. *Int. J. Automot. Technol.* **2019**, *21*, 563–569. [CrossRef]
14. Kang, Y.; Hedrick, J. Emergency braking control of a platoon using string stable controller. *Int. J. Automot. Technol.* **2004**, *5*, 89–94.
15. Alam, A.; Gattami, A.; Johansson, K.H. An experimental study on the fuel reduction potential of heavy duty vehicle platooning. In Proceedings of the 13th International IEEE Conference on Intelligent Transportation Systems, Funchal, Portugal, 19–22 September 2010; pp. 19–22.
16. Liang, K.-Y.; Martensson, J.; Johansson, K.H. Heavy-Duty Vehicle Platoon Formation for Fuel Efficiency. *IEEE Trans. Intell. Transp. Syst.* **2015**, *17*, 1051–1061. [CrossRef]
17. Ludwig, J. *Concentration Heat and Momentum Limited*; CHAM Technical Report TR326; POLIS, Phoenics On-line Information System: London, UK, 2008.
18. Chen, Y.-S.; Kim, S.-W. *Computation of Turbulent Flows Using an Extended K-Epsilon Turbulence Closure Interim Report*; No. NAS 1.26: 179204; NASA: Huntsville, AL, USA, 1987.
19. Kim, C.H. A streamline design of a high-speed coach for fuel savings and reduction of carbon dioxide. *Int. J. Automot. Eng.* **2011**, *2*, 101–107. [CrossRef]
20. World Nuclear Association. Heat Values of Various Fuels. Available online: http://www.world-nuclear.org/information-library/facts-and-figures/heat-values-of-various-fuels.aspx (accessed on 15 August 2021).
21. K-Petro (Korea Petroleum Quality & Distribution Authority). Quality Standard Chart according to Laws. Available online: https://www.kpetro.or.kr/eng/lay1/S210T239C379/contents.do (accessed on 15 August 2021).
22. Suppes, G.J.; Storvick, T.S. *Sustainable Power Technologies and Infrastructure: Energy Sustainability and Prosperity in a Time of Climate Change*; Academic Press: Cambridge, MA, USA, 2015; Chapter 5.
23. Guendehou, S.; Koch, M.; Hockstad, L.; Pipatti, R.; Yamada, M. *Draft 2006 IPCC Guidelines for National Greenhouse Gas Inventories*; Institute for Global Environmental Strategies: Hayama, Japan, 2006; Chapter 5.
24. Davila, A.; del Pozo, E.; Aramburu, E.; Freixax, A. *Environmental Benefits of Vehicle Platooning*; 2013-26-0142; SAE International: Warrendale, PA, USA, 2013.
25. Chan, E. SARTRE automated platooning vehicles. In *Towards Innovative Freight and Logistics*; Wiley: Hoboken, NJ, USA, 2016; Volume 2, pp. 137–150.
26. KOTI (The Korea Transport Institute). Report 62. 2021. Available online: https://www.koti.re.kr/user/bbs/BD_selectBbs.do?q_bbsCode=1093&q_bbscttSn=20210726174721314 (accessed on 20 August 2021).

energies

Article

Evaluation Method of Naturalistic Driving Behaviour for Shared-Electrical Car

Shaobo Ji [1,*], Ke Zhang [1], Guohong Tian [2], Zeting Yu [1], Xin Lan [1], Shibin Su [3] and Yong Cheng [1]

1 College of Energy and Power Engineering, Shandong University, Jinan 250061, China; 202134527@mail.sdu.edu.cn (K.Z.); yuzt1979@126.com (Z.Y.); lampxane@163.com (X.L.); cysgdb@126.com (Y.C.)
2 Department of Mechanical Engineering Sciences, University of Surrey, Guildford GU2 7XH, UK; g.tian@surrey.ac.uk
3 Research Management Department, Hisense TransTech Co., Ltd., Qingdao 266071, China; sushibin@hisense.com
* Correspondence: ytjobo@126.com

Abstract: Evaluation of driving behaviour is helpful for policy development, and for designing infrastructure and an intelligent safety system for a car. This study focused on a quantitative evaluation method of driving behaviour based on the shared-electrical car. The data were obtained from the OBD interface via CAN bus and transferred to a server by 4G network. Eleven types of NDS data were selected as the indexes for driving behaviour evaluation. Kullback–Leibler divergence was calculated to confirm the minimum data quantity and ensure the effectiveness of the analysis. The distribution of the main driving behaviour parameters was compared and the change trend of the parameters was analysed in conjunction with car speed to identify the threshold for recognition of aberrant driving behaviour. The weights of indexes were confirmed by combining the analytic hierarchy process and entropy weight method. The scoring rule was confirmed according to the distribution of the indexes. A score-based evaluation method was proposed and verified by the driving behaviour data collected from randomly chosen drivers.

Keywords: driving behaviour evaluation; naturalistic driving study; shared-electrical car; Kullback–Leibler divergence; analytic hierarchy process; entropy weight method

Citation: Ji, S.; Zhang, K.; Tian, G.; Yu, Z.; Lan, X.; Su, S.; Cheng, Y. Evaluation Method of Naturalistic Driving Behaviour for Shared-Electrical Car. *Energies* **2022**, *15*, 4625. https://doi.org/10.3390/en15134625

Academic Editor: Giovanni Lutzemberger

Received: 10 May 2022
Accepted: 22 June 2022
Published: 24 June 2022

1. Introduction

Road accidents kill approximately 1.24 million people every year and they are the eighth leading cause of death globally [1]. Aberrant driving and violation of traffic rules cause 74% of traffic accidents [2]. In addition, these behaviours also lead to excessive fuel consumption and vehicle emissions [3]. Therefore, it is necessary to understand the influence of driving behaviour on road risks and vehicle performance. Additionally, quantitative methods of the aberrant driving behaviour should be proposed to improve the driving behaviour.

In former studies, driving behaviour data have been mainly obtained by the following methods: driver self-reported survey [4], driver behaviour questionnaires [5], driver simulators [6], field tests and Naturalistic Driving Studies (NDS) [7]. The first two methods are subjective evaluation methods. For the driver simulators and field tests, the driving behaviour may be different due to the pre-arranged test environment and procedure. Naturalistic driving data were obtained with an unobtrusive data acquisition system during everyday driving. NDS can observe the driving behaviour in a natural driving condition without experimental control. Therefore, the method can accurately reflect driving habits [8]. NDS can be categorized further into on-site study and individual driver study [9]. For the on-site study, naturalistic driving data can be collected with video cameras or microwave and other equipment at a particular site. The individual driver study can obtain various driving behaviour data, such as vehicle speed, acceleration, location and vehicle clearance and so on. For the individual driver study, abundant driving behaviour data can provide multi-dimensional analysis for driving behaviour.

NDS data from the study of individual drivers can be obtained by Global Position System (GPS), video cameras, independent sensors, mobile phones and On-Board Diagnostics (OBD). GPS can provide vehicle location directly and vehicle speed can be estimated based on the location. The acceleration and deceleration behaviour of drivers were studied using GPS in [10,11]. Video cameras were used to capture the drivers' facial expressions and eye movements to analyse the driving behaviour [12]. Video cameras were also used to record drivers' body movements, such as feet movements, to evaluate the reaction time of the drivers [13]. Independent sensors such as accelerometer [14], Radar sensor [15] and Inertial Measurement Unit (IMU) [16] were also used to obtain driving behaviour data. Nowadays, most mobile phones are equipped with GPS and an accelerometer. Driving behaviour such as acceleration, braking and speeding were studied using mobile phones in [17]. OBD II interface was mandatory for vehicles and the system can collect variable vehicle information from the Electronic Control Units (ECU) of the vehicles via the Controller Area Network (CAN) bus. OBD II interface can collect vehicle status and operation information, including vehicle speed, acceleration, position of accelerator/ brake pedal, angle of steering wheel and fuel consumption and so on [18]. Considering the abundant information and reliability of the OBD II, the data collected from OBD was used to analyse the driving behaviour [19].

Driving behaviour can be influenced by driver's driving ability, driver characteristics, driving duration and driver's distraction [20]. Driving ability was influenced by the driver's experience, skill and knowledge. Compared with experienced drivers, young drivers had a higher rate of traffic accidents [21]. Driver characteristics include age, gender, and education level and etc. Drivers' behaviour was influenced by the drivers' age. Young drivers had a higher probability of accidents than middle-aged and older drivers due to their higher tendency of speeding [22]. Most studies showed that the drive behaviour of males was more aggressive that of than females and that males had higher risk of having an accident [23]. The behaviour of drivers with a high education level was more compliant, such as less lane-changing [24]. Driving duration had a significant influence on driving behaviour and there was more speeding for the drivers who had a longer driving distance [25]. A driver can be distracted by the driving environment, their mobile phone, their co-passenger and so on [26]. The distractions had adverse impacts on road safety, especially when the driver glanced away from the road.

Driving behaviour has a great influence on the road safety and vehicle performance. The evaluation of driving behaviour is helpful in providing positive feedback to drivers so they reduce the dangerous driving, thus avoiding traffic accidents and enhancing vehicle performance. According to the conclusion of the previous paragraph, driving behaviour is influenced by multiple factors. Considering the stochastic feature of the driving behaviour, it is better to extract the driving behaviour feature from a large sample, including the driver selection and driving route. Nowadays, shared-electrical cars are used in several cities in China, the driver and driving route are random for each trip, and the driving behaviour is purely naturalistic. The driving behaviour data contains drivers of different ages, genders and driving experiences. This makes it suitable for the evaluation of the driving behaviour. While there have been a few studies that have conducted an evaluation of the driving behaviour using data from shared-electrical cars, the statistical characteristics of NDS data with a large and stochastic sample is still unclear, and should be studied in more depth.

To bridge the knowledge gap, this paper was conducted using the data from shared-electrical cars used in Shanghai and Tianjin cities of China. On this basis, a quantitative evaluation method of driving behaviour was proposed and verified. This paper was organized as follows. Firstly, the NDS data obtained from the OBD-II interface of the shared-electrical car was pre-treated to improve the data quality. Secondly, an estimation method was employed to confirm the appropriate amount of NDS data. Thirdly, the relationship between different driving behaviour parameters was studied. Finally, an evaluation of driving behaviour was proposed and verified in practical application. The study flow chart is shown in Figure 1.

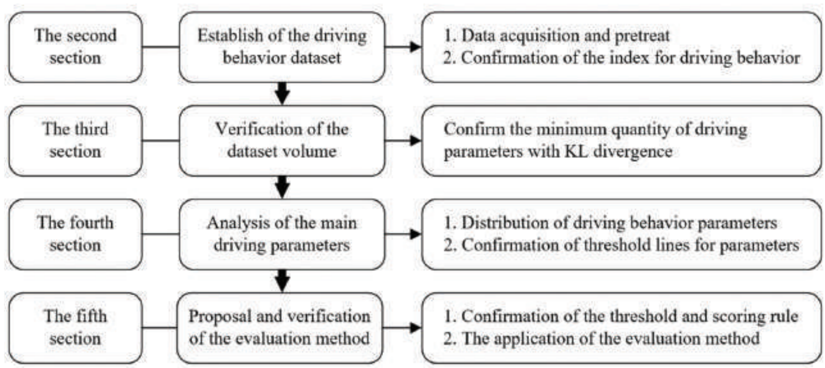

Figure 1. The main study flow chart.

2. Data Acquisition and Treatment

2.1. Data Acquisition

The NDS data were collected from 400 electrical cars, in which 305 cars were shared-electrical cars and others were online car-hiring cars. A data acquisition system was used to obtain the NDS data from the OBD-II interface via CAN bus. All the sampled data were sent to a server by a 4G network. The data were saved and treated thereafter for driving behaviour analysis. The data acquisition process is shown in Figure 2. The data were collected during a period of about four months. The total car mileage was about 1.2 million kilometres, with the total car travelling hours adding up to about 45,000, and the sample points totaling about 1.28×10^9.

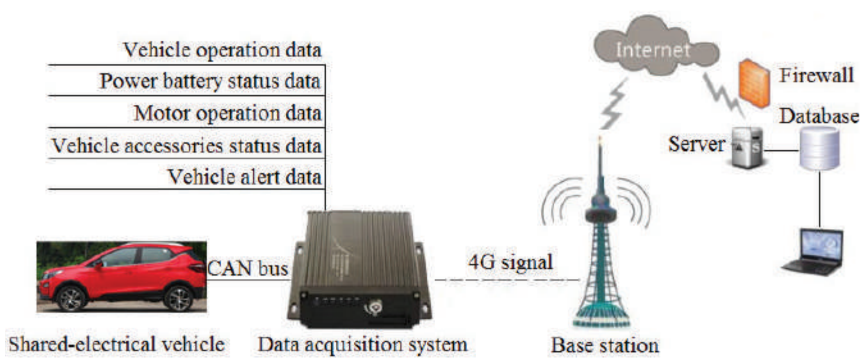

Figure 2. The acquisition process of the NDS data.

The data acquisition system can obtain more than 50 driving behaviour parameters, including vehicle operation, power battery status, motor operation, vehicle accessories status and vehicle alert. The primary data were shown in Table 1. All the data were collected at a rate of 10 Hz, which was adequate for transient process analysis, such as acceleration or deceleration.

Table 1. The primary parameters collected by the data acquisition system.

Signal Type	The Primary Parameters
Vehicle operation	Vehicle speed, mileage, position of the acceleration and brake pedal, steering wheel angle.
Power battery status	Total voltage and current of the battery pack, insulation resistance and temperature.
Motor operation	Voltage, current, motor speed, motor torque and temperature.
Vehicle accessories status	Voltage and current of the air conditioner, Voltage and current of the DC-DC.
Vehicle alert	Alert signal of power battery, motor and thermal management system.

It should be noted that the collected data mentioned above were obtained from the OBD-II interface, and do not include any personal information, such as GPS data.

2.2. Data Treatment

The vehicle data were collected in 'Charge', 'Standby' and 'Operation' phases. For the analysis of driving behaviour, the data collected in the 'Charge' and 'Standby' phases were neglected. A valid driving event was recognised by both the power-on status and the vehicle speed being greater than zero. When the vehicle speed was zero for less than 10 min with power-on status, it was considered in the same driving event. Figure 3 showed an example of the vehicle speed versus time in a complete driving event.

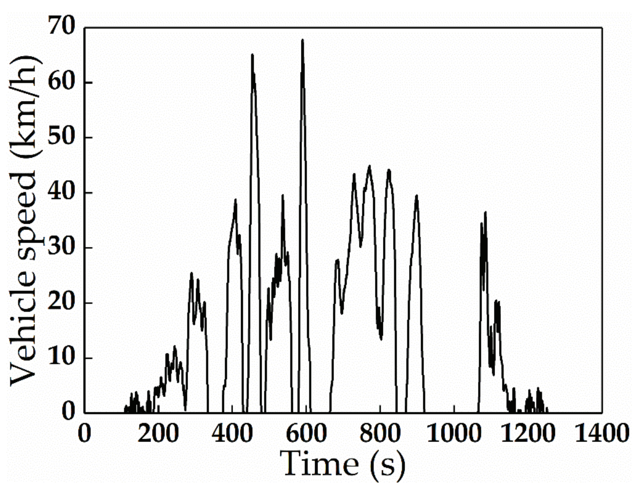

Figure 3. The vehicle speed versus time in a complete driving event.

The data acquisition and transmission can be affected by occasional interferences, such as the voltage fluctuation in the vehicle start and stop phase, abnormal power failure of the data acquisition system, the interruption of the communication signal caused by tunnels or tall buildings and so on [27]. The data received by the server include occasional flaws; therefore, a data quality control method must be used before processing. The sliding-window averaging filter was implemented to reduce the random noise. The filter can be expressed as follows:

$$x[k] = \frac{1}{M}\sum_{i=0}^{M-1} x[k-i] \quad (1)$$

where i is the number of the original data, $x[k-i]$ is the original data, M is the length of the sliding-window averaging filter, which is set to five, and $x[k]$ is the treated data.

The vehicle data were obtained from the ECUs of the vehicles via CAN bus. Most of the data were deemed normal. To eliminate the occasional abnormal data, the box diagram method was used, which was introduced in the previous paper [28]. The sliding-window averaging filter and box diagram method were used to treat the original data. Figure 4a showed the treatment effect of the filter on vehicle velocity. It can be seen that the signal fluctuation was eliminated but the trend remained the same. Figure 4b showed the treatment effect of the box diagram method for the acceleration and the abnormal value can be eliminated effectively.

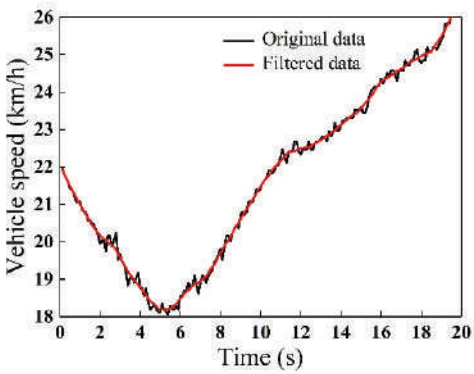

(**a**)

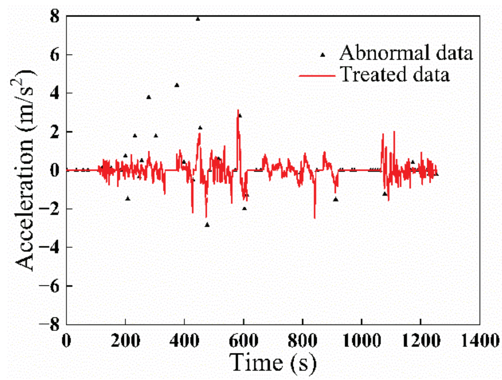

(**b**)

Figure 4. The comparison of the signal with different treat method: (**a**) Sliding-window averaging filter; (**b**) The box diagram method.

2.3. The Indexes for Driving Behaviour

There were multiple indexes to evaluate the driving behaviour. This study mainly focused on the indexes related to driving safety, including frequent adjustment of vehicle speed and steering wheel, rapid acceleration, sudden braking, rapid turning, fatigue driving and power consumption. The proposed evaluation method of driving behaviour was based on 11 indexes. The index, symbol, definition and unit are listed in Table 2. All values were calculated based on a complete driving event.

Table 2. The indexes used to evaluate the driving behaviour.

Number	Index	Symbol	Definition	Unit
1	Standard deviation of vehicle speed	v_{std}	$v_{std}=\sqrt{\frac{\sum_{i=1}^{n}(v_i-v_m)^2}{n}}$	km/h
2	Average value of acceleration	${a_m}^+$	${a_m}^+=\frac{\sum_{i=1}^{n}{a_i}^+}{n}$	m/s^2
3	Average value of deceleration	${a_m}^-$	${a_m}^-=\frac{\sum_{i=1}^{n}{a_i}^-}{n}$	m/s^2
4	Standard deviation of acceleration	${a_{std}}^+$	${a_{std}}^+=\sqrt{\frac{\sum_{i=1}^{n}({a_i}^+-{a_m}^+)^2}{n}}$	m/s^2
5	Standard deviation of deceleration	${a_{std}}^-$	${a_{std}}^-=\sqrt{\frac{\sum_{i=1}^{n}({a_i}^--{a_m}^-)^2}{n}}$	m/s^2

Table 2. *Cont.*

Number	Index	Symbol	Definition	Unit
6	The number of rapid acceleration per 100 km	F_a	$F_a = \frac{N_a}{D} \times 100$	times/100 km
7	The number of sudden braking per 100 km	F_d	$F_d = \frac{N_d}{D} \times 100$	times/100 km
8	The number of rapid turning per 100 km	F_t	$F_t = \frac{N_t}{D} \times 100$	times/100 km
9	The number of speeding during steering per 100 km	F_{st}	$F_{st} = \frac{N_{st}}{D} \times 100$	times/100 km
10	Driving time per trip	T	-	hour
11	Power consumption per 100 km	P_m	$P_m = \frac{W}{D} \times 100$	kW·h/100 km

where i is the number of sample point, n is the total number of sample point in a complete driving event, v_i is the vehicle speed of each sample point, v_m is the average speed in a complete driving event, a_i^+ is the acceleration of each sample point, a_i^- is the deceleration of each sample point, N_a, N_d, N_t and N_{st} are the number of occurrences of rapid acceleration, sudden braking, rapid turning and speeding during steering, respectively, in a complete driving event, D is the mileage in a complete driving event, and W is the power consumption in a complete driving event.

3. Quantity Estimation of Driving Behaviour Data

For an individual driver, the driving style is relatively stable after a certain period of driving experience and the statistical characteristics will be convergent [29]. The evaluation accuracy of driving behaviour depends on the volume of the NDS dataset, which should cover as many of the driving behaviour characteristics as possible. From the statistical perspective, if the NDS data are adequate, the distribution density of the data will remain the same with additional sample data. In this case, the amount of NDS data can be considered suitable for driving behaviour analysis. To ensure the appropriate quantity of dataset, the amount of NDS data was estimated by Kullback–Leibler (KL) divergence [30]. The quantity estimation of a given dataset $x = \{x_i\}_{i=1}^n$ included the following two steps.

Firstly, the distribution density ($f_n(x)$) of the dataset (x) was calculated with the kernel density method, which was a non-parametric method, and the equations are as follows.

$$f_n(x) = \frac{1}{n}\sum_{i=1}^{n}\frac{1}{h}K(\frac{x - x_i}{h}) \tag{2}$$

$$h = 1.06{\cdot}\sigma{\cdot}n^{-1/5} \tag{3}$$

$$K(u) = \frac{1}{2\pi}\exp(-\frac{u^2}{2}) \tag{4}$$

where n is the length of the dataset, σ is standard deviation of the dataset.

Secondly, the KL divergence was calculated to assess the difference in kernel density between the two datasets with the data length of n and $n + m$, respectively. Assuming the kernel densities of the two datasets are expressed as $f_n(x)$ and $f_{m+n}(x)$, the KL divergence of the two datasets can be expressed as Equation (5). If KL remains as a small value with the increase in m, it indicates that the kernel density is almost unchanged with the adjustment of the dataset and the quantity of the dataset is adequate. The variation value of KL can affect the data quantity, which was set as $KL < 1 \times 10^{-5}$ in this study.

$$KL(f_{n+m}(x)||f_n(x)) = \int f_{n+m}(x) \times \log\frac{f_{n+m}(x)}{f_n(x)} \tag{5}$$

The KL divergence of different driving behaviour parameters was calculated and Figure 5 showed the changing trend of vehicle speed, acceleration, steering wheel angle and steering wheel speed. It can be seen that the KL of different parameters decreased with the increase in data quantity. Although the convergence rate of the parameters was different, the KL convergence of the four parameters all satisfied the requirement when the data quantity exceeded 231×10^5. The similar calculation of KL was applied to other driving behaviour parameters. Based on this analysis, the quantity of the sampled data in this study was considered adequate.

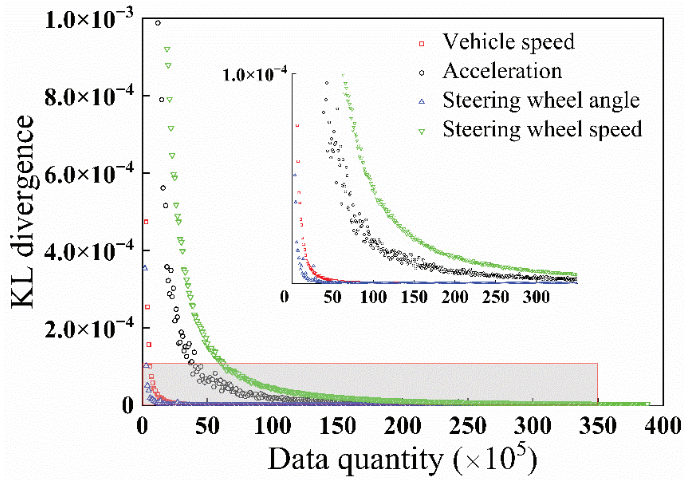

Figure 5. The *KL* of different parameters versus data quantity.

4. Study on the Relationship between Different Driving Behaviour Parameters

4.1. Statistical Characteristics of the Main Driving Behaviour Parameters

Vehicle speed, acceleration, deceleration, steering wheel angle and steering wheel speed contain abundant information reflecting driving behaviour. The statistics of these parameters were firstly calculated to understand the general characteristics of the driving behaviour.

According to Figure 5, the *KL* of vehicle speed converged when the data quantity exceeded 20×10^5. The vehicle speed was selected randomly from the total dataset of shared-electrical vehicles to the quantity of 20×10^5. The distribution characteristic of the vehicle speed is shown in Figure 6. Most of the vehicles' speeds were lower than 80 km/h and the average speed was 33.4 km/h. The relatively low speed was mainly attributed to the heavy urban traffic. The largest proportion of the speed was lower than 5 km/h, which reflected the frequent starting or parking mode due to red lights or traffic jams in urban traffic.

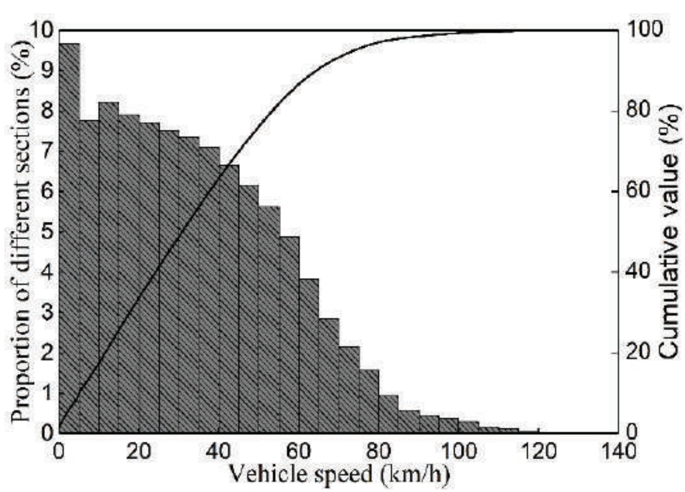

Figure 6. The distribution characteristic of the vehicle speed.

According to Figure 5, the *KL* of acceleration and deceleration converged when the data quantity exceeded 163×10^5. The corresponding data quantity of acceleration and deceleration were selected randomly from the total dataset of shared-electrical vehicle. The distribution characteristic was compared and shown in Figure 7. Over 90% of the acceleration and deceleration were lower than 1.5 m/s^2. The average values of acceleration and deceleration were 2.05 and 2.72 m/s^2, respectively. Compared to deceleration, acceleration was mainly located within the small value sections, which was mainly attributed to the heavy traffic.

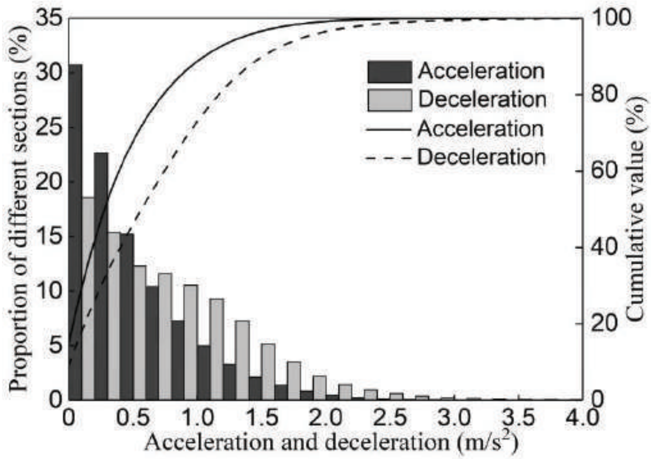

Figure 7. The distribution characteristic of acceleration and deceleration.

The *KL* of steering wheel angle converged when the data quantity was more than 10×10^5, and the corresponding quantity of steering wheel angle data was selected randomly. The distribution characteristic of steering wheel angle is shown in Figure 8. Over 60% of the steering wheel angle was lower than 25°, which meant that most of the angle change was attributed to the slight adjustment in driving direction. The percentage decreased with the increase in steering wheel angle until 300°, and these steering actions were mainly due to lane-changing or vehicle turning. There was also angle distribution around 550°, and this was mainly caused by vehicle U-turn or parking.

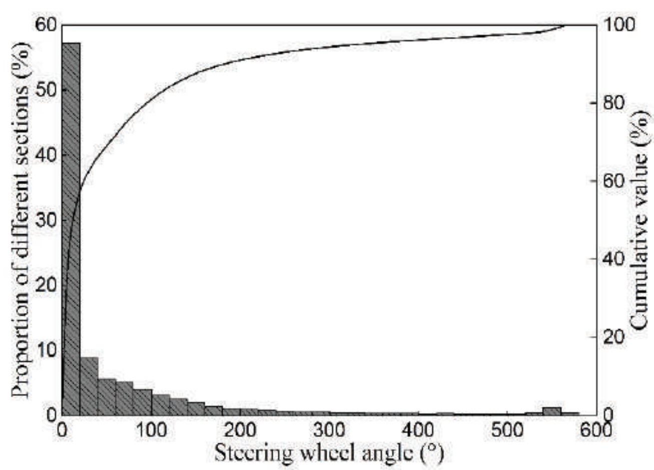

Figure 8. The distribution characteristic of steering wheel angle.

The *KL* of steering wheel speed converged when the data quantity was more than 231×10^5. The same amount of steering wheel speed data was selected randomly and compared in Figure 9. According to the steering characteristic, the steering wheel speed can be classified to steering speed (positive values) and return speed (negative values). Comparison showed that the two speeds had a similar changing pattern. Most of the steering speeds and return speeds were lower than 25°/s, which meant that the majority of the steering actions were careful. The averages of the steering speed and return speed were calculated, which were 38.11°/s and 30.35°/s, respectively. The steering speed was larger than the return speed, which corresponded to the normal driving habit.

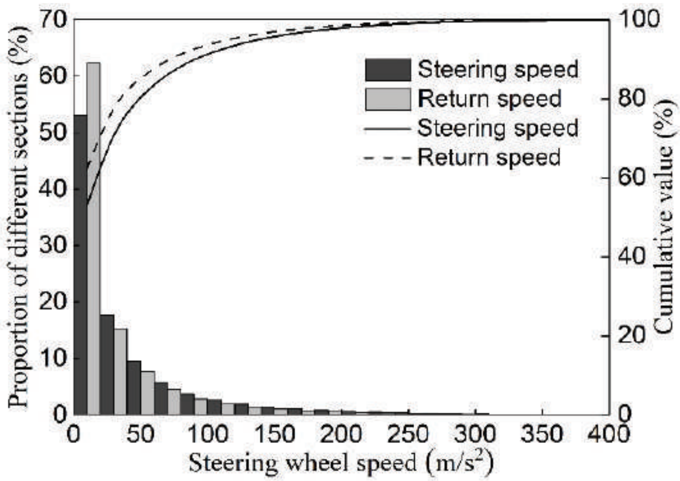

Figure 9. The distribution characteristic of steering wheel speed.

4.2. Statistical Characteristics of Parameters at Different Vehicle Speed

The acceleration, deceleration, steering wheel angle and steering wheel speed are affected by vehicle speed. To reveal the influence of speed on different driving parameters, the statistical characteristics of the parameters at different vehicle speeds were analysed. The analysis can provide guidance for threshold settings of driving behaviour evaluation.

Figure 10a showed the distribution characteristic of acceleration and deceleration versus vehicle speed. The acceleration decreased, along with the increase in vehicle speed. The deceleration firstly increased and then decreased with the increase in vehicle speed, and the inflection point was approximately 25 km/h. An explanation of this scenario is introduced in the following section. The overall change trend suggested that the acceleration and deceleration approached zero with the increase in vehicle speed. This can be explained by the fact that the higher vehicle speeds normally appeared during smooth traffic and the vehicle speed change will reduce accordingly in this situation. Additionally, the drivers tended to keep the speed stable to ensure safety at high vehicle speeds. Figure 10b showed the distribution comparison of acceleration and deceleration at different vehicle speeds. The acceleration distribution was relatively stable in a wide range of vehicle speeds from 0 to 60 km/h and the largest proportion of acceleration appeared around the speed of 20 km/h, which was the vehicle starting condition. The deceleration was mainly distributed in the lower speed condition and the largest proportion of deceleration appeared at speeds ranging from 0 to 5 km/h.

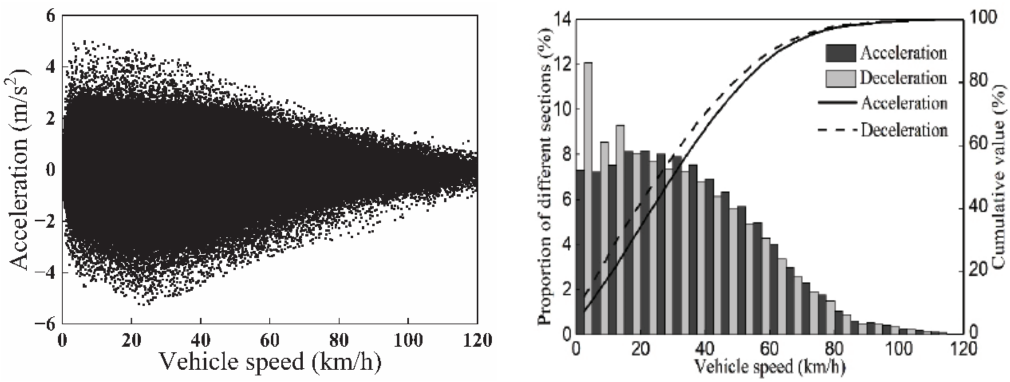

(**a**) (**b**)

Figure 10. The distribution characteristic of acceleration and deceleration versus vehicle speed: (**a**) Overall trend; (**b**) Comparison of distribution characteristic.

Figure 11 showed the different quantile values of acceleration and deceleration at different vehicle speeds. It can be seen that the acceleration increased significantly during the speed from 0 to 5 km/h, which was attributed to the electric motors' high torque output at low speed. The quantile of the acceleration decreased with the increase in speed. This can be explained by the fact that the drivers tended to accelerate the vehicle more rapidly at lower speed conditions. The quantile of the deceleration firstly increased and then decreased. The reason for this is that the shared-electrical cars have braking energy recovery and the maximum braking torque appears at around 25 km/h, which led to this inflection point. The braking energy recovery in the deceleration phase was the main difference between the electrical vehicles and vehicles powered by Internal Combustion Engine (ICE).

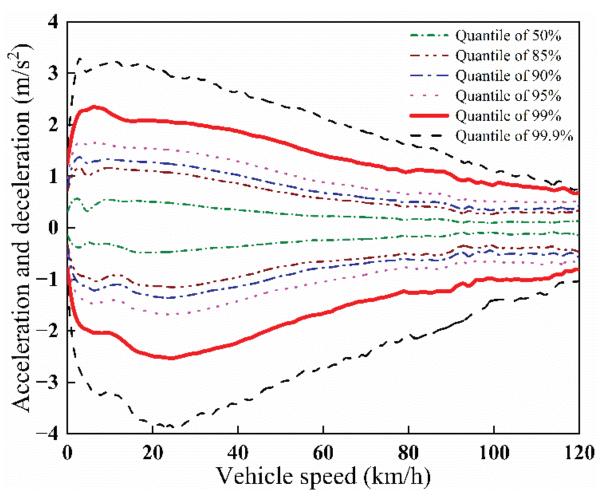

Figure 11. The comparison of different quantile value for acceleration and deceleration.

To evaluate the abnormal acceleration or deceleration, some researchers employed the fixed threshold value. According to Figure 11, both the acceleration and deceleration tended to decrease with the increase in vehicle speed in general. Therefore, it was reasonable that the threshold of abnormal acceleration or deceleration changed with speed. To confirm the threshold, a linear fit was applied to the quantile of acceleration and deceleration during the speed range from 10 to 120 km/h. The linear fit of the acceleration is expressed as Equation (6).

$$f(x) = \beta_1 x + \beta_2 \tag{6}$$

where x is vehicle speed and β_1 and β_2 are the coefficients of linear fit. The linear fit result is shown in Table 3, in which R^2 is the coefficient of determination.

Table 3. The linear fit result of the acceleration.

Coefficient	50%	85%	90%	95%	99%	99.9%
β_1	−0.0042	−0.0090	−0.0102	−0.0118	−0.0150	−0.0238
β_2	0.5312	1.2056	1.4002	1.7076	2.5000	3.5534
R^2	0.9123	0.9351	0.9386	0.9477	0.9708	0.9930

Similarly, the quantile of deceleration also had a linear fitted. Considering the piece-wise characteristic of the deceleration, the piece-wise linear fit was employed, which is shown in Equation (7).

$$f(x) = \begin{cases} \beta_1 x + \beta_2 x < 25\text{km/h} \\ \beta_3 x + \beta_4 x \geq 25\text{km/h} \end{cases} \tag{7}$$

where x is vehicle speed and β_1, β_2, β_3 and β_4 are the coefficients of linear fit. The linear fit result is shown in Table 4.

Table 4. The linear fit result of the deceleration.

Coefficient	50%	85%	90%	95%	99%	99.9%
β_1	−0.0087	−0.0128	−0.0146	−0.0182	−0.030	−0.0565
β_2	−0.2903	−0.8529	−1.0147	−1.2648	−1.8500	−2.6433
β_3	0.0047	0.0105	0.012	0.0144	0.0220	0.0301
β_4	−0.5456	−1.3544	−1.5801	−1.9741	−3.150	−4.57
R^2	0.8266	0.8263	0.8402	0.8838	0.9494	0.9220

The linear fit result of the acceleration and deceleration were compared in Figure 12. Greater acceleration and deceleration can cause a feeling of discomfort and risk of traffic accidents. According to the quantile and distribution of acceleration and deceleration, the quantile value of 99% was arbitrarily employed to distinguish the abnormal acceleration and deceleration in the following evaluation of driving behaviour.

Vehicle speed has a great influence on driving safety and it is dangerous to steer heavily at high speeds. Figure 13 showed the comparison of distribution and quantile of steering wheel angle at different speeds. Most of the steering action occurred at the speed of 20 km/h, and the steering wheel angle decreased with the increase in speed. The trend corresponded to the driving habits that the steering demand was decreased with the increasing speed to ensure driving safety. The quantile value of the steering wheel angle was almost unchanged when the steering wheel angle was larger than 300°. This indicated that drivers tended to decrease vehicle speed at high steering angle conditions to avoid traffic accidents.

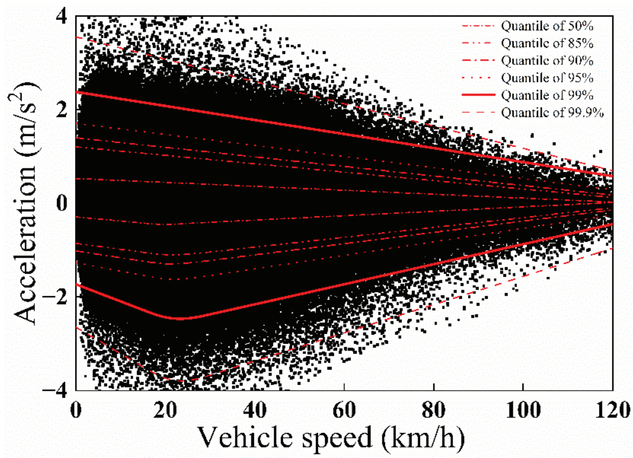

Figure 12. The linear result of quantile for acceleration and deceleration.

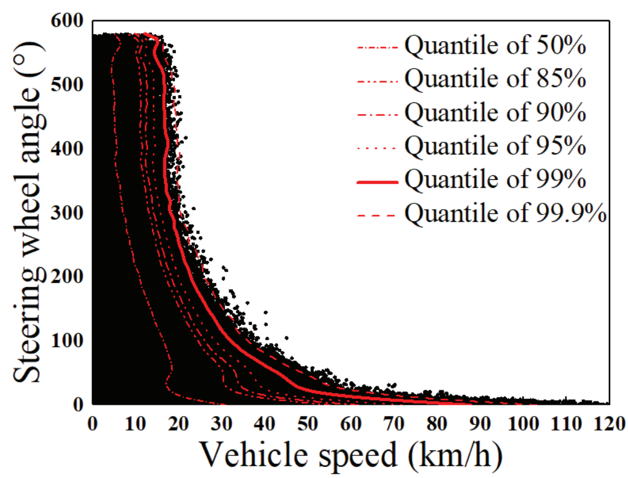

Figure 13. The comparison of distribution and quantile for steering wheel angle at different speeds.

Rapid steering can reduce the lateral stability of vehicles. Steering wheel speed reflects the operation speed of the drivers on the steering wheels. A faster speed is usually associated with a higher risk of rollover and skid of the vehicle. Figure 14 showed the distribution of steering wheel speed versus vehicle speed. The maximum steering wheel speed can reach approximately 600°/s. The high steering wheel speeds mainly occurred at vehicle speeds lower than 30 km/h, which suggested that drivers tended to turn the steering wheel rapidly at safe speeds. The trends of steering speed and return speed were similar. They both decreased with the increase in vehicle speed. Considering the similar trend, the quantiles of the steering speed was obtained. The comparison of the quantile showed that the steering speed was almost unchanged when the vehicle speed was higher than 60 km/h, which meant that most of the steering actions were gentle at high vehicle speeds to ensure driving safety.

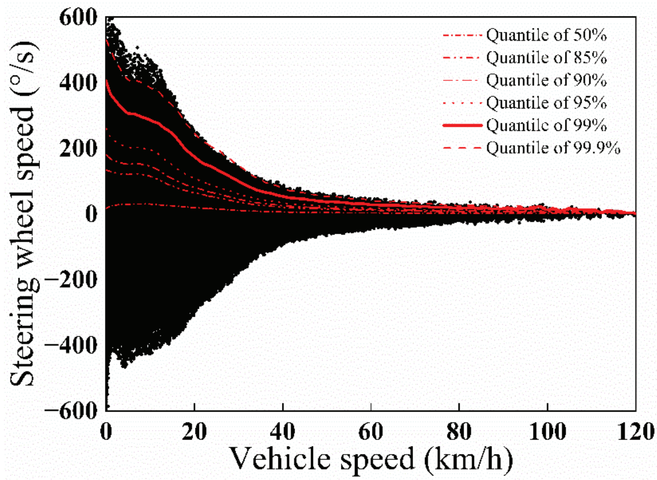

Figure 14. The comparison of distribution and quantile for steering wheel speed at different speeds.

The changing trend of the steering wheel speed was also exponentially fitted with vehicle speed to obtain the threshold of rapid turning. The exponential fitting equation is expressed as Equation (8).

$$f(x) = a + b \times x^c \tag{8}$$

where x is vehicle speed and a, b and c are the coefficients of exponential fit. The exponential fit result is shown in Table 5.

Table 5. The exponential fit result of the steering wheel speed.

Coefficient	50%	85%	90%	95%	99%	99.9%
a	0.97	5.82	7.64	9.83	19.56	3.80
b	−53.27	−209.30	−270.77	−373.06	−680.00	−692.02
c	0.948	0.940	0.936	0.936	0.935	0.949
R^2	0.9932	0.9982	0.9985	0.9985	0.9942	0.9935

Considering the influence of the speed on the safety of steering action, the evaluation of the rapid turning should consider the speed. According to the distribution and quantile of rapid turning, the quantile of 99% was selected as the threshold to distinguish the abnormal steering action, which is shown in Figure 15. The threshold of rapid turning decreased with the increase in vehicle and the setting method of the threshold can distinguish the rapid turning more effectively.

The previous analysis investigated the influence of vehicle speed on driving behaviours, such as acceleration, deceleration and steering action. According to the analysis, the threshold of aberrant driving behaviours were established to identify rapid acceleration, sudden braking, and rapid turning. In the next section, these thresholds were employed to calculate the number of occurrences for aberrant driving behaviour, which can be used to evaluate the driving behaviours.

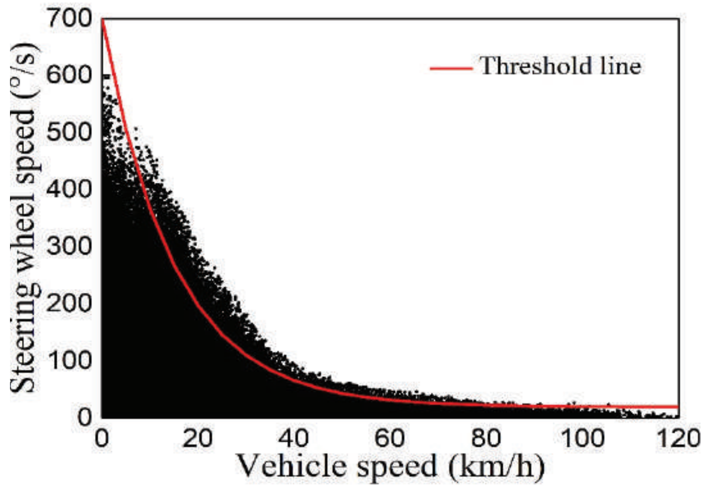

Figure 15. The distribution of steering wheel speed and threshold of abnormal steering action.

5. Evaluation Method of Driving Behaviour

5.1. Confirmation of Weight and Scoring Rule

According to the previous analysis, 11 indexes related to driving safety were utilized to evaluate driving behaviour. The evaluation result is influenced by the weight of indexes which can be confirmed by either the subjective or objective evaluation method. Subjective evaluation confirms the weight according to experience. Objective evaluation calculates the weight based on the relationship between the indexes. This study confirmed the weight of indexes by combining the subjective and objective evaluation method.

The comprehensive multi-index evaluation system was composed of two hierarchies. The first layer was the criterion layer, which consisted of three indexes: driving action, vehicle operation and fatigue driving/power consumption. The second layer was the index layer that consisted of the 11 indexes. The detailed index structure is shown in Table 6.

Table 6. The detailed index structure of driving behaviour evaluation.

Criterion Layer	Index Layer	Symbol of the Index
vehicle operation (u_1)	The number of rapid accelerations per 100 km	u_{11}
	The number of sudden brakings per 100 km	u_{12}
	The number of rapid turns per 100 km	u_{13}
	The number of speeding occurrences during steering per 100 km	u_{14}
driving action (u_2)	Standard deviation of vehicle speed	u_{21}
	Average value of acceleration	u_{22}
	Average value of deceleration	u_{23}
	Standard deviation of acceleration	u_{24}
	Standard deviation of deceleration	u_{25}
fatigue driving/power consumption (u_3)	Time of a driving event	u_{31}
	Power consumption per 100 km	u_{32}

Firstly, the weights of the indexes were preliminarily determined with the Analytic Hierarchy Process (AHP) method, which was a subjective evaluation. According to the experience, the judgement matrix was confirmed and used to indicate the relative importance degree of the indexes in the same layer. Assuming the index number of criterion layer m and the number of index layer n, the weight of indexes for the criterion layer ($AB_i(i = 1, 2, \ldots, m)$) and index layer ($AS_j(j = 1, 2, \ldots, n)$) can be calculated by Equation (9).

$$AB_i = \frac{\sqrt[m]{M_i}}{\sum_{i=1}^{m} \sqrt[m]{M_i}} \quad AS_j = \frac{\sqrt[n]{N_j}}{\sum_{j=1}^{n} \sqrt[n]{N_j}} \tag{9}$$

where M_i and N_j are the product of value in every row of the judgement matrix.

Secondly, the weight was further confirmed by the Entropy Weight Method (EWM), which was an objective evaluation. The EWM confirmed the weight of indexes according to the difference in the samples. Assuming the evaluation objectives are expressed as $A_i(i = 1, 2, \ldots, m)$, the indexes are as follows: $X_j(i = 1, 2, \ldots, n)$, AX'_{ij} is the original value of the jth index in the ith sample and AX_{ij} is the treated value by the Equation (10). The weight of index (EW_j) can be calculated by EWM method using Equation (11).

$$AX_{ij} = \frac{AX'_{ij} - \min(AX'_{ij})}{\max(AX'_{ij}) - \min(AX'_{ij})} \tag{10}$$

$$EW_j = \frac{1 + (1/\ln m) \sum_{i=1}^{m} P_{ij} \ln P_{ij}}{\sum_{j=1}^{n} (1 + (1/\ln m) \sum_{i=1}^{m} P_{ij} \ln P_{ij})} \tag{11}$$

where P_{ij} is the weight of the j_{th} index in the i_{th} sample and this can be expressed as Equation (12).

$$P_{ij} = \frac{AX_{ij}}{\sum_{i=1}^{m} AX_{ij}} \tag{12}$$

Finally, the comprehensive index weight (τ_j) can be calculated from AS_j and EW_j using Equation (13). Then, the normalisation can be applied to index layer, which is expressed as Ω_{ij}. The final weight (W_j) can be obtained from the product of Ω_{ij} and AB_i, as shown in Equation (14).

$$\tau_j = \frac{AS_j \cdot EW_j}{\sum_{j=1}^{n} (AS_j \cdot EW_j)} \tag{13}$$

$$W_j = \frac{AB_i \cdot \Omega_{ij}}{\sum_{i=1}^{m} (AB_i \cdot \Omega_{ij})} (i = 1, \ldots, m; j = 1, \ldots, n) \tag{14}$$

The judgement matrix was established based on the questionnaire introduced in previous studies [31–33], as shown in Table 7. The values in the matrix indicated the relative importance degree of the indexes. The final weights (W_j) were calculated by combining the AHP and EWM, which were shown in Table 8. It can be seen that the number of speeding occurrences during steering per 100 km had the maximum value of the weight and score. This suggests that the speeding during steering was the most dangerous behaviour among the selected indexes. Other indexes with higher weight or score were also risky in terms of causing traffic accidents.

Table 7. The judgement matrix for evaluation of the driving behaviour.

Criterion Layer	Index Layer
$\begin{array}{cccc} \mu & \mu_1 & \mu_2 & \mu_3 \\ \mu_1 & 1 & 3 & 2 \\ \mu_2 & 1/3 & 1 & 1/2 \\ \mu_3 & 1/2 & 2 & 1 \end{array}$	$\begin{array}{ccccc} \mu_1 & \mu_{11} & \mu_{12} & \mu_{13} & \mu_{14} \\ \mu_{11} & 1 & 2 & 1/2 & 1/2 \\ \mu_{12} & 1/2 & 1 & 1/3 & 1/3 \\ \mu_{13} & 2 & 3 & 1 & 1 \\ \mu_{14} & 2 & 3 & 1 & 1 \end{array}$ $\begin{array}{cccccc} \mu_2 & \mu_{21} & \mu_{22} & \mu_{23} & \mu_{24} & \mu_{25} \\ \mu_{21} & 1 & 2 & 1 & 2 & 1 \\ \mu_{22} & 1/2 & 1 & 1/2 & 1 & 1/2 \\ \mu_{23} & 1 & 2 & 1 & 2 & 1 \\ \mu_{24} & 1/2 & 1 & 1/2 & 1 & 1/2 \\ \mu_{25} & 1 & 2 & 1 & 2 & 1 \end{array}$ $\begin{array}{ccc} \mu_3 & \mu_{31} & \mu_{32} \\ \mu_{31} & 1 & 2 \\ \mu_{32} & 1/2 & 1 \end{array}$

Table 8. The final weight for different indexes.

Index	Weight (W_j)	Value (Percentage)
The number of rapid accelerations per 100 km	0.0858	9
The number of sudden brakings per 100 km	0.0677	7
The number of rapid turns per 100 km	0.1580	16
The number of speeding occurrences during steering per 100 km	0.2280	22
Standard deviation of vehicle speed	0.0428	4
Average value of acceleration	0.0233	2
Average value of deceleration	0.0206	2
Standard deviation of acceleration	0.0434	4
Standard deviation of deceleration	0.0333	4
Driving time per trip	0.1525	15
Power consumption per 100 km	0.1445	15

After the confirmation of the index weight, the scoring rule for different indexes was set to accurately evaluate the driving behaviour. The distribution of the 11 indexes was analysed and compared in Figure 16. Figure 16a shows the distribution of the number of rapid accelerations per 100 km. It can be seen that the number gradually decreased and in over 90% of cases, it was lower than 50 times. According to the distribution and the weight of the index, the scoring rule was set with a cut-off point of 50. The other scoring rules of the indexes were confirmed with the similar treatment by combining the distribution and the weight, and the results are shown in Table 9.

5.2. Proposed Driving Behaviour Evaluation Method

Based on the previous analysis, a driving behaviour evaluation method was proposed. This method included driving behaviour data acquisition, data pre−processing, recognition of the aberrant driving behaviour by statistics, index value calculation and output of the score. The flow chart of the evaluation process is shown in Figure 17.

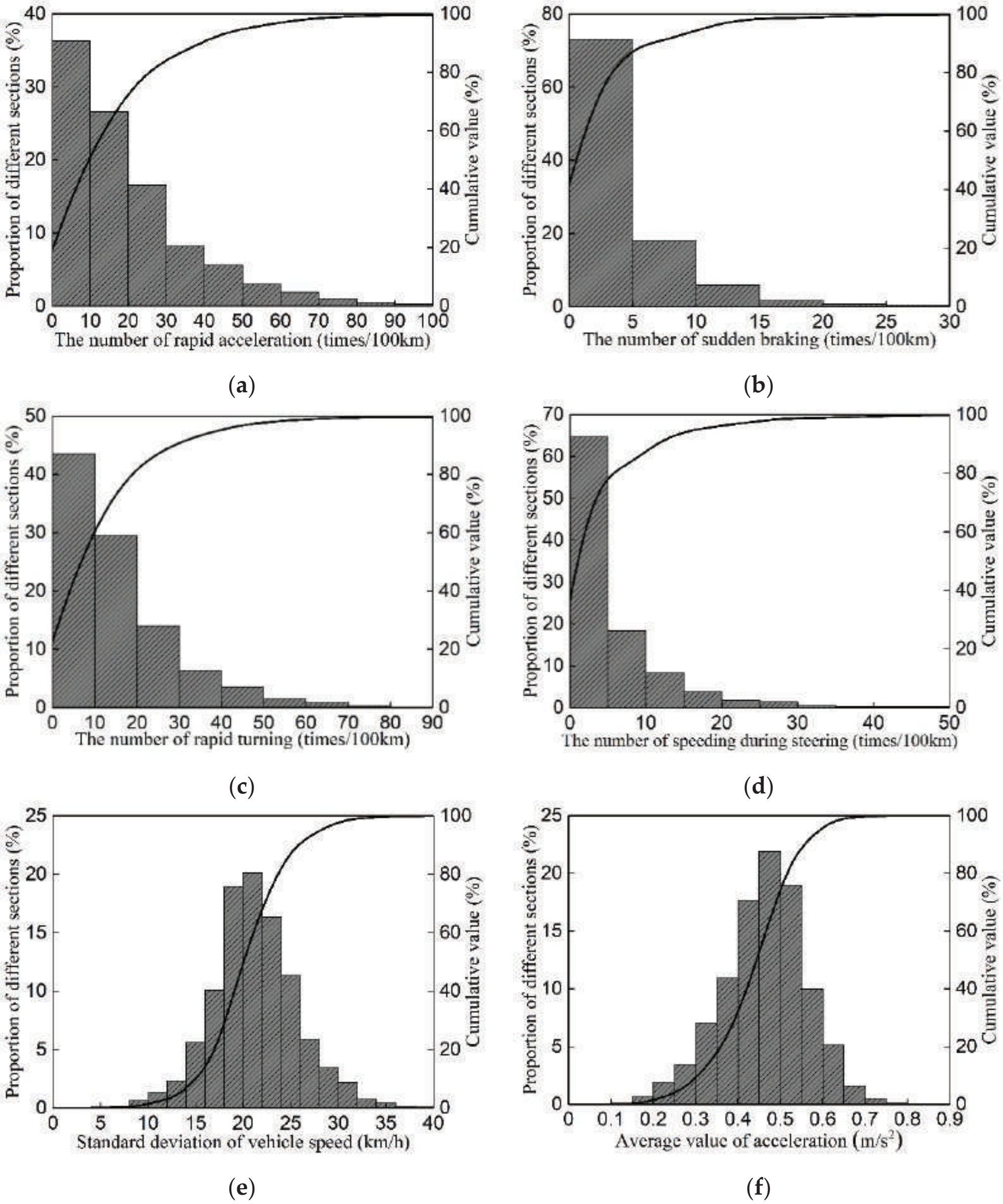

Figure 16. *Cont.*

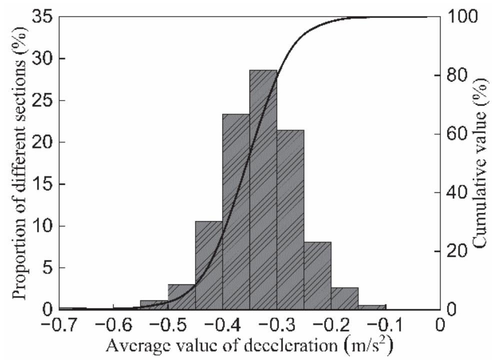

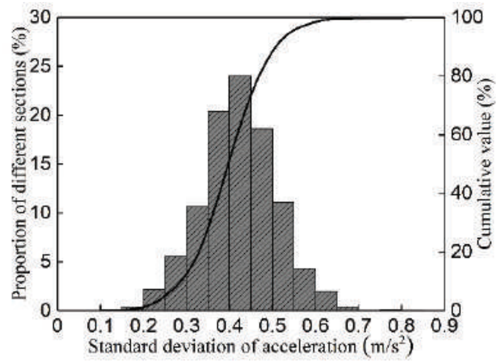

(**g**) (**h**)

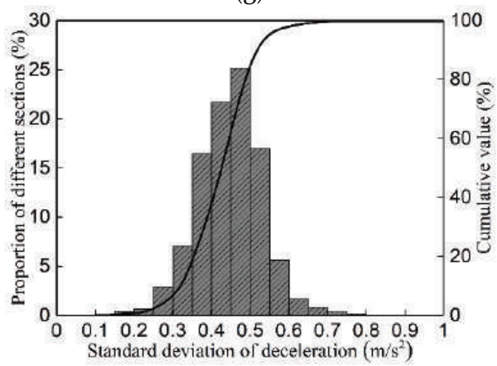

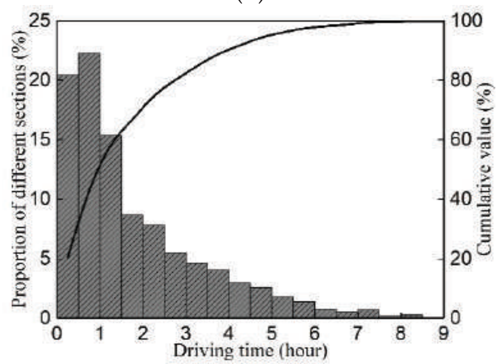

(**i**) (**j**)

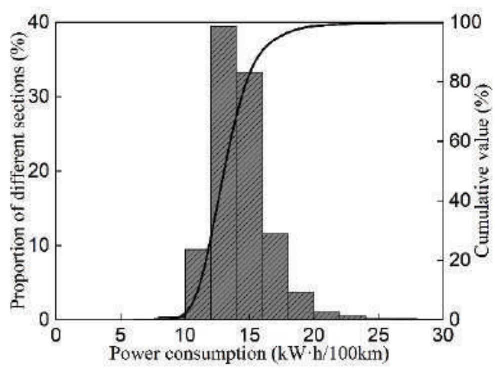

(**k**)

Figure 16. The distribution of different indexes: (**a**) The number of rapid accelerations per 100 km; (**b**) The number of sudden brakings per 100 km; (**c**) The number of rapid turns per 100 km; (**d**) The number of speeding occurences during steering per 100 km; (**e**) Standard deviation of vehicle speed; (**f**) Average value of acceleration; (**g**) Standard deviation of acceleration; (**h**) Average value of deceleration; (**i**) Standard deviation of deceleration; (**j**) Driving time per trip; (**k**) Power consumption.

Table 9. The scoring rule of different indexes.

Index	Unit	Score	Score Rule
The number of rapid acceleration per 100 km	times/100 km	9	$y=\begin{cases}9-0.18x; 0\le x\le 50\\0; x>50\end{cases}$
The number of sudden braking per 100 km	times/100 km	7	$y=\begin{cases}7-0.28x; 0\le x\le 25\\0; x>25\end{cases}$
The number of rapid turning per 100 km	times/100 km	16	$y=\begin{cases}16-0.32x; 0\le x\le 50\\0; x>50\end{cases}$
The number of speeding during steering per 100 km	times/100 km	22	$y=\begin{cases}22-0.88x; 0\le x\le 25\\0; x>25\end{cases}$
Standard deviation of vehicle speed	km/h	4	$y=\begin{cases}4; 0\le x\le 20\\2; 20<x\le 35\\0; x>35\end{cases}$
Average value of acceleration	m/s^2	2	$y=\begin{cases}2; 0\le x\le 0.5\\1; 0.5<x\le 0.7\\0; x>0.7\end{cases}$
Standard deviation of acceleration	m/s^2	4	$y=\begin{cases}4; 0\le x\le 0.4\\2; 0.4<x\le 0.8\\0; x>0.8\end{cases}$
Average value of deceleration	m/s^2	2	$y=\begin{cases}2; -0.35\le x\le 0\\1; -0.5\le x<0.35\\0; x<-0.5\end{cases}$
Standard deviation of deceleration	m/s^2	4	$y=\begin{cases}4; 0\le x\le 0.4\\2; 0.4<x\le 0.8\\0; x>0.8\end{cases}$
Driving time per trip	hour	15	$y=\begin{cases}15; t\le 4\\5; 4<t<8\\0; t\ge 8\end{cases}$
Power consumption	kW·h/100 km	15	$y=\begin{cases}15; 0<x\le 15\\15-3(x-15); 15<x\le 20\\0; x>20\end{cases}$

To verify the effectiveness of the evaluation method, thirty drivers were selected from the online car−hiring. The driving behaviour data were selected in one month with 2227 driving events. The scoring result for each driving event was calculated and compared in Figure 18. Most of the scoring results were located from 70 to 100, which indicates that most of the driver behaviours were cautious. There were also some scoring results lower than 60, which can be considered as unsafe driving behaviours. To quantitatively evaluate the driving behaviour of a driver, the average score for every driver in a month was obtained by averaging the score of each driving event, which is shown in Figure 18b. The comparison result showed that the score difference was considerable for each driver. The evaluation result suggested that the scores of the driver number 2 and 14 were relatively low.

In order to investigate the reasons for the low scores of drivers 2 and 14, the score of the four indexes were compared in Figure 19. The four indexes were the number of rapid accelerations per 100 km, the number of sudden brakings per 100 km, the number of rapid turns per 100 km and the number of speeding occurrences during steering per 100 km, which were closely related with aberrant driving behaviour. The scores of drivers 2 and 14 were also compared with the average scores of the thirty drivers. It can be seen that the scores of the selected four indexes for drivers 2 and 14 were obviously lower than the average scores. Additionally, the score of driver number 14 was lower than that of driver number 2. A lower score meant more aberrant driving behaviour, which showed the effectiveness of the evaluation method. The scoring result can be an important reference for the passenger transport company to distinguish the driver with abnormal or dangerous driving behaviour. The driving behaviour scores can also be an important basis for evaluation for the insurance company to collect the premium.

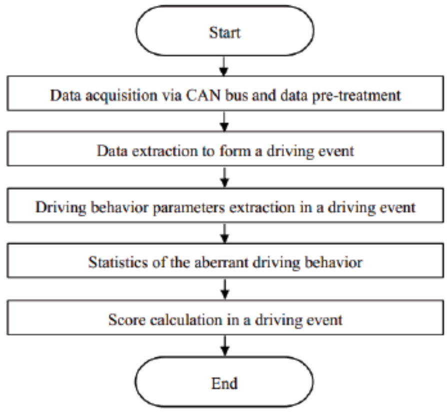

Figure 17. The evaluation flow chart of driving behaviour.

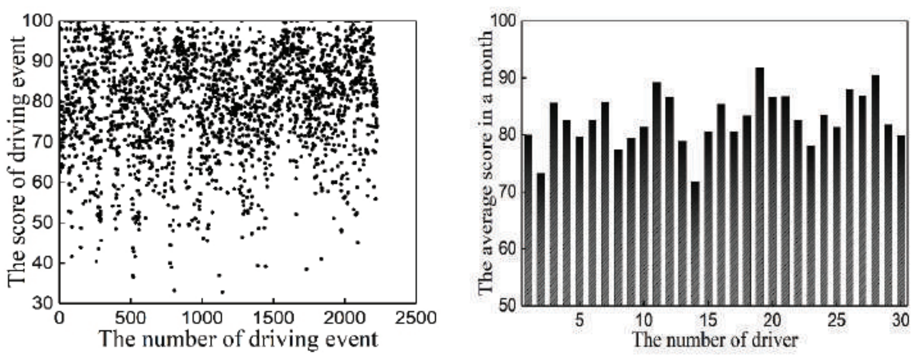

(**a**) (**b**)

Figure 18. The evaluation result of driving behaviour: (**a**) The score distribution of driving events; (**b**) The score for every driver.

Figure 19. The comparison of scores for four indexes (numbers from 1 to 4 represent the number of rapid accelerations per 100 km, the number of sudden brakings per 100 km, the number of rapid turns per 100 km and the number of speeding occurrences during steering per 100 km, respectively).

6. Conclusions

This study proposed a quantitative evaluation method of driving behaviour based on NDS data collected from shared-electrical cars and online car-hiring services. Data acquisition, treatment method and data volume verification were analysed to ensure the effectiveness of the dataset. The distribution characteristics of the main driving behaviour parameters were studied. On this basis, the evaluation method was proposed and verified. The main conclusions were shown as follows. The main differences between the electrical vehicles and vehicles powered by ICE were in the deceleration phase. There was braking energy recovery for the electrical vehicles. Therefore, the conclusion can be basically applied to the ICE vehicles.

1. The NDS data were collected from the OBD−II interface via CAN bus with the rate of 10 Hz. This sampling frequency satisfies the requirement of transient process analysis. The sliding-window averaging filter and the box diagram method were used to improve the data quality. Eleven indexes were selected to evaluate the driving behaviour, including vehicle running data, driver operation data and power consumption of the vehicles.
2. *KL* divergence was applied to confirm the appropriate data quantity for the driving behaviour analysis. The result showed that the minimum data quantity for vehicle speed, acceleration, steering wheel angle and steering wheel speed were 20×10^5, 63×10^5, 10×10^5, 231×10^5, respectively, with the variation value of *KL* lower than 1×10^5.
3. The changing trend of acceleration and deceleration, steering wheel angle and steering wheel speed versus vehicle speed were compared. Based on the distribution characteristics, the thresholds of aberrant driving were determined in correlation with vehicle speed to enhance the recognition accuracy of the aberrant driving behaviour. The thresholds can be used to evaluate the aberrant driving behaviour.
4. The weights for the 11 indexes were obtained by combining the AHP and EWM methods. The scoring rules of the 11 indexes were confirmed based on the distribution of the indexes. An evaluation method of driving behaviour was proposed and verified according to the driving behaviour data of the car-hiring driver.

In future research, more parameters will be considered including, road slope, weather, driving experience and so on. Additionally, other useful sensors will be used to obtain more driving behaviour parameters. On this basis, the scoring rule will be further optimized and the accuracy of the evaluation method can be subsequently improved.

Author Contributions: Formal analysis, X.L.; methodology, Y.C.; software, K.Z. and S.S.; validation, Z.Y.; writing—original draft, S.J.; writing—review and editing, G.T. All authors have read and agreed to the published version of the manuscript.

Funding: This research was funded by National Key Research and Development Program, grant number 2020YFB1600501; Major Technology Innovation Projects of Shandong Province, grant number 2019TSLH0203; Natural Science Foundation of Shandong Province, grant number ZR2020ME180; National Natural Science Foundation of China, grant number 51976107.

Institutional Review Board Statement: Ethical review and approval were waived for this study due to the reason that the driving behaviour data in this study was obtained from the vehicle operation data and did not involve any personal information, such as GPS data and so on.

Informed Consent Statement: Informed consent was obtained from all subjects involved in the study.

Data Availability Statement: The data were obtained from the OBD−II interface, which only contained the vehicle and components operation data. The driving behaviour data were obtained from the vehicle operation data.

Conflicts of Interest: The authors declare that they have no known competing financial interest or personal relationships that could have appeared to influence the work reported in this paper.

Abbreviations

AHP	Analytic Hierarchy Process
CAN	Controller Area Network
ECU	Electronic Control Units
EWM	Entropy Weight Method
GPS	Global Positioning System
ICE	Internal Combustion Engine
IMU	Inertial Measurement Unit
KL	Kullback–Leibler
NDS	Naturalistic Driving Study
OBD	On-Board Diagnostics

References

1. Singh, H.; Kathuria, A. Analyzing driver behavior under naturalistic driving conditions: A review. *Accid. Anal. Prev.* **2021**, *150*, 105908. [CrossRef] [PubMed]
2. Singh, S. *Critical Reasons for Crashes Investigated in the National Motor Vehicle Crash Causation Survey*; National Center for Statistics and Analysis: Washington, DC, USA, 2015.
3. Tanvir, S.; Chase, R.T.; Roupahil, N.M. Development and analysis of eco-driving metrics for naturalistic instrumented vehicles. *J. Intell. Transp. Syst.* **2021**, *25*, 235–248. [CrossRef]
4. Ersan, Ö.; Üzümcüoğlu, Y.; Azık, D.; Fındık, G.; Kaçan, B.; Solmazer, G.; Özkan, T.; Lajunen, T.; Öz, B.; Pashkevich, A.; et al. The relationship between self and other in aggressive driving and driver behaviors across countries. *Transp. Res. Part F Traffic Psychol. Behav.* **2019**, *66*, 122–138. [CrossRef]
5. Deng, Z.; Chu, D.; Wu, C.; He, Y.; Cui, J. Curve safe speed model considering driving style based on driver behaviour questionnaire. *Transp. Res. Part F Traffic Psychol. Behav.* **2019**, *65*, 536–547. [CrossRef]
6. Han, H.; Kim, S.; Choi, J.; Park, H.; Yang, J.H.; Kim, J. Driver's avoidance characteristics to hazardous situations: A driving simulator study. *Transp. Res. Part F Traffic Psychol. Behav.* **2021**, *81*, 522–539. [CrossRef]
7. Papazikou, E.; Thomas, P.; Quddus, M. Developing personalised braking and steering thresholds for driver support systems from SHRP2 NDS data. *Accid. Anal. Prev.* **2021**, *160*, 106310. [CrossRef]
8. Akamatsu, M.; Green, P.; Bengler, K. Automotive technology and human factors research: Past, present, and future. *Int. J. Veh. Technol.* **2013**, *2013*, 1–27. [CrossRef]
9. Precht, L.; Keinath, A.; Krems, J.F. Effects of driving anger on driver behavior—Results from naturalistic driving data. *Transp. Res. Part F Traffic Psychol. Behav.* **2017**, *45*, 75–92. [CrossRef]
10. Ellison, A.B.; Greaves, S.P.; Bliemer, M.C.J. Driver behaviour profiles for road safety analysis. *Accid. Anal. Prev.* **2015**, *76*, 118–132. [CrossRef]
11. Shridhar Bokare, P.; Kumar Maurya, A. Study of effect of speed, acceleration and deceleration of small petrol car on its tail pipe emission. *Int. J. Traffic Transp. Eng.* **2013**, *3*, 465–478. [CrossRef]
12. Sun, Q.; Xia, J.; Nadarajah, N.; Falkmer, T.; Foster, J.; Lee, H. Assessing drivers' visual-motor coordination using eye tracking, GNSS and GIS: A spatial turn in driving psychology. *J. Spat. Sci.* **2016**, *61*, 299–316. [CrossRef]
13. Sheykhfard, A.; Haghighi, F. Performance analysis of urban drivers encountering pedestrian. *Transp. Res. Part F Traffic Psychol. Behav.* **2019**, *62*, 160–174. [CrossRef]
14. Bokare, P.S.; Maurya, A.K. Acceleration-deceleration behaviour of various vehicle types. *Transp. Res. Procedia* **2017**, *25*, 4733–4749. [CrossRef]
15. Chen, R.; Kusano, K.D.; Gabler, H.C. Driver behavior during overtaking maneuvers from the 100-car naturalistic driving study. *Traffic Inj. Prev.* **2015**, *16*, S176–S181. [CrossRef]
16. Mahapatra, G.; Maurya, A.K. Study of vehicles lateral movement in non-lane discipline traffic stream on a straight road. *Procedia Soc. Behav. Sci.* **2013**, *104*, 352–359. [CrossRef]
17. Papadimitriou, E.; Argyropoulou, A.; Tselentis, D.I.; Yannis, G. Analysis of driver behaviour through smartphone data: The case of mobile phone use while driving. *Saf. Sci.* **2019**, *119*, 91–97. [CrossRef]
18. Saleh, K.; Hossny, M.; Nahavandi, S. Driving behavior classification based on sensor data fusion using LSTM recurrent neural networks. In Proceedings of the 2017 IEEE 20th International Conference on Intelligent Transportation Systems (ITSC), Yokohama, Japan, 16–19 October 2017.
19. Sangster, J.; Rakha, H.; Du, J. Application of naturalistic driving data to modeling of driver car-following behavior. *Transp. Res. Rec.* **2013**, *2390*, 20–33. [CrossRef]
20. Jachimczyk, B.; Dziak, D.; Czapla, J.; Damps, P.; Kulesza, W. IoT on-board system for driving style assessment. *Sensors* **2018**, *18*, 1233. [CrossRef]
21. Mayhew, D.R.; Simpson, H.M. The safety value of driver education and training. *Inj. Prev. J. Int. Soc. Child Adolesc. Inj. Prev.* **2002**, *8* (Suppl. 2), ii3–ii8.

22. Zhao, Y.; Yamamoto, T.; Morikawa, T. An analysis on older driver's driving behavior by GPS tracking data: Road selection, left/right turn, and driving speed. *J. Traffic Transp. Eng.* **2018**, *5*, 56–65. [CrossRef]
23. Feng, F.; Bao, S.; Sayer, J.R.; Flannagan, C.; Manser, M.; Wunderlich, R. Can vehicle longitudinal jerk be used to identify aggressive drivers? An examination using naturalistic driving data. *Accid. Anal. Prev.* **2017**, *104*, 125–136. [CrossRef] [PubMed]
24. Das, A.; Ghasemzadeh, A.; Ahmed, M.M. Analyzing the effect of fog weather conditions on driver lane-keeping performance using the SHRP2 naturalistic driving study data. *J. Saf. Res.* **2019**, *68*, 71–80. [CrossRef] [PubMed]
25. Kong, X.; Das, S.; Jha, K.; Zhang, Y. Understanding speeding behavior from naturalistic driving data: Applying classification based association rule mining. *Accid. Anal. Prev.* **2020**, *144*, 105620. [CrossRef] [PubMed]
26. Morgenstern, T.; Schott, L.; Krems, J.F. Do drivers reduce their speed when texting on highways? A replication study using European naturalistic driving data. *Saf. Sci.* **2020**, *128*, 104740. [CrossRef]
27. Hallmark, S.L.; Tyner, S.; Oneyear, N.; Carney, C.; McGehee, D. Evaluation of driving behavior on rural 2-lane curves using the SHRP 2 naturalistic driving study data. *J. Saf. Res.* **2015**, *54*, 17.e1–27. [CrossRef]
28. Ji, S.; Chen, Q.; Shu, M.; Tian, G.; Liao, B.; Lv, C.; Li, M.; Lan, X.; Cheng, Y. Influence of operation management on fuel consumption of coach fleet. *Energy* **2020**, *203*, 117853. [CrossRef]
29. Sagberg, F.; Selpi; Bianchi Piccinini, G.F.; Engström, J. A review of research on driving styles and road safety. *Hum. Factors* **2015**, *57*, 1248–1275. [CrossRef]
30. Wang, W.; Liu, C.; Zhao, D. How much data is enough? A statistical approach with case study on longitudinal driving behavior. *IEEE Trans. Intell. Veh.* **2017**, *2*, 85–98. [CrossRef]
31. Wang, Z. Research on Vehicle Insurance Pricing Based on UBI Driving Behaviour Score. Master's Thesis, Hunan University, Hunan, China, 2019.
32. Peng, J. Research on Usage-Based Insurance Premiums and Driving Behaviour Scoring Based on GID. Master's Thesis, Nanjing University of Posts and Telecommunications, Nanjing, China, 2016.
33. Tselentis, D.I.; Yannis, G.; Vlahogianni, E.I. Innovative motor insurance schemes: A review of current practices and emerging challenges. *Accid. Anal. Prev.* **2017**, *98*, 139–148. [CrossRef]

sustainability

MDPI

Article

A High-Gain DC Side Converter with a Ripple-Free Input Current for Offshore Wind Energy Systems

Ran Tao [1], Jingpeng Yue [1], Zhenlin Huang [1], Ranran An [1], Zou Li [2] and Junfeng Liu [2,*]

1 Guangdong Key Laboratory of New Technology for Smart Grid, Guangzhou 510062, China
2 School of Automation Science and Engineering, South China University of Technology, Guangzhou 510641, China
* Correspondence: jf.liu@connect.polyu.hk

Abstract: Considering that the distance between offshore wind farms and onshore converters is getting farther and farther, dc transmission becomes increasingly more applicable than conventional ac transmission. To reduce the transmission loss, a feasible solution is using a high-gain dc/dc converter to boost the rectified output voltage to thousands of volts. Thus, a novel single-switch high-gain dc/dc converter with a ripple-free input current is presented in this paper. The structure consists of two cells—a coupled-inductor cell and a switched-capacitor cell. The coupled-inductor cell in the proposed converter provides a ripple-free input current. The switched-capacitor cell provides a high voltage gain. The converter has a simple control strategy due to the use of a single switch. Moreover, the output capacitor is charged and discharged continuously by a 180° phase shift to eliminate the output voltage ripple. A steady-state analysis of the converter is proposed to determine the parameters of the devices. In addition, a 240 W, 40/308 V laboratory prototype at 35 kHz switching frequency has been developed, in which the input current ripple is only 1.1% and a peak efficiency of 94.5% is reached. The experimental results verify the validity and feasibility of the proposed topology.

Keywords: dc/dc converter; high voltage gain; ripple-free input current; offshore wind farms

Citation: Tao, R.; Yue, J.; Huang, Z.; An, R.; Li, Z.; Liu, J. A High-Gain DC Side Converter with a Ripple-Free Input Current for Offshore Wind Energy Systems. *Sustainability* **2022**, *14*, 11574. https://doi.org/10.3390/su141811574

Academic Editors: Wenbin Yu and Guang Zeng

Received: 19 August 2022
Accepted: 8 September 2022
Published: 15 September 2022

1. Introduction

With the beginning of global carbon neutrality, offshore wind energy has become one of the main and growing sources of renewable energy worldwide [1–3]. The European Commission stated that the offshore wind power capacity in Europe would reach 450 GW by 2050, making it a key part of renewable energy [4]. Compared with its onshore counterpart, an offshore wind farm has the merits of less land occupation, higher wind speeds, and more stable wind conditions [5–7]. However, there are some problems that need to be solved, such as the difficulties of installation and maintenance [8,9]. Once an accident occurs, the long time for fault correction will have an adverse impact on the continuous power supply. Moreover, with the increase in offshore distance, conventional high voltage ac (HVAC) transmission is no longer suitable for long-distance offshore wind farms, as it brings higher power loss and significant power fluctuation [10–12].

Considering the above problems, high voltage dc (HVDC) transmission appears to be a more promising solution for long-distance and large-scale offshore wind farms [13–15]. The traditional HVAC transmission system of an offshore wind farm consists of a medium voltage ac (MVAC) collection grid as shown in Figure 1. Each wind turbine is connected to a transformer to boost the turbine's output voltage. To avoid the use of large volume transformers, a HVDC transmission system uses a medium voltage dc (MVDC) collection grid as shown in Figure 2 [16–18], where the traditional MV transformers are replaced by MV step-up dc/dc converters. The use of MV dc/dc converters can significantly reduce the volume and weight of the offshore platforms which leads to lower installation costs. Meanwhile, due to the low output voltage generated by wind turbines, high-gain dc/dc converters become one of the key levels of MV dc collection grids [19–21]. In the existing research, there are bidirectional and unidirectional high-gain dc/dc converters. However, there is no need for bidirectional power flow capacity due to the inherent characteristics of offshore wind farms, so a simpler unidirectional dc/dc converter is more applicable for offshore wind energy systems [22]. In addition to a high voltage gain, there are some other challenges such as low input current ripple, high conversion efficiency, and high-power density. To overcome these challenges, a large amount of relevant research has been done.

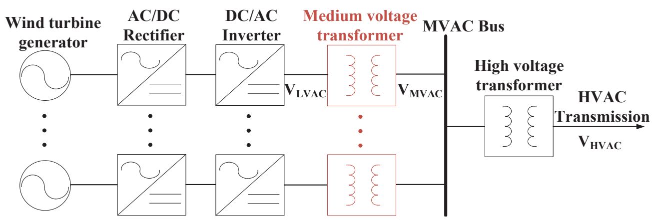

Figure 1. HVAC transmission system with MVAC grid.

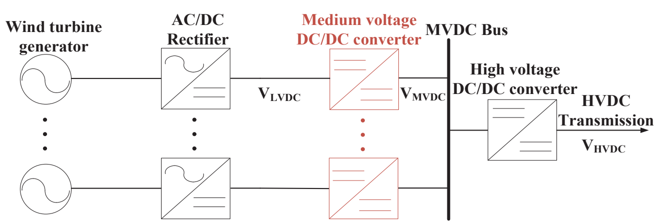

Figure 2. HVDC transmission system with MVDC grid.

To reduce the power loss and maintain high efficiency, researchers have generated much interest in high-gain dc/dc converters for offshore wind farms. In [23], a high-gain resonant switched-capacitor (RSC) dc/dc converter was introduced, which provided low switching losses and high efficiency by the resonant switching transitions. In addition, the voltage gain was increased through the series-modular configuration. However, to reach a high voltage gain, lots of switching devices and passive components were used in the topology. Meanwhile, the voltage stress increment of the switches and diodes blocked its application in offshore wind energy systems. To reduce the number of power switches, [24,25] both presented step-up dc/dc converters which worked only by one switch. The control of the converters was easy, and the conduction loss of the switch was decreased due to the use of a single-switch structure. But the voltage gain was not high enough. In [26], a high-power multilevel step-up dc/dc converter was studied with the merits of outstanding dynamic performance and low voltage stress. Although there was a filter inductor in this converter that could reduce the input current ripple, the step-up ratio was not high enough for offshore wind farms. Moreover, the concept of modularization used in offshore wind farms has attracted considerable interests recently due to its high reliability and excellent expandability [27–30]. Nevertheless, a complex switching scheme is usually required in the modular structure. Furthermore, a large number of power devices connected in series increase the volume and weight of the offshore platforms and may raise the overall costs.

In order to ensure the long-distance and stable transmission of electricity, a ripple-free input current is necessary for a high-gain dc/dc converter. Generally, bulky and huge electrolytic capacitors are used at the input stage of the dc/dc converters to decrease the large input current ripple. To avoid the use of bulky electrolytic capacitors, a filter inductor is placed at the input stage to reduce the current ripple [31]. However, the current ripple still exists, and the effect is not ideal. By utilizing the interleaved structure of switches and inductors on the input side, the input current ripple was significantly reduced in [32]. Nevertheless, the switching scheme is relatively complex and the input direct current still consists of a little ripple. An improved dc/dc converter with a ripple-free input current was proposed in [33]. The input current ripple was reduced to zero with the use of the coupled inductor. Moreover, the converter can reach a high voltage gain through the use of a transformer. However, the use of too many magnetic components also limits its application in offshore wind farms due to the increase in volume and weight. Nonetheless, the coupled inductor is a promising component to achieve a ripple-free input current.

Considering the above problems, this paper presents a single-switch high-gain dc/dc converter with a ripple-free input current. The proposed converter combines the coupled inductor with the switch-capacitor structure and has the following features by comparing with the existing converters: (1) high voltage gain; (2) ripple-free input current; (3) simplicity of control strategy; (4) low voltage stress across the components; (5) high efficiency. Given all of the advantages, the converter is very suitable for offshore wind energy systems.

The rest of this paper is organized as follows. The proposed topology and operating principle are discussed in Section 2. The detailed steady-state analysis is presented in Section 3. The performance comparisons of the converters are provided in Section 4. Section 5 illustrates the parameters design and the selection of the components. Experimental results are shown in Section 6. Finally, conclusions are drawn in Section 7.

2. Topology and Operating Principle

2.1. Topology

Figure 3a shows the proposed single-switch dc/dc converter with a high voltage gain and a ripple-free input current. A coupled inductor L_C is inserted at the input stage to eliminate the input current ripple. Figure 3b shows the equivalent circuit of the converter where the coupled inductor L_C is described by the magnetic inductor L_m, the leakage inductor L_k, and the ideal transformer (turns ratio $n = N_s/N_p$). The switched-capacitor cell uses only one switch with a new arrangement of the diodes and capacitors to raise the voltage gain significantly. The control strategy is very simple due to the use of one switch which can reduce the incidence of failure in offshore wind energy systems. The theoretical waveforms of the main devices are shown in Figure 4. The voltage at both ends of the primary side and the secondary side of the coupled inductor are defined as v_p and v_s, respectively. The analysis of the converter during a switching period T_S can be divided into two operating modes, and they are shown in Figure 5.

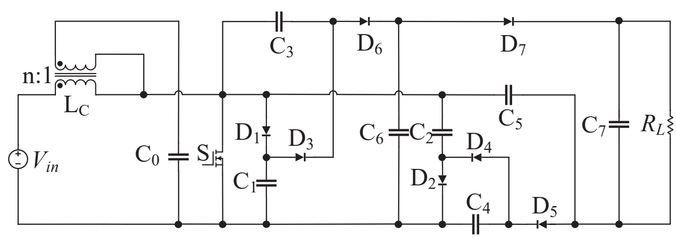

(**a**)

Figure 3. *Cont.*

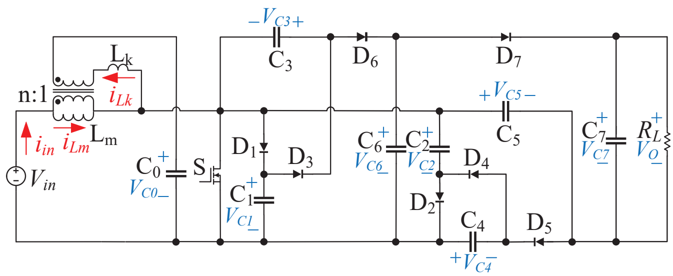

(**b**)

Figure 3. Proposed dc/dc converter: (**a**) Topology; (**b**) Equivalent circuit.

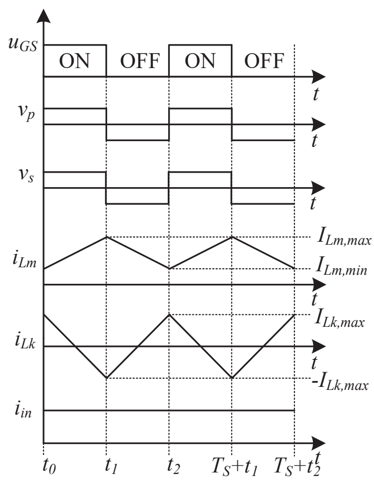

Figure 4. Theoretical waveforms of the proposed converter.

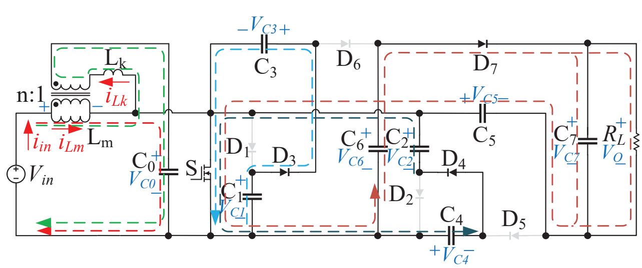

(**a**)

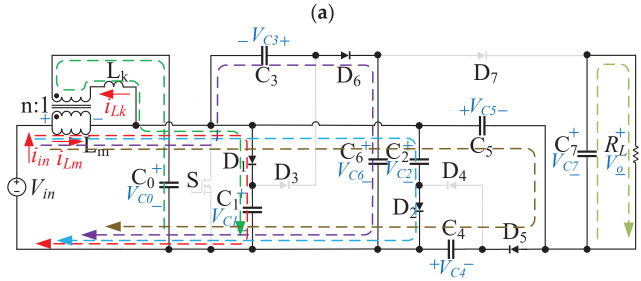

(**b**)

Figure 5. Operating modes of the proposed converter: (**a**) Mode 1; (**b**) Mode 2.

2.2. Operating Principle

Since the circuit is controlled by one switch, there are only two operating modes during a switching period. The following assumptions are made before the analysis.

(1) All the switches, capacitors, diodes, and inductors used in the circuit are assumed to be ideal components;
(2) All the capacitors are large enough to maintain output voltage constant;
(3) V_{in} is an ideal dc voltage source, and the load is modeled by a pure resistor R_L.

Mode 1 [t_0,t_1] in Figure 5a: In this mode, the switch S begins to conduct under the action of the gate driving signal. The current i_{Lm} increases linearly from its minimum value due to the positive voltage. The diodes D_1, D_2, D_5, and D_6 are reverse biased. The magnetic inductor L_m starts to be charged by the input voltage source V_{in}. C_1 is discharged to C_3 through diode D_3 and C_2 is discharged to C_4 through diode D_4. Meanwhile, C_5 and C_6 are discharged in series to C_7 and R_L through diode D_7. Figure 6 shows the simplified equivalent circuits in this mode.

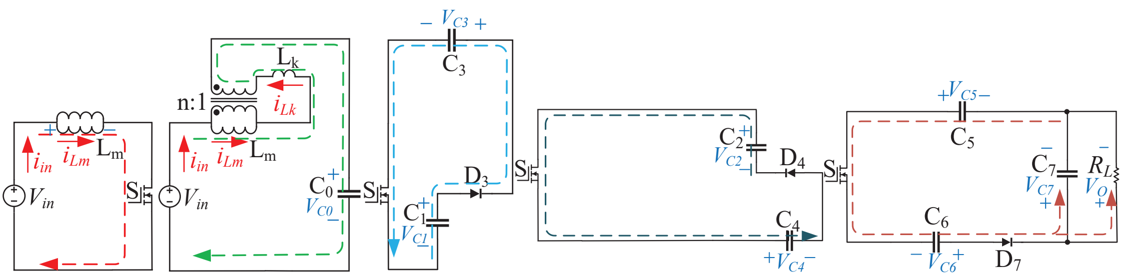

Figure 6. Simplified equivalent circuits of Mode 1.

Here, the voltages across the capacitors, diodes, inductor, and load are defined as V_{C0}–V_{C7}, V_{D1}–V_{D7}, v_{Lm}, v_{Lk}, and V_O, respectively. Similarly, the currents flowing through the input voltage source, magnetic inductor, and leakage inductor are defined as i_{in}, i_{Lm}, and i_{Lk}, respectively.

Mode 2 [t_1,t_2] in Figure 5b: At t_1, the switch S is turned off. The diodes D_3, D_4, and D_7 are reverse biased. The input voltage source V_{in} and magnetic inductor L_m are discharged in series to C_1 and C_2, respectively. Meanwhile, the input voltage source V_{in}, magnetic inductor L_m, and C_4 are discharged in series to C_5 through diode D_5. The input voltage source V_{in}, magnetic inductor L_m, and C_3 are discharged in series to C_6 through diode D_6. Therefore, the current i_{Lm} starts to decrease linearly from its maximum value, and the output capacitor C_7 is discharged to the load R_L. This mode ends when the driving signal of the switch S comes in the next period. Figure 7 shows the simplified equivalent circuits in this mode.

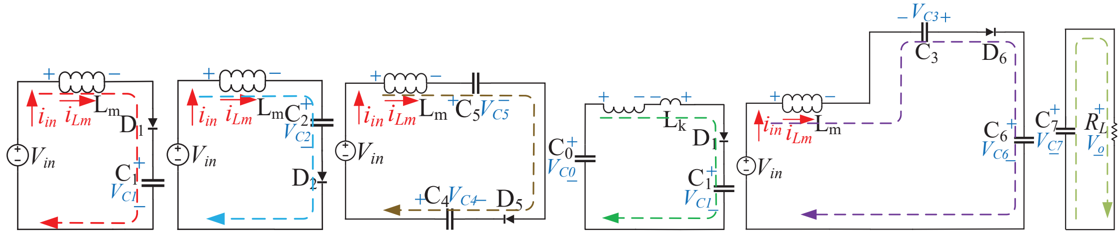

Figure 7. Simplified equivalent circuits of Mode 2.

3. Steady-State Analysis

3.1. Voltage Gain

Referring to Figures 5a and 6, when the switch is turned on, the following equations can be obtained according to Kirchhoff's voltage law, where $v_{Lm(on)}$ is the voltage across the magnetic inductor when the switch is turned on.

$$\begin{cases} v_{\mathrm{Lm}(on)} = V_{in} \\ V_{C3} = V_{C1} \\ V_{C4} = V_{C2} \\ V_{C5} + V_{C6} = V_{C7} = V_O \end{cases} \tag{1}$$

Similarly, from Figures 5b and 7, the voltage relationship of each loop can be expressed as follows, where $v_{Lm(off)}$ is the voltage across the magnetic inductor when the switch is turned off.

$$\begin{cases} V_{in} - v_{\mathrm{Lm}(off)} = V_{C1} = V_{C2} \\ V_{in} - v_{\mathrm{Lm}(off)} + V_{C4} = V_{C5} \\ V_{in} - v_{\mathrm{Lm}(off)} + V_{C3} = V_{C6} \\ V_O = V_{C7} \end{cases} \tag{2}$$

By applying the volt-second balance principle to the magnetic inductor L_m under steady-state conditions, the equation is given below:

$$\int_{t_0}^{t_0+T_S} v_{Lm} dt = 0 \tag{3}$$

where v_{Lm} is the voltage across the magnetic inductor.

From (1)–(3), the steady-state voltage expressions of the capacitors and the load are given below, where D is the duty cycle.

$$\begin{cases} V_{C1} = V_{C2} = V_{C3} = V_{C4} = \frac{V_{in}}{1-D} \\ V_{C5} = V_{C6} = \frac{2V_{in}}{1-D} \\ V_O = V_{C7} = \frac{4V_{in}}{1-D} \end{cases} \tag{4}$$

Therefore, the voltage gain M of the proposed converter can be derived as follows:

$$M = \frac{V_O}{V_{in}} = \frac{4}{1-D} \tag{5}$$

3.2. Ripple-Free Condition

As shown in Figure 5, the direction of the current can be obtained. From Figure 5a, when the switch S is turned on, the voltage v_{Lm} across L_m is V_{in}. Hence, the current i_{Lm} increases linearly from its minimum value $I_{Lm,min}$ as follows:

$$i_{Lm}(t) = I_{Lm,\min} + \int_{t_0}^{t} \frac{V_{in}}{L_m} dt \tag{6}$$

The voltage v_{Lk} across L_k is $-(V_{C0} - nV_{in})$. Therefore, the current i_{Lk} decreases linearly from its maximum value $I_{Lk,max}$ as follows:

$$i_{Lk}(t) = I_{Lk,\max} - \int_{t_0}^{t} \frac{V_{C0} - nV_{in}}{L_k} dt \tag{7}$$

Since the average inductor voltage must be zero under the steady-state conditions, the voltage V_{C0} can be shown as follows:

$$V_{C0} = V_{in} \tag{8}$$

It is apparent that the input current i_{in} is the sum of i_{Lm} and ni_{Lk}. Therefore, combining (6)–(8), i_{in} can be derived as follows:

$$i_{in}(t) = I_{Lm,\min} + nI_{Lk,\max} + \int_{t_0}^{t} \left(\frac{1}{L_m} - \frac{n(1-n)}{L_k}\right)V_{in}dt \tag{9}$$

To achieve a ripple-free condition, the variation of input current must be zero during this stage as follows:

$$\frac{d}{dt}i_{in}(t) = 0 \tag{10}$$

From (9) and (10), since ($I_{Lm,min}$ + $nI_{Lk,max}$) is a constant value, the input current ripple is eliminated with the following condition:

$$L_k = n(1-n)L_m \tag{11}$$

Consequently, the input current i_{in} in Mode 1 is only determined by

$$i_{in}(t) = I_{Lm,\min} + nI_{Lk,\max} \tag{12}$$

Similarly, with the turn-off of the switch S shown in Figure 5b, the voltage v_{Lm} across L_m is $-(V_{C1} - V_{in})$. The current i_{Lm} decreases linearly from its maximum value $I_{Lm,max}$ as follows:

$$i_{Lm}(t) = I_{Lm,\max} - \int_{t_1}^{t} \frac{V_{C1} - V_{in}}{L_m}dt \tag{13}$$

The voltage v_{Lk} across L_k is ($V_{C1} - V_{C0}$ + nv_{Lm}), which can also be written as $(1 - n)$ $(V_{C1} - V_{in})$. Therefore, the current i_{Lk} increases linearly from its minimum value $-I_{Lk,max}$ as follows:

$$i_{Lk}(t) = -I_{Lk,\max} + \int_{t_1}^{t} \frac{(1-\mathrm{n})(V_{C1} - V_{in})}{L_k}dt \tag{14}$$

Combining (13) and (14), the input current i_{in} can be derived as follows:

$$i_{in}(t) = I_{Lm,\max} - nI_{Lk,\max} + \int_{t_1}^{t} \left(\frac{n(1-\mathrm{n})}{L_k} - \frac{1}{L_m}\right)\frac{DV_{in}}{1-D}dt \tag{15}$$

Since ($I_{Lm,max} - nI_{Lk,max}$) is a constant value, the input current ripple is also eliminated with the condition of (11). Therefore, the input current i_{in} in Mode 2 is only determined by

$$i_{in}(t) = I_{Lm,\max} - nI_{Lk,\max} \tag{16}$$

From Figures 4 and 5a, the value of Δi_{Lm} can be obtained as follows:

$$\Delta i_{Lm} = I_{Lm,\max} - I_{Lm,\min} = \frac{V_{in}}{L_m}DT_S \tag{17}$$

From (7), (8), and Figure 4, the maximum value $I_{Lk,max}$ can be derived as follows:

$$I_{Lk,\max} = \frac{(1-\mathrm{n})V_{in}}{2L_k}DT_S \tag{18}$$

Combining (11), (17), and (18), $I_{Lk,max}$ can be further expressed by

$$I_{Lk,\max} = \frac{1}{2n}\frac{V_{in}}{L_m}DT_S = \frac{1}{2n}(I_{Lm,\max} - I_{Lm,\min}) \tag{19}$$

From (19), it can be concluded that

$$i_{in}(t) = I_{Lm,\min} + nI_{Lk,\max} = I_{Lm,\max} - nI_{Lk,\max} \tag{20}$$

Consequently, the input current i_{in} is a constant value during the whole switching period with the condition of (11).

3.3. Voltage Stress Analysis

Referring to the circuit diagrams shown in Figure 5 and according to Kirchhoff's voltage law, the following voltage relationships can be obtained:

$$\begin{cases} V_{DS} = V_{D1} = V_{C1} \\ V_{D2} = V_{D4} = V_{C4} \\ V_{D3} = V_{C3} \\ V_{D5} = V_{C5} - V_{C2} \\ V_{D6} = V_{C6} - V_{C1} \\ V_{D7} = V_{C7} - V_{C4} - V_{C6} \end{cases} \tag{21}$$

where V_{DS} and V_{D1}~V_{D7} are the voltage stresses of the switch S and the diodes D_1~D_7, respectively.

From (4), the simplified voltage stress relationship is given as follows:

$$V_{DS} = V_{D1} = V_{D2} = V_{D3} = V_{D4} = V_{D5} = V_{D6} = V_{D7} = \frac{V_{in}}{1-D} \tag{22}$$

Therefore, all the diodes and the switch have the same voltage stress which means the same type of diodes can be selected. Due to the relatively low voltage stress, the components with a lower-rated voltage and a lower on-resistance can be used to further reduce the power losses and costs.

3.4. Real-Gain Analysis

In fact, all the active and passive components contain some non-idealities in practice that influence the voltage gain and efficiency of high-gain dc/dc converters. Figure 8 shows the equivalent circuits of the proposed topology considering all the non-idealities in the two operating modes. In Figure 8, R_{Lp} and R_{Ls} are the equivalent series resistance (ESR) of the primary and secondary sides of the coupled inductor, respectively, R_{C0}–R_{C7} are the ESRs of capacitors, R_{D1}–R_{D7} are the forward diode resistances of diodes, V_{d1}–V_{d7} are the forward voltage drops of diodes, and R_S is the on-state resistance of the switch.

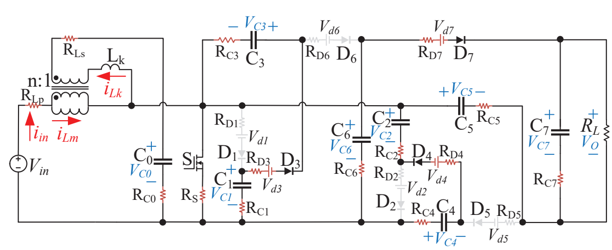

(**a**)

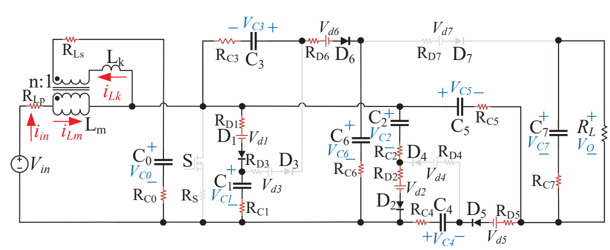

(**b**)

Figure 8. The equivalent circuits considering all the non-idealities: (**a**) Mode 1; (**b**) Mode 2.

Referring to Figure 8a, when the switch is turned on, the following equations can be obtained according to Kirchhoff's voltage law.

$$\begin{cases} v_{\mathrm{Lm}(on)} + i_{in}R_{Lp} = V_{in} \\ V_{C3} = V_{C1} - i_S R_S - i_{D3}(R_{C1} + R_{C3} + R_{D3}) - V_{d3} \\ V_{C4} = V_{C2} - i_S R_S - i_{D4}(R_{C2} + R_{C4} + R_{D4}) - V_{d4} \\ V_{C7} = V_{C5} + V_{C6} - i_S R_S - i_{D7}(R_{C5} + R_{C6} + R_{C7} + R_{D7}) - V_{d7} \end{cases} \tag{23}$$

Similarly, from Figure 8b, the voltage relationship of each loop can be expressed as follows when the switch is turned off.

$$\begin{cases} V_{C1} = V_{in} - v_{Lm(off)} - i_{in}R_{Lp} - i_{D1}(R_{C1} + R_{D1}) - V_{d1} \\ V_{C2} = V_{in} - v_{Lm(off)} - i_{in}R_{Lp} - i_{D2}(R_{C2} + R_{D2}) - V_{d2} \\ V_{C5} = V_{in} - v_{Lm(off)} + V_{C4} - i_{in}R_{Lp} - i_{D5}(R_{C4} + R_{C5} + R_{D5}) - V_{d5} \\ V_{C6} = V_{in} - v_{Lm(off)} + V_{C3} - i_{in}R_{Lp} - i_{D6}(R_{C3} + R_{C6} + R_{D6}) - V_{d6} \\ V_O = V_{C7} - i_O R_{C7} \end{cases} \tag{24}$$

By applying the volt-second balance principle to the magnetic inductor L_m, the real-gain of the proposed converter can be deduced and is given below after simplification.

$$V_O = \frac{1}{H} \cdot \left[V_{in} - \frac{1-D}{4}(V_{d1} + V_{d2} + V_{d3} + V_{d4} + V_{d5} + V_{d6} + V_{d7}) \right] \tag{25}$$

where the parameter H is defined as follows:

$$H = \frac{1-D}{4} + \frac{4R_{Lp}}{(1-D)R_L} + \frac{(3+D)R_S}{4R_L} + \frac{1-D}{4R_L} \cdot \begin{bmatrix} (R_{D1} + R_{D2} + R_{D3} + R_{D4} + R_{D5} + R_{D6} + R_{D7}) + \\ 2(R_{C1} + R_{C2} + R_{C3} + R_{C4} + R_{C5} + R_{C6} + R_{C7}) \end{bmatrix} \tag{26}$$

3.5. Losses Analysis

The power losses of the proposed converter are caused by diodes, capacitors, the switch, and the coupled inductor.

In the diodes D_1-D_7, the forward voltage drop and forward resistance are the reasons for the power loss $P_{D,}$ and it can be derived as follows:

$$P_D = V_d I_D + R_D {I_D}^2 \tag{27}$$

where V_d, R_D, and I_D are the forward voltage drop, the forward resistance, and the average current of the diodes, respectively.

As for capacitors C_0–C_7, the power loss P_C caused by the ESR can be calculated by

$$P_C = \frac{f_S \cdot C \cdot \Delta U^2}{2} \tag{28}$$

where C and ΔU represent the capacitance and voltage ripple of the capacitor, respectively.

As for switch S, the power losses comprise conduction loss $P_{S\text{-}C}$ and switching loss $P_{S\text{-}S}$. The on-resistance is the reason for the conduction loss of a switch. By defining the on-resistance and rms current of the switch as R_{DSon} and I_S, respectively, the conduction loss $P_{S\text{-}C}$ can be obtained as follows:

$$P_{S\_C} = {I_S}^2 R_{DSon} \tag{29}$$

The switching loss $P_{S\text{-}S}$ can be estimated by linearizing the voltage and current of the switch during the turn-on and turn-off processes as follows:

$$\begin{cases} P_{S\_S_{ON}} = V_{DS} \cdot I_{on} \cdot t_{ondelay} \cdot f_S/6 \\ P_{S\_S_{OFF}} = V_{DS} \cdot I_{off} \cdot t_{offdelay} \cdot f_S/6 \end{cases} \tag{30}$$

where I_{on} and I_{off} are the turn-on and turn-off currents, and $t_{ondelay}$ and $t_{offdelay}$ are the turn-on and turn-off time delays.

As for the coupled inductor, the power losses are mainly composed of copper loss $P_{L\text{-}copper}$ and core loss $P_{L\text{-}core}$. According to [34], the theoretical estimation formula of copper loss can be obtained as follows:

$$P_{L\_copper} = {I_L}^2 r_L \tag{31}$$

where I_L and r_L represent the rms current and the ESR of the coupled inductor, respectively.

The core loss can be calculated by

$$P_{L\_core} = K_{Fe} \cdot V_e \cdot f_S \cdot \left(\frac{\Delta B}{2}\right)^{\alpha} \tag{32}$$

where K_{Fe} and α are constants determined by the core material, V_e is the volume of the core, and ΔB is decided by the current ripple of the coupled inductor.

The total power loss of the proposed converter can be obtained as follows:

$$P_{total} = P_D + P_C + P_{S\_C} + P_{S\_S_{ON}} + P_{S\_S_{OFF}} + P_{\mathrm{L\_copper}} + P_{\mathrm{L\_core}} \tag{33}$$

In order to exhibit the losses distribution of the proposed converter intuitively, the losses of each component at 240 W are calculated through (27)–(32) and shown graphically in Figure 9. It can be seen that most of the total power loss occurs in the diodes, which is mainly caused by the large output current. However, the conduction loss of the switch is significantly reduced due to the use of a single switch compared with other multi-switch high-gain converters.

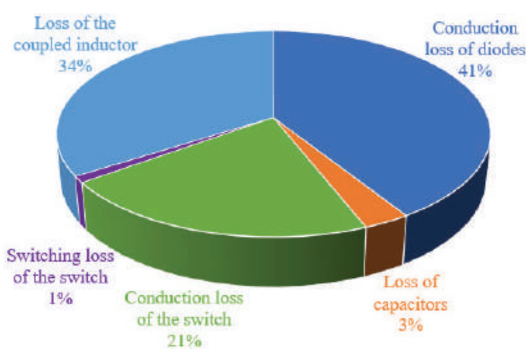

Figure 9. Loss distribution of the proposed converter.

4. Performance Comparisons

The performance indexes of relevant high-gain dc/dc converters are summarized in Table 1, including the number of switches, voltage gain, voltage stress of switches and diodes, total standing voltage (TSV), and input current ripple. According to [35], the total voltage rating of switching power devices can be reflected by TSV which is defined as

$$TSV = \frac{\sum_{i=1}^{n} V_{Sn} + \sum_{j=1}^{m} V_{Dj}}{V_o} \tag{34}$$

where V_{Sn} and V_{Dj} represent the voltage stress of each switch and diode, respectively.

Table 1. Comparisons among different converters.

Parameters	[24]	[25]	[26]	[32]	Proposed
Number of switches	1	1	3	2	1
Voltage gain	$\frac{3D}{1-D}$	$\frac{3+D}{2(1-D)}$	$\frac{1+D}{1-D}$	$\frac{D(1+D)}{(1-D)^2}$	$\frac{4}{1-D}$
Voltage stress of switches	$\frac{V_O}{3D}$	$\frac{2V_O}{3+D}$	$\frac{V_O}{3(1+D)}$	$\frac{V_O}{1+D}$, $\frac{(1-D)V_O}{D(1+D)}$	$\frac{V_O}{4}$
Voltage stress of diodes	$\frac{V_O}{3D}$	$\frac{V_O}{3+D}$, $\frac{2V_O}{3+D}$	$\frac{V_O}{3(1+D)}$	$\frac{V_O}{1+D}$, $\frac{(1-D)V_O}{D(1+D)}$	$\frac{V_O}{4}$
TSV	$\frac{4}{3D}$	$\frac{8}{3+D}$	$\frac{3}{1+D}$	$\frac{2+D}{D(1+D)}$	2
Input current ripple	Low	High	High	Low	Zero

Figure 10 gives the comparison curves of different converters in Table 1. From Figure 10a, the proposed converter has the highest voltage-boosting capability compared to other converters in the optimal duty cycle range. From Table 1, the switches and diodes of all the converters have the same maximum voltage stress. Thus, the maximum voltage stress curve of switches and diodes is plotted in Figure 10b. The voltage stress in the proposed converter is lower than other converters except for the converter in [26]. Although the voltage stress in [26] is lower when the duty cycle is greater than 1/3, its voltage gain is much lower than that in the proposed converter. Similarly, Figure 10c shows that the proposed converter has the lowest TSV when the duty cycle is smaller than 0.5. The TSV in [26] is lower than that in this paper when the duty cycle is greater than 0.5; however, its voltage gain is also much lower. It can be deduced from Table 1 and Figure 10 that the proposed converter has a high voltage gain and a low voltage stress. That is to say, the active power devices with low withstand voltage can be selected.

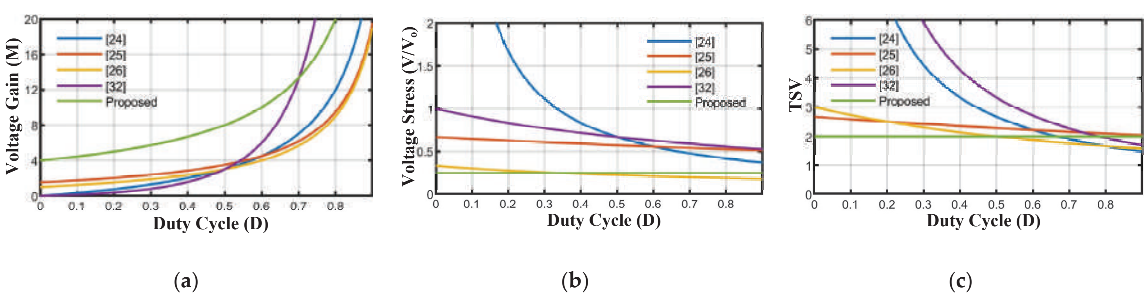

Figure 10. Comparative results of the converters versus the duty cycle D: (**a**) Voltage gain; (**b**) Voltage stress of switches and diodes; (**c**) TSV.

Moreover, from Table 1, the number of switches used in [24,25] and the proposed converter is the smallest. The proposed converter uses only one switch which can significantly simplify the control strategy. Meanwhile, the proposed converter has the lowest input current ripple, and it achieves a ripple-free input current condition which is of great importance in offshore wind energy systems. Owing to the ripple-free input current, the HVDC transmission will be more stable. Consequently, the proposed converter is well suited for offshore wind farms due to the above-mentioned superiorities.

5. Design Guideline

5.1. Design of the Coupled Inductor

To achieve ripple-free conditions, the converter should operate in CCM mode which means the current i_L must be continuous. Thus, combining the current waveform in Figure 4 and (13), the minimum value $I_{Lm,min}$ should be greater than zero. Equation (13) can also be written as follows:

$$I_{Lm,\min} = I_{Lm}(1 + \frac{\lambda}{2}) - \frac{V_{C1} - V_{in}}{L_m}(1 - D)T_S \tag{35}$$

where λ is the ripple rate of the current i_{Lm}.

Since the average current I_{Lk} is zero, the average current on the primary side of the coupled inductor is also zero. The average current I_{Lm} can be expressed by

$$I_{Lm} = I_{in} \tag{36}$$

Combining (4), (35), and (36), the minimum value of L_m can be obtained below:

$$L_{m,\min} = \frac{2V_{in}T_S D}{(2 + \lambda)I_{in}} \tag{37}$$

Therefore, to ensure that the circuit operates under CCM mode, L_m should be selected with the following condition:

$$L_m > L_{m,\min} \tag{38}$$

When the value of L_m is determined, L_k can be determined by (11).

5.2. Design of Capacitors

In mode 1, the current flowing through C_0 is i_{Lk}. The currents flowing through C_3, C_4, and C_7 are i_{D3}, i_{D4}, and i_{D7}, respectively. Assuming that the capacitor voltage ripple rate is x_c%, the minimum values of the capacitors C_3, C_4, and C_7 can be obtained from the capacitor's characteristic equation as follows:

$$C_{n\min} = \int_0^{DT_S} \frac{i_{Dn}}{x_c\%V_{Cn}} dt \tag{39}$$

and C_{0min} can be expressed by

$$C_{0\min} = \int_0^{DT_S} \frac{i_{Lk}}{x_c\%V_{C0}} dt \tag{40}$$

Similarly, in mode 2, the currents flowing through C_1, C_2, C_5, and C_6 are i_{D1}, i_{D2}, i_{D5}, and i_{D6}, respectively. Thus, the minimum values of the capacitors C_1, C_2, C_5, and C_6 can be obtained as follows:

$$C_{n\min} = \int_{DT_S}^{T_S} \frac{i_{Dn}}{x_c\%V_{Cn}} dt \tag{41}$$

5.3. Selection of Switch and Diodes

For switch S and diodes D_1-D_7, according to the voltage stress relationship obtained from (22) and considering an appropriate margin, the maximum withstand voltage value is given below:

$$V_{DS} = V_{D1} = V_{D2} = V_{D3} = V_{D4} = V_{D5} = V_{D6} = V_{D7} = \frac{k_V V_{in}}{1 - D} \tag{42}$$

where k_V represents the voltage margin factor.

6. Experimental Results

To verify the validity and feasibility of the proposed topology, a 240 W laboratory prototype converter at 35 kHz switching frequency was designed. Detailed parameters and selected components are given in Table 2. Since the experimental leakage inductance of the coupled inductor was about 2 uH, an auxiliary inductor was connected in series with the secondary side of the coupled inductor to meet the requirements. The main voltage and current experimental waveforms of the converter are shown in Figure 11.

Table 2. Parameters of the converter.

Parameters	Value/Model
Input voltage V_{in}/V	40
Output voltage V_O/V	308
Switching frequency f_S/kHz	35
Magnetic inductor L_m/uH	250
Leakage inductance L_k/uH	62.5
Turn ratio n	1:2
Capacitor C_0/uF	330
Diodes D_1–D_7	MBR10200CT
Switch	IRFP260NPBF

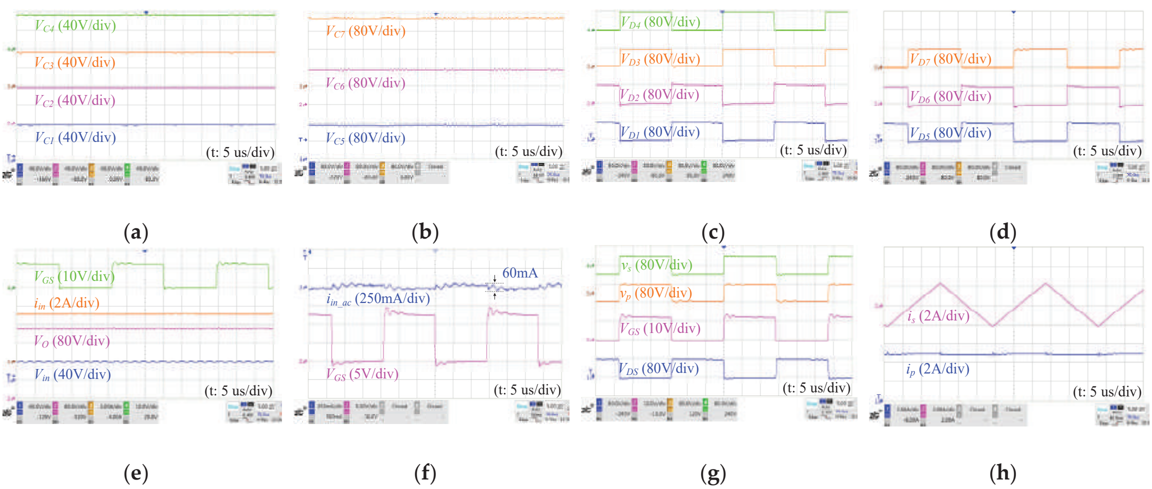

Figure 11. Experimental waveforms of the prototype: (**a**) V_{C1}, V_{C2}, V_{C3}, and V_{C4}; (**b**) V_{C5}, V_{C6}, and V_{C7}; (**c**) V_{D1}, V_{D2}, V_{D3}, and V_{D4}; (**d**) V_{D5}, V_{D6}, and V_{D7}; (**e**) V_{in}, V_O, i_{in}, and V_{GS}; (**f**) $i_{in\text{-}ac}$, and V_{GS}; (**g**) V_S, V_{GS}, v_p, and v_s; (**h**) i_p and i_s.

From Figure 11a, V_{C1}–V_{C4} reach nearly 80 V. Due to the R_{DSon} of the switch and the forward voltage drop of the diodes, V_{C1}–V_{C4} are slightly lower than the theoretical values. From Figure 11b, V_{C5} and V_{C6} reach nearly 160 V, and V_{C7} reaches nearly 320 V. Due to the loss of devices on different loops, V_{C5}–V_{C7} are also slightly lower than the theoretical values.

From Figure 11c,d, the voltage stresses on the diodes D_1–D_7 are about 80 V which is consistent with the theoretical analysis. Figure 11e shows that the output voltage reaches up to 308 V under 40 V input voltage. Hence, the experimental results verify that the proposed converter has the characteristic of high voltage gain. According to the theoretical calculation, the output voltage should have been 320 V under ideal conditions. The difference between experimental results and ideal conditions is caused by the non-idealities in the circuit. As can be seen from the waveform of i_{in} in Figure 11e, the input current i_{in} is constant. The ac component of i_{in} shown in Figure 11f is about 60 mA. The ripple rate of i_{in} is only 1.1%, thus the proposed converter provides a ripple-free input current through the aforementioned parameter design. From Figure 11g, the voltages at both ends of the primary and secondary sides of the coupled inductor change at the same time and have the same value. Figure 11h shows the currents of the coupled inductor, where i_p and i_s represent the current on the primary and secondary sides of the coupled inductor, respectively. Also, the voltage and current waveforms of the coupled inductor in Figure 11g,h are consistent with the theoretical waveforms in Figure 4.

In summary, the experimental results verify the validity and feasibility of the proposed converter. Some deviations from the theoretical analysis are inevitable. The proposed converter exhibits an efficiency of 93.7% at a 240 W load. Figure 12 shows the measured efficiency curve of the proposed converter under different loads and the maximum efficiency is 94.5%. Figure 13 shows the photograph of the experimental prototype.

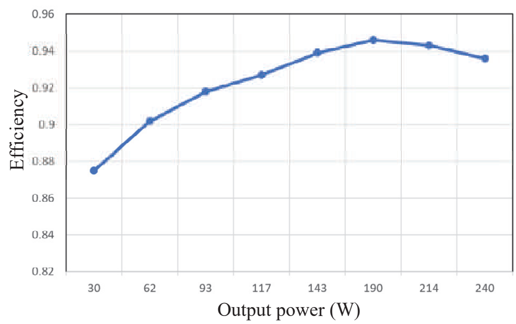

Figure 12. Measured efficiency of the proposed converter.

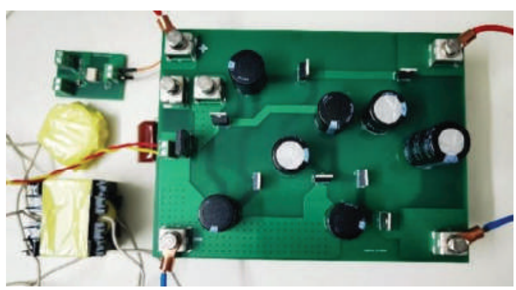

Figure 13. Photograph of the experimental prototype.

7. Conclusions

Aiming at the MVDC system in offshore wind farms, a novel single-switch high-gain dc/dc converter with a ripple-free input current is proposed in this paper. Since the converter uses only one switch, the control strategy is not complicated which is beneficial for the stability of offshore wind energy systems. The converter provides a high voltage gain through a switched-capacitor structure. Additionally, the converter provides a ripple-free input current by utilizing a coupled inductor which can avoid the use of a large electrolytic capacitor. Hence, the volume and weight of the converter are reduced. Moreover, the output capacitor is charged and discharged continuously by a 180° phase shift to eliminate output voltage ripple which can further improve the stability of the systems. The steady-state characteristic under CCM of the converter is analyzed. Comparisons of the proposed converter with its counterparts show various beneficial characteristics as follows: (1) high voltage gain; (2) ripple-free input current; (3) simple control strategy; (4) low voltage stress on devices; and (5) high efficiency. Finally, to verify the validity and feasibility of the proposed converter, a laboratory prototype has been built for a power of 240 W, input and output voltages of 40 and 308 V, respectively, and a switching frequency of 35 kHz. The input current ripple is only 1.1% and the maximum efficiency is measured to be 94.5%.

Experimental results confirm that the proposed converter is well suited for high-gain offshore wind energy applications.

Author Contributions: Conceptualization, R.T. and J.Y.; methodology, R.T. and Z.L.; software, Z.H.; validation, Z.L. and J.L.; formal analysis, Z.L.; investigation, R.A.; resources, R.A.; data curation, Z.H.; writing—original draft preparation, R.T. and Z.L.; writing—review and editing, J.L. and J.Y.; project administration, J.L. All authors have read and agreed to the published version of the manuscript.

Funding: This research was supported by the Open Fund of Guangdong Key Laboratory of New Technology for Smart Grid under GDDKY2021KF02.

Institutional Review Board Statement: Not applicable.

Informed Consent Statement: Not applicable.

Data Availability Statement: Not applicable.

Conflicts of Interest: The authors declare no conflict of interest.

References

1. Fjellstedt, C.; Ullah, M.I.; Forslund, J.; Jonasson, E.; Temiz, I.; Thomas, K. A Review of AC and DC Collection Grids for Offshore Renewable Energy with a Qualitative Evaluation for Marine Energy Resources. *Energies* **2022**, *15*, 5816. [CrossRef]
2. Lam, J.; Jain, P.K. A High Efficient Medium Voltage Step-up DC/DC Converter with Zero Voltage Switching (ZVS) and Low Voltage Stress for Offshore Wind Energy Systems. In Proceedings of the 2014 16th European Conference on Power Electronics and Applications, Lappeenranta, Finland, 26–28 August 2014; IEEE: Piscataway, NJ, USA, 2014; pp. 1–10.
3. Lee, Y.; Vakil, G.; Feldman, R.; Watson, A.J.; Wheeler, P.W. A High-Power DC-DC Converter Based Dual Active Bridge for MVDC Grids on Offshore Wind Farms. In Proceedings of the 2016 18th European Conference on Power Electronics and Applications (EPE'16 ECCE Europe), Karlsruhe, Germany, 5–9 September 2016; IEEE: Piscataway, NJ, USA, 2016; pp. 1–10.
4. Abeynayake, G.; Van Acker, T.; Hertem, D.V.; Liang, J. Analytical Model for Availability Assessment of Large-Scale Offshore Wind Farms Including Their Collector System. *IEEE Trans. Sustain. Energy* **2021**, *12*, 1974–1983. [CrossRef]
5. Basbas, H.; Liu, Y.-C.; Laghrouche, S.; Hilairet, M.; Plestan, F. Review on Floating Offshore Wind Turbine Models for Nonlinear Control Design. *Energies* **2022**, *15*, 5477. [CrossRef]
6. Wang, B.; Tian, M.; Lin, T.; Hu, Y. Distributed Complementary Control Research of Wind Turbines in Two Offshore Wind Farms. *Sustainability* **2018**, *10*, 553. [CrossRef]
7. Vagiona, D.; Kamilakis, M. Sustainable Site Selection for Offshore Wind Farms in the South Aegean—Greece. *Sustainability* **2018**, *10*, 749. [CrossRef]
8. Torres, J.P.N.; De Jesus, A.S.; Marques Lameirinhas, R.A. How to Improve an Offshore Wind Station. *Energies* **2022**, *15*, 4873. [CrossRef]
9. Bernal-Camacho, D.F.; Fontes, J.V.H.; Mendoza, E. A Technical Assessment of Offshore Wind Energy in Mexico: A Case Study in Tehuantepec Gulf. *Energies* **2022**, *15*, 4367. [CrossRef]
10. Rong, F.; Wu, G.; Li, X.; Huang, S.; Zhou, B. ALL-DC Offshore Wind Farm With Series-Connected Wind Turbines to Overcome Unequal Wind Speeds. *IEEE Trans. Power Electron.* **2019**, *34*, 1370–1381. [CrossRef]
11. Bahmani, M.A.; Thiringer, T.; Rabiei, A.; Abdulahovic, T. Comparative Study of a Multi-MW High-Power Density DC Transformer with an Optimized High-Frequency Magnetics in All-DC Offshore Wind Farm. *IEEE Trans. Power Delivery* **2016**, *31*, 857–866. [CrossRef]
12. Hu, P.; Yin, R.; Wei, B.; Luo, Y.; Blaabjerg, F. Modular Isolated LLC DC/DC Conversion System for Offshore Wind Farm Collection and Integration. *IEEE J. Emerg. Sel. Top. Power Electron.* **2021**, *9*, 6713–6725. [CrossRef]
13. Herrera, D.; Tricarico, T.; Oliveira, D.; Aredes, M.; Galván-Díez, E.; Carrasco, J.M. Advanced Local Grid Control System for Offshore Wind Turbines with the Diode-Based Rectifier HVDC Link Implemented in a True Scalable Test Bench. *Energies* **2022**, *15*, 5826. [CrossRef]
14. Xie, L.; Cheng, F.; Wu, J. Control Strategy for Offshore Wind Farms with DC Collection System Based on Series-Connected Diode Rectifier. *Sustainability* **2022**, *14*, 7860. [CrossRef]
15. Liu, H.; Dahidah, M.; Naayagi, R.T.; Armstrong, M.; Yu, J. Unidirectional DC/DC Modular Multilevel Converter for Offshore Windfarm with the Control Strategy Based on Stationary Frame. *J. Eng.* **2019**, *2019*, 4309–4314. [CrossRef]
16. Liu, J.; Li, B.; Li, L.; Liu, X.; Wu, J.; Xu, D.; Wei, T.; Li, W. A High Step-up Ratio DC-DC Converter with Fault Blocking Capability for Offshore Wind Farms. In Proceedings of the 2021 IEEE 12th Energy Conversion Congress & Exposition-Asia (ECCE-Asia), Singapore, 24 May 2021; IEEE: Singapore, 2021; pp. 702–707.
17. Dincan, C.; Kjaer, P.; Chen, Y.; Munk-Nielsen, S.; Bak, C.L. Analysis of a High-Power, Resonant DC–DC Converter for DC Wind Turbines. *IEEE Trans. Power Electron.* **2018**, *33*, 7438–7454. [CrossRef]
18. Zhao, X.; Li, B.; Zhang, B.; Xu, D. A High-Power Step-Up DC/DC Converter Dedicated to DC Offshore Wind Farms. *IEEE Trans. Power Electron.* **2022**, *37*, 65–69. [CrossRef]

19. Deng, F.; Chen, Z. Control of Improved Full-Bridge Three-Level DC/DC Converter for Wind Turbines in a DC Grid. *IEEE Trans. Power Electron.* **2013**, *28*, 314–324. [CrossRef]
20. Chen, W.; Huang, A.; Lukic, S.; Svensson, J.; Li, J.; Wang, Z. A Comparison of Medium Voltage High Power DC/DC Converters with High Step-up Conversion Ratio for Offshore Wind Energy Systems. In Proceedings of the 2011 IEEE Energy Conversion Congress and Exposition, Phoenix, AZ, USA, 17–22 September 2011; IEEE: Piscataway, NJ, USA, 2011; pp. 584–589.
21. Liu, H.; Dahidah, M.S.A.; Yu, J.; Naayagi, R.T.; Armstrong, M. Design and Control of Unidirectional DC–DC Modular Multilevel Converter for Offshore DC Collection Point: Theoretical Analysis and Experimental Validation. *IEEE Trans. Power Electron.* **2019**, *34*, 5191–5208. [CrossRef]
22. Denniston, N.; Massoud, A.M.; Ahmed, S.; Enjeti, P.N. Multiple-Module High-Gain High-Voltage DC–DC Transformers for Offshore Wind Energy Systems. *IEEE Trans. Ind. Electron.* **2011**, *58*, 1877–1886. [CrossRef]
23. Parastar, A.; Seok, J.-K. High-Gain Resonant Switched-Capacitor Cell-Based DC/DC Converter for Offshore Wind Energy Systems. *IEEE Trans. Power Electron.* **2015**, *30*, 644–656. [CrossRef]
24. Banaei, M.R.; Sani, S.G. Analysis and Implementation of a New SEPIC-Based Single-Switch Buck–Boost DC–DC Converter With Continuous Input Current. *IEEE Trans. Power Electron.* **2018**, *33*, 10317–10325. [CrossRef]
25. Saravanan, S.; Babu, N.R. Design and Development of Single Switch High Step-Up DC–DC Converter. *IEEE J. Emerg. Sel. Topics Power Electron.* **2018**, *6*, 855–863. [CrossRef]
26. Gandomkar, A.; Parastar, A.; Seok, J.-K. High-Power Multilevel Step-Up DC/DC Converter for Offshore Wind Energy Systems. *IEEE Trans. Ind. Electron.* **2016**, *63*, 7574–7585. [CrossRef]
27. Hu, Y.; Zeng, R.; Cao, W.; Zhang, J.; Finney, S.J. Design of a Modular, High Step-Up Ratio DC–DC Converter for HVDC Applications Integrating Offshore Wind Power. *IEEE Trans. Ind. Electron.* **2016**, *63*, 2190–2202. [CrossRef]
28. Abbasi, M.; Lam, J. A Step-Up Transformerless, ZV–ZCS High-Gain DC/DC Converter With Output Voltage Regulation Using Modular Step-Up Resonant Cells for DC Grid in Wind Systems. *IEEE J. Emerg. Sel. Topics Power Electron.* **2017**, *5*, 1102–1121. [CrossRef]
29. Parastar, A.; Kang, Y.C.; Seok, J.-K. Multilevel Modular DC/DC Power Converter for High-Voltage DC-Connected Offshore Wind Energy Applications. *IEEE Trans. Ind. Electron.* **2015**, *62*, 2879–2890. [CrossRef]
30. Yin, R.; Shi, M.; Hu, W.; Guo, J.; Hu, P.; Wang, Y. An Accelerated Model of Modular Isolated DC/DC Converter Used in Offshore DC Wind Farm. *IEEE Trans. Power Electron.* **2019**, *34*, 3150–3163. [CrossRef]
31. Zhang, J.; Sha, D.; Ma, P. A Dual Active Bridge DC–DC-Based Single Stage AC–DC Converter With Seamless Mode Transition and High Power Factor. *IEEE Trans. Ind. Electron.* **2022**, *69*, 1411–1421. [CrossRef]
32. García-Vite, P.M.; Rosas-Caro, J.C.; Martínez-Salazar, A.L.; Chavez, J.d.J.; Valderrábano-González, A.; Sánchez-Huerta, V.M. Quadratic Buck–Boost Converter with Reduced Input Current Ripple and Wide Conversion Range. *IET Power Electron.* **2019**, *12*, 3977–3986. [CrossRef]
33. Do, H.-L. Improved ZVS DC-DC Converter With a High Voltage Gain and a Ripple-Free Input Current. *IEEE Trans. Circuits Syst. I* **2012**, *59*, 846–853. [CrossRef]
34. Yang, N.; Zeng, J.; Hu, R.; Liu, J. Analysis and Design of an Isolated High Step-Up Converter Without Voltage-Drop. *IEEE Trans. Power Electron.* **2022**, *37*, 6939–6950. [CrossRef]
35. Liu, J.; Lin, W.; Wu, J.; Zeng, J. A Novel Nine-Level Quadruple Boost Inverter With Inductive-Load Ability. *IEEE Trans. Power Electron.* **2019**, *34*, 4014–4018. [CrossRef]

World Electric Vehicle Journal

Article

How to Cross the Chasm for the Electric Vehicle World's Laggards—A Case Study in Kuwait

Andri Ottesen [1,*], Sumayya Banna [2] and Basil Alzougool [2]

1 LSE Middle East Centre (MEC)—Sustainability Research and Consultancy (CSRC), Australian University (AU), West Mishref P.O. Box 1411, Kuwait
2 LSE Middle East Centre (MEC), Arab Open University (AOU), Ardiya P.O. Box 830, Kuwait
* Correspondence: a.ottesen@au.edu.kw

Abstract: Ever since the discovery of oil in 1938, the State of Kuwait has increasingly sought out international brands in the car market due to the high purchasing power of Kuwaiti nationals. However, the makers of electric vehicles (EVs) have not been able to penetrate this market, with the exception of innovators and early adopters. The phenomenon in disruptive innovation theory—called "Crossing the Chasm"—regarding a mass market appeal has not yet occurred in Kuwait. Through deep interviews with 12 Kuwaiti owners of EVs and automotive dealers who sold either EVs or Hybrid Electric Vehicles (HEVs), 10 key reasons for this phenomenon have been previously revealed, which were used to develop an extensive questionnaire. A total of 472 car drivers aged from 18 to 30, identified as the "early majority", completed the questionnaire to achieve the objective of identifying the factors required to create a mass market for EVs in Kuwait. The results demonstrated that potential customers highly preferred three different types of attributes of EVs: environmental, financial, and technological. There were significant differences in the identified attributes preferred by Kuwaiti individuals for EVs in terms of the number of cars owned and the sector of employment. Moreover, the results of our study indicate that potential customers are very willing to buy EVs in the future, considering both their financial and infrastructure attributes. There were further significant differences in the identified necessary conditions to buy EVs in terms of educational level and monthly income. This study discusses a variety of valuable promotional tactics, which may be implemented in conjunction with public incentives and policy changes in the State of Kuwait. This information is considered useful for marketers and designers who wish to tap into this lucrative market, which is significantly different from that in the global North.

Keywords: electric vehicles; disruptive innovation; customer preferences; emerging market; Kuwait; EV infrastructure

Citation: Ottesen, A.; Banna, S.; Alzougool, B. How to Cross the Chasm for the Electric Vehicle World's Laggards—A Case Study in Kuwait. *World Electr. Veh. J.* **2023**, *14*, 45. https://doi.org/10.3390/wevj14020045

Academic Editors: Wenbin Yu and Guang Zeng

Received: 23 December 2022
Revised: 30 January 2023
Accepted: 6 February 2023
Published: 8 February 2023

1. Introduction

This paper is the fifth published paper stemming from the project called "Breaking the Internal Combustion Engine Reign: A Mixed-Methods Study of Attitudes Towards Using and Purchasing Electric Vehicles in Kuwait," funded by the Kuwait Foundation for Scientific Advancement (KFAS) and managed by the Middle East Center of the London School of Economics. The project is complementary to the research of the KFAS on infrastructure and top-down policy, as well as research conducted by the National Laboratory of the Kuwaiti Institute for Scientific Research (KISR), mainly focused on EV batteries and their charging capacity under extreme heat conditions. This study, on the other hand, follows a bottom-up approach to capture customer preferences and attitudes towards EVs through the use of information gained from deep interviews with existing owners and automotive dealers in order to develop an extensive questionnaire, which we issued to potential consumers. The final outcome of this study is a series of suggestions for national and local governments, service providers, and automobile dealers that wish to break into this market, of which policies, practices, procedures, and infrastructural and automobile design are likely to yield the biggest impact, in terms of making EVs appealing to mainstream automobile consumers [1–4].

The concept of sustainable mobility is changing for the better. EV sales are expected to increase dramatically in the coming years; in particular, EV sales have been predicted to rise from 2.7% at present to 58% by 2040 [5]. Accordingly, European Economic Area (EEA) countries are seeking to ban the sales of all fossil-fueled cars by 2040 in order to achieve net-zero emissions by 2050 and have stated their apparent intentions to halt investing in new ICE platforms and models to end ICE vehicle production [6,7]. Hence, major car manufacturers have agreed to stop producing new ICE cars by 2040. For instance, some developed countries—namely, Norway, Iceland, and the Netherlands—are at the forefront of this transition, with up to 20% of their car fleet being fully or partially electric [8]. On the other hand, some developing countries—particularly those such as Kuwait—are considered to be the world's laggards regarding EV adoption, with less than 1/1000th of the world's average [3]. Consumer mindsets have also shifted toward sustainable mobility [9]. Consequently, the EV landscape in Kuwait needs to be examined and inspected, particularly from the perspective of consumer behaviors.

The concepts of consumer behavior and awareness are changing as more consumers come to accept alternative and sustainable mobility modes [10]. Customer preferences have been studied by numerous researchers and marketers in order to support the strategic planning and decision-making of business managers [11,12]. The acknowledgment of customer preferences provides useful insights for serving and executing EV marketing campaigns, which might lead them to better design features that might be appealing to new EV customers in the target market. Consequently, this might enhance customer satisfaction and, hence, create an EV community beyond early adopters or early users of EVs.

Although researchers have begun to examine the EV landscape worldwide, very little research has examined this landscape in emerging markets such as that of Kuwait. Furthermore, limited research has considered conventional car drivers in this context. Therefore, the aim of this study was twofold:

(i) To identify the preferences of EV early majority/pragmatic consumers in Kuwait, as perceived by conventional ICE car drivers;
(ii) To examine the influence of several selected demographic variables on preferences of early majority/pragmatic consumers, which might sway them to switch over from ICE vehicles to EVs, thus creating a mass market for EVs in Kuwait.

The present study hence contributes to various existing bodies of literature: (i) Five types of attributes—financial/economic, technological, infrastructure, brand, and social/environmental attributes—are considered collectively and comprehensively within a single choice set for EVs. It is important to note that, while the attributes have been examined separately among existing studies, they have not been collectively considered previously; (ii) emphasis is placed on conventional car drivers, which has not been explored previously in the literature; and (iii) this study fills a gap in the existing literature by adding more significant knowledge on the EV phenomenon, in terms of preferences, along with consumer demographic background data obtained from a large-scale survey in Kuwait.

The burgeoning sustainable development needs to be accomplished through the use of green energy to protect human health and the environment, ensuring the target of zero CO_2 by 2050 for all countries [13–15]. Regarding sustainable consumption, the automotive industry has undergone a major transformation and is endeavoring to lessen the environmental damage (e.g., air pollution, carbon footprints, greenhouse gas emissions) caused by excessive oil consumption, which is expected to reach 100,600,000 barrels per day by the end of 2023, compared with 3,100,000 barrels in 2021 [16]. The industry is trying to rapidly increase the production investment into EVs, as well as shifting the consumer response in this regard.

2. Problem Statement and Significance: Highest EV Adopters vs. the Lowest Ones

Even though geographically different, Kuwait and Norway have many similarities in terms of their wealth accumulation, economy, and population. As of the end of 2022, Norway had a population of 5.5 million, whereas Kuwait had close to 4.3 million residents [17]. Both nations are heavily reliant on oil production for wealth generation, with Kuwait in 10th and Norway in 13th place, in terms of wealth derived from such production. Kuwait's crude oil reserves account for 6.1% of the world's reserves—the 6th highest in the world. Petroleum production accounts for over half of Kuwait's GDP, 92% of its export revenues, and 90% of its governmental income. In comparison, Norwegian oil reserves only account for 0.3% of world reserves, or only 18th in the world [18]. However, Norwegians have invested their proceeds from oil more prudently, as they have accumulated a 1.1 trillion-USD sovereign wealth fund, compared with the 0.8 trillion-USD sovereign fund in Kuwait. [19]. In terms of GDP per capita (adjusted for purchasing power), these countries are also similar, with Norway having USD 78,128 vs. USD 51,528 GDP per capita for Kuwait, according to IMF estimates for 2022 [20].

One of the reasons that Kuwait has a lower GDP per capita than Norway is because of the high number of relatively low-paid ex-pats living in Kuwait. Expats account for 70% of the population of Kuwait, of which one-fourth are low-paid domestic workers, which equates to one domestic worker for every two Kuwaiti citizens. Norway, on the other hand, has a very homogeneous population, with only 20% of the population being immigrants or first-generation. In Norway, half of the immigrants are now citizens—something that would be next to impossible in Kuwait [17]. When it comes to car ownership, the rate is 2.3 million in Kuwait vs. 3.4 million in Norway. The reason for this difference can mainly be explained in terms of restrictions on acquiring driving licenses for ex-pats, who only own about 500,000 cars [3]. Kuwaiti citizens are about six times more likely to have a car than the ex-pats living there. Surprisingly, the lower number of cars in Kuwait has not led to lower CO_2 emissions than Norway. Kuwait emits 21 tCO_2e/person, with transport being the third-highest greenhouse gas (GHG)-emitting sector. Ground transportation only accounts for 12% of the total release of GHGs. Although this percentage might appear low, in comparison to other sectors, one should keep in mind that the emissions per capita in Kuwait are ranked the second highest in the world (after Qatar) and are about three times higher than the average in the European Union. This ratio also holds with respect to oil-producing Norway, which emits approximately one-fifth of the per capita emissions of Kuwait (6.7 tCO_2e/person) [21].

One of the reasons for this stark difference is that Norway has already replaced 20% of its ground transportation fleet with Electric Vehicles (about 800,000 EVs), with plans for 100% replacement. As a result, Norway achieved a 3% permanent reduction in the country's release of GHGs [22]. As this transition has yet to take place in Kuwait and EVs on Kuwaiti streets, only account for a fraction of a percent (around 300 at the end of 2021 and 600 at the end of 2022), mass EV adoption offers a tremendous opportunity to lower GHG emissions in Kuwait. EVs, as a replacement for Internal Combustion Engine (ICE) cars, offer a viable solution to Kuwait's pledge to lower GHG emissions. This would allow progress to be made towards both the United Nations, through their Nationally Determined Contributions (NDCs), and for their own national vision for the State of Kuwait by 2035, especially towards achieving its sustainability goal number 13, which states that Kuwait must "Take urgent action to combat climate change and its impacts" [23].

In a recently published article by the authors, entitled "How to sell zero-emission vehicles when petrol is almost for free" [3], as well as in research conducted by the Kuwait Institute for Scientific Research (KISR) on EV battery performance in high-temperature environments [24,25], we can state the ten main reasons for the ultra-low EV adoption rate in Kuwait:

1. Absence of fast-charging and powerful EV public charging stations that rely on 300 kW Direct Current (DC to DC), which could charge the most popular large-battery EVs in Kuwait to an 80% charge in about 20 min [26].

2. The reluctance of Kuwaiti landlords (as ex-pats are not permitted to own real estate by law in the State of Kuwait) to allow ex-pat-owners of EVs to install fast-charging 11 kW EV amplifier wall-boxes in or around their rented apartments, which could reduce the charging-time from up to 48 h for the biggest batteries down to only 5–10 h.
3. The State of Kuwait subsidizes petrol for its residents and, as a result, has one of the world's lowest retail gasoline prices (at USD 0.34 per liter). In comparison, one liter of retail petrol costs just over USD 2 (almost six times more) in Norway [27].
4. Neither the State of Kuwait nor its municipalities offer financial incentives to buy or own EVs instead of ICE cars. In comparison, Norway offers a long list of incentives, including
    a. Import and value-added tax exceptions from the purchasing price;
    b. Road tax exceptions;
    c. Ferry and toll-road fee exceptions;
    d. Permission to drive EVs on designated fast lanes for buses;
    e. Free municipal parking.

These incentives make it both cheaper to buy and own EVs over ICE cars in Norway, whereas the opposite is true for purchasing EVs in Kuwait. Furthermore, when considering the potential depreciation in value when re-selling, maintenance costs, as well as low fuel costs due to subsidies, drivers in Kuwait still simply do not see any economic benefit to converting to EVs, mainly as the purchasing cost is about 20% higher than equivalent ICE cars [3].

5. The lack of an EV community and exposure, stemming from the low number of EVs on the streets, indicate that EVs have not yet "crossed the chasm" in Kuwait—a term used for a disruptive innovation in which a certain type of technology eventually takes over the existing one [28]. The main hurdle is when the market is dominated by an early niche market made up of "innovators and techies" on the one hand, along with "visionaries and early adopters," while the market has not yet reached the "early-majority or the pragmatists." The reasons for this inability to reach the mass market can be explained by the Technology Acceptance Model (TAM), which provides two explanations: "the lack of perceived usefulness" along with "the unease of use" [29]. Our study supports this theory, as the most commonly sold EV in 2021 in Kuwait was the Porsche Taycan EV for approximately USD 200,000. This was bought primarily as the third or fourth car by affluent Kuwaiti males in their fifties and sixties as a status symbol rather than as a primary mode of transport. According to a dealership interview, the benefit of ownership for buyers was not primarily environmental but rather to be significantly faster than supercars such as those of Ferrari, Lamborghini, and so on, as the gearless EV powertrain allows for acceleration which no ICE car can compete with [3].
6. Potential EV drivers have apprehension as to how many years the battery will last in the extreme heat of Kuwait, as many have witnessed their cell phones automatically shutting down outside or inside of a car due to heat exposure. Generally, there is an 8-year guarantee on the battery (or about 150,000 km driven). The average life of an ICE car is 12–13 years, about 5 years longer than the EV battery warranty lasts. As a new EV car battery in the ninth year might cost more than the market value of the car at that time, replacing the battery might not be deemed worth the money. Thus, the life of the battery might dictate the life of the car. With potentially 30–40% less lifetime, rapid depreciation might represent the highest cost of ownership to EV owners. Luckily, KISR—the National Laboratory of Kuwait—has researched this phenomenon and has and will continue to publish data that will hopefully appease the concerns of consumers regarding this issue.
7. The almost total lack of maintenance, due to EVs only having 20 moving parts vs. up to 2000 in ICE cars, can actually pose a problem. EV owners complain that because EVs do not need as much maintenance, dealerships are reluctant to build up technical capacity or parts inventories. For example, Tesla does not even have a dealership in

Kuwait, as all updates and inspections are conducted online. Such a lack of facilities has proven problematic in the case of accidents or other mishaps [3].

8. EV owners have pointed out that the ground clearance of the car is especially important for EVs in Kuwait (i.e., the distance from the lowest point of the car to the ground). High speedbumps in residential areas aiming to keep out low-riding power cars are a problem, as they may damage the battery at the bottom of the EV.
9. Some efforts have been made by municipalities, shopping centers, and transportation authorities to have designated parking spaces with or without charging facilities. However, as no penalty is typically levied on ICE car drivers—in contrast to those who park in handicapped parking spaces—virtually all EV owners we talked to complained that the designated parking was not respected as exclusive to EVs.
10. Although farfetched, there is a moderate to strong correlation when comparing the percentage of women in national congresses worldwide, and the percentage of EVs sold that year. For example, the national parliament in Norway is represented by 46% women, with 9 out of 19 ministers being women. The Kuwait parliament, on the other hand, only has 2 women out of 50 seats and 1 woman out of 12 ministers. Several studies conducted by the Organization for Economic Cooperation and Development (OECD), among others, have demonstrated that women in power demonstrate more environmental concern than their male counterparts. This ratio might explain, in part, why the State of Kuwait has been slower than Norway to provide a support system for EV adoption [4].

Our research did not indicate that the perceived safety of EVs was a problem for current EV owners or potential EV drivers in Kuwait, as EVs are generally viewed as safer than ICE cars. This notion corresponds to American safety data from 2021, which states that EVs are about 60 times less likely to catch fire than a combustion engine car [30]; or, as Ian Must worded it, "What part of combustion in an Internal combustion engine do you not understand" [31]. Neither was the price of electricity for charging the EV a problem, as this is also subsidized and only costs about KWD 0.009 (or about USD 0.03) per kWh for a home, amounting to about USD 15 per month for average EV use [32]. Finally, our interviewees were largely aware that, due to about 3-fold higher efficiency of EV engines over ICEs regarding the transformation of the energy from the tank/battery to the wheels, EVs are still significantly environmentally friendlier than ICE vehicles, even though electricity is made using natural gas in Kuwait and more CO_2 is emitted in the construction of an EV due to the size of its battery [33].

Whether one of these ten reasons for the low EV adoption rate is more prevalent than the other is not the focal point of this paper. Experience from the oil-producing country Norway clearly indicates that mass adoption of EVs is a viable option for lowering greenhouse gas emissions and is a worthwhile tool for the State of Kuwait to meet its national and international commitments to lowering such emissions. Additional benefits derived from mass EV adoption potentially include improved air quality (as EVs are emission-free) and reduced sound pollution (as EV engines are also soundless).

3. Literature Review

In the recent literature, several reviews related to barriers and opportunities that affect the economics and development of public charging infrastructures have been conducted [34,35]. Reviews have comprehensively studied aspects such as charging solutions and optimization techniques, charging scheduling, data mining, load forecasting, wireless charging technologies, cybersecurity of onboarding charging systems, power system quality in smart microgrids and multi-microgrid networks, the application of green energy to supply EV loads, and prediction-based mechanisms for dynamic response schemes compatible with smart prosumer behaviors [36–49].

This study is a part of wider research, starting with a pilot study with 50 participants [2], that attempted to provide initial insight into new conventional car purchasing behaviors among consumers in Kuwait. Interestingly, the study concluded that there are three potential new conventional car buyer segments. The first was identified as the 'Value Seeker' group, as early majority pragmatists which are not likely to become early adopters of EVs in the GCC region. The second segment is the 'Performance Seeker' group, mainly including early-adopter younger men who prefer EVs due to their high torque (0 to 100 km in a few seconds). Finally, the third segment was the 'Safety Seekers,' a niche market mainly consisting of environmentally conscious younger women who may prefer to drive EVs, with low maintenance as a predictive determining factor for EV adoption in the GCC region in the future. It is clear that, as the study was only a pilot study delivering various predictions, there was a lack of empirical evidence. These predictions were certainly not based on collective factual data but, instead, based on the assumptions and subjective interpretations of the authors. This study was followed by qualitative deep interviews with automotive dealers in Kuwait, as well as several EV (Tesla) owners [3]. This study revealed that two dealerships dominated the market: Porsche and Mercedes. As of 2022, there was no dealership for Tesla, and these cars were imported from neighboring countries (e.g., Saudi Arabia, Bahrain, and the United Emirates). The interviews confirmed that were market niches for EVs, as per the pilot study. The majority of women, according to Mercedes car dealers, preferred to buy EVs due to environmental concerns, their soundlessness, and lack of maintenance. However, contradictory to the pilot study, the high torque and high performance of EVs did not affect their purchase by younger men but, instead, men in their 50 s to 60 s who were not environmentally concerned at all but were attracted by technology, luxury, and the faster pick-up to 100 km than high-performance ICE sports cars. A large, extended survey superseded these two studies. The purpose of this study was two-fold, including studying how to facilitate mass EV adaptation to lower the CO_2 emissions in Kuwait, which is the second-highest in the world per capita, by examining attitudes towards EVs and the environment [1]. The present study, on the other hand, explores the marketing potential of EVs. Hence, we conducted an extensive literature review to identify the attributes of EVs that have been studied around the world (i.e., developed, developing countries, and the MENA region) as perceived by potential customers of EVs (see Table 1 and Figure 1).

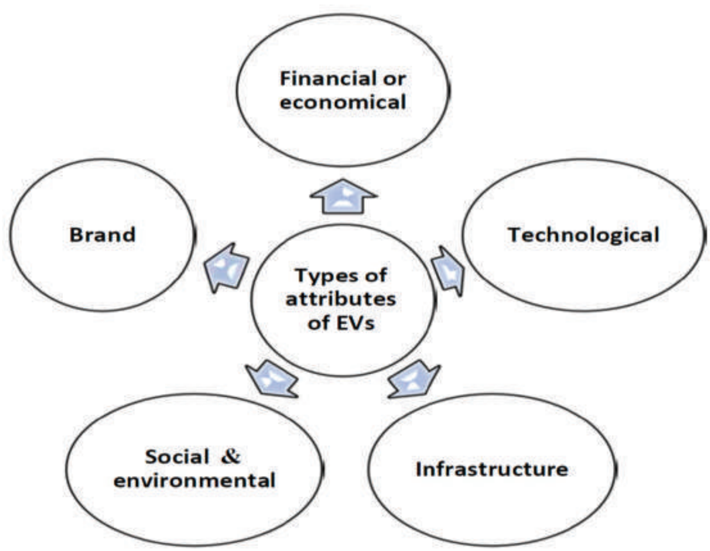

Figure 1. Types of attributes of EVs, as identified by potential customers around the world. Source: Authors 2023.

Table 1. Types of attributes of EVs as identified by potential customers around the world.

Types of Attributes	Industrialized Countries (Global North)	Developing Countries (Global South Excluding MENA Region)	MENA Region (Arab World)
Financial or economical attributes	Archsmith et al. (2021) [50], Mandys (2021) [51], Guerra and Daziano (2020) [52] Miranada and Delgado (2020) [53], Higueras-Castillo et al. (2019) [54], Rietmann and Lieven (2019) [55], Kowalska-Pyzalska et al. (2021–22) [56,57]	De Oliveira et al. (2022) [58], Lashari et al. (2021) [59], Dasharathraj et al. (2020) [60], Colak and Kaya (2020) [61], Li et al. (2020) [62], Bhalla et al. (2018) [63], Zhang et al. (2018) [64]	Eneizan (2019, Jordan) [65]
Technological attributes	Mandys (2021) [51], Archsmith et al. (2021), [50], Higueras-Castillo et al. (2019) [54]	De Oliveira et al. (2022) [58], Kim et al. (2022) [66] Ho and Huang (2022) [67], Kowalska-Pyzalska et al. (2021–22) [56,57], Kongklaew et al. (2021) [68], Khurana et al. (2020) [69], Colak and Kaya (2020) [61], Khurana et al. (2020) [70], Dasharathraj et al. (2020) [60], Haider et al. (2019) [70]	Hamwi (2022, Kuwait) [24,25]
Infrastructure attributes	Archsmith et al. (2021) [50], Miranada and Delgado (2020) [53], Guerra and Daziano (2020) [52], Rietmann and Lieven (2019) [55], Ottesen and Banna (2018) [71], Hardman et al. (2018) [72]	Kim et al. (2022) [66], De Oliveira et al. (2022) [58], Kongklaew et al. (2021) [68], Khurana et al. (2020) [70], Bhaskar et al. (2020) [73], Haider et al. (2019) [70], Bhalla et al. (2018) [63]	Shareeda et al. (2021, Bahrain) [74], Jreige et al. (2021, Lebanon) [75]
Social and environmental attributes	Archsmith et al. (2021) [50], Higueras-Castillo et al. (2020) [54], Miranada and Delgado (2020) [53], Vilchez et al. (2019) [76], Rietmann and Lieven (2019) [55]	Fan and Chen (2022) [77], Kim et al. (2022) [66], De Oliveira et al. (2022) [58], Dasharathraj et al. (2020) [60], Colak and Kaya (2020) [61], Haider et al. (2019) [70], Lin and Wu (2018) [78], Zhang et al. (2018) [35]	Al-Buenain et al. (2021, Qatar) [79], Shareeda et al. (2021, Bahrain), [74], Eneizan (2019, Jordan), [65]
Brand attributes	Kowalska-Pyzalska et al. (2021–22) [56,57]	Vongurai (2020) [80], Dasharathraj et al. [60]	

As shown in Table 1, five types of attributes have been investigated in the previous literature, including financial/economic, technological, infrastructure, brand, and social/environmental attributes. However, most studies have investigated one, two, and/or three types of these attributes, while no study has examined these five attributes collectively. Specifically, financial/economic attributes include features relating to the cost of EVs, such as purchase price, repair cost, maintenance costs, insurance costs, charging costs, warranty, and guarantee costs. Technological attributes encompass features relating to the technology used in EVs, such as battery life, battery performance, driving range, maximum speed, recharging time, acceleration, technology advancement, operating condition (i.e., heater and air condition), safety, trust, reliability, and engine performance (i.e., low noise). Infrastructure attributes include features relating to the infrastructure supporting EVs, such as charging stations and networks, commercial and public recharging infrastructure, home-based charging infrastructure, road and public infrastructure. Social and environmental attributes include features related to the governmental policies that serve social and environmental purposes, such as free parking spots, reduction in sales price, governmental subsidies and incentive policies, health and safety, tax reduction policy, and penalizing policies for conventional cars, as well as environmental friendliness. These four attribute types have been extensively investigated in the previous literature from both developed and developing countries. Brand attributes, including features such as design, brand reputation, credibility, and comfort, have been investigated to a lesser extent in the previous literature in both developed and developing countries. However, very little research has explored all five attribute types in the MENA region, particularly in Kuwait. Furthermore, little research has examined these types from the perspectives of conventional car drivers as potential customers.

It is necessary to point out that the previous literature investigating consumers' preferences for EVs typically considered a single layer of the five attributes, while other valuable factors for prediction were ignored and neglected. Interestingly, very few studies examined more than the two attributes in combination. Therefore, for the present study, we aimed to investigate all five types of attributes together in order to provide a comprehensive and up-to-date holistic picture of EV preferences. As such, the present paper helps to address this fundamental gap in the literature. Another advantage is that, by considering all five attribute types altogether, we hope to lay a solid foundation for upcoming studies to consider future re-occurring issues, as well as assist in the prediction of possible solutions for promoting the adoption of EVs, based on the present findings of this study.

In light of the above, none of the studies in the existing literature have specifically explored consumer preferences regarding EVs in Kuwait, as a critical part of the MENA region. Moreover, few studies have considered conventional car drivers in a similar context. Therefore, there is a need to explore consumer preferences for EVs from the perspective of conventional car drivers in order to identify which of these five types of attributes are considered most important by potential consumers in Kuwait, as this region constitutes a very promising market. Hence, we aimed to fill this gap in the literature by adding more significant knowledge, as stated in the introduction.

4. Data Collection and Methodology

4.1. Research Instrument

We employed a survey method by issuing a questionnaire to 472 conventional car drivers in order to achieve the objective of this study. This is part of a wider study, called "Breaking the ICE reign: mixed method study of attitudes towards buying and using EVs in Kuwait". A large-scale online questionnaire was used to provide a broader picture of the EV landscape in Kuwait and to confirm the prior survey results. A pilot test evaluation of the questionnaire has been described by Ottesen et al. (2022) [2], following which some changes and revisions were made to the format and overall design of the questionnaire. The first part focuses on data related to the demographic characteristics of the respondents, covering gender, age, marital status, education, nationality, employment, field of employment, number of cars owned by the household, job role, and household income. This first part consisted of 10 items concerning the demographic characteristics of the respondents. The second part of the questionnaire consisted of 18 closed-ended questions, which served to enrich our understanding regarding the preferences and viewpoints of conventional car drivers in Kuwait.

4.2. Sampling Procedures and Size

As this study aimed to collect data about EVs, we focused on the drivers and owners of conventional cars, who could be considered potential buyers of EVs. We decided to use the random sampling technique for data collection. For this study, the population is composed of all people who drive and/or own conventional cars in Kuwait. As the population of this study was over 100,000, the minimum required sample size for survey research was 384, as suggested by Krejcie and Morgan [81], and any sample size over 500 was considered very good, as recommended by Comrey and Lee [82]. A large sample size enables the collection of meaningful demographic data and allows one to reach actionable conclusions regarding the population. We stopped collecting data after collecting questionnaires from 604 participants. The final sample included 472 (78.1% response rate) questionnaires, which were used in the subsequent analysis.

4.3. Data Collection Procedure

Two web links were formulated, one for the Arabic version and another for the English version of the questionnaire. The authors formulated the questionnaire using Google Forms, which is a validated tool used for data collection. The researchers distributed the questionnaires among several groups in Kuwait who usually drive and/or own conventional cars, including students, the general public, faculty members, and tutors, in order to collect their feedback and comments using the two web-based links. The respondents to the questionnaire had to be at least 18 years old and conventional car drivers/owners to participate in the study. The data collection stage started in February 2022 and ran until May 2022. The purposes of the study were explained to participants, and they were asked to complete the questionnaire. The instructions for completing the questionnaire were given on the cover page in order to avoid any misunderstanding about the issue. To ensure the objectivity of the study, the respondents were asked one qualifying question to ensure whether they drive and/or own a conventional car. Only after this were they allowed to answer the rest of the questionnaire. A total of 604 persons participated in this study. After removing 132 questionnaires (i.e., those who did not have or drive a car), a total of 472 questionnaires were analyzed. As shown in Table 2, there was an approximate gender balance within the data (238 males and 234 females). Additionally, 64% of the sample (n = 304) were in the age category of 26 to 60 years, reflecting the car ownership status in Kuwait.

Table 2. Summary of the demographic characteristics of the respondents.

Variable	Categories	N = 472	%
Gender	Male	238	50.4%
	Female	234	49.6%
Age Range	18–25 years	168	35.6%
	26–39 years	222	47.0%
	40–49 years	61	12.9%
	50–60 years	21	4.4%
Marital Status	Single	272	57.6%
	Married without kids	37	7.8%
	Married with 1 kid	35	7.4%
	Married with 2 kids	42	8.9%
	Married with 3 kids or more	86	18.2%
Ethnicity	Kuwaiti	287	60.8%
	Arab Non-Kuwaiti	144	30.5%
	Asian Non-Arab	38	8.1%
	American, European, or Australian	2	0.4%
	African Non-Arab	1	0.2%
Number of Cars in household	One car	62	13.1%
	Two cars	139	29.4%
	Three cars	70	14.8%
	Four cars	66	14.0%
	Five cars or more	135	28.6%

Table 2. *Cont.*

Variable	Categories	N = 472	%
Educational Level	Less than high school	8	1.7%
	High School diploma	108	22.9%
	Trade/Commerce degree	55	11.7%
	Bachelor's degree	259	54.9%
	Master's degree	31	6.6%
	PhD	11	2.3%
Employment	Private sector	176	37.3%
	Public sector	152	32.2%
	Unemployed	83	17.6%
	Self-employed	35	7.4%
	Family-owned business	26	5.5%
Field of employment	Other private services	139	29.4%
	Government and Ministries	125	26.5%
	Family business	61	12.9%
	Education—government or private	46	9.7%
	Oil and Gas sector	32	6.8%
	Large Kuwaiti corporation	29	6.1%
	Health Care—government or private	26	5.5%
	Military or police	14	3.0%
Which of the following best describes your role in industry?	Middle Management	102	21.6%
	Administrative Staff	80	16.9%
	Upper Management	59	12.5%
	Student—Not working	54	11.4%
	Lower Management	38	8.1%
	Support Staff	34	7.2%
	Temporary Employee	28	5.9%
	Self-employed/Business Partner	27	5.7%
	Trained Professional expert	22	4.7%
	Researcher	12	2.5%
	Consultant	8	1.7%
	Skilled Laborer	8	1.7%
Monthly Income	Less than KWD 500 (USD 1650)	149	31.6%
	KWD 500–999	104	22.0%
	KWD 1000–1499	111	23.5%
	KWD 1500–1999	59	12.5%
	KWD 2000 and above (USD 6600)	49	10.4%

4.4. Statistical Analysis

We conducted statistical analysis using IBM SPSS 19 software. Descriptive statistics (i.e., frequencies and percentages) were computed to analyze the data relating to the demographic characteristics and closed-ended questions. Therefore, no hypothesis was formulated, as the study was conducted to explore the prevalence of attributes of EVs among potential consumers. ANOVA and *t*-tests were also conducted in order to determine significant differences. The *t*-test was used to compare the mean scores of two different groups of one independent variable that had only two distinct categories and one continuous dependent variable [82], while ANOVA was used to determine whether statistically significant differences in means occurred between more than two groups [83]; that is, ANOVA was used when considering one independent variable with more than two distinct or continuous categories and one continuous dependent variable.

4.5. Data Analysis and Findings

A summary of the demographic characteristics of the respondents is presented in Table 2. An approximately equal number of males (50.4%) and females (49.6%) completed the questionnaire. Approximately half of the participants (47%) were in the age range of 26 to 39 years, while more than a third of them (35.6%) were in the age range of 18 to 25 years. More than half of the respondents were single (57.6%), while approximately a fifth of them (18.2%) were married with three or more children. Approximately two-thirds (60.8%) of the participants were Kuwaiti. More than half of the respondents (54.9%) had a bachelor's degree. More than a quarter of the participants owned two cars (29.4%) or five or more cars (28.6%). More than a third of participants (37.3%) were employed in the private sector, while approximately another third of them (32.2%) were employed in the public sector. Approximately a third of participants (29.4%) worked in other private services, more than a quarter of them (26.5%) worked in the government and ministries sector, and more than a fifth of them (21.6%) were in middle management. The monthly income of more than half of the participants (53.6%) was less than KWD 1000 (USD 3300).

The following scale is used to facilitate reporting the rest of the results:

- High agreement: Calculated mean ($M \geq 3.5$);
- Medium agreement: Calculated mean ($2.5 \geq M < 3.5$);
- Low agreement: Calculated mean ($M < 2.5$)

With regard to the most favorable features of EVs, as perceived by participants (see Table 3 and Figure 2), the participants highly agreed on three features: namely, environmental friendliness, with lower CO_2 leading to better air quality (M = 3.74), much lower fuel price than gasoline (M = 3.54), and soundless engine (M = 3.52). Other features had a medium agreement, such as increased safety in terms of fire and crash tests (M = 3.49), faster and more powerful air conditioning (M = 3.46), much faster acceleration from 0 to 100 km (M = 3.32), and much lower maintenance and associated costs (M = 3.24).

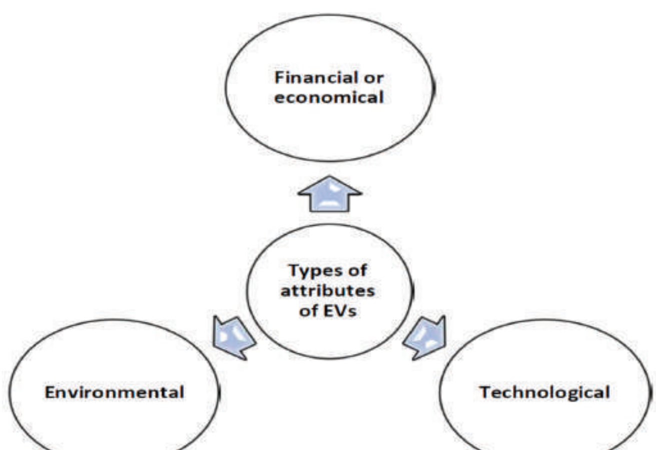

Figure 2. Attributes of EVs highly preferred by consumers in Kuwait. Source: Authors 2023.

Table 3. The most favorable features of EVs as perceived by participants (N = 472).

Type of Attribute (Features)	To What Extent You Agree/Disagree about the Most Favorable Features of EV?	Mean	SD
Social attributes—pro-environmental	Environmental friendliness, less CO_2 that leads to better air quality	3.74	1.308
Financial/economic attributes	Much lower fuel price than gasoline	3.54	1.279
Technological attributes	Soundless engine	3.52	1.305
Technological attributes	Increased safety in terms of fire and crash tests	3.49	1.305
Technological attributes	Faster and more powerful air conditioning	3.46	1.246
Technological attributes	Much faster acceleration (from 0 to 100 km)	3.32	1.236
Financial/economic attributes	Much lower maintenance and associated cost	3.24	1.311

With regard to the requirements to buy EVs, as perceived by participants (see Table 4 and Figure 3), participants highly agreed on two requirements; namely, if the guarantee of the battery would last at least 10 years or 150,000 km (M = 3.54), and if there was a fast-charging station within 5 km from almost every place in Kuwait (M = 3.51). Other requirements had a medium agreement, such as if they start to see a noticeable change in air quality due to people driving EVs (M = 3.47) if the range (how long they can drive) per full charge would be at least 400 km (M = 3.47), if they had a cool and unique design (M = 3.43), if the price was the same or lower than an equivalent gasoline car (M = 3.39) if the re-selling value would be equivalent or higher than that of a gasoline car (M = 3.39), and if the price of gasoline would increase three-fold (M = 3.33).

Table 4. The requirements to buy EVs as perceived by participants (N = 472).

Types of Attributes (Features)	I Would Buy an EV if ...	Mean	SD
Financial/economic attributes	If the guarantee of the battery lasted at least 10 years or 150,000 km	3.54	1.189
Infrastructure attributes	If there was a fast-charging station within 5 km from almost every place in Kuwait	3.51	1.193
Social attributes—pro-environmental	If I start to see noticeable change in air quality because people are driving EVs	3.47	1.162
Technological attributes	If the range (how far you can drive) per full charge would be at least 400 km	3.47	1.160
Brand attribute	If they were cool and unique design	3.43	1.217
Financial/economic attributes	The price was same or lower than equivalent gasoline car	3.39	1.287
Financial/economic attributes	If the reselling value was equivalent or higher than gasoline car	3.39	1.164
Financial/economic attributes	If gasoline prices increased three-fold	3.33	1.220
Infrastructure attributes	There was a special EV lane on major highways such as highway 30 and 40	3.27	1.165
Social attributes—social acceptance	If most of my friends or family bought an EV	2.97	1.152

The *t*-test and ANOVA were conducted to determine significant differences between the most favorable features of EVs identified in the study in terms of four background variables having two groups (i.e., gender, marital status, ethnicity, and the number of cars owned) and four background variables with more than two groups (i.e., age range, education, employment, and monthly income), respectively. The results are summarized in Table 5. When the mean score of features was compared across the eight background variables, there were strong significant differences in the mean scores of the features regarding the number of cars owned and employment. Participants who had one or two cars highly agreed on the environmental friendliness (M = 3.91, p = 0.02) and soundless engine (M = 3.68, p = 0.024) attributes of EVs, while participants who had three cars or more moderately agreed on the soundless engine feature, and highly agreed on the environmental friendliness of EVs. Furthermore, participants employed in the public sector highly agreed on the environmental friendliness (M = 3.91, p = 0.001), much lower fuel price (M = 3.69, p = 0.004), and soundless engine (M = 3.68, p = 0.011) of EVs, while participants who were employed in a family-owned business moderately agreed on these features. On the other hand, no significant differences in the most favorable features of EVs identified in the study could be related to the other six background variables of the participants.

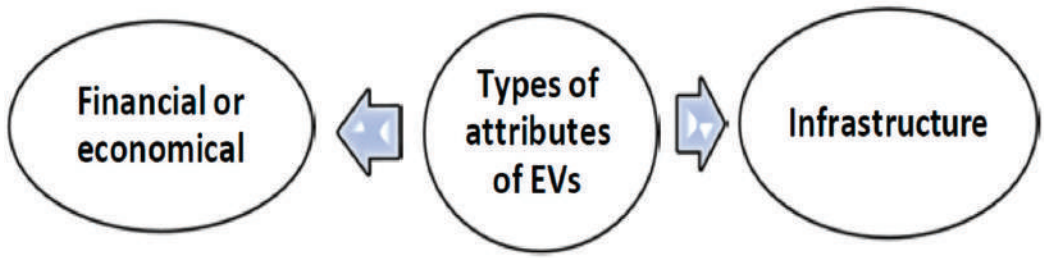

Figure 3. Types of attributes of EVs in Kuwait as identified by customers as highly necessary to buy EVs in the near future. Source: Authors 2023.

Table 5. Comparison of mean scores of the highly preferred favorable features of EVs in terms of eight background variables of the participants.

Variables	Categories (N)	The Highly Preferred Favorable Features of EVs		
		Environmental Friendliness, Less CO_2 and Sod That Lead to Better Air Quality	Much Lower Fuel Price than Gasoline	Soundless Engine
		Mean	Mean	Mean
Gender	Male (N = 238)	3.79	3.63	3.61
	Female (N = 234)	3.70	3.46	3.42
	Sig. (2-tailed)	0.482	0.163	0.113
Marital Status	Single (N = 272)	3.69	3.57	3.43
	Married (N = 200)	3.82	3.51	3.64
	Sig. (2-tailed)	0.277	0.668	0.084
Ethnicity	Kuwaiti (N = 287)	3.73	3.56	3.57
	Non-Kuwaiti (N = 185)	3.76	3.52	3.43
	Sig. (2-tailed)	0.805	0.728	0.247
Number of cars	One to Two cars (N = 201)	3.91	3.65	3.68
	Three cars or more (N = 271)	3.62	3.46	3.40
	Sig. (2-tailed)	0.020	0.117	0.024
Age Range	18–25 years (N = 168)	3.67	3.49	3.40
	26–39 years (N = 222)	3.75	3.55	3.55
	40–60 years (N = 82)	3.89	3.65	3.67
	Sig. (2-tailed)	0.447	0.655	0.260

Table 5. *Cont.*

Variables	Categories (N)	The Highly Preferred Favorable Features of EVs		
		Environmental Friendliness, Less CO_2 and Sod That Lead to Better Air Quality	Much Lower Fuel Price than Gasoline	Soundless Engine
		Mean	Mean	Mean
Education	Less than high school (N = 8)	3.00	3.00	3.00
	High School diploma (N = 108)	3.83	3.67	3.44
	Trade/Commerce degree (N = 55)	3.38	3.31	3.15
	Bachelor's degree (N = 259)	3.78	3.56	3.65
	Master's degree (N = 31)	4.00	3.55	3.55
	Ph.D. (N = 11)	3.64	3.64	3.36
	Sig. (2-tailed)	0.118	0.499	0.104
Monthly Income	Less than KD 500 (N = 149)	3.61	3.45	3.34
	KD 500–999 (N = 104)	3.75	3.53	3.52
	KD 1000–1499 (N = 111)	3.89	3.77	3.74
	KD 1500 and above (N = 108)	3.77	3.46	3.55
	Sig. (2-tailed)	0.392	0.204	0.105
Employment	Self-employed (N = 35)	3.77	3.69	3.46
	Family-owned business (N = 26)	2.81	2.81	2.77
	Private sector (N = 176)	3.81	3.63	3.58
	Public sector (N = 152)	3.91	3.69	3.68
	Unemployed (N = 83)	3.58	3.28	3.35
	Sig. (2-tailed)	0.001	0.004	0.011

Furthermore, the *t*-test and ANOVA were conducted to determine significant differences in the necessary requirements to buy EVs identified in the study in terms of the four background variables having two groups (i.e., gender, marital status, ethnicity, and the number of cars owned) and the four background variables with more than two groups (i.e., age range, education, employment, and monthly income), respectively. The results are summarized in Table 6. When the mean score of features was compared across the eight background variables, there were strong significant differences in the mean scores of the two requirements with respect to the education level and monthly income of participants. Participants who had a master's degree or Ph.D. highly agreed on if there was a fast-charging station within 5 km from almost every place in Kuwait (Ph.D. mean = 4.18, Master's mean = 3.81, $p = 0.002$), while participants who had a bachelor's degree moderately agreed on this condition. Furthermore, participants who had a monthly income between KD 1000 and 1499 or KD 1500 and above highly agreed on if the guarantee of the battery would last at least 10 years or 150,000 km (M = 3.81, M = 3.60, $p = 0.014$), and if there was a fast-charging station within 5 km from almost every place in Kuwait (M = 3.82, M = 3.52, $p = 0.009$), while participants who had a monthly income less than KD 500 moderately agreed on these features. On the other hand, no significant differences in the necessary requirements to buy EVs identified in the study were observed with respect to the other six background variables of the participants.

Table 6. Comparison of mean scores of the identified necessary requirements to buy EVs in terms of eight background variables of the participants.

Variables	Categories (N)	I Would Buy an EV if . . .	
		If the Guarantee of the Battery Would Last as Least 10 Years or 150.000 km	**If There Was a Fast-Charging Station Within 5 km from Almost Every Place in Kuwait**
		Mean	**Mean**
Gender	Male (N = 238)	3.57	3.51
	Female (N = 234)	3.51	3.51
	Sig. (2-tailed)	0.592	0.998
Marital Status	Single (N = 272)	3.55	3.53
	Married (N = 200)	3.53	3.48
	Sig. (2-tailed)	0.837	0.666
Ethnicity	Kuwaiti (N = 287)	3.60	3.58
	Non-Kuwaiti (N = 185)	3.45	3.41
	Sig. (2-tailed)	0.189	0.136
Number of cars	One to Two cars (N = 201)	3.56	3.56
	Three cars or more (N = 271)	3.52	3.48
	Sig. (2-tailed)	0.705	0.486
Age Range	18–25 years (N = 168)	3.53	3.55
	26–39 years (N = 222)	3.48	3.42
	40–60 years (N = 82)	3.72	3.68
	Sig. (2-tailed)	0.288	0.198
Education	Less than high school (N = 8)	2.63	2.13
	High School diploma (N = 108)	3.41	3.64
	Trade/Commerce degree (N = 55)	3.55	3.36
	Bachelor's degree (N = 259)	3.60	3.47
	Master's degree (N = 31)	3.68	3.81
	PhD (N = 11)	3.64	4.18
	Sig. (2-tailed)	0.206	0.002
Monthly Income	Less than KD 500 (N = 149)	3.44	3.43
	KD 500–999 (N = 104)	3.33	3.30
	KD 1000–1499 (N = 111)	3.81	3.82
	KD 1500 and above (N = 108)	3.60	3.52
	Sig. (2-tailed)	0.014	0.009
Employment	Self-employed (N = 35)	3.40	3.34
	Family-owned business (N = 26)	3.00	3.12
	Private sector (N = 176)	3.56	3.52
	Public sector (N = 152)	3.64	3.66
	Unemployed (N = 83)	3.52	3.42
	Sig. (2-tailed)	0.129	0.162

5. Discussion

We aimed to examine the consumer preferences of what we labeled as the 'early majority or pragmatists' (83% of the sample was under 40 years old and 75% had at least some level of higher education) regarding the EV market in Kuwait, as well as to explore any differences in these identified preferences with respect to their demographic background. According to the findings, drivers highly preferred three different types of attributes for EVs: Environmental attributes (e.g., in terms of leading to better air quality), financial attributes (e.g., in terms of lower fuel price), and technological attributes (e.g., in terms of their soundless engines). This means that drivers in Kuwait can be expected to prefer EVs over gasoline cars in the future due to their environmental, economic, and technological values. This result is consistent with previous studies in other countries [35,61,62,78]. One plausible explanation for this result is that drivers in Kuwait care about the triple bottom line of sustainability. The government could, therefore, implement awareness plans and agendas to better inform consumers about environmental issues and promote sustainability. This finding implies that the driving force for the adoption of EVs could be the promotion of sustainability. We believe that this form of promotion should be applied by car manufacturers in Kuwait, targeting a wider segment of the population in order to increase the rate of adoption of EVs.

There was a strongly significant difference in the identified preferred attributes for EVs in terms of the employment sector of and the number of cars owned by participants. Participants who were employed in the public sector highly preferred the three types of attributes for EVs more than those who worked in a family-owned business. This means that individuals in Kuwait who are employed in the public sector may prefer EVs over gasoline cars in the future due to their environmental, financial, and technological values. Furthermore, participants who owned one or two cars highly preferred the environmental and technological attributes of EVs, more than those who owned three or more cars. No significant differences in financial attributes could be related to the number of cars owned by participants. This means that individuals in Kuwait who own one or two cars can be expected to prefer EVs over gasoline cars in the future due to their environmental and technological values only, and they do not care as much about the price of fuel. These results characterize individuals who own a maximum of two cars and are employed in the public sector as a potential segment of EV consumers in Kuwait who place value on environmental and technological attributes, particularly regarding better air quality and having a soundless engine. This implies that manufacturers and dealerships should consider targeting these potential buyers and should continually create or maintain a competitive advantage over their competitors in terms of innovating technologies that respond to the evolving nature of environmental concerns. On the other hand, no significant differences in the three preferred attributes for EVs identified in the study could be related to the other six background variables of the participants.

Additionally, drivers were found to be highly willing to buy EVs in the future when considering their financial and infrastructure attributes. This means that drivers in Kuwait can be expected to buy EVs in the future on two conditions: Economy in battery life and the availability of nearby fast-charging station infrastructure. This result is consistent with previous studies in other countries [35,78]. One possible explanation for this result is that drivers in Kuwait are aware of both the importance of the battery life in EVs, as they commonly witness their cell phone turning off due to heat exposure and are aware of the poor EV infrastructure EVs in Kuwait. As such, the manufacturers of EVs should update consumers on the development of battery technology in a timely manner, as well as encourage the government to invest in infrastructure that supports EVs in Kuwait. This implies that EV recharging infrastructure should be accessible and available in all residential areas of Kuwait. This finding implies that the Ministry of Transport should adhere to the suggestions proposed by prior studies concerning the recharging scheduling and optimization of recharging networking in order to prevent any potential infrastructure issues [36–38]. Hence, we recommend that policymakers and government regulators start constructing infrastructure-related facilities to promote of the adoption of EVs in Kuwait in a secure manner.

We observed a strongly significant difference in the identified necessary conditions to buy EVs when considering the educational level and monthly income of participants. Participants who had a master's degree or Ph.D. were more willing to buy EVs in the future for their infrastructure attributes compared with those who had a bachelor's degree. No significant differences in financial attributes could be related to the educational level of participants. This means that people in Kuwait who had a master's degree or Ph.D. would buy EVs in the future on one condition only; namely, the availability of infrastructure (i.e., nearby fast-charging stations), and they care less about the battery life of EVs. This result characterized highly educated individuals as a potential segment of EVs in Kuwait who favor infrastructure (i.e., recharging networks). Surprisingly, this segment was unique and distinct from other groups, as they did not present favorable attributes highly related to the product itself. This signifies the important role of manufacturers in providing recharging stations and making them accessible across the country of Kuwait. Further, participants who had a monthly income of KWD 1000 (USD 3300) and above were highly willing to buy EVs in the future due to their financial and infrastructure attributes. This means that individuals in Kuwait who have a monthly income of KD 1000 and above can be expected to buy EVs in the future on two conditions: Their economic battery life and the availability of infrastructure (in terms of nearby fast-charging stations). This result characterized individuals who earned KD 1000 and above as a potential segment of EVs in Kuwait who place value on battery warranties and the required infrastructure (i.e., recharging stations) being accessible and widespread. This requires marketers to tailor sustainable products and place emphasis on warranties and guarantees associated with EVs. On the other hand, no significant differences in the two necessary conditions to buy EVs identified in the study could be related to the other six background variables of the participants.

One interesting finding of this study was that drivers were not highly willing to buy EVs in the future due to their brand attributes. This result contradicts the existing literature [56,57], in which brand attributes were considered important by consumers. One plausible explanation for this result is that drivers in Kuwait are already aware of the quality design, brand reputation, credibility, and comfort of EVs, such that there is no need to consider the brand as an important condition to buy EVs in the future. This result deserves further investigation in future research.

6. Limitations and Future Studies

First, although the present study utilized a quantitative questionnaire, it remained essentially focused on a qualitative approach using descriptive statistics due to the lack of a focus on hypothesis testing and empirical testing. For this reason, a range of reliability tests was not conducted for this study. Therefore, future studies should involve empirical investigations of various hypotheses and variables, which may yield a more reliable conclusion regarding the relevant population in Kuwait. Second, the generalizability of the results was limited by the lack of information regarding non-participants. Finally, future studies should place emphasis on both EV owners and managers of car dealership companies, collecting their viewpoints and obtaining more insight into EV-related phenomena in Kuwait. Such a proposed further study should emphasize the 'late majority' EV market, composed of drivers over the age of 40 with a lower level of education, which might reveal some perceptions based on outdated safety records (e.g., perceived safety in terms of fire) or even loyalty to gasoline (as it is the main source of wealth in Kuwait).

7. Conclusions and Implications

This is the first known study exploring consumer preferences for EVs in Kuwait in terms of which factors are influential for the 'early majority' (i.e., a part of the general market vs. a niche one) that could influence their purchasing behavior in favor of EVs. In this way, we provided a comprehensive and up-to-date picture of the preferences regarding this market. Potential consumers highly preferred three different types of attributes for EVs: environmental, financial, and technological. There were strongly significant differences in the identified preferred attributes of individuals in Kuwait for EVs with respect to the number of cars owned and sector of employment. Drivers who valued EVs most typically owned a maximum of two cars and were employed in the public sector, as well as being environmentally and technologically sensitive. Moreover, potential customers were highly willing to buy EVs in the future due to both their financial and infrastructure attributes. There were also strong significant differences in the identified necessary conditions to buy EVs in terms of educational level and monthly income. Drivers who expressed early interest in adopting EVs were typically highly educated, of mid-range income, and concerned regarding the availability of nearby fast-charging stations. This implies that the upfront purchasing price of EVs might not be important to this segment of the market in Kuwait.

The theoretical and practical implications of this study are significant. On a theoretical level, this study contributes to the limited literature on EVs in developing countries in general and Kuwait in particular, which can help researchers to compare the adoption of EVs between developing and developed countries. On a practical level, the findings suggest that drivers in Kuwait prefer EVs over gasoline cars due to their environmental, economic, and technological benefits. Therefore, marketing campaigns should highlight these values when targeting segments, including car drivers and owners. The number of cars owned by people in Kuwait was found to play an important role in preferring EVs over gasoline cars. People in Kuwait who owned one or two cars preferred EVs due to their environmental and technological benefits alone. Furthermore, the employment sector also plays an important role in the preference for EVs over gasoline cars. People in Kuwait who were employed in the public sector preferred EVs due to their environmental, economic, and technological values. Therefore, there is a need for the customization of marketing campaigns in order to address the preferences of each group.

Moreover, the results of this study suggested that drivers in Kuwait can be expected to use EVs in the future if fast-charging station infrastructure was available in a widespread manner. Therefore, policymakers and government agencies should be encouraged to start building and providing these stations in order to promote the adoption of EVs. Furthermore, this study suggested that drivers in Kuwait can be expected to use EVs in the future for economic purposes, particularly in terms of a long-lasting battery. As such, the manufacturers of EVs should try to develop batteries that last as long as possible.

The availability of nearby fast-charging station infrastructure for EVs was found to be a very important pre-condition for people in Kuwait who have a master's degree or Ph.D. to buy EVs. Therefore, it is important to raise awareness among this group of people about available charging stations in Kuwait. Monthly income was also found to play an important role in encouraging the purchase of EVs in Kuwait. Therefore, marketing campaigns should target this group of people, especially those who earn a monthly salary of more than KD 1000 (KWD 3300). These campaigns should highlight the economic value of EVs and the available EV charging infrastructure. We also suggest that the government develops subsidy programs and financial support for EV buyers in order to combat the elevated EV purchase prices.

Author Contributions: A.O. is the principal investor of the project and is responsible for the conceptualization, methodology, and editing, as well as funding acquisition and administration. S.B. and B.A. were responsible for the literature review, conceptualization, synthesis, methodology, validation, formal analysis, data curation, writing—original draft preparation, and editing. All authors have read and agreed to the published version of the manuscript.

Funding: This paper is a part of a wider study called "Breaking the ICE reign: mixed method study of attitudes towards buying and using EVs in Kuwait." The study was funded by the Kuwait Foundation for the Advancement of Sciences and administrated by the Middle East Center of the London School of Economics and Political Science and the LSE Research Ethics Committee approval.

Institutional Review Board Statement: This study was approved by the London School of Economics and Political Science Ethics Committee (00558000004KJE9AAO, dated 24 November 2021).

Informed Consent Statement: Informed statement about the usage and purpose of the study was included in the questionnaire, as directed by the LSE Ethics Committee.

Data Availability Statement: Not applicable.

Conflicts of Interest: The authors declare no conflict of interest.

References

1. Ottesen, A.; Banna, S.; Alzougool, B. Attitudes of Drivers towards Electric Vehicles in Kuwait. *Sustainability* **2022**, *14*, 12163. [CrossRef]
2. Ottesen, A.; Banna, S. Why so few EVs are in Kuwait and how to amend it. *Int. J. Eng. Technol.* **2021**, *10*, 181–189. Available online: https://www.sciencepubco.com/index.php/ijet/issue/view/559 (accessed on 30 January 2023). [CrossRef]
3. Ottesen, A.; Toglaw, S.; AlQuaoud, F.; Simovic, V. How to Sell Zero Emission Vehicles when the Petrol is almost for Free: Case of Kuwait. *J. Manag. Sci.* **2022**, *9*, 1–20. [CrossRef]
4. Ottesen, A.; Banna, S.; Alzougool, B.; Simovic, V. Driving factors for women's switch to electric vehicles in conservative Kuwait. *J. Women Entrep. Educ.* **2022**, *3*, 1–21.
5. Rosellon, M.A.D. *Clean Energy Technology in the Philippines: Case of the Electric Vehicle Industry (No. 2021-15)*; PIDS Discussion Paper Series; Public Institute for Development Study Manila: Makati, Philippines, 2021.
6. Pardi, T. *Heavier, Faster and Less Affordable Cars: The Consequence of EU Regulations for Car Emissions*; ETUI Research Paper-Report 7; European Trade Union Institute: Brussels, Belgium, 2022.
7. Kalghatgi, G. Is it really the end of internal combustion engines and petroleum in transport? *Appl. Energy* **2018**, *225*, 965–974. [CrossRef]
8. Bloomberg, N.E.F. Electric Vehicle Outlook. 2022. Available online: https://about.bnef.com/electric-vehicle-outlook/ (accessed on 30 January 2023).
9. Tirachini, A. Ride-hailing, travel behavior and sustainable mobility: An international review. *Transportation* **2020**, *47*, 2011–2047. [CrossRef]
10. Yegin, T.; Ikram, M. Analysis of Consumers' Electric Vehicle Purchase Intentions: An Expansion of the Theory of Planned Behavior. *Sustainability* **2022**, *14*, 12091. [CrossRef]
11. Cid-López, A.; Hornos, M.J.; Carrasco, R.A.; Herrera-Viedma, E. Decision-making model for designing telecom products/services based on customer preferences and non-preferences. *Technol. Econ. Dev. Econ.* **2022**, *28*, 1818–1853. [CrossRef]
12. Musumali, B. An Analysis why customers are so important and how marketers go about in understanding their decisions. *Bus. Mark. Res. J.* **2019**, *23*, 230–246.
13. Crespo, B.; Míguez-Álvarez, C.; Arce, M.E.; Cuevas-Alonso, M.; Míguez, J.L. The Sustainable Development Goals: An Experience on Higher Education. *Sustainability* **2017**, *9*, 1353. [CrossRef]
14. Ikram, M.; Sroufe, R.; Awan, U.; Abid, N. Enabling Progress in Developing Economies: A Novel Hybrid Decision-Making Model for Green Technology Planning. *Sustainability* **2021**, *14*, 258. [CrossRef]
15. Ikram, M.; Ferasso, M.; Sroufe, R.; Zhang, Q. Assessing Green Technology Indicators for Cleaner Production and Sustainable Investments in a Developing Country Context. *J. Clean. Prod.* **2021**, *322*, 129090. [CrossRef]
16. IEA. Oil Market Report. 2022. Available online: https://www.iea.org/reports/oil-market-report-august-2022 (accessed on 28 January 2023).
17. Worldometer. Norway and Kuwait Population. 2023. Available online: https://www.worldometers.info/world-population (accessed on 28 January 2023).
18. World Population Review—Reserve by Country. 2023. Available online: https://worldpopulationreview.com/country-rankings/oil-reserves-by-country (accessed on 28 January 2023).
19. Sovern Investor Leadership Conference. 2023. Available online: https://www.swfinstitute.org/fund-rankings/sovereign-wealth-fund (accessed on 28 January 2023).
20. IMF. GDP Per Capita. 2023. Available online: https://www.imf.org/external/datamapper/NGDPDPC@WEO/OEMDC/ADVEC/WEOWORLD (accessed on 28 January 2023).
21. World Bank (2023) CO2 Emission (Metric Ton Per Capita). Available online: https://data.worldbank.org/indicator/EN.ATM.CO2E.PC (accessed on 28 January 2023).
22. Alvik & Bakken. How Norway's EVs Have Cut Emission Globally. 2021. Available online: https://eto.dnv.com/2019/how-norways-evs-have-cut-emissions-globally (accessed on 20 January 2023).
23. UN Sustainable Development Goals Report Kuwait. 2022. Available online: https://www.un.org/sustainabledevelopment/climate-change/ (accessed on 28 January 2023).
24. Hamwi, H.; Rushby, T.; Mahdy, M.; Bahaj, A.S. Effect of High Ambient Temperature on Electric Vehicle Efficiency and Range: Case Study of Kuwait. *Energies* **2022**, *15*, 3178. [CrossRef]

25. Hamwi, H.; Alasseri, R.; Aldei, S.; Al-Kandari, M. A Pilot Study of Electric Vehicle Performance, Efficiency, and Limitation in Kuwait's Harsh Weather and Environment. *Energies* **2022**, *15*, 7466. [CrossRef]
26. Charged Kuwait. Charging Station in Kuwait. 2023. Available online: https://www.chargedkw.com/where-to-charge (accessed on 28 January 2023).
27. Global Petrol Prices. Gasoline Prices, Liter, 19th of December 2022. Available online: https://www.globalpetrolprices.com/gasoline_prices/ (accessed on 22 December 2022).
28. Christensen, C.; Horn, M.B.; Johnson, C. *Disrupting Class: How Disruptive Innovation Will Change the Way the World Learns*, 2nd ed.; MacGraw Hill: New York, NY, USA, 2011.
29. Muller, J.M. Comparing Technology Acceptance for Autonomous Vehicles, Battery Electric Vehicles, and Car Sharing—A study across Europe, China and North America. *Sustainability* **2019**, *11*, 4333. [CrossRef]
30. National Transportation Safety Board. 2021. Available online: https://data.ntsb.gov/Docket/?NTSBNumber=HWY19SP002 (accessed on 28 January 2023).
31. Insider. Elon Musk Calls Gas-Power Cars a Passing Fad. 2019. Available online: https://www.businessinsider.com/teslas-elon-musk-calls-gas-powered-cars-a-passing-fad-2019-8 (accessed on 28 January 2023).
32. Global Petrol Prices. Kuwait Electricity Prices. 2022. Available online: https://www.globalpetrolprices.com/Kuwait/electricity_prices/#:~{}:text=Kuwait%2C%20June%202022%3A%20The%20price,of%20power%2C%20distribution%20and%20taxes (accessed on 28 January 2023).
33. United State Environmental Agency. Electric Vehicle Myths. 2022. Available online: https://www.epa.gov/greenvehicles/electric-vehicle-myths#Myth1 (accessed on 28 January 2023).
34. Nour, M.; Chaves-Ávila, J.P.; Magdy, G.; Sánchez-Miralles, Á. Review of Positive and Negative Impacts of Electric Vehicles Charging on Electric Power Systems. *Energies* **2020**, *13*, 4675. [CrossRef]
35. Zhang, Q.; Li, H.; Zhu, L.; Campana, P.E.; Lu, H.; Wallin, F.; Sun, Q. Factors influencing the economics of public charging infrastructures for EV—A review. *Renew. Sustain. Energy Rev.* **2018**, *94*, 500–509. [CrossRef]
36. Mansouri, S.A.; Nematbakhsh, E.; Jordehi, A.R.; Tostado-Véliz, M.; Jurado, F.; Leonowicz, Z. A Risk-Based Bi-Level Bidding System to Manage Day-Ahead Electricity Market and Scheduling of Interconnected Microgrids in the presence of Smart Homes. In Proceedings of the IEEE International Conference on Environment and Electrical Engineering and 2022 IEEE Industrial and Commercial Power Systems Europe (EEEIC/I&CPS Europe), Prague, Czech Republic, 28 June–1 July 2022; pp. 1–6. [CrossRef]
37. Mansouri, S.A.; Nematbakhsh, E.; Ahmarinejad, A.; Jordehi, A.R.; Javadi, M.S.; Marzband, M. A hierarchical scheduling framework for resilience enhancement of decentralized renewable-based microgrids considering proactive actions and mobile units. *Renew. Sustain. Energy Rev.* **2022**, *168*, 112854. [CrossRef]
38. Mansouri, S.A.; Jordehi, A.R.; Marzband, M.; Tostado-Véliz, M.; Jurado, F.; Aguado, J.A. An IoT-enabled hierarchical decentralized framework for multi-energy microgrids market management in the presence of smart prosumers using a deep learning-based forecaster. *Appl. Energy* **2023**, *333*, 120560. [CrossRef]
39. Aziz, H.; Tabrizian, M.; Ansarian, M.; Ahmarinejad, A. A three-stage multi-objective optimization framework for day-ahead interaction between microgrids in active distribution networks considering flexible loads and energy storage systems. *J. Energy Storage* **2022**, *52*, 104739. [CrossRef]
40. Ravi, S.S.; Aziz, M. Utilization of electric vehicles for vehicle-to-grid services: Progress and perspectives. *Energies* **2022**, *15*, 589. [CrossRef]
41. Ben Slama, S. Prosumer in smart grids based on intelligent edge computing: A review on Artificial Intelligence Scheduling Techniques. *Ain Shams Eng. J.* **2021**, *13*, 101504. [CrossRef]
42. Solanke, T.U.; Ramachandaramurthy, V.K.; Yong, J.Y.; Pasupuleti, J.; Kasinathan, P.; Rajagopalan, A. A review of strategic charging–discharging control of grid connected electric vehicles. *J. Energy Storage* **2020**, *28*, 101193. [CrossRef]
43. Ahmad, A.; Khan, Z.A.; Saad Alam, M.; Khateeb, S. A review of the electric vehicle charging techniques, standards, progression and evolution of EV technologies in Germany. *Smart Sci.* **2018**, *6*, 36–53. [CrossRef]
44. Ahmadi, A.; Tavakoli, A.; Jamborsalamati, P.; Rezaei, N.; Miveh, M.R.; Gandoman, F.H.; Heidari, A.; Nezhad, A.E. Power quality improvement in smart grids using electric vehicles: A review. *IET Electr. Syst. Transp.* **2019**, *9*, 53–64. [CrossRef]
45. Ahmad, A.; Alam, M.S.; Chabaan, R. A Comprehensive Review of Wireless Charging Technologies for Electric Vehicles. *IEEE Trans. Transp. Electrif.* **2017**, *4*, 38–63. [CrossRef]
46. Amjad, M.; Ahmad, A.; Rehmani, M.H.; Umer, T. A review of EVs charging: From the perspective of energy optimization, optimization approaches, and charging techniques. *Transp. Res. Part D Transp. Environ.* **2018**, *62*, 386–417. [CrossRef]
47. Knez, M.; Zevnik, G.K.; Obrecht, M. A review of available chargers for electric vehicles: United States of America, European Union, and Asia. *Renew. Sustain. Energy Rev.* **2019**, *109*, 284–293. [CrossRef]
48. Al-Ogaili, A.S.; Hashim Tengku, T.J.; Rahmat, N.A.; Ramasamy, A.K.; Marsadek, M.B.; Faisal, M.; Hannan, M.A. Review on scheduling, clustering, and forecasting strategies for controlling electric vehicle charging: Challenges and recommendations. *IEEE Access* **2019**, *7*, 128353–128371. [CrossRef]
49. Adnan, N.; Nordin, S.M.; Rahman, I.; Amini, M.H. A market modeling review study on predicting Malaysian consumer behavior towards widespread adoption of PHEV/EV. *Environ. Sci. Pollut. Res.* **2017**, *24*, 17955–17975. [CrossRef]

50. Archsmith, J.; Muehlegger, E.; Rapson, D. Future Paths of Electric Vehicle Adoption in the United States: Predictable Determinants, Obstacles and Opportunities. NBER Working Paper No. w28933. 2021. Available online: https://ssrn.com (accessed on 30 January 2023).
51. Mandys, F. Electric vehicles and consumer choices. *Renew. Sustain. Energy Rev.* **2021**, *142*, 110874. [CrossRef]
52. Guerra, E.; Daziano, R. Electric vehicles and residential parking in an urban environment: Results from a stated preference experiment. *Transp. Res. Transp. Environ. Part D Transp. Environ.* **2020**, *79*, 10222. [CrossRef]
53. Miranda, J.L.; Delgado, C.J.M. Determinants of Electric Car Purchase Intention in Portugal. In *Governance and Sustainability (Developments in Corporate Governance and Responsibility)*; Crowther, D., Seifi, S., Eds.; Emerald Publishing Limited: Bingley, UK, 2020; Volume 15, pp. 161–172.
54. Higueras-Castillo, E.; Molinillo, S.; Coca-Stefaniak, J.; Liébana-Cabanillas, F. Potential Early Adopters of Hybrid and Electric Vehicles in Spain—Towards a Customer Profile. *Sustainability* **2020**, *12*, 4345. [CrossRef]
55. Rietmann, N.; Lieven, T. How policy measures succeeded to promote electric mobility—Worldwide review and outlook. *J. Clean. Prod.* **2019**, *206*, 66–75. [CrossRef]
56. Kowalska-Pyzalska, A.; Kott, M.; Kott, J. How Much Polish Consumers Know about Alternative Fuel Vehicles? Impact of Knowledge on the Willingness to Buy. *Energies* **2021**, *14*, 1438. [CrossRef]
57. Kowalska-Pyzalska, A.; Michalski, R.; Kott, M.; Skowrońska-Szmer, A. Consumer preferences towards alternative fuel vehicles. Results from the conjoint analysis. *Renew. Sustain. Energy Rev.* **2022**, *155*, 111776. [CrossRef]
58. De Oliveira, B.; Ribeiro da Silva, M.; Jugend, H.; De Camargo Fiorini, D.; Carlos Eduardo, P. Factors influencing the intention to use electric cars in Brazil. *Transp. Res. Part A Policy Pract.* **2022**, *155*, 418–433. [CrossRef]
59. Lashari, Z.A.; Ko, J.; Jang, J. Consumers' Intention to Purchase Electric Vehicles: Influences of User Attitude and Perception. *Sustainability* **2021**, *13*, 6778. [CrossRef]
60. Dasharathraj, S.; Smaran, S.; Lewlyn, R.; Nithesh, N.; Chetana, M.; Namesh, M.; Nilakshman, S. Barriers to widespread adoption of plug-in electric vehicles in emerging Asian markets: An analysis of consumer behavioral attitudes and perceptions. *Cogent Eng.* **2020**, *7*, 1796198. [CrossRef]
61. Colak, M.; Kaya, I. Providing the spark: Impact of financial incentives on battery electric vehicle adoption. *J. Environ. Econ. Manag.* **2020**, *98*, 102295.
62. Li, L.; Wang, Z.; Chen, L.; Wang, Z. Consumer preferences for battery electric vehicles: A choice experimental survey in China. *Transp. Res. Part D Transp. Environ.* **2020**, *78*, 102185. [CrossRef]
63. Bhalla, P.; Ali, I.; Nazneen, A. A Study of consumer perception and purchase intention of electric vehicles. *Eur. J. Sci. Res.* **2018**, *149*, 362–368.
64. Zhang, X.; Bai, X.; Shang, J. Is subsidized electric vehicles adoption sustainable: Consumers' perceptions and motivation toward incentive policies, environmental benefits, and risks. *J. Clean. Prod.* **2018**, *192*, 71–79. [CrossRef]
65. Eneizan, B. The adoption of electrics vehicles in Jordan based on theory of planned behavior. *Am. J. Econ. Bus. Manag.* **2019**, *2*, 1–14. [CrossRef]
66. Kim, S.; Choi, J.; Yi, Y.; Kim, H. Analysis of Influencing Factors in Purchasing Electric Vehicles Using a Structural Equation Model: Focused on Suwon City. *Sustainability* **2022**, *14*, 4744. [CrossRef]
67. Ho, J.C.; Huang, Y.H.S. Evaluation of electric vehicle power technologies: Integration of technological performance and market preference. *Clean. Responsible Consum.* **2022**, *5*, 100063. [CrossRef]
68. Kongklaew, C.; Phoungthong, K.; Prabpayak, C.; Chowdhury, S.; Khan, I.; Yuangyai, N.; Yuangyai, C.; Techato, K. Barriers to Electric Vehicle Adoption in Thailand. *Sustainability* **2021**, *13*, 12839. [CrossRef]
69. Khurana, A.; Kumar, R.; Sidhpuria, M. A Study on the Adoption of Electric Vehicles in India: The Mediating Role of Attitude. *Vision* **2020**, *24*, 23–34. [CrossRef]
70. Haider, S.W.; Zhuang, G.; Ali, S. Identifying and bridging the attitude-behavior gap in sustainable transportation adoption. *J. Ambient. Intell. Humaniz. Comput.* **2019**, *10*, 3723–3738. [CrossRef]
71. Ottesen, A.; Banna, S. Early Adopter Nation for Electric Vehicles: The Case of Iceland. In *Gulf Conference on Sustainable Built Environment*; Bumajdad, A., Bouhamra, W., Alsayegh, O., Kamal, H., Alhajraf, S., Eds.; Springer: Cham, Switzerland, 2020. [CrossRef]
72. Hardman, S.; Jenn, A.; Tal, G.; Axsen, J.; Beard, G.; Daina, N.; Figenbaum, E.; Jakobsson, N.; Jochem, P.; Kinnear, N.; et al. A review of consumer preferences of and interactions with electric vehicle charging infrastructure. *Transp. Res. Part D Transp. Environ.* **2018**, *62*, 508–523. [CrossRef]
73. Bhaskar, M.G.; Narahari, N.S.; Guptha, C.K.G. Consumer Preferences for mid-Segment electric cars—An Indian Perspective. *Int. J. Eng. Res. Technol.* **2020**, *9*, 1303–1309. [CrossRef]
74. Shareeda, A.; Al-Hashimi, M.; Hamdan, A. Smart cities and electric vehicles adoption in Bahrain. *J. Decis. Syst.* **2021**, *30*, 321–343. [CrossRef]
75. Jreige, M.; Abou-Zeid, M.; Kaysi, I. Consumer preferences for hybrid and electric vehicles and deployment of the charging infrastructure: A case study of Lebanon. *Case Stud. Transp. Policy* **2021**, *9*, 466–476. [CrossRef]
76. Vilchez, J.J.G.; Smyth, A.; Kelleher, K.; Lu, H.; Rohr, C.; Harrison, G.; Thiel, C. Electric Car Purchase Price as a Factor Determining Consumers' Choice and their Views on Incentives in Europe. *Sustainability* **2019**, *11*, 6357. [CrossRef]

77. Fan, R.; Chen, R. Promotion policies for electric vehicle diffusion in China considering dynamic consumer preferences: A network-based evolutionary analysis. *Int. J. Environ. Res. Public Health* **2022**, *19*, 5290. [CrossRef]
78. Lin, B.; Wu, W. Why people want to buy electric vehicle: An empirical study in first-tier cities of China. *Energy Policy* **2018**, *112*, 233–241. [CrossRef]
79. Al-Buenain, A.; Al-Muhannadi, S.; Falamarzi, M.; Kutty, A.A.; Kucukvar, M.; Onat, N.C. The Adoption of Electric Vehicles in Qatar Can Con-tribute to Net Carbon Emission Reduction but Requires Strong Government Incentives. *Vehicles* **2021**, *3*, 618–635. [CrossRef]
80. Vongurai, R. Factors Affecting Customer Brand Preference toward Electric Vehicle in Bangkok, Thailand. *J. Asian Financ. Econ. Bus.* **2020**, *7*, 383–393. [CrossRef]
81. Krejcie, R.V.; Morgan, D.W. Determining sample size for research activities. *Educ. Psychol. Meas.* **1970**, *30*, 607–610. [CrossRef]
82. Comrey, A.L.; Lee, H.B. *A First Course in Factor Analysis*; Erlbaum: Hillsdale, NJ, USA, 1992.
83. Pallant, J. *SPSS Survival Manual: A Step-by-Step Guide to Data Analysis Using SPSS for Windows (Version 15)*, 7th ed.; Allen & Unwin: London, UK, 2022.

designs

Article

Optimal Hybridization with Minimum Fuel Consumption of the Hybrid Fuel Cell Train

Mario Mišić [1,*], Marinko Stojkov [1], Rudolf Tomić [2] and Mario Lovrić [1]

[1] Mechanical Engineering Faculty, University of Slavonski Brod, 35000 Slavonski Brod, Croatia
[2] Faculty of Mechanical Engineering and Naval Architecture, University of Zagreb, 10000 Zagreb, Croatia
* Correspondence: mario.misic@yahoo.com

Abstract: This paper describes a numerical study of the optimal distribution of energy between fuel cells and auxiliary energy storages in the hybrid train. Internal combustion engines (ICEs) are currently under pressure from environmental agencies due to their harmful gas emissions, and pure battery vehicles have a short range; a hybrid train powered by fuel cells, batteries, and supercapacitors can provide a viable propulsion solution. In this study, special energy management on the mountain railway with optimal power distribution and minimum hydrogen consumption is proposed. Considering the characteristics of the mountain railway, the vehicle uses recuperation of regenerative braking energy and thus charges additional power devices, and hybridization optimization gives favorable power to each power source device with a minimum consumption of hydrogen in the fuel cell. In this study, a simulation model was created in a Matlab/Simulink environment for the optimization of hybridized power systems on trains, and it can be easily modified for the hybridization of any type of train. Optimization was performed by using Sequential quadratic programming (SQP). The results show that this hybrid train topology has the ability to recover battery and supercapacitor state of charge (SOC) while meeting vehicle speed and propulsion power requirements. The effect of battery and supercapacitor parameters on power distribution and fuel consumption was also simulated.

Keywords: optimization; hybridization; train; fuel cells; power management; SQP

Citation: Mišić, M.; Stojkov, M.; Tomić, R.; Lovrić, M. Optimal Hybridization with Minimum Fuel Consumption of the Hybrid Fuel Cell Train. *Designs* **2023**, *7*, 45. https://doi.org/10.3390/designs7020045

Academic Editors: Wenbin Yu and Guang Zeng

Received: 3 February 2023
Revised: 10 March 2023
Accepted: 13 March 2023
Published: 16 March 2023

1. Introduction

Since greenhouse gases have a great impact on the environment, various measures are being taken to reduce or perhaps even eliminate harmful emissions of exhaust gases. Trains are not big polluters in themselves [1], but limits for harmful gas emissions are still prescribed for diesel trains by Leaflet UIC624 (Table 1).

In order to decrease or completely eliminate the harmful emission of exhaust gases, hybrid vehicles powered by a fuel cell can be introduced [2,3]. Such vehicles do not pollute the environment, unlike diesel vehicles, and compared to pure battery vehicles, they have a much longer range.

The advantages of introducing hybrid fuel cell trains are:

- Zero harmful emissions of exhaust gases;
- Energy savings by recuperation of regenerative braking;
- Reduced mass of all power sources;
- Optimal power distribution on each auxiliary power source.

Hybrid vehicles can have numerous advantages over each individual component. A supercapacitor could enable instantaneous cold-start operation of auxiliary devices while the fuel cell warms up. If the temperature is not too low, the battery could run the train from the depot to the departure station during a cold start. A hybrid system can allow all drive components to be smaller in size and operate with greater efficiency since none would have to provide full load and capacity.

Table 1. UIC624 ICE Emission Standards [4].

Stage	Date	Power, P [kW]	Engine Speed, r [min^{-1}]	CO	HC	NOx	PM	Smoke
				g/kWh				
UIC I	up to 31 December 2002			3	0.8	12	-	1.6–2.5 [a]
UIC II	1 January 2003	$P \leq 560$		2.5	0.6	6.0	0.25	
		$P > 560$	$r > 1000$	3	0.8	9.5	0.25 [b]	
			$r \leq 1000$	3	0.8	9.9	0.25 [b]	

[a]—Bosch smoke number (BSN) = 1.6 for engines with an air throughput of above 1 kg/s; BSN = 2.5 for engines below 0.2 kg/s; linear BSN interpolation applies between these 2 values. [b]—For engines above 2200 kW, a PM emission of 0.5 g/kWh is accepted on an exceptional basis until 31 December 2004.

Fuel cells could have zero harmful emissions of exhaust gases only if the fuel is hydrogen. In general, fuel cells can also work with methanol, natural gas, and gasoline. Since such fuels, in addition to hydrogen, contain carbon, it is impossible to avoid the exhaust gas carbon dioxide. Since the aim of this paper is to achieve zero harmful emissions of exhaust gases, only hydrogen is considered as a fuel. When using hydrogen as fuel, a chemical process produces water and energy.

Software and algorithms for simulations and optimization can contribute significantly to research. Matlab software has already been used to develop train motion simulations with Object Oriented Programming (OOP). Research in [5] shows the movement of a train with optimal driving times, which was compared with the actual railway. It showed that the simulation is very effective and applicable for the research and application of train operations.

Likewise, ADVISOR software is also a good modeling and cost-effectiveness analysis tool that was used to introduce a fuel cell hybrid locomotive. According to the traction characteristics of the Indian WDM-7 locomotive and the fuel cell as the main power source, in a certain driving cycle, the dynamic performance of the hybrid system was verified using an advanced vehicle simulator [6].

Fuel cells, batteries, and supercapacitors are very expensive devices, and it is necessary to efficiently determine their hybridization ratios. The aim is to reduce the power of the fuel cell to the lowest value and to design the battery and supercapacitor with the lowest losses [7]. In ref. [8], the numerically verified methods of hybridization are presented, and thus the optimal values of the power source are selected.

The possibility of installing fuel cells in trains has already been researched [9]. In the mentioned paper, the operation of the shunting locomotive according to the actual working cycle is presented. Energy management and power distribution between power sources were developed but without optimization. Since the shunting locomotive has demanding work, it still works on a straight railway in shorter time intervals. This is a good template for simulating a train on a mountain railway and can still show better system performance.

Matlab-Simulink™ (M/S™) can also be used to develop tools such as TrEnO, which provides tools for optimizing total energy consumption [10]. The tool is also able to estimate the efficiency, power dissipation, and thermal behavior of the traction system components. It is used during the conceptual faze of train prototypes to optimize the overall traction and braking of trains on a given railway.

The SQP optimization tool is incorporated into the M/S™ environment [11]. One of the first steps is to model the train speed trajectory. The minimum energy consumption can be set as an optimization goal, and a trade-off between energy consumption and accuracy can be made using the train trajectory model [12].

In this study, the SQP algorithm is used to optimize the hybridization of power sources of the train [13]. The model uses SQP to find the optimal hybridization ratio between the fuel cell, the battery, and the supercapacitor according to the trajectory of the train movement on the mountain railway between Knin and Perković in Croatia. The simulation itself calculates the power of the fuel cell, battery, and supercapacitor according to the given load currents of each power source [14]. The aim is the lowest consumption of hydrogen in fuel cells [15].

The energy management developed in this paper is based on SOC control. It is designed to maintain the charge of the battery and supercapacitor with optimal values, and the design was developed based on the prototype of a passenger train and a mountain railway.

2. Materials and Methods

2.1. Model and Topology of the Train

The train model in this work is based on the HŽ7022 prototype train of Croatian Railways. The train's propulsion system is modeled as a hybrid of a fuel cell (FC), battery, and supercapacitor.

A passenger train has a uniform demand for maximum power during acceleration and cruising for reduced power that must overcome the force of movement resistance. In order to analyze the electricity demand of the train, a typical timetable with a railway profile was set according to the real railway in Croatia between Knin and Perković [16].

The simulation model in M/S™ calculates the traction power at the wheels according to the railway trajectory and calculates the distribution of total train power between the power sources. The traction system topology used in trains can be connected in series or in parallel. The traction hybrid system for this train is connected in series [17] (Figure 1). Induction motors are connected to an IGBT (insulated gate bipolar transistor) converter that is connected to DC/DC converters that are directly connected to power sources [18]. The battery and supercapacitor are connected to bidirectional DC/DC converters for charging/discharging, while FC is connected to a chopper, a converter in one direction [19].

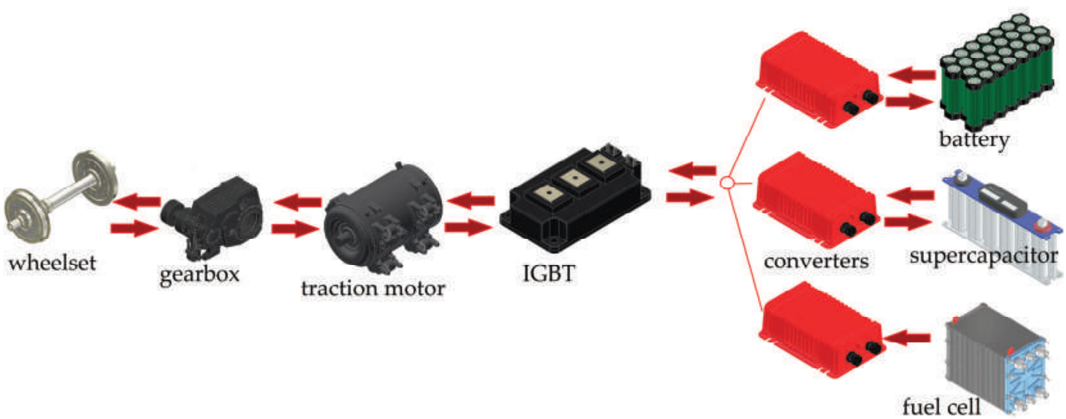

Figure 1. Power flow according to traction system topology.

According to the existing DMU (diesel multiple unit) train that will be converted into a hybrid fuel cell train, the maximum traction power is 1255 kW, and the maximum traction force is 125 kN. In a hybrid fuel cell train, the total power will be obtained from the fuel cell and auxiliary energy storage devices and taken over by the IGBT. The voltage on the IGBT is 2.4 kV, which is provided by the converters of power devices that receive a voltage of 0.8 kV. Such a high voltage generally corresponds well to the requirements of the drive system and enables lower losses in the power system.

The advantage of such a parallel system is the different voltages of the power sources. Each power source can work at its nominal voltage because the converter will raise the voltage to 2.4 kV, which is necessary for IGBT. However, it is desirable that the voltages of all power sources are approximately the same and as high as possible because the losses will be the lowest.

2.2. Energy Management System

The power flow passes with losses, and the energy management coordinates the operation of power devices and distributes the power to devices according to the hybridization ratio (Figure 2). When accelerating, energy management uses a fuel cell, battery, and supercapacitor for traction. For cruising, the supercapacitor performs traction until a state of charge SOC_{sc} = 0.01, and then the battery is used. If, during acceleration and cruising, the climb is greater than 15%, all devices are switched on. If SOC_b = 0.2, traction is performed by supercapacitor, and fuel cell will charge the battery. The battery drives the traction only after the supercapacitor is discharged (SOC_{sc} = 0.01). Regenerative braking will first charge the supercapacitor to SOC_{sc} =1, and the battery only will be charged after supercapacitor is fully charged. Energy management does not allow SOC_b = 0.2 and SOC_{sc} = 0.01 at the same time.

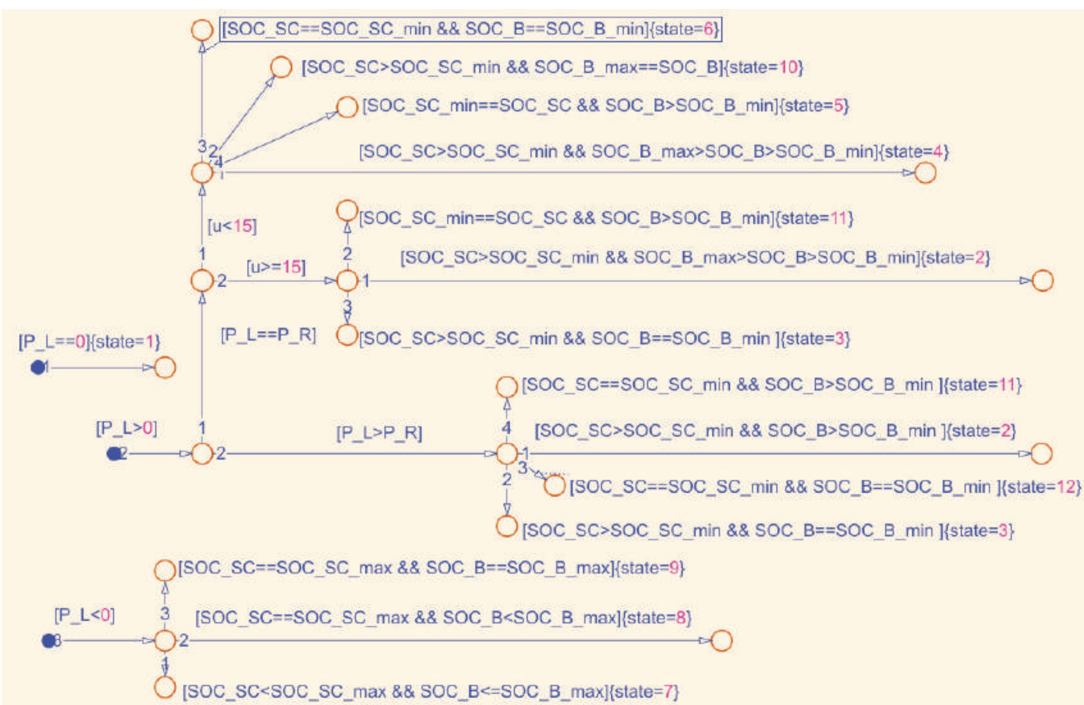

Figure 2. Energy management.

The hybridization ratio is affected by the total power, the properties of the railway, and the strength of the discharge currents of the fuel cell, battery, and supercapacitor.

2.3. Traction Force

Total power of the train is calculated as

$$P_{tot} = F_{tot} \cdot v_{tr} = (P_{fc} \cdot \eta_{fc} \cdot \eta_{dc} + P_b \cdot \eta_{dc} + P_{sc} \cdot \eta_{dc}) \cdot \eta_{ti} \cdot \eta_{tm} \cdot \eta_{gb}, \quad (1)$$

where F_{tot} *is* the total force for movement in N, v_{tr} is the train speed in m/s, P_{fc} is the fuel cell power in W, η_{fc} is the fuel cell efficiency, η_{dc} is the DC/DC converter efficiency, P_b is the battery power in W, P_{sc} is the supercapacitor power in W, η_{ti} is the traction inverter efficiency, η_{tm} is the traction motor efficiency, and η_{ti} is the gear box efficiency. For regenerative braking, each efficiency is calculated reciprocally ($1/\eta$), except for the fuel cell.

The total power (the total force) must be sufficient to overcome all resistances of the train:

$$F_{tot} \cdot a = F_{tr,\max} - F_{dr} - F_{gr} - F_{cu} \tag{2}$$

$$a = \pm\frac{1}{m_{tot}}(F_{tr,\max} - (r_{rr} + r_{pm} \cdot v_{tr} + r_{ar} \cdot v_{tr}{}^2)) - g \cdot (g_{rt} + \frac{0.5g}{R-30}), \tag{3}$$

$$v_{tr} = \int a\mathrm{d}t, \tag{4}$$

where F_{tr} is the traction force on wheels in N (positive for traction, negative for braking); m_{tot} is the total mass of the train in kg, increased by 6% due to the inertia of the rotating masses [20]; r_{rr} is the rolling resistance force in N; r_{pm} is the resistance coefficient of parasitic movements in N/kmh^{-1}; r_{ar} is the air resistance coefficient in N/(kmh^{-1})^2; v_{tr} is the train speed in km/h; g is the gravitational acceleration; g_{rt} is the gradient of the railway in ‰; and R is the radius of curvature of the railway in m.

The traction force of the train is achieved up to the critical speed through torque, and after that, through the power of the traction motor. The torque is constant, and therefore the traction force is also constant. The manufacturer always provides the highest constant traction force on the wheels resulting from the torque. When a critical speed is reached, the traction force decreases with increasing speed. Accordingly, the traction force is:

$$F_{tr,\max} = \begin{cases} F_{tr,\max};\ \forall 0 \le v_{tr} \le v_{cr} \\ F_{tr,\max} = \frac{P_{tot}}{v_{tr}};\ \forall v_{cr} < v_{tr} \le v_{\max} \end{cases} \tag{5}$$

For acceleration, the train will use the maximum traction force; for cruising, the traction force will be equal to the total movement resistance forces; and for regenerative braking, it will use the maximum braking force (Figure 3).

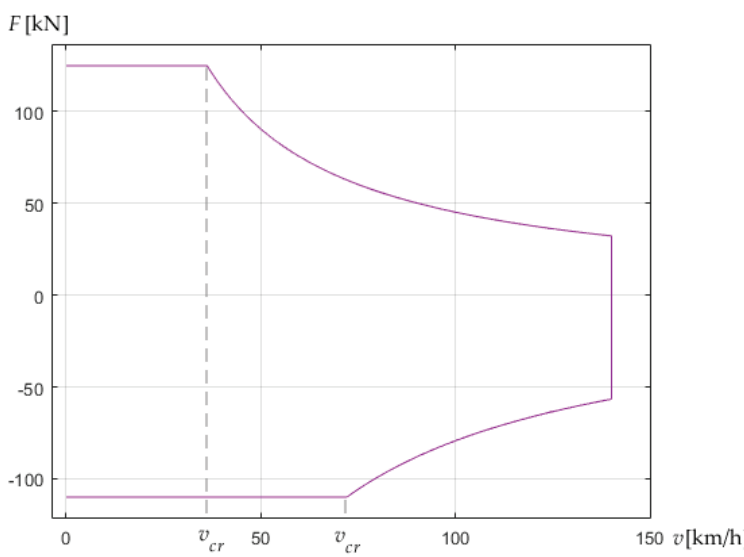

Figure 3. Traction properties of the train.

In Figure 4, the railway profile is depicted. The yellow line represents the gradient of the railway in ‰, the red line represents the speed limit, and the blue line represents train speed.

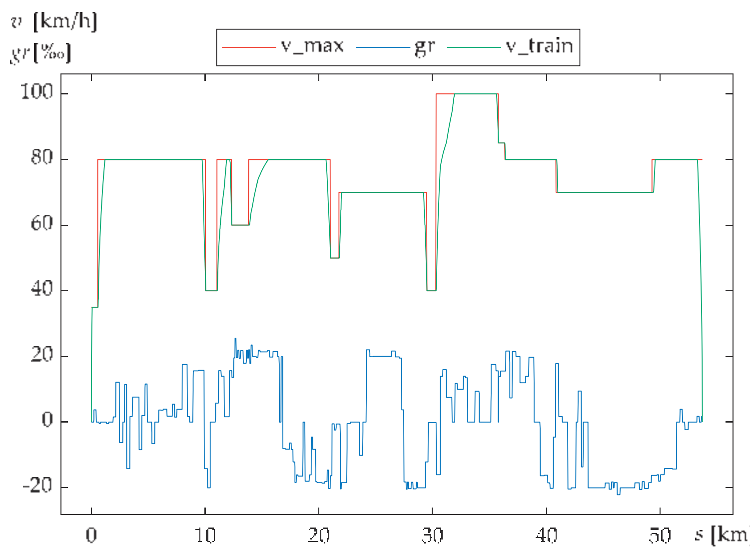

Figure 4. The railway profile.

In Figure 5, red line represents power demand, and green line represents resistance force of the railway.

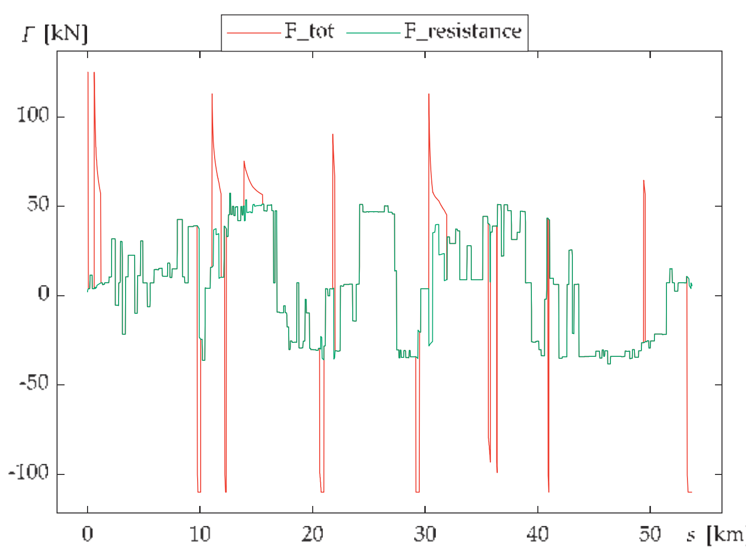

Figure 5. Demand force and the resistance force of the railway.

Based on the railway profile data depicted in Figure 5 and train parameters, resistance power and demand power were calculated. Figure 4 shows the calculated power distribution on the railway. Green line represents calculated resistance power, and red line represents the necessary traction power for the simulated train.

The railway is extremely hilly and full of radiuses, which thoroughly tests the endurance of all power sources and shows whether regenerative braking can store enough energy to make the system sustainable.

2.4. Fuel Cell

Fuel cells are devices that convert chemical energy into electrical energy. The fuel cell system contains a fuel supply system, an air supply system, a water management system, and a fuel cooling system. They include AFC (alkaline fuel cell), PEMFC (Polymer Electrolyte Membrane), DMFC (Direct Methanol), PAFC (Phosphoric Acid), MCFC (Molten Carbonate), and SOFC (Solid Oxide). Only PEMFC has zero harmful emissions of exhaust gases.

PEMFC operates at relatively low temperatures and has a high power density. It cannot change the output power very fast, so PEMFC has slow dynamics. This can be compensated by faster dynamics from storage devices. The voltage of one cell is about 1 V with a current density of 0.5 A/cm^2 to 1 A/cm^2. To obtain higher power, the cells are joined in stacks. The fuel is hydrogen, and pure oxygen or oxygen from the air can be used as an oxidant.

PEMFC can reach 1.3 kW/L power density, 0.6 kW/L system power density, and 0.6 kW/kg mass-specific power density. It operates at low temperatures and can be started and operated in sub-zero temperatures, although normal operating temperatures are 20–90 °C [21]. For the above reasons, PEMFC was chosen for this study, even though other cells exist.

The load power of the fuel cell stack is:

$$P_{fc} = U_{fc} \cdot I_{Load,fc} \tag{6}$$

$$P_{fc} = (E_{oc} - U_{act} - U_{ohm}) I_{Load,fc} \tag{7}$$

where U_{fc} is the fuel cell stack voltage in V, $I_{Load,fc}$ is the fuel cell current load in A, E_{oc} is the open circuit voltage in V, U_{ohm} is the ohmic voltage drop in V, and U_{act} is the activation voltage drop in V [22].

2.5. Battery

Lithium iron phosphate ($LiFePO_4$) is the safest cathode material used for the high-power modules required in hybrid vehicles. The advantages of this type of battery are the theoretical specific capacity of 170 Ah/kg and greater thermal stability against the release of oxygen, which makes it safer and more tolerant under extreme operating conditions [23].

It can change the output power much faster than a fuel cell, so it can compensate for power in the fuel cell. In the nominal operating range of the battery, during discharge, the voltage changes slightly. When the rated capacity is discharged, the battery enters the operating range, where the battery voltage decreases rapidly.

The load power of the battery cell for discharging is:

$$P_b = U_b \cdot I_{Load,b} \tag{8}$$

$$P_b = \left(E_0 - K\frac{Q_b}{Q_b - I_{load,b} \cdot t} I_{load,b} \cdot t - K\frac{Q_b}{Q_b - I_{load,b} \cdot t} I_{load,b} - R_b \cdot I_{load,b} + A \cdot e^{(-B \cdot I_{load,b} \cdot t)}\right) I_{load,b} \tag{9}$$

where U_b is the battery cell voltage in V, E_0 is the constant voltage in V, K is the polarization constant or the polarization resistance in Ω, Q_b is the standard battery capacity in Ah, $I_{Load,b}$ is the battery current load in A, R_b is the battery internal resistance in Ω, A is the voltage drop during the exponential zone in V, and B is the exponential time inverse constant in Ah^{-1}.

The load power of battery for charging is:

$$P_b = (E_0 - K\frac{Q_b}{Q_b - I_{load,b} \cdot t} I_{load,b} \cdot t - K\frac{Q_b}{I_{load,b} \cdot t - 0.1Q_b} I_{load,b} - R_b \cdot I_{load,b} + A \cdot e^{(-B \cdot I_{load,b} \cdot t)}) I_{load,b} \quad (10)$$

State of charge is:

$$SOC_b = 1 - \frac{1}{Q_b}\int I_{Load,b}\mathrm{d}t \quad (11)$$

2.6. Supercapacitor

Supercapacitor (EDCL, Electrochemical Double Layer Capacitors) is a device used for energy storage, and it has high energy and power densities, high efficiency (almost 95%), and long lifetime. The main property of supercapacitor is the possibility of rapid charging and discharging without loss of efficiency (>95%) during thousands of cycles [24].

Supercapacitors can be recharged in a very short time and have an excellent ability to change the output power very fast, faster than battery, and to operate with frequent peak power demands. All these reasons improve the efficiency of the vehicle and save energy, so they are suitable for installation. They especially show their excellent properties during regenerative braking.

The load power of the supercapacitor cell is:

$$P_{sc} = U_{sc} \cdot I_{Load,sc} \quad (12)$$

$$P_{sc} = (U_1 + R_1 \cdot I_{Load,sc}) \cdot I_{Load,sc} \quad (13)$$

$$P_{sc} = (\frac{-C_0 + \sqrt{{C_0}^2 + 2C_v \cdot Q_1}}{C_v} + R_1 \cdot I_{Load,sc}) \cdot I_{Load,sc} \quad (14)$$

where U_{sc} is the voltage of the supercapacitor cell in V, R_1 is the resistance of the supercapacitor's main cell in Ω, $I_{Load,sc}$ is the supercapacitor's load current in A, U_1 is the voltage of the supercapacitor's main cell in V, C_0 is the constant capacitance in F, C_v is the constant parameter in F/V, and Q_1 is the instantaneous charge in the supercapacitor's main cell in As.

State of charge is:

$$SOC_{sc} = 1 - \frac{1}{Q_{sc}}\int I_{Load,sc}\mathrm{d}t \quad (15)$$

2.7. Method of Sequential Quadratic Programming

To solve the nonlinearity and non-convexity of the resulting optimal control problem, sequential quadratic programming is used [25]. SQP is used to optimally control the management of power sources with the aim of the lowest amount of fuel consumption.

The main objective function for minimization is:

$$\min f(x) = \int_{t_0}^{t_f} P_{tot}(v(t), s(t), u(t))\mathrm{d}t \quad (16)$$

where $v(t)$ is the speed of the train; $s(t)$ is the distance; and $u(t)$ is the set of all variables that affect driving, as shown by Equation (3).

To obtain the minimum fuel consumption, which is directly a function of energy, it is necessary to determine the discrete-time formulation of the problem. The problem of energy consumption is defined by hybridization ratios [26]. Minimization is achieved by composing a Quadratic Programming (QP) subproblem based on the quadratic approximation of the Lagrange function [27].

$$L(x, \lambda) = f(x) + \sum_{i=1}^{m} \lambda_i g_i(x) \quad (17)$$

where $f(x)$ is the main objective function, $g_i(x)$ are the inequality constraints, λ_i are Lagrange multipliers under the non-negativity constraint, and m is the total number of restrictions.

QP subproblem is given by

$$\begin{array}{l} \min\limits_{d\in\Re^n} \frac{1}{2} d^T H_k d + \nabla f(x_k)^T d \\ \nabla g_i(x_k)^T d + g_i(x_k) = 0,\ i = 1,\ldots,m_e \\ \nabla g_i(x_k)^T d + g_i(x_k) \leq 0,\ i = m_e+1,\ldots,m \end{array} \tag{18}$$

where d is the number of iterations, H_k is the Hessian Matrix, and m_e is the equality constraints number. Updated, the Hessian Matrix is:

$$H_{k+1} = H_k + \frac{q_k q_k^T}{q_k^T s_k} - \frac{H_k s_k s_k^T H_k^T}{s_k^T H_k s_k} \tag{19}$$

where

$$\begin{array}{l} s_{k+1} = x_{k+1} - x_k \\ q_k = (\nabla f(x_{k+1}) + \sum\limits_{i=1}^{m} \lambda_i \nabla g_i(x_{k+1})) - (\nabla f(x_k) + \sum\limits_{i=1}^{m} \lambda_i \nabla g_i(x_k)) \end{array} \tag{20}$$

Duration of the simulation in time, boundary conditions, and time-dependent constraints and control variables are:

$$g_i(x) = \begin{cases} I_{sc,\min} \leq I_{Load,sc} \leq I_{sc,\max} \\ I_{b,\min} \leq I_{Load,b} \leq I_{b,\max} \\ SOC_{sc,\min} \leq SOC_{sc} \leq SOC_{sc,\max} \\ SOC_{b,\min} \leq SOC_b \leq SOC_{b,\max} \\ hr_{sc,\min} \leq hr_{sc} \leq hr_{sc,\max} \\ hr_{b,\min} \leq hr_b \leq hr_{b,\max} \end{cases} \tag{21}$$

where $I_{Load,sc}$ is the discharge current of the supercapacitor, $I_{Load,b}$ is the discharge current of the battery, SOC_{sc} is the state of charge of the supercapacitor, SOC_b is the state of charge of the battery, hr_{sc} is the supercapacitor hybridization ratio, and hr_b is the battery hybridization ratio.

2.8. Model Parameters

In the simulation model, the PEMFC modules "Ballard" Fcvelocity-HD6, rechargeable LFP battery "Lithium Werks" 26650, and "Maxwell" supercapacitor BCAP3000 were used (Table 2). According to the proportion of hybridization, the power used to discharge the battery and the supercapacitor was determined. In the simulation model, it was set that the algorithm optimizes the discharge current and thus obtains the optimal hybridization ratio for both the battery and the supercapacitor. As a result, the optimal discharge current of both the battery and the supercapacitor was obtained. The load currents are:

$$I_{Load,sc} = \frac{hr_{sc} \cdot P_{tot}}{U_{sc} \cdot n_{par,sc} \cdot n_{ser,sc}} \tag{22}$$

$$I_{Load,b} = \frac{hr_b \cdot P_{tot}}{U_b \cdot n_{par,b} \cdot n_{ser,b}} \tag{23}$$

where $n_{par,sc}$ is the number of supercapacitor cells in parallel, $n_{ser,sc}$ is the number of supercapacitor cells in series, $n_{par,b}$ is the number of battery cells in parallel, $n_{ser,b}$ is the number of battery cells in series, and P_{tot} is demand power.

Table 2. Power sources properties.

Fuel Cell Stack			Battery Cell		
Rated power	P_{fc}	150 kW	Rated voltage	U_0	3.3 V
Idle power	$P_{fc,\min}$	6 kW	Rated capacity	Q_0	2.56 Ah
Maximum load current	$I_{fc,\max}$	320 A	Maximum charging current	$I_{ch,\max}$	10 A
Mass	m_{fc}	404 kg	Maximum discharging current	$I_{dis,\max}$	20 A
Average hydrogen consumption	m_{H2}	2.5 g/s	Mass	m_B	76 g
Supercapacitor Cell			**Train**		
Nominal capacitance	C_{sc}	3000 F	Tractive power	$P_{tr,\max}$	1255 kW
Rated voltage	U_{sc}	2.7 V	Tractive force	$P_{tr,\max}$	125 kN
Maximum discharging current	$I_{sc,\max}$	160 A	Braking power	$P_{br,\max}$	2200 kW
Mass	m_{sc}	506.7 g	Braking force	$P_{br,\max}$	110 kN
			Mass	m_{tot}	191 t

The fuel cell stack load current is:

$$I_{Load,fc} = \frac{hr_{fc} \cdot P_{tot}}{U_{fc} \cdot n_{par,sc}} \tag{24}$$

where hr_{fc} is the fuel cell stack hybridization ratio, and $n_{par,fc}$ is the number of fuel cell stacks in parallel.

First, the optimization parameters with boundaries in the simulation and the objective function with the final desired value are selected (Figure 6).

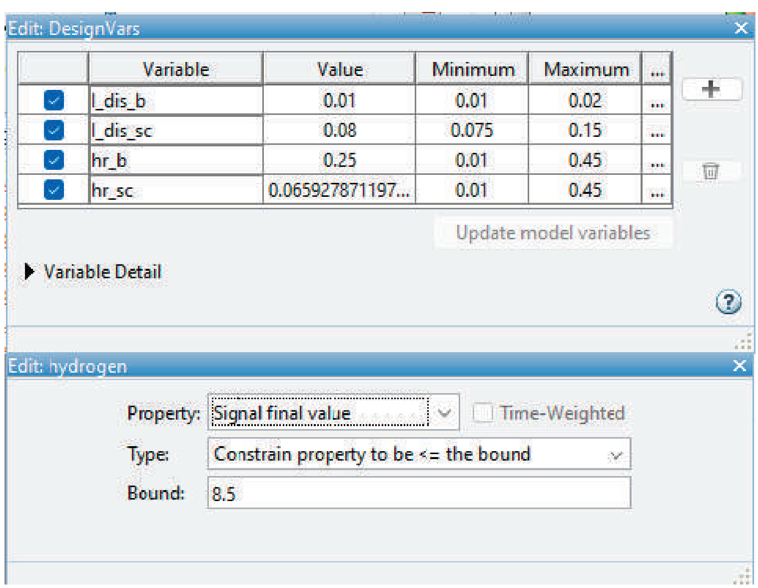

Figure 6. Setting of the main objective function, constraints, and boundaries (current in kA).

Boundaries for the hybridization ratio have been proven, and it has already been shown that with the ratio hr_b/hr_{fc} = 0.33, the vehicle can travel the most kilometers per kilogram of hydrogen. Since the supercapacitor also participates in traction, the upper boundary is 0.45 for both energy stores, as there is space for optimization. If the system does not converge, the values will expand [28].

Energy storages discharge current constraints are set according to the manufacturer's datasheet.

3. Results and Discussion

In the simulation, randomly selected parameters were taken and then optimized. Simulation results are values for the battery hybridization ratio, supercapacitor hybridization ratio, battery discharge current, and supercapacitor discharge current. Optimal parameter values for the presented study were obtained through iteration (Table 3, Figure 7).

Table 3. Optimized parameters.

Parameter		Start	Optimized
Battery hybridization ratio	hr_b	0.25	0.39
Supercapacitor hybridization ratio	hr_{sc}	0.05	0.06592787
Battery discharge current	$I_{dis,b}$	0.01 kA	0.017 kA
Supercapacitor discharge current	$I_{dis,sc}$	0.090.08 kA	0.0801 kA

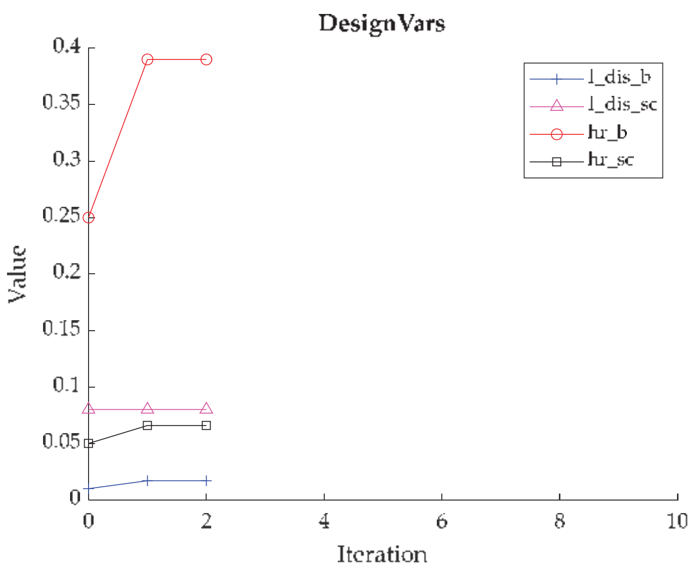

Figure 7. Iteration of parameters.

The optimal values were calculated through 2 iterations. Figure 7 depicts the iteration process.

With the optimal parameters for the proposed hybrid system, the consumption of hydrogen is 8 kg over a distance of 53.71 km, which the train travels in 2717 s. During acceleration or when driving uphill, energy management uses the power of the fuel cell, the battery, and the supercapacitor together. When cruising, the supercapacitor is first completely discharged, and then the battery is used. In order not to discharge both the battery and the supercapacitor at the same time, energy management determines the optimal hybridization ratio. Likewise, if only the supercapacitor is pulling the train, the fuel cell charges the battery. The hybridization ratio of the fuel cell is obtained by $hr_{fc} = 1 - hr_b - hr_{sc}$, which determines the power of the fuel cell and can be said to be optimal.

All that data can be graphically shown with the presented simulation model. Figure 8 shows the difference in hydrogen consumption for randomly selected and optimized parameters of the propulsion system. The optimized solution yields a decrease in fuel consumption of 14.7%. That is a saving of 1.373 kg of hydrogen compared to the initial solution.

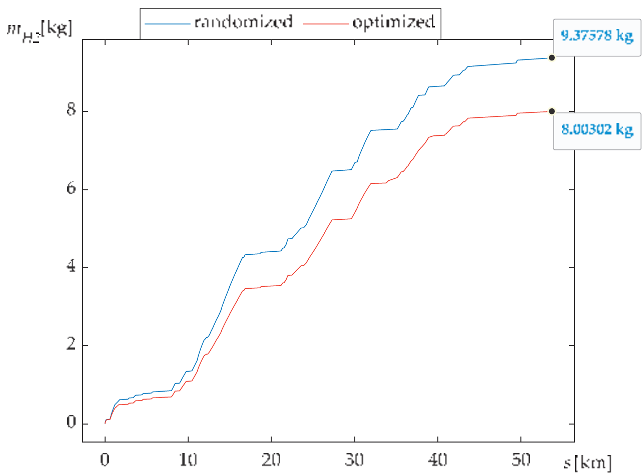

Figure 8. Consumption of the hydrogen (red is optimized, blue is randomized).

Since hydrogen consumption is a consequence of energy consumption, the consumed energy for the optimized solution is 216.99 kWh (Figure 9). Compared to the initial solution of 283.15 kWh, the optimized system results in a decrease in energy consumption of 23.37%. Due to the optimal selection of parameters and energy management that uses power sources according to given conditions, savings are possible. The profile of the railway with pronounced uphills and downhills enables regenerative braking, which is optimally used to discharge and charge the energy storage and thus save energy (Figure 10).

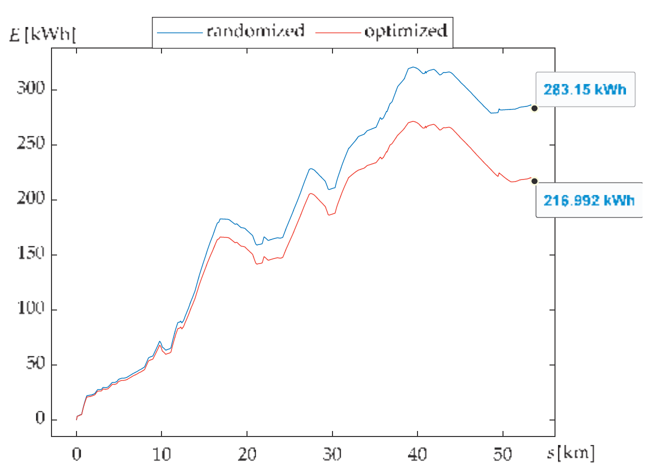

Figure 9. Demand of the energy (red is optimized, blue is randomized).

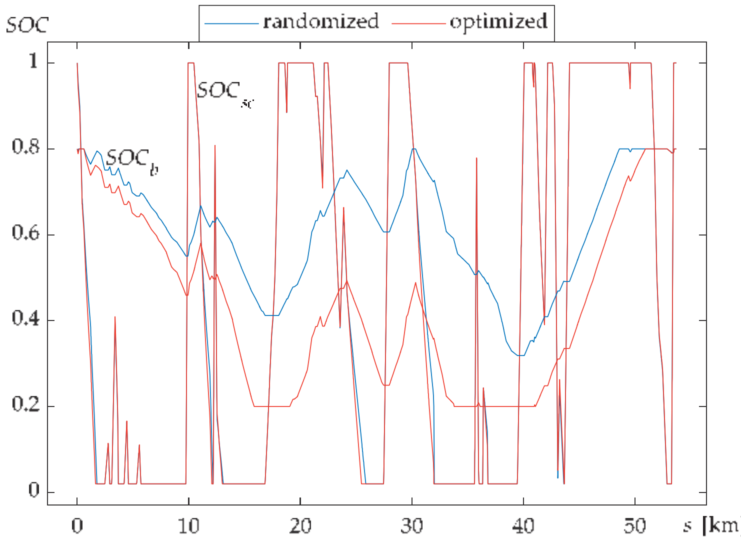

Figure 10. SOC of the battery and the supercapacitor (red is optimized, blue is randomized).

Due to the different losses in the devices, according to the hybridization ratios, the total power of all power sources will not always be the same. Consequently, with the optimal hybridization ratio, a lower required total power to propel the train was achieved. By comparing the required train power on the modeled railway for the initial and optimized drive system, this was revealed during acceleration and regenerative braking (Figure 11).

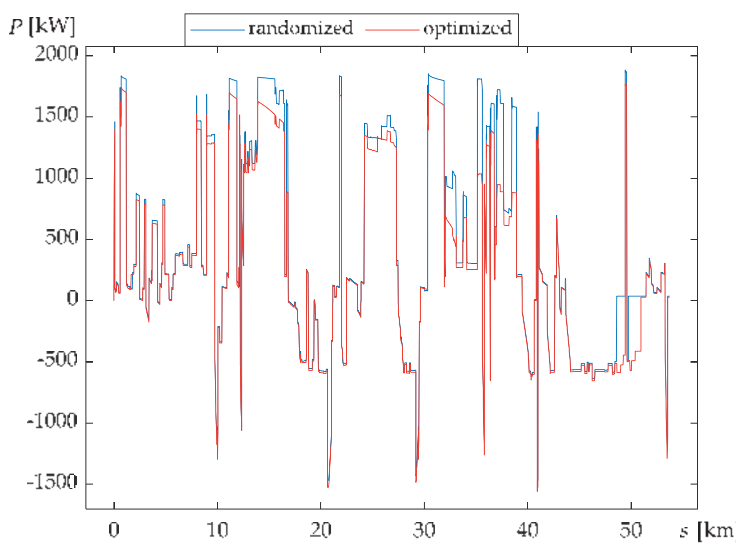

Figure 11. Demand for power (red is optimized, blue is randomized).

According to all losses, the highest power of all power sources is 1772 kW. According to the optimal hybridization ratio, the fuel cell consumes 964 kW. This power requires 7 stacks of fuel cells, which have a total mass of 2828 kg. The fuel cell with 7 stacks has 1050 kW, which means that the rest of the optimal value is used to propel auxiliary devices.

Since the hybridization ratio and discharge current of the battery package are found through optimization, the battery package has a power of 691 kW. The operating voltage of each power source is 800 V, so 243 cells will be connected in series in the battery package. According to the discharge current in the battery package, 52 cells will be connected in parallel. The mass is 960 kg.

The same types of parameters affect the supercapacitor. According to the operating voltage, 296 cells are connected in series in a supercapacitor package. By optimizing the hybridization ratio and the discharge current, the supercapacitor package has a power of 117 kW, and 2 cells are connected in parallel. According to this connection, the mass is 302 kg.

4. Conclusions

This paper presents the development of a hybrid power train system with fuel cells and presents the parameters of each component. A new energy management strategy based on railway loads and the state of charge of the energy storage is proposed. Then, the system was optimized using the SQP method, and the hydrogen consumption was calculated. By optimizing using Matlab/Simulink, it was shown that the mass of the train and the consumption of hydrogen could be reduced.

Because the railway is sharp and demanding, the energy management had to be different than what is usually set. Big uphill transits consume a lot of energy, but traveling downhill can be used for energy regeneration, which is why supercapacitor charging is used when traveling downhill, while the battery is charged via the fuel cell only when the supercapacitor conducts the traction itself. Nevertheless, the simulation showed that the train could overcome such a railway and, at the same time, find the lowest hydrogen consumption with optimal hybridization parameters and discharge currents. The result is a 14.7% decrease in hydrogen fuel consumption and 23.37% less energy consumed.

The current fuel cell systems do not leave much space for optimization. Only by optimally choosing the hybridization ratios of the battery and the supercapacitor can the power of the fuel cell be said to be optimal. The batteries and supercapacitors are delivered in smaller cells, and they give the possibility of optimization.

On the existing train prototype, the total mass of 3 diesel engines and 3 alternators is around 7300 kg. By optimizing the hybrid train with fuel cells, the mass of the power sources (including converters and inverter) was obtained at less than 4091 kg, which indicates that a fuel cell hybrid train is favorable for mass reduction. Therefore, it can be argued that a fuel cell hybrid train can have the same acceleration as a diesel train, which is important in passenger traffic.

The presented simulation model could be a useful tool in the conceptual development phase of future hybrid train propulsion systems and train modifications and shorten the development time of future environmentally friendly railway systems.

Author Contributions: Conceptualization, M.M.; methodology, R.T.; software, M.M.; validation, M.S., M.L. and R.T.; formal analysis, R.T.; investigation, M.M.; writing—original draft preparation, M.M.; writing—review and editing, M.S. and R.T.; visualization, M.L.; All authors have read and agreed to the published version of the manuscript.

Funding: This research received no external funding.

Institutional Review Board Statement: Not applicable.

Informed Consent Statement: Not applicable.

Data Availability Statement: Battery: https://lithiumwerks.com/ (accessed on 1 February 2023). Supercapacitor: https://maxwell.com/products/ultracapacitors/ (accessed on 1 February 2023). Fuel cell: https://www.ballard.com/ (accessed on 1 February 2023).

Conflicts of Interest: The authors declare no conflict of interest.

References

1. Cui, Z.; Chen, J.; Li, C.; Yin, Y.; Hao, M. The Calculation and Analysis of Carbon Emission in Traction Power Supply System of High-Speed Rail. *Tech. Gaz.* **2023**, *30*, 226–234.
2. Shang, W.; Yu, S.; Zhang, G.; Li, Q.; Chen, W. Fuel cell hybrid locomotive system based on equivalent consumption minimization strategy. In Proceedings of the Chinese Automation Con-Gress (CAC), Jinan, China, 20–22 October 2017. [CrossRef]
3. Abdelrahman, A.; Attia, Y.; Woronowicz, K.; Youssef, M. Hybrid Fuel Cell/Battery Rail Car: A Feasibility Study. *IEEE Trans. Transp. Electrif.* **2016**, *2*, 493–503. [CrossRef]
4. International Union of Railways. *UIC Code 624-Exhaust Emission Tests for Diesel Traction Engines*; International Union of Railways: Paris, France, 2017; ISBN 978-2-7461-2575-9.
5. Sumpavakup, C.; Kulworawanichpong, T. Multi-Train Movement Simulation Using MATLAB Object-Oriented Programming. *Appl. Mech. Mater.* **2015**, *763*, 153–158. [CrossRef]
6. Sarma, U.; Ganguly, S. Modelling and cost-benefit analysis of PEM fuel-cell-battery hybrid energy system for locomotive application. In Proceedings of the Technologies for Smart-City Energy Security and Power (ICSESP), Bhubaneswar, India, 28–30 March 2018.
7. Saw, L.; Somasundaram, K.; Ye, Y.; Tay, A. Electro-thermal analysis of Lithium Iron Phosphate battery for electric vehicles. *J. Power Sources* **2014**, *249*, 231–238. [CrossRef]
8. Tsukahara, K.; Kondo, K. A study on methods to design and select energy storage devices for Fuel Cell hybrid powered railway vehicles. In Proceedings of the 39th Annual Conference of the IEEE Industrial Electronics Society, Vienna, Austria, 10–13 November 2013.
9. Guo, L.; Yedavalli, K.; Zinger, D. Design and modeling of power system for a fuel cell hybrid switcher locomotive. *Energy Convers. Manag.* **2011**, *52*, 1406–1413. [CrossRef]
10. Malvezzi, M.; Pugi, L.; Conti, R.; Toni, P.; Tesi, S.; Meli, E.; Rindi, A. A Tool for Pre-diction and Optimization of Railway Traction Systems with Respect to an Expected Mis-sion Profile. *Chem. Eng. Trans.* **2013**, *33*, 7.
11. Angalaeswari, S.; Jamuna, K. Optimal Energy Management Using Sequential Quadratic Programming Algorithm for Stand Alone PV System. *Int. J. Appl. Eng. Res.* **2017**, *12*, 12250–12255.
12. Liu, X.; Xun, J.; Ning, B.; Liu, T.; Xiao, X. Moving Horizon Optimization of Train Speed Profile Based on Sequential Quadratic Programming. In Proceedings of the International Conference on Intelligent Rail Transportation (ICIRT), Singapore, 12–14 December 2018.
13. Khalik, Z.; Padilla, G.; Romijn, T.; Donkers, M. Vehicle Energy Management with Ecodriving: A Sequential Quadratic Programming Approach with Dual Decomposition. In Proceedings of the Annual American Control Conference (ACC), Milwaukee, WI, USA, 27–29 June 2018.
14. Ning, Q.; Xuan, D.; Nan, Y.; Kim, Y. Modeling and Simulation for Fuel Cell-Battery Hybrid Electric Vehicle. In Proceedings of the International Conference on Computer Modeling and Simulation, Washington, DC, USA, 20–22 February 2009.
15. Barbir, F. *PEM Fuel Cells: Theory and Practice*; Elsevier Inc.: Waltham, MA, USA, 2013.
16. *Croatian Railways-Infrastructure, Izvješće o Mreži*; Croatian Railways-Infrastructure: Zagreb, Croatia, 2022.
17. Furuta, R.; Kawasaki, J.; Kondo, K. Hybrid Traction Technologies with Energy Storage Devices for Nonelectrified Railway Lines. *IEEJ Trans. Electr. Electron. Eng.* **2010**, *5*, 291–297. [CrossRef]
18. Sehrili, E.; Cetinceviz, Y. Comparasion of Average Curent Controlled PFC SEPIC and CUK Converter Feeding Current Controlled SRM. *Tech. Gaz.* **2020**, *29*, 1789–1795. [CrossRef]
19. Lai, C.-M. Development of a Novel Bidirectional DC/DC Converter Topology with High Voltage Conversion Ratio for Electric Vehicles and DC-Microgrids. *Energies* **2016**, *9*, 410. [CrossRef]
20. Serdar, J. *Lokomotive-Opci Dio*; Sveucilisna Naklada Liber: Zagreb, Croatia, 1977.
21. Mench, M. *Fuel Cell Engines*; John Wiley & Sons, Inc.: Hoboken, NY, USA, 2008.
22. Hong, Z.; Han, Y.; Li, Q.; Chen, W. Design of Energy Management System for Fuel Cell/Supercapacitor Hybrid Locomotive. In Proceedings of the IEEE Vehicle Power and Propulsion Conference (VPPC), Hangzhou, China, 17–20 October 2016. [CrossRef]
23. Beninati, S.; Damen, L.; Mastragostino, M. Fast sol–gel synthesis of LiFePO4/C for high power lithium-ion batteries for hybrid electric vehicle application. *J. Power Sources* **2009**, *194*, 1094–1098. [CrossRef]
24. Tashima, D.; Samantara, A. *Supercapacitors for the Next Generation*; IntechOpen: London, UK, 2022.
25. Kyoungcheol, O.; Jeongmin, K.; Dongho, K.; Donghoon, C.; Hyunsoo, K. Optimal power distribution control for parallel hybrid electric vehicles. In Proceedings of the IEEE International Con-Ference on Vehicular Electronics and Safety, Xi'an, China, 14–16 October 2005.
26. Ghandriz, T.; Jacobson, B.; Murgovski, N.; Nilsson, P.; Laine, L. Real-Time Predic-tive Energy Management of Hybrid Electric Heavy Vehicles by Sequential Programming. *IEEE Trans. Veh. Technol.* **2021**, *70*, 4113–4128. [CrossRef]

27. Shivappriya, S.N.; Karthikeyan, S.; Prabu, S.; Pérez de Prado, R.; Parameshachari, B.D. A Modified ABC-SQP-Based Combined Approach for the Optimization of a Parallel Hybrid Electric Vehicle. *Energies* **2020**, *13*, 4529. [CrossRef]
28. Jeong, K.; Oh, B. Fuel economy and life-cycle cost analysis of a fuel cell hybrid ve-hicle. *J. Power Sources* **2022**, *105*, 58–65. [CrossRef]

designs

MDPI

Article

Energy-Efficient Control of a Gas Turbine Power Generation System

Marwan Al-Shami, Omar Mohamed * and Wejdan Abu Elhaija

Department of Electrical Engineering, King Abdullah I School of Graduate Studies and Scientific Research, Princess Sumaya University for Technology, Amman 11941, Jordan; marwan-996@hotmail.com (M.A.-S.); elhaija@psut.edu.jo (W.A.E.)
* Correspondence: o.mohamed@psut.edu.jo

Abstract: Gas turbines are used in the energy sectors as propulsion and power generation technologies. Despite technological advances in power generation and the emergence of numerous energy resources, gas turbine technology remains important due to its flexibility in load demand following, dynamical behavior, and the ability to work on different fuels with minor design changes. However, there would be no ambitious progress for gas turbines without reliable modeling and simulation. This paper describes a novel approach for modeling, identifying, and controlling a running gas turbine power plant. A simplified nonlinear model structure composed of s-domain transfer functions and nonlinear blocks represented by rate limiters, saturations, and look-up tables has been proposed. The model parameters have been optimized to fit real-world data. The verified model was then used to design a multiple PI/PD control to regulate the gas turbine via the inlet guide vane and fuel vales. The aim is to raise and stabilize the compressor's differential pressure or pressure ratio, as well as raise the set-point of the temperature exhausted from the combustion turbine; as a result, energy efficiency has been improved by an average of 237.16 MWh saving in energy (or 8.96% reduction in fuel consumption) for a load range of 120 MW to 240 MW.

Keywords: gas turbine; whale optimizer; modeling; identification; control

Citation: Al-Shami, M.; Mohamed, O.; Abu Elhaija, W. Energy-Efficient Control of a Gas Turbine Power Generation System. *Designs* **2023**, *7*, 85. https://doi.org/10.3390/designs7040085

Academic Editors: Wenbin Yu and Guang Zeng

Received: 5 June 2023
Revised: 27 June 2023
Accepted: 28 June 2023
Published: 3 July 2023

1. Introduction

1.1. Background and Motivation

Natural gas, hydrogen, fuel oil, and biogas are all fuels that can be used to power a gas turbine (GT), if the GT is properly configured or manufactured [1,2]. Apart from this input flexibility, the GT is classified as a flexible energy resource due to its output flexibility to follow the dynamics of electricity demand in a stable and efficient manner [3,4]. Therefore, investing more research effort into development of more efficient gas turbines can be very useful in terms of fuel, energy, and the environment. The issue of improvement in such devices is an endless research problem that requires continuous work by recent and future engineers with multidisciplinary objectives or various collaborative disciplines, such as Electrical Engineering, Artificial Intelligence, Mechanical Engineering, Chemical Engineering, and so on. The recent energy crisis caused by instabilities in the Middle East and Arabian region has made research even more difficult. Flexibility is thus an inherent feature of GTs due to its thermodynamic operational characteristic. The thermodynamics of a very basic GT is demonstrated below, where Figure 1 represents the basic components of a gas turbine and the corresponding temperature–entropy diagram is shown in Figure 2. The air compression is demonstrated by the isentropic process (1–2), in the isobaric process (2–3), the air/fuel mixture is combusted, then expanded in the isentropic gas turbine process (3–4) to create useful work for power production. In process (4–1), the output heat at constant pressure is then either rejected into the atmosphere or injected to a heat recovery steam generator (HRSG) to produce more power from the exhausted gas.

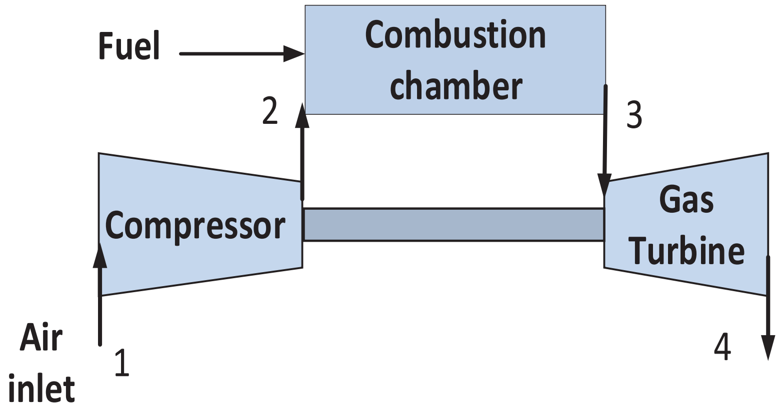

Figure 1. Main components of gas turbine unit [3].

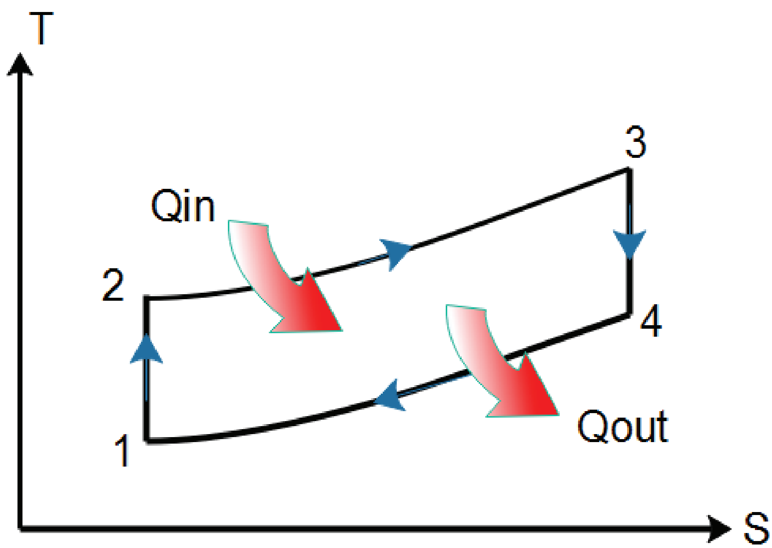

Figure 2. Temperature–Entropy (or T–S) diagram [3].

Despite technological advances in intensive research of control system technology, the directed research methodology continues to hold analogous steps towards successful control system implementation. The case under study may be far more complex for dual fuel GTs, which has been adopted in this paper, in which there are two main operating modes: the premix mode where the pilot valve and natural gas valve supply gas to the combustion chamber, and the diffusion mode where the fuel oil is permitted through the pilot valve from the fuel boosting system. In the case of low loads, the diffusion mode is better for stable combustion before, whereas the premix mode is preferable for high, peak, or near peak loads for more efficient operation. However, the situation could be further improved in the premix mode, which is the most likely situation, by proper control system design. The steps for control system design for energy-efficient improvement are depicted in Figure 3 with emphasis on our own research, which has the major steps to be explained throughout the paper context.

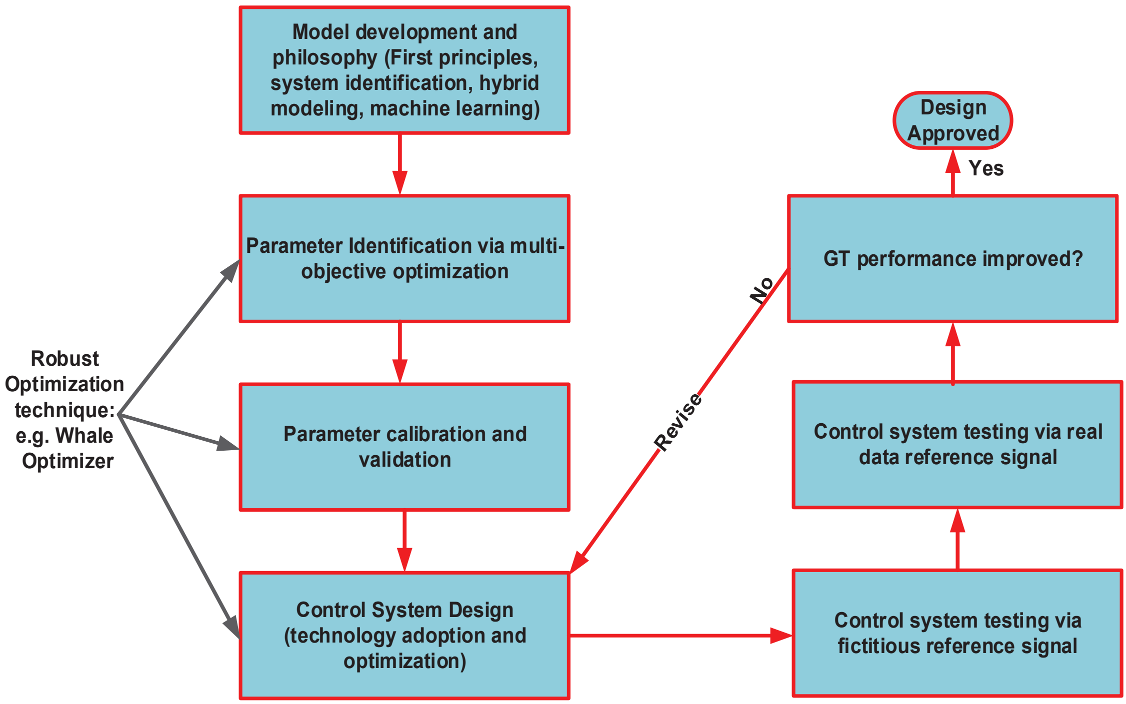

Figure 3. Directed research steps for GT control system development.

The importance of modeling GTs can be further clarified by the literature review and the explained paper contribution to theory, knowledge, and practice. This is detailed in the next subsection.

1.2. Literature Review and Paper Contributions

The control system design of Gas Turbines (GTs) has become a challenge across the world due to its intricate requirements, as its multi-timescale dynamics are naturally nonlinear and its process requirements are critical. Having multiple constraints add a huge computational load on classical control algorithms, therefore, its control requirements have raised the bar and require careful attention and intensive research.

Renewable energy sources are becoming increasingly popular; however, their intermittent nature poses a problem when integrated into the grid because it causes fluctuations in the levels of electricity generated; thus, controlling such fluctuations necessitates radical control techniques. Having the load change instantly necessitates the use of a controller that allows the power plant to respond to load changes without violating or exceeding the predefined limits or set-points, while keeping the power plant's efficiency as high as possible and meeting all of these requirements in a timely manner.

Fast load following operations, which are becoming more popular, have recently reduced plant efficiencies and shortened equipment life as load following capabilities have become more critical. This can have disastrous consequences because it increases mechanical and thermal stresses when the plant is not operating at full capacity. As a result, more intricate design requirements have been added in order to satisfy both load following capabilities and power efficiency.

The most recent control schemes are focused on increasing efficiency, lowering capital costs and running costs, reducing emissions, and enhancing operational flexibility. Being able to design and implement an optimizer that solves metaheuristic algorithms such as implementing the whale optimizer algorithm can be a potential solution.

The use of whale optimizer for of enhancing load following capabilities will ultimately minimize operating costs while explicitly fulfilling and satisfying the physical constraints associated with these power plants without causing huge burdens on the computational load. However, such a controller could require generous investment into the initial investment to fulfill these requirements.

The control of gas turbines has proven to be challenging due to their nonlinear multi-timescale dynamics, along with intrinsic constraints that need to be satisfied. Nowadays, classical control methods are adopted such as PID controllers [5], since PID controllers have the ability to offset the proportional controller which is considered a major advantage of such controllers along with their quicker response time. However, their limitations are highlighted by their high steady-state error and precincts in feedback loop stability.

The main components of a GT that need to be included in the design and analyzed are the compressor, combustion chamber, turbine, and generator. The models that have been used recently for these nonlinear systems are obtained from identification techniques only around a certain operating region. Thus, requiring improved control strategies that minimize operating costs and consider the physical constraints that exist within such a system is needed. One option which was analyzed in one of previous studies was the model predictive controller (MPC) [5–7].

The natural plant's operation begins with the compressor. The compressor is in charge of drawing filtered air from its surroundings and pressurizing it to the appropriate levels. Pressurized gas is important because having a higher-pressure gas increases the kinetic energy stored in the gas particles, thus the potential to produce more energy, but the levels to which the pressure can be leveled up must be carefully maintained. The compressed air then enters the heart of the operation, the combustion chamber, where it is mixed with natural gas, allowing it to ignite and reach high temperatures and pressures. In some cases, fuel oil must be fed into the system. It is then expanded through the turbine, causing the turbine's blades to rotate and the generator to begin producing electricity. With its nonlinear dynamics, all of these processes require careful thought and design because they are interrelated and affect one another.

The firing temperature and gas flow control the turbine's output. The inlet guide vane, which is connected to the compressor and controls the amount of gas entering the combustion chamber, is another important mechanism. The desired load is determined by the firing temperature, the inlet guide vane (IGV), and the exhaust temperature. Furthermore, the amount of fuel fed into the system and ignited has a direct impact on the load.

The gas turbine has six main controllers, each are interconnected and interdependent on one another, which are [5]:

1. Starting controller, which sets the right amount of fuel for ignition.
2. Run up controller takes over; this controller will begin during start-up and until the right speed is reached where the next controller takes over.
3. Frequency and load controller, which takes control of the turbine speed before reaching the synchronous speed, also known as full load.
4. Maximum load controller, as the name suggests, limits the maximum active power generated.
5. Temperature controllers, controls the inlet and outlet turbine temperature by controlling the variable guide vane (VGV).
6. Maximum Turbine Inlet Temperature Limiter: its main function is to limit the inlet temperature of the turbine in times of malfunction and in times of rapid load changes.

One of the most important components and working parts of the system is the variable guide vanes, which are manually handled by controlling the firing angle to acquire the desired mass flow rate; they are, in other words, responsible for regulating the amount of mass flow into the combustion chamber, and thus will ultimately control the temperature and this is crucial for the thermodynamics of the power plant. The other major components are the combustion chamber and the turbine, the fuel mass flow rate is controlled by a separate controller [7,8].

Overall, the mechanical output power of the gas turbine is the difference between the generated power of the turbine and the power consumed by the compressor. The energy is converted from chemical energy which is stored in the fuel that will be ignited, to mechanical energy, which is yielded for the turbine which will in turn rotate the shaft connected to the generator, which will in turn converts the energy to electrical energy.

It is important that a control system be designed in order to maintain constant power when the demand is so, execute the demand changes that are required, and keep a stable output voltage. A controller design was inspired from Montazer Ghaem gas power plant. They developed a controller to control the rotor speed during the start-up and changes in power demand.

Furthermore, Shete and Jape [9] have stated that during operations, gas turbines are typically operating in high-temperature and high-speed environments. The paper then has introduced Fuzzy Modified Model Reference Adaptive Controller for the speed by controlling the input fuel flowing into the combustion chamber.

Previously, PID controllers were the solution for this system because they can respond to such robust responses and can be easily tuned, but the system's efficiency becomes a concern. An alternative solution, however, has been proposed that uses a fuzzy modified model reference adaptive controller (FMMRAC) to adapt to these responses. This model is based on Rowen's model [9], a thermodynamics-based model that represents an improved and well-established GT model.

Another study simulates the behavior of a high-efficiency gas turbine with advanced cycles obtained through the use of a regenerator, an intercoder, an economizer, and steam or water injection. These components necessitate research into efficiency optimization in design, off-design, and especially transient conditions [10]. Although the addition of these components improves the overall efficiency of the system, they change the system dynamics and present some challenges to existing control schemes because these additions affect system dynamics and increase the computational load.

Gas turbines exist as single shafted or multi-shafted, where multi-shafted are assumed to be superior because they are able to adapt better, have better cost effectiveness with load variations, the mechanical inertia is much lower, and even the electromechanical time constants are at least half or a quarter of that of a single shafted gas turbine [11]. Therefore, even though multi-shafted turbines need a more generous investment and the constraints may be amplified, the benefits of implementing multi-shafted turbines enhance flexibility and working conditions.

The rotational speed is usually controlled mostly by the change in the amount of fuel supply or fuel mass flow rate to the combustion chamber which will ignite. When using gas turbine plants in isolated power system stations, frequency and voltage deviations may be neglected which will greatly affect the power quality.

Another valid solution suggested is the use of a prognostic algorithm that introduces a forecast parameter which has the ability to perfect classical control methods with minimal costs. The use of Automatic Speed Regulator (ASR) or Automatic Voltage Regulator (AVR) will limit the overshooting and transient time of voltage which provides some supremacy to PID controllers, and will maintain the rotor rotational speeds without the need for costly complicated adjustments to be implemented to control the rotational speed in the system [12], which is vital for safe performance of the GT.

The AVR and ASR results, as well as the conclusions that can be drawn from them, allows additional loads to be connected to the system in the event of load shredding abruptly.

Nowadays, industrial heavy-duty gas turbines have proven to be more reliable and more widely spread [13], especially using a hybrid system along with a pilot valve that provides fuel oil when needed, makes the gas turbines more efficient to use.

Gas turbines are composed of many interrelated systems: thermal, mechanical, and electrical to be exact. Their interaction and their dependence require deep understanding of modelling since this interaction complicates the requirements to reach an acceptable modelling accuracy.

Two main control loops are needed in the system, one is the speed governor loop for load frequency control, and the exhaust temperature control loop for energy efficiency preservation, these control the output torque and the exhaust temperature, in which these directly control the turbine behavior. The maximum allowable harvested power depends on many factors including the frequency of the system and the exhaust temperature. The temperature control limits the exhaust temperature through the cooling air system.

The complications of gas turbines basically stem from the concept of having working fluids inside them, as they are operating under high temperature and pressure, and are working under thermodynamic processes such as combustion and expansion, which have been already described as the Brayton cycle. The high temperature and pressure add to the thermal stresses that the components of the GT will be exposed to, and will affect the lifespan of the GT.

The cycle begins with the compression of air in the compressor to increase its pressure, then the compressed air is mixed with the fuel generating a high-temperature flue, which is finally expanded in the turbine in order to produce mechanical energy, which is responsible for producing the electrical power.

Other considerations that fuel control systems require in aerospace engineering are as follows [14]:

- Provides the necessary fuel for the combustion chamber;
- Controls the fuel requirements for the start-up process;
- Limits the maximum speed of the gas turbine; and
- Limits the maximum fuel flow.

Other studies that focus on power generation application of gas turbines, including this study in the present paper, usually express a combined cycle that also incorporates a gas turbine along with a heat recovery steam generator and speed, temperature, and IGV control. These combined cycles provide higher efficiency, lower unit cost, quicker construction, and have less emissions. These combined cycles differ from conventional plants in terms of their dynamic performance [15].

The existing temperature control is reflected in the open-loop system as a proportional and integral controller (PI) which limits the fuel request. It compares the exhaust temperature with the reference temperature, where the difference represents the error variable which will instigate the proper action on the controller.

Other research analyzes the transient cases where simulation and modelling of a gas power plant is important, which are start-up, variable loads, and unexpected shutdowns. As a result, the control schemes that are implemented must be chosen with great care and caution [16]. The effect of fast load following operation is basically negative to plant efficiency and reduces the equipment lifespan. As renewable sources of energy become more widespread, along with the knowledge of renewable sources of energy having an intermittent property, conventional plants must cycle their loads more often and follow the fluctuations in energy demand [17].

Natural gas combined cycles have been recognized to be more efficient, have fewer capital costs, produce less emissions, and have higher operational flexibility than coal. However, the impacts of load following capabilities disturbed by renewables may negatively affect plant efficiency, and increase the thermal and mechanical stresses on the equipment compared to operating on the base conditions, because load following focuses on decreasing the deviation between the reference and the actual without prioritizing the capabilities of the actual GT. The outage probability increases during load following, and thus increases the maintenance costs.

To promote plant efficiency, dynamic optimization must be maximized under load following. However, there are a few points to keep in mind:

1. Stresses should be kept within certain limits.
2. Temperatures should also be kept within a narrow range.
3. Maximum overall cycle efficiency should be maintained.

These constraints, which are also imposed on the multi-objective function, make it more difficult to generate a feasible solution, particularly with a high ramp rate; thus, relaxing the ramp rate is more necessary and required to solve this dilemma. It is assumed that, first, the average ramp rate is satisfied rather than the instantaneous ramp rate, and that, second, the average ramp rate can be relaxed if necessary. However, these assumptions or considerations are dependent on the system's state and operation, whether ramping up or down. When ramping up, the deviation of the average ramp rate from the desired rate is minimized to maximize efficiency. When the optimizer sees a whole ramping down, a larger relaxation, it will relax as much as possible because lowering the ramp rate improves efficiency. The desired ramp rate is the most important parameter to satisfy when using the lexicographic approach during load following operations, because all other operational objectives are naturally ordered in terms of priority. As load increases during ramp-up operations, the efficiency of the optimizer will be also improved, so simply solving a single objective optimization problem by maximizing efficiency leads to the minimization of ramp rate relaxation. The multi-objective problem becomes apparent during ramp-down operations and must be resolved.

The tradeoff that can be concluded from this reference is between the relaxation in the ramp rate and the thermal efficiency of the power plant, which means that it is difficult to satisfy both at the same time at maximum levels, but there could be some operating point where they can be both satisfied at acceptable levels. The optimal MIMO controllers may emphasize different aspects in control theory and practical characteristics, such as load following capability [18], H_2 and H_∞ for GT control as a subsystem of a combined cycle unit [19], or decentralized active disturbance rejection [20]. The latter is applicable to other power plants, fueled even by coal [21].

From a deep investigation of the literature, Whale Optimizer (WO) is still not applied and evaluated in the field of gas turbines' modeling and control. Although WO has been applied for a coal unit [22], it is worth investigating specifically on GT control system because of the high number of differences in the design, characteristics, and practical viability between the two types of power plants, which offers an opportunity for more novel achievements in this research area. The contributions of this paper are then stated as follows:

- A simplified nonlinear model of a practically operating GT has been developed and the parameters are identified by WO. The model accurately captures the turbine dynamics from 120 MW to 220 MW. The issue of petameters' calibration has been supported by the results over a wide range of settings. Moreover, the effect of relaxation of parameters on the model robustness has been investigated for the first time, which leads to high accuracy for a broader range of power changes.
- A MIMO PI/PD controller has been optimized and incorporated into the model of the existing GT as additional loops and the controller parameters have been tuned and calibrated by WO to improve the existing controller performance in terms of fuel consumption, and hence the energy efficiency. The likely operation of the adopted GT is the premix mode. Therefore, in light of this practically feasible assumption, the overall efficiency is found to be improved with significant reduction in gas consumption. This aspect has been validated through simulations of the lower natural gas consumption for the same power trends from data of existing GTs.

The rest of the paper is organized as follows: Section 1.3 presents an overview on WO, Section 2 explains the modeling approach and depicts the model simulation results, Section 3 shows the control strategy and verifies the practical feasibility, and Section 4 concludes the paper with some research findings and future recommendations.

1.3. An Overview on Whale Optimization Algorithm

There are various levels of algorithm problems, one of which is metaheuristic problems. Such problems necessitate the use of sophisticated optimization techniques. Whale optimization, which has been used in this study, is a metaheuristic algorithm that implements the hunting and feeding techniques used by whales. It can thus be implemented into power plant control schemes because it requires simple concepts, does not require gradient information, has the ability to bypass local optima, which is necessary in many scenarios, and is more important [23]. Whale optimization technique involves two main processes:

1. Exploration; which is basically a general search, where the optimizer includes all information in the search area.
2. Exploitation; which is basically an explicit search, where it investigates details in promising areas in the region of the local search.

The challenge lies in finding a balance between both processes and finding the optima in the least amount of time. "Why study whales?" one may ask. Whales are actually one of the smartest creatures scientifically as they possess twice the amount of spindle cells as humans do, and the methods they use to acquire or hunt for food are extraordinary. They use a method called bubble-net feeding either in an upward spiral or double loops. Basically, they begin by creating a bubble shape, in one of the two directions mentioned previously, around the prey and then swim up to the surface. A mathematical model has been done in one of the papers for the three main stages of their "feeding" method.

1. Encircling the prey. It is basically suggested as the first or closest value to the optima or "first guess", where then the best search agent is defined, and other search agents will update their position towards the best search agent. One of the variables is a random vector which allows the search to go beyond and search all possible regions.
2. Bubble-net attacking method, also known as exploitation. This stage consists of two approaches: either shrinking encircling mechanism or spiral updating position, each having equal probability of occurring at any interval.
3. Search for the prey (exploration), this stage basically begins the search in other promising regions.

The basic difference between exploitation and exploration is the concept of searching either locally or globally, as the exploration stage does, which is essentially determined by the value of the vector A being higher or less than 1. The basic flow chart of WO is shown in Figure 4, where X_i and X^* are the initial population and the best search agent, respectively.

According to the results of this paper, the WO tends to exploit extensively in the early stages because the first guess should be close to the optimal value, but it does lean into the early stages to switch abruptly between exploration and exploitation. Another critical parameter is the death penalty function, which considers the main objective function that must be resolved and optimized while ignoring infeasible solutions. Because of the aforementioned literature and brief background on WO, the method of modeling, identification, and control proposed in this research is expected to be superior to other techniques discussed above; the only way to determine this is to apply previous techniques of tuning the models on our developed model and observe the differences. This will involve using GA and GWO and comparing them to WO in terms of model accuracies and control system performance, which will eventually lead to valuable contributions in the field of gas turbine modeling and control.

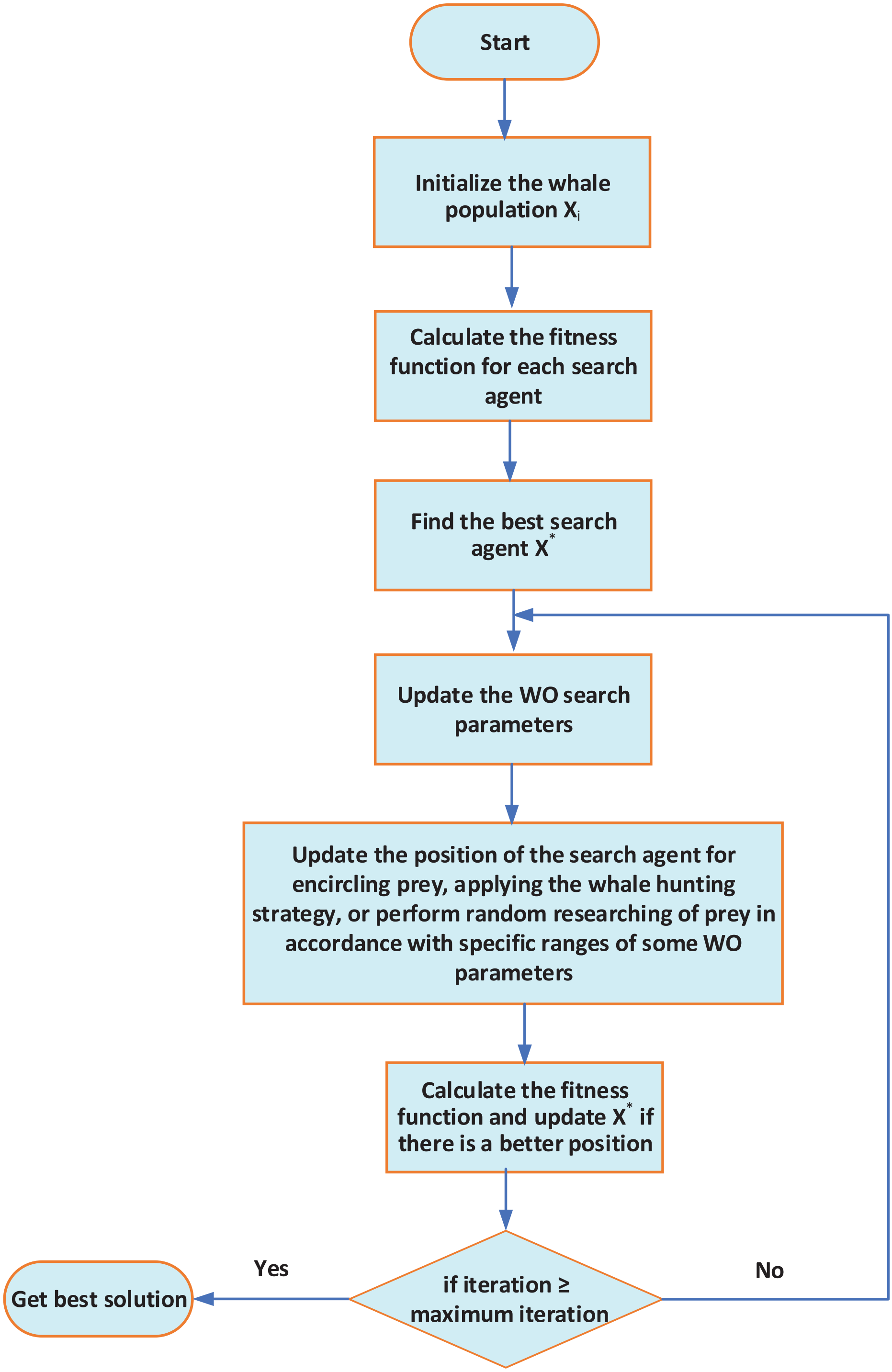

Figure 4. The flow chart of the basic working mechanism of a whale optimizer.

2. Modeling and Optimum Parameter Identification via WO

This section focuses on modeling the GT and MATLAB simulations for the approach of the GT modeling and identifying its unknown parameters. The power plant is fueled by natural gas and fuel oil which may be regulated via inlet guide vanes, and the data covers the operation from 120 MW to about 240 MW, which have been reproduced from Open Access previous publications of the corresponding author [6].

The inputs of the power plant are as follows: Natural gas valve, pilot valve, and compressor output pressure ratio. They are all represented by their normalized percentages of opening. The outputs of the power plant are active power measured in megawatts (MW) and exhaust temperature measured in degree Celsius. The final model structure is shown in Figure 5

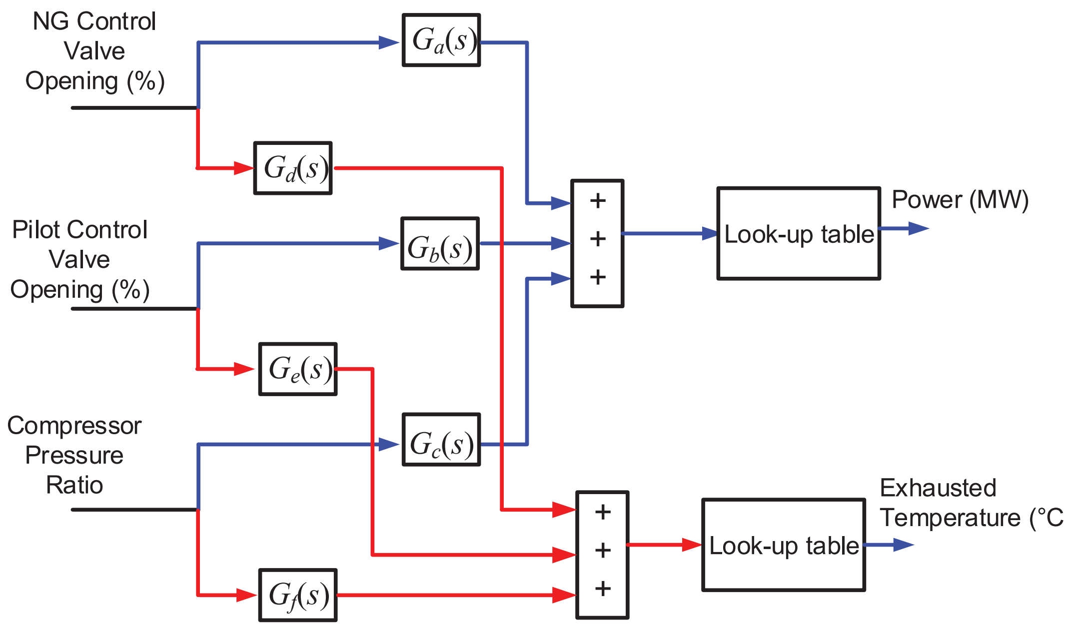

Figure 5. The Mathematical Model of the Gas Turbine, Red: the input signal flows through the system to the exhausted temperature, Blue: the input signal flows through the system to the output power.

The transfer functions of the system in Figure 5 are adopted to be as follows:

$$G_a(s) = \frac{a_1 s + a_2}{a_3 s^2 + a_4 s + a_5} \tag{1}$$

$$G_b(s) = \frac{b_1 s^2 + b_2 s + b_3}{b_4 s^2 + b_5 s + b_6} \tag{2}$$

$$G_c(s) = \frac{c_1 s^2 + c_2 s + c_3}{c_4 s^2 + c_5 s + c_6} \tag{3}$$

$$G_d(s) = \frac{d_1 s + d_2}{d_3 s^2 + d_4 s + d_5} \tag{4}$$

$$G_e(s) = \frac{e_1 s + e_2}{e_3 s^2 + e_4 s + e_5} \tag{5}$$

$$G_f(s) = \frac{f_1}{f_2 s^2 + f_3 s + f_4} \quad (6)$$

The chosen order of the numerator and denominator for each function is selected through several trails and comparison before inclusion of the WO optimizer in order to ensure realistic dynamical influences of the three inputs to the two outputs. Furthermore, the nonlinear region of operation has been emulated through look-up tables, which represents the nonlinear components in the model. Then, the parameters of every transfer function have been tuned by WO by tightening and relaxation of the bounds of the parameters.

First, data for an actual dual fuel gas turbine power plant has been taken, where it was resampled into intervals of 30 s, having a total of 2040 samples, which represents operating time of exactly 17 h. The model parameters were initially guessed by trial and error, then the implemented model was embedded into the code that represents the cost function. The cost function is the squared error between measured and simulated results. WO, with carefully chosen settings, was used to compute the optimum set of parameters. In order to ensure that the parameters are able to yield close enough results to the actual values of the model, the error has been calculated several times with changing WO setting parameters and the lower and upper bounds of every model parameter. It has been done for 10 iterations through 30 iterations of the whale optimizer. The constraints on the parameters were set as 0.05. To analyze the difference in the results when the whale optimizer constraints are relaxed and tightened, the simulation was done when the constraints were tightened to 0.005 and then relaxed to 0.1. The effect of parameters' relaxation is shown in Table 1 and the optimum set of parameters, based on the best case, are given in Table 1, and the optimum set of parameters is shown in Table 2. Simulation results for the selected set of data have been depicted in Figures 6–10. The next stage is dedicated for controller development. The simulated trajectory has the ability to follow the actual trajectory of the power plant, however, there is some clear deviation at some points, which proves the need for a modified version of the power plant. A controller should be embedded in the design to improve the input and output. The parameters were identified offline, and it took several hours to obtain the final optimal set of parameters.

Table 1. The effect of WO iterations and relaxation of the bounds of model parameters.

Iterations	**Root Mean Square Error**	
	Tightened to 0.005	**Relaxed to 0.1**
Ten	0.0878	0.0880
Twenty	0.0886	0.0947
Thirty	0.0891	0.0880

Table 2. Optimum set of parameters.

Function	**Parameters**						
$G_a(s)$	a_1–a_5	2.8957	9.9945	0.1080	1.8984	2.6918	-
$G_b(s)$	b_1–b_6	0.4933	3.0072	0.4927	0.1004	0.2988	0.2991
$G_c(s)$	c_1–c_6	0.8924	0.7027	0.9986	0.1070	0.3047	0.4919
$G_d(s)$	d_1–d_5	0.5063	0.6916	0.9079	0.5970	0.2011	-
$G_e(s)$	e_1–e_5	0.9963	1.1993	0.3048	0.9044	0.1900	-
$G_f(s)$	f_1–f_4	0.8568	0.8017	0.6997	0.0962	-	-

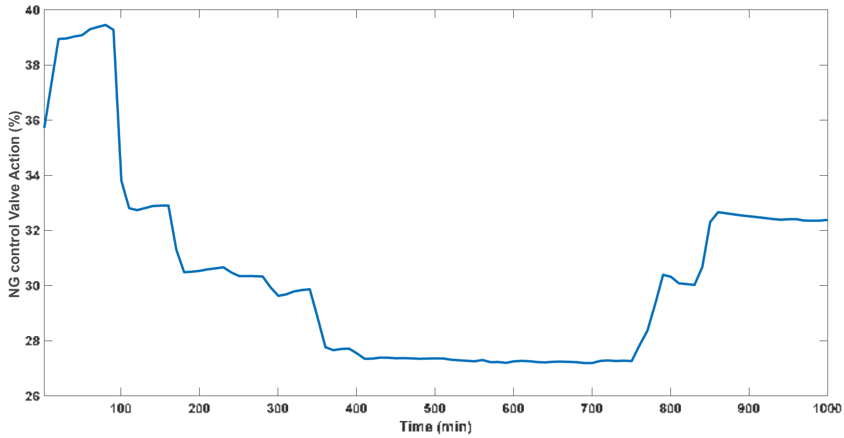

Figure 6. Input NG control valve opening.

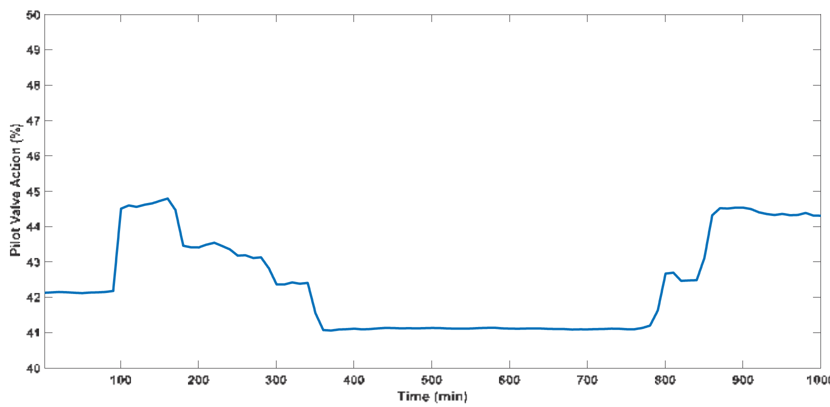

Figure 7. Input Pilot control valve opening.

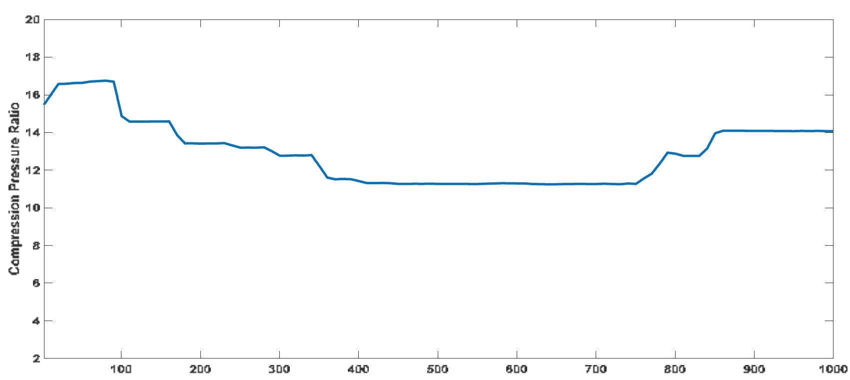

Figure 8. Compression pressure ratio.

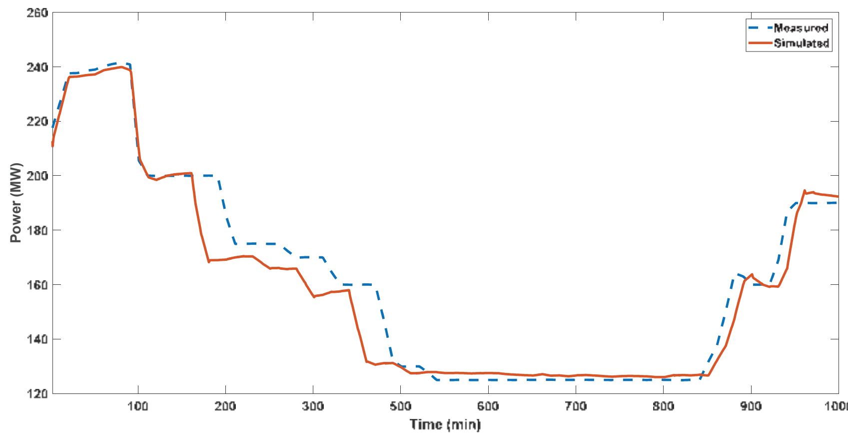

Figure 9. Measured and simulated output power responses.

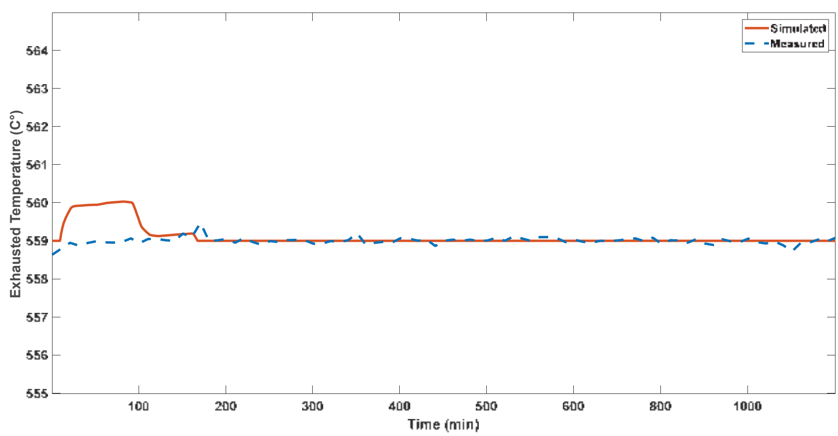

Figure 10. Measured and simulated exhausted temperature responses.

3. Control System Design and Testing via WO

The control system configuration has been assumed to correct the action over the existing control system [3]. It is well known that the identification that has been applied in Section 2 is a closed-loop identification, therefore, one must ensure the proposed controller will not interfere with existing control. From control theory point of view, nothing ensures that except authentic simulations of the proposed controller and comparison–that is rooted from experience–with existing performance. The MIMO controller has been assumed to have two PI controllers, one to regulate the NG and Pilot control valves together and the other to control the compression ratio through the IGV. The coupling control element between the two PI controllers has been chosen to be the PD controller. This structure has been widely accepted for thermal power plant control in general with different control philosophies and parameter tuning [3,6,19–21]. The proposed control system is shown in Figure 11. The rate limiters and saturations help avoid undesirable stresses that may result from extensive changes in the control signals.

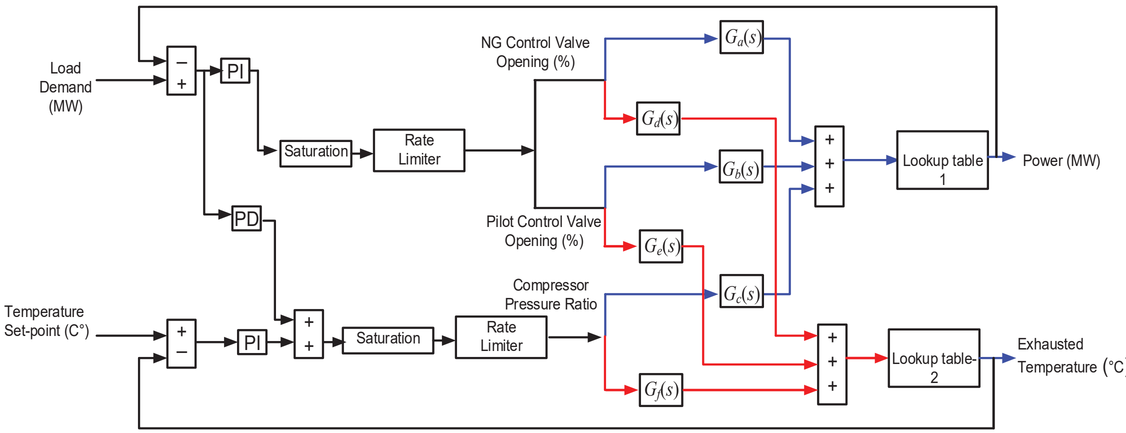

Figure 11. Simulink model with the suggested controller.

The controller has been tuned by WO to minimize the error between set-point and output from the model. It has been tested first with a fictitious pulse load signal that varies from 120 MW to 240 MW, whereas the temperature signal has been constant at 560 °C. The two signals have been implemented into the model, with the addition of loop controllers, along with rate limiters and saturation blocks. The PI/PD controllers have been optimized to follow the signals introduced to the model, with their appropriate parameters. Two proportional-integral (PI) controllers were needed along with one proportional-derivative (PD) controller. Table 3 shows the optimal set of the controller parameters.

Table 3. Controller Parameters.

	PI Controller Parameters for the Fuel Preparation System	**PI Controller Parameters for the Compressor**	**Coupling PD Parameters**
K_P	3	0.35	2.65
K_I	10.1	2	-
K_D	-	-	0.2526

The reason why the signals were designed as such: signal one demonstrates the change in active power, and this will prove whether the controller can satisfy the load following capabilities, and whether the exhaust temperature can be controlled in such a manner that would keep it at a constant value. As can be seen in Figures 12 and 13, after introducing the controller with their appropriate parameters, the power plant is capable of following the load demand signal rapidly, even though the signal increased by 120 MW as it would during sudden load application and rejection, the power plant is able to satisfy this change in a timely manner.

The power plant is also capable of stabilizing the exhaust temperature. Keep in mind that it has been able to do so with no considerable changes to the exhaust temperature and was kept at 560 degrees Celsius. This proves the success and validity of the controller in a mathematical sense; however, another practical test is required to ensure the energy-efficient aspect of the controller. One way to ensure this is to apply the data signal of the load demand as a reference set-point to the controller with a little bit higher temperature reference signal. As a consequence, the control system decisions for the fuel preparation system have shown uneven changes in the control actions. Figures 14 and 15 shows higher pilot valve action requirement while the NG valve action is lower. The improvement could be decided with full confidence through the total consumed fuel during premix mode, which is depicted in Figure 16. The average fuel reduction has been 8.96% fuel consumption, which is equivalent to about 237.16 MWh average energy savings for the entire time window of operation.

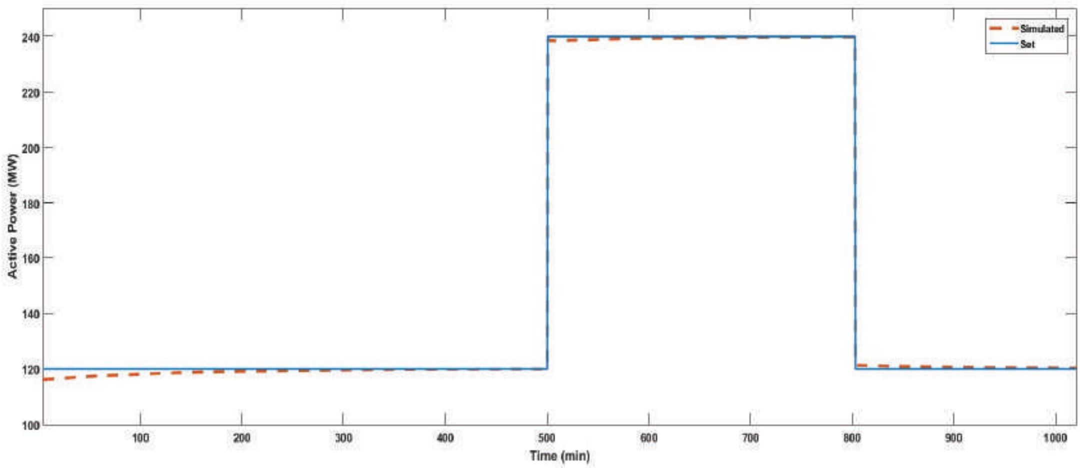

Figure 12. Active power simulated after implementing the controller (dashed orange) along with the actual active power signal that should be followed (blue).

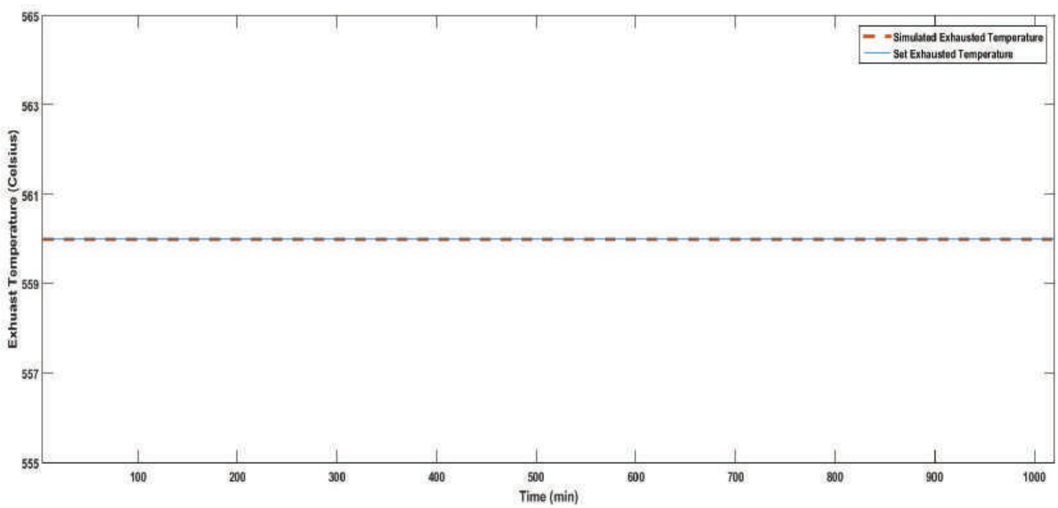

Figure 13. Exhaust temperature simulated after implementing the controller (dashed orange) along with the actual exhaust temperature signal that should be followed (blue).

Overall, there are fewer running costs and less use of raw materials which is necessary and a non-ending goal for the design of most power plants. Figure 17 shows that high and constant compression is required for compressor pressure output ratio response with the controller, where the value was constant during the simulation period which fundamentally proves that the efficiency of the plant has been improved, but higher input should be invested through the compressor. Figure 17 shows that more kinetic energy should be invested to the compressor through higher and constant compression ratio over the existing or measured case, in which the energy conservation principle can be proved. As can be seen in Figures 18 and 19, the active power was followed during the whole 17 h, almost perfectly taking into consideration that the total input has dropped from the actual value yet the yield of active power stayed the same. The exhaust temperature shows almost a 4 degrees Celsius increase over the actual value with no fluctuations, which is also significant to prove the controller has improved overall.

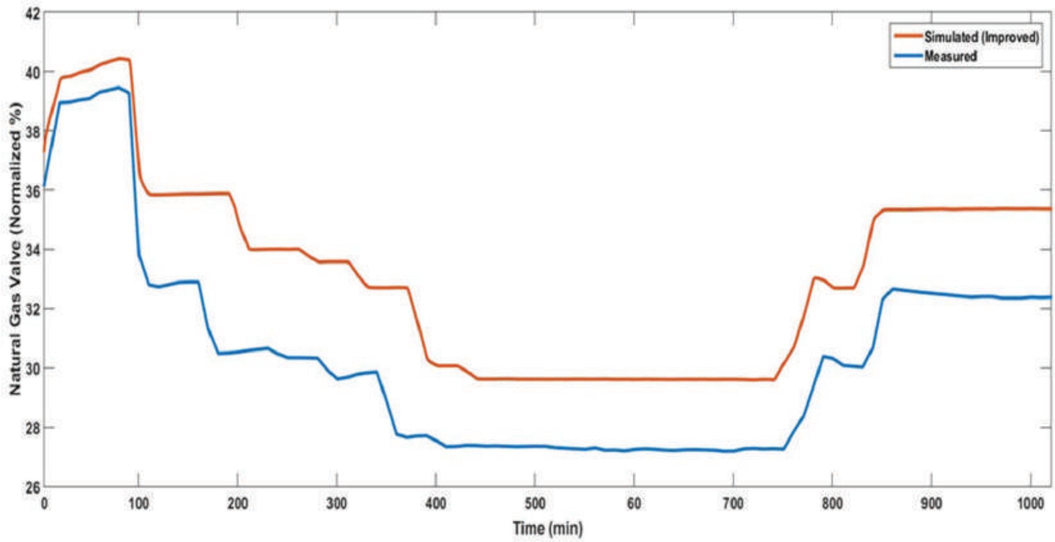

Figure 14. The Pilot valve dynamics, showing the existing and actual fuel oil (diffusion mode)/natural gas (premix mode) consumption (blue) and the simulated (improved dynamics (orange)). Notice: higher fuel consumption from the Pilot valve.

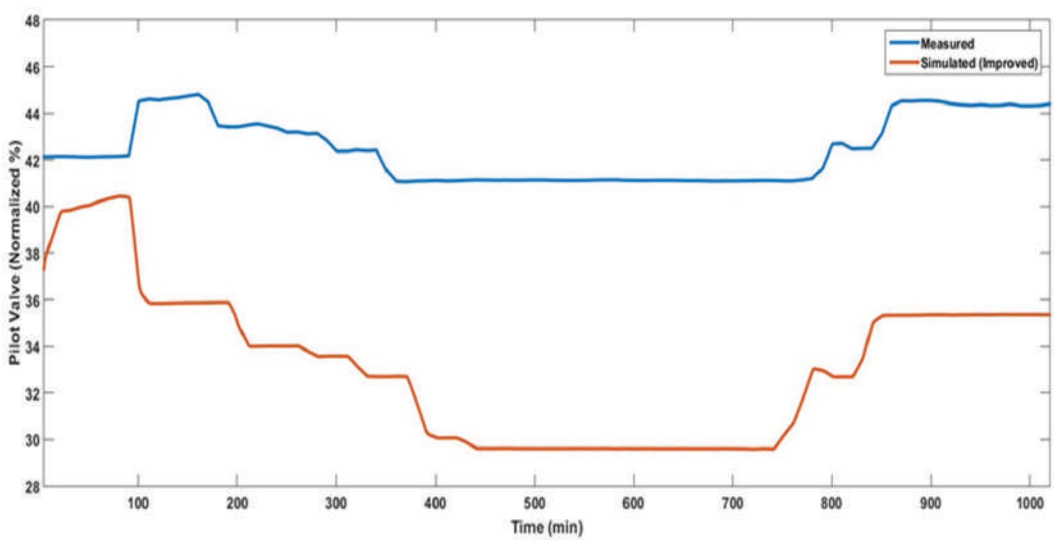

Figure 15. The NG valve dynamics, showing much lower fuel consumption with the simulated (improved with the controller) (orange) and the existing case (blue).

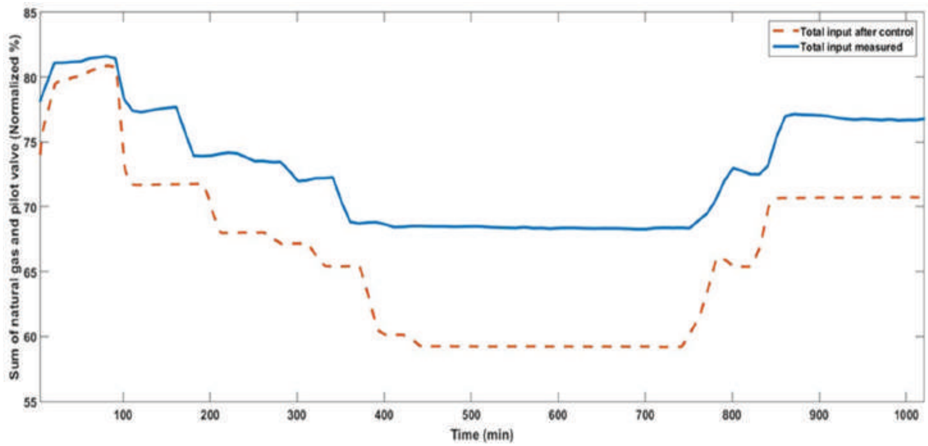

Figure 16. Total fuel input to the plant (pilot valve flow + NG flow) showing significant reduction in fuel or natural gas consumption (dashed orange) if operated totally on NG (i.e., premix mode) over the existing operation fuel consumption (blue).

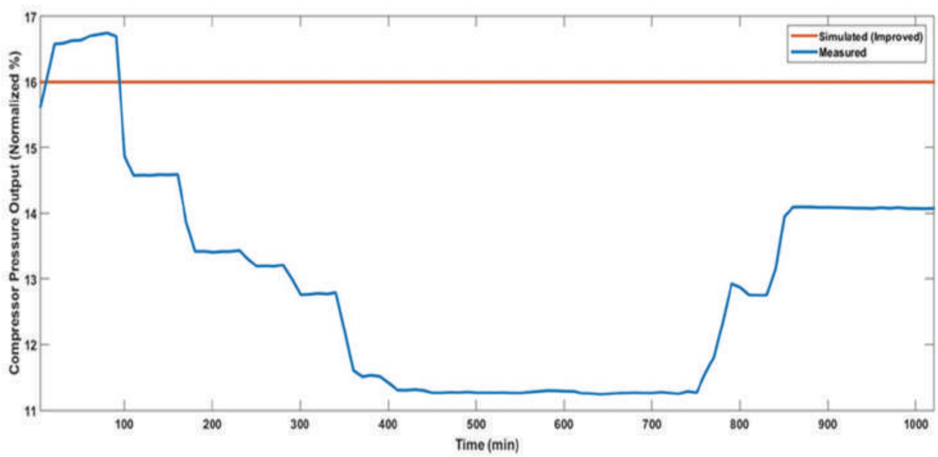

Figure 17. Compressor ratios in the improved (ornage) and existing case (blue).

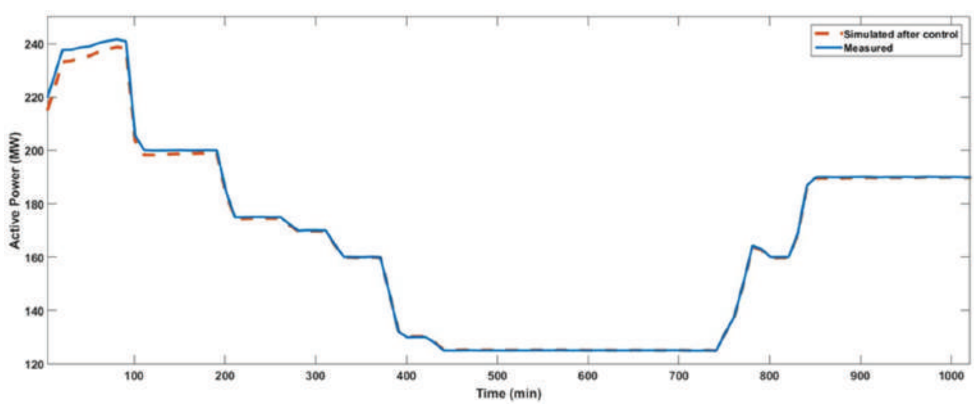

Figure 18. GT output (dashed orange) following the load demand (blue solid).

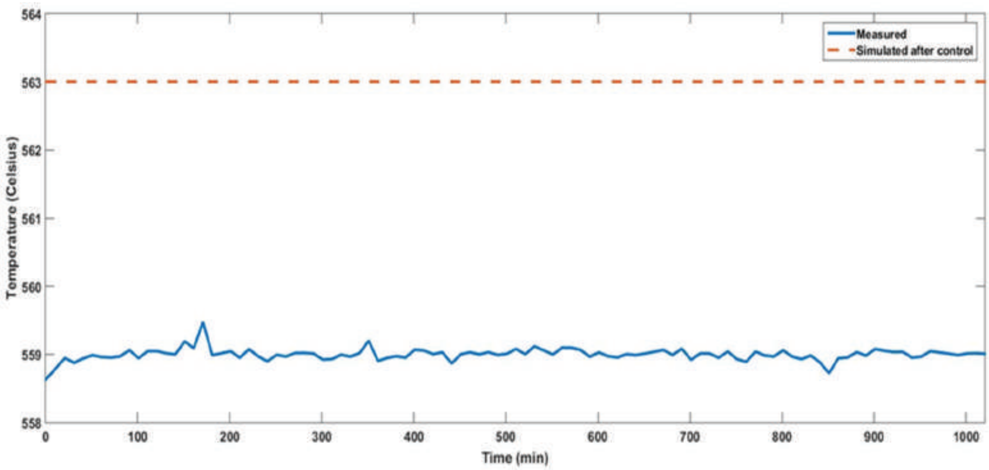

Figure 19. Exhaust temperature, the actual exhausted temperature (blue) along with the improved exhausted temperature response (dashed orange).

The next section concludes the research findings and recommends future points.

4. Conclusions

In this paper, a new simplified model for capturing the essential dynamical performance for a heavy-duty GT has been presented. The model embeds linear and nonlinear components, and the unknown parameters have been optimized using WO with sufficient relaxation of the bounds of the parameter. The model outputs have been verified from a load range of 120 MW up to 240 MW with reasonable accuracy. In addition, a MIMO PI/PD controller has been designed with optimal adjustments of the control parameters by WO. It has been shown that the controller regulates the essential outputs of the plant with more efficient operation. Thereby, it has been proven that WO is a robust optimizer for GT modeling, identification, and control.

There are some future opportunities to investigate, for example, using different metaheuristic optimizers for quantified comparison with WO in terms of accuracy and computation requirements. Different and modern GTs could also be tested with this control strategy, which are fueled by hydrogen or biogas. An economic feasibility study of the control practical implementation in real time is also a scientific merit that could be achieved.

Author Contributions: Conceptualization, O.M.; methodology, M.A.-S., O.M. and W.A.E.; software, M.A.-S.; validation, M.A.-S.; formal analysis, M.A.-S. and O.M.; investigation, O.M. and W.A.E.; resources, O.M. and W.A.E.; data curation, O.M.; writing—original draft preparation, M.A.-S. and O.M.; writing—review and editing, O.M. and W.A.E.; supervision, O.M. and W.A.E. All authors have read and agreed to the published version of the manuscript.

Funding: This research received no external funding.

Data Availability Statement: Data available on request due to preferability to be on request to ensure suitable usage by specialists.

Conflicts of Interest: The authors declare no conflict of interest.

References

1. Mom, J.A. Introduction to gas turbines. In *Modern Gas Turbine Systems*; Jansohn, P., Ed.; Woodhead Publishing Series in Energy; Woodhead Publishing: Cambridge, UK, 2013; pp. 3–20.
2. Prade, B. Gas turbine operation and combustion performance issues. In *Modern Gas Turbine Systems*; Jansohn, P., Ed.; Woodhead Publishing Series in Energy; Woodhead Publishing: Cambridge, UK, 2013; pp. 383–422, 423e.
3. Mohamed, O.; Khalil, A. Progress in Modeling and Control of Gas Turbine Power Generation Systems: A Survey. *Energies* **2020**, *13*, 2358. [CrossRef]
4. Alsarayreh, M.; Mohamed, O.; Matar, M. Modeling a Practical Dual-Fuel Gas Turbine Power Generation System Using Dynamic Neural Network and Deep Learning. *Sustainability* **2022**, *14*, 870. [CrossRef]
5. Shahin, S.; Elkhashap, A.; Abdelgelil, M.; Hamad, M.S. Nonlinear Model Predictive Control for Power Generation Gas Turbines. In Proceedings of the 2021 International Telecommunications Conference (ITC-Egypt), Alexandria, Egypt, 13–15 July 2021; pp. 1–6.
6. Mohamed, O.; Wang, J.; Khalil, A.; Limhabrash, M. Predictive control strategy of a gas turbine for improvement of combined cycle power plant dynamic performance and efficiency. *SpringerPlus* **2016**, *5*, 980. [CrossRef] [PubMed]
7. Tayyah, A.; AlShami, M.; Daboubi, O. Design of a Discrete Time Model Predictive Control for a Fossil Fueled Power Plant. B.Sc. project document, Princess Sumaya University for Technology, Amman, Jordan, 2019.
8. Kanashev, E.A.; Rozhko, E.V. Experimental Research of Gas Turbine Unit Control Systems Using Simulation Model. In Proceedings of the 2018 International Russian Automation Conference (RusAutoCon), Sochi, Russia, 9–16 September 2018; pp. 1–6.
9. Shete, S.A.; Jape, V.S. Design of a Fuzzy Modified Reference Adaptive Controller for a Gas Turbine Rotor Speed Control using T-S Fuzzy Mechanism. In Proceedings of the 2017 International Conference on Technological Advancements in Power and Energy (TAP Energy), Kollam, India, 21–23 December 2017.
10. Rowen, W.I. Simplified Mathematical Representations of Heavy-Duty Gas Turbines. *ASME J. Eng. Gas Turbines Power* **1983**, *105*, 865–869. [CrossRef]
11. Camporeale, S.M.; Fortunato, B. Dynamic Analysis and Control of Turbo-Gas Power Plant. In Proceedings of the IECEC-97 Proceedings of the Thirty-Second Intersociety Energy Conversion Engineering Conference (Cat. No.97CH6203), Honolulu, HI, USA, 27 July–1 August 1997; Volume 3, pp. 1702–1707.
12. Bulatov, Y.N.; Kryukov, A.V.; Van Huan, N. Simulation of Gas Turbine Power Plants with Voltage and Speed Prognostic Regulators. In Proceedings of the 2020 International Russian Automation Conference (RusAutoCon), Sochi, Russia, 6–12 September 2020; pp. 160–164.
13. Patrascioiu, C.; Popescu, M. Control System for Natural Gas Compression of Sinca Plant. In Proceedings of the 2020 12th International Conference on Electronics, Computers and Artificial Intelligence (ECAI), Bucharest, Romania, 25–27 June 2020.
14. Talah, D.; Bentarzi, H. Modeling and Analysis of Heavy-Duty Gas Turbine Based on Frequency Dependent Model. In Proceedings of the 2020 International Conference on Electrical Engineering (ICEE), Istanbul, Turkey, 25–27 September 2020; pp. 1–4.
15. Ma, S.; Tan, J.; Ning, Y.; Gao, Z. Modeling and Simulation of Gas Turbine Starter and Fuel Control System. In Proceedings of the 2017 36th Chinese Control Conference (CCC), Dalian, China, 26–28 July 2017; pp. 2149–2154.
16. Zhang, Q.; So, P.L. Dynamic Modelling of a Combined Cycle Plant for Power System Stability Studies. In Proceedings of the 2000 IEEE Power Engineering Society Winter Meeting. Conference Proceedings (Cat. No.00CH37077), Singapore, 23–27 January 2000; Volume 2, pp. 1538–1543.
17. Al-Dalwi, K.K.; Vural, A.M. Modeling and Simulation of Bazyan Gas Power Plant. In Proceedings of the 2017 4th International Conference on Electrical and Electronic Engineering (ICEEE), Ankara, Turkey, 8–10 April 2017; pp. 163–169.
18. Wang, Y.; Bhattacharyya, D.; Turton, R. Multiobjective Dynamic Optimization for Optimal Load-Following of Natural Gas Combined Cycle Power Plants under Stress Constraints. *Ind. Eng. Chem. Res.* **2021**, *60*, 14251–14270. [CrossRef]
19. Haji Haji, V.; Fekih, A.; Monje, C.A.; Fakhri Asfestani, R. H_2, H_∞, H_2/H_∞, and *μ-synthesis* controllers for the speed and temperature control of a real gas turbine unit in a combined cycle power plant. *Energy Sci. Eng.* **2019**, *7*, 2205–2222. [CrossRef]
20. Shi, G.; Wu, Z.; He, T.; Li, D.; Ding, Y.; Liu, S. Decentralized active disturbance rejection control design for the gas turbine. *Meas. Control* **2020**, *53*, 1589–1601. [CrossRef]
21. Wu, Z.; Li, D.; Xue, Y.; Chen, Y. Gain scheduling design based on active disturbance rejection control for thermal power plant under full operating conditions. *Energy* **2019**, *185*, 744–762. [CrossRef]
22. Qasem, M.; Mohamed, O.; Abu Elhaija, W. Parameter Identification and Sliding Pressure Control of a Supercritical Power Plant Using Whale Optimizer. *Sustainability* **2022**, *14*, 8039. [CrossRef]
23. Mirjalili, S.; Lewis, A. The Whale Optimization Algorithm. *Adv. Eng. Softw.* **2016**, *95*, 51–67. [CrossRef]

sustainability

MDPI

Review

Carbon Footprints of Active and Non-Active Transport Modes: Hierarchy and Intergenerational Narrative Analyses

Nestor Asiamah [1,2,*], Kofi Awuviry-Newton [3], Whitney Nesser [4] and Evelyn N. Alvarez [5]

1 Division of Interdisciplinary Research and Practice, School of Health and Social Care, University of Essex, Colchester CO4 3SQ, UK
2 Department of Gerontology, Africa Centre for Epidemiology, Accra North P.O. Box AN 16284, Ghana
3 College of Sport, Health and Engineering, Victoria University, Melbourne, VIC 8001, Australia; kofi.awuviry-newton@vu.edu.au
4 Department of Applied Clinical and Educational Sciences, Indiana State University, 401 North Seventh Street, Terre Haute, IN 47809, USA; whitney.nesser@indstate.edu
5 Department of Public Health, California State University, 5151 State University Drive, ST 305, Los Angeles, CA 90032, USA; evelyna@calstatela.edu
* Correspondence: n.asiamah@essex.ac.uk; Tel.: +44-7763489544

Abstract: This paper aimed to (1) develop a hierarchy for understanding the impacts of active and non-active transport modes on the environment and (2) analyse the adoption of active transportation between older and younger people. A narrative review with two parts was adopted to develop the hierarchy. In the first part, a framework was adopted to map active and non-active transport modes onto three operational boundaries of greenhouse gas emission to develop the hierarchy. In the second part, an intergenerational theoretical framework was developed to analyse the adoption of active transportation between older and younger people. The review suggests that the only active transport modes with no or negligible carbon footprint are walking, running, and swimming without a product that adds to atmospheric greenhouse gases. The evidence that younger people perform higher active transportation behaviour is inconsistent and is, therefore, inconclusive. This review suggests a need for manufacturers to prioritise the production of active vehicles (e.g., wheelchairs and scooters) that are biodegradable, recyclable, and small.

Keywords: carbon footprint; active transportation; older adults; generations; health

Citation: Asiamah, N.; Awuviry-Newton, K.; Nesser, W.; Alvarez, E.N. Carbon Footprints of Active and Non-Active Transport Modes: Hierarchy and Intergenerational Narrative Analyses. *Sustainability* **2023**, *15*, 12795. https://doi.org/10.3390/su151712795

Academic Editors: Wenbin Yu and Guang Zeng

Received: 30 July 2023
Revised: 21 August 2023
Accepted: 22 August 2023
Published: 24 August 2023

1. Introduction

Research assessing carbon dioxide equivalent emissions often called a carbon footprint [1] has gained momentum in recent years in response to an increase in global greenhouse gas emissions from individuals [1,2]. A parallel development is the acceleration of research on the health-sustainability dimension of transportation, with an emphasis on avoiding or decreasing per capita carbon footprint through active transportation, defined as walking or cycling to a place [3]. This definition undermines other forms of active transportation, resulting in active transportation being operationally defined as moving to places in ways involving physical activity but not involving the combustion of fossil fuels. This definition was informed by the above health-sustainability research agenda that emphasises the role of active transportation in health and environmental protection [1,2]. This agenda ought to progress since one-fifth of greenhouse gas emissions come from transportation involving the combustion of fossil fuels alone [1,2].

Walking, for example, may involve a negligible emission of greenhouse gases each time it is performed. In this review, any such travel behaviour is treated as an active transport mode with a zero-carbon footprint. The term "transport mode" has been used in the literature [4] to refer to different ways to travel between places (e.g., walking, bicycling, and driving). In this paper, therefore, we use this phrase to refer to various ways to travel.

The literature to date suggests that walking may be the ultimate physical activity for older adults because it requires less physical strength and energy expenditure [5,6]. As such, it can be sustained over the life course by all age groups, an idea that recalls a recent debate in gerontology about the role of older adults in environmental activism [7,8]. This debate has portrayed older adults as victims of ageism championed by younger adults who are concerned about climate change and the future [9]. Younger generations are concerned that older adults are responsible for climate change since older adults generally lead environmental policy interventions that have been unproductive [7,8]. An aspect of the literature also suggests that older adults have had more time to contribute to the emission of greenhouse gases and are less interested in pro-environmental behaviours, such as active transportation [9]. These ageist views imply older adults contribute less to environmental sustainability through active transportation.

Ageist views about older adults threaten the solidarity needed between older and younger generations to fight climate change [7–9]. Pro-environment behaviours (e.g., walking) are potentially the best ways to reduce carbon footprint and achieve sustainability goals [10,11], but their positive influence on the environment depends on how many people practice them. When ageist views are prevalent in climate crises and sustainability discussions, initiatives become divisive and undermine the significant role older adults can play in overcoming the climate crisis. This is particularly important, especially in a world where the population is rapidly ageing [12] and sustainability initiatives include many older adults.

Given the above concerns, the authors aimed to develop a heuristic for understanding the carbon footprints of active and non-active transport modes. This heuristic is needed because, though studies suggest active modes of transportation are the best ways to minimise per capita emission of greenhouse gases [10,11], there is no framework describing their respective carbon footprints. The authors further analysed the adoption of active transportation between older and younger people through a theoretical framework delineating active transportation behaviour across four generations (i.e., children, adolescents, adults, and older adults).

This review is significant for some reasons. Though studies have reported active and non-active transport modes with their potential carbon footprints, this review is the first to put these forms of transportation on a hierarchy, enabling stakeholders to better appraise the role active transportation plays in campaigns for a safer environment. The hierarchy may serve as a model for empirically investigating the relative impacts of transport modes on the environment. It is generally assumed that active modes of transportation protect the environment, but this review suggests otherwise. With this review, individuals may consider ways to use active vehicles (e.g., bicycles, scooters, and wheelchairs) without generating a carbon footprint. The hierarchy can encourage manufacturers to consider opportunities for designing vehicles to make them more active. Our intergenerational analysis may correct the assumption that the adoption of active transport modes is not necessarily higher among younger people. This contribution of the review is a way to better value the role of older adults in pro-environment campaigns, encourage stakeholders to include older adults in such campaigns, and ensure that as many older adults as possible are included in campaigns encouraging active transportation adoption, given that there may be more older people than younger ones in the world in the coming decades.

2. Search Methodology in Brief

A narrative review was adopted, and the PRISMA (Preferred Reporting Items for Systematic Reviews and Meta-Analyses) guideline was followed to search and review the literature. The search aimed to identify up-to-date documents reporting active or non-active transportation concerning greenhouse gas emissions and its personal as well as psychosocial predictors. Appendix A is the review work plan showing the inclusion and exclusion criteria, search terms, and SPIDER (Sample, Phenomenon of Interest, Design, Evaluation, Research type) tool used. Appendix B is the PRISMA flowchart reached using the inclusion and exclusion criteria to select suitable documents. The databases searched were PubMed, ProQuest, PsychInfo, CINAHL, Google Scholar, and Scopus. MeSH (Medical Subject Headings) terms were identified and developed into a search string using PubMed. These databases were searched twice as shown in Appendix A.

The steps taken in the review were (1) systematic searches; (2) screening of titles and abstracts of 5% of the studies twice to pilot the inclusion criteria; (3) screening of full texts by one of the authors; and (4) checking of data extraction for 20% of studies. Two researchers independently piloted abstract and title screening on 5% of the records downloaded. Inconsistencies in the pilot results were discussed and resolved before proceeding to the next stage. The titles and abstracts of the remaining 95% of the records were screened by the individual researchers. Subsequently, the full texts of the records selected through title and abstract screening were assessed for inclusion in the review against the inclusion criteria. The lists of references of included studies were examined to select relevant articles that had not been downloaded into the bank of records realised from our screening of titles and abstracts. Appendix B is the PRISMA flowchart resulting from the review. To ensure that quality documents were reviewed, we focused on peer-reviewed journals indexed in Web of Science, Scopus, or PubMed.

Only 26 documents were deemed appropriate for this review (see Appendix B), though other complementary documents outside the scope of the search were used. Data were extracted independently by one author and a research assistant with a piloted data extraction Excel sheet. The author and research assistant discussed in person to resolve minor disagreements in data extraction. Seven of the studies [13–19] reported active transport modes, namely, walking, running (i.e., jogging), swimming, bicycling, skating (including skateboarding and roller skating), skiing, surfing, scooter or wheelchair use (including kick scooter use), and rowing. Non-active transport modes dependent on fossil fuels include motorcycling, driving a car, ship travel, train travel, and air travel. A study [1] reported a framework that could be used to assess the carbon footprint of transport modes. Some studies [19–29] also assessed the relationship between age, pro-environment behaviour, and active transportation adoption.

3. A Framework for Assessing Carbon Footprint

This review focused on the carbon footprint of individuals and how this can be reduced or avoided through active transportation. To meet this aim, a carbon footprint is defined as the exclusive total amount of carbon dioxide emissions that are directly or indirectly caused by an activity or accumulated over the lifespan of a product [1]. This definition suggests that a carbon footprint can be generated directly or indirectly by an individual through daily behaviours. A direct example is driving a petrol- or diesel-dependent car, which directly releases greenhouse gases into the atmosphere. Indirect examples are producing non-biodegradable waste through the consumption of products (e.g., a canned drink) or felling down trees to provide services or products. Non-biodegradable waste produces greenhouse gases [30], whereas the felling of trees would increase the concentration of greenhouse gases in the atmosphere by reducing the proportion of trees absorbing these gases while releasing oxygen.

The foregoing definition makes Wicker's framework [1] for assessing carbon footprint ideal for the current review. It comprises three operational boundaries or scopes that specify whether some behaviours generate a carbon footprint. These behaviours are within three scopes. Scope 1 comprises direct emissions resulting from onsite fuel consumption, including all emissions from combustions relating to the use of vehicles. This includes behaviours causing emissions from travelling to a destination, with a typical example being driving a car. Scope 2 encompasses direct emissions from purchased electricity, heating, and cooling. This category includes heating or cooling a vehicle while travelling and wearing, for example, an electric jacket to keep warm while walking during the winter. Scope 3 concerns indirect emissions occurring during the lifespan of a product, including emissions resulting from the production and distribution of a product and management of waste.

Indirect emissions relate to the production of products requiring a supply chain dependent on the transportation of goods and individuals.

To use the above framework [1], the authors decided whether individual transport behaviours can directly or indirectly produce any greenhouse gas per unit of time. Each transport behaviour was mapped onto all three operational scopes with a "yes" (i.e., scope applicable) or "no" (i.e., scope not applicable) decision, which allowed us to determine whether the behaviour generates a carbon footprint directly or indirectly. To achieve reliable results, two researchers with expertise in transportation research performed independent mappings, which produced consistent findings. A zero-carbon footprint was achieved if a transport behaviour, hereby referred to as absolute active transportation, did not result in a greenhouse gas emission across the three scopes. Any active transport behaviour that was associated with emission for at least one scope had a carbon footprint and could be referred to as partial active transportation.

Whether an individual would use or adopt an active transport mode depends on several factors, such as the social and physical environment, as well as age [27,31]. In view of these factors, the adoption of active transportation between older and younger people is analysed through a theoretical framework explaining unique opportunities and barriers to active transportation across four generations. Children between 0 and 12 years who cannot make transport decisions for themselves are the first generation, whereas teenagers and adolescents aged 13–17 years who can make transport decisions but are dependent on parents are the second generation. Adults aged 18–49 years who can make transport decisions and may be independent of their parents are the third generation. The minimum for what is considered old age differs between countries; the United Kingdom (UK), for instance, sets the minimum old age at 65 years [32], whereas Ghana sets it at 60 years [33]. Globally, the minimum old age is 50 years [32,34]. Although the minimum age of 50 is not a good indicator of the individual's health and physiological conditions [34], it is a globally acceptable baseline. Thus, older people are operationally defined as individuals aged 50 years or higher and are the fourth generation.

4. Carbon Footprint and a Hierarchy of Active Transport Modes

The hierarchy of active transport modes is the pyramidal heuristic showing the relative impacts of transport modes on the environment. This framework was developed by mapping identified transport modes onto the operational scopes, which are recalled and operationalised as follows:

Scope 1—direct emissions resulting from onsite fuel consumption, including all emissions from combustions relating to the use of vehicles.

With this scope, any transport behaviour not involving the combustion of fossil fuel and not emitting a greenhouse gas does not generate a carbon footprint. As such, any transport behaviour that involves the combustion of fossil fuel applies to this scope and is mapped onto it with "yes" (with red colour).

Scope 2—direct emissions from purchased electricity, heating, and cooling. These emissions come from the use of air-conditioning systems that may be part of vehicles.

This scope does not require the direct combustion of fossil fuel in transportation but involves heating or cooling through air conditioning, which results in the emission of greenhouse gases [35]. Individuals with pro-environment behaviours may decide to drive an electric car, but they may use heating or cooling systems in the car (e.g., an air-conditioner) which produce greenhouse gases. Someone walking during the winter may wear a jacket with an inbuilt or mobile heating system, which may generate a carbon footprint. Therefore, any transport behaviour that uses a heating or cooling system and could emit greenhouse gases applies to this scope and is mapped onto it with "yes".

Scope 3—emissions that occur during the lifespan of a product, including those from the production and distribution of a product and management of waste from this product.

Any product whose production indirectly increases the concentration of greenhouse gases in the atmosphere is considered environmentally unfriendly. For instance, the production of products dependent on wood requires the felling of trees that absorb some greenhouse gases, such as carbon dioxide. From this perspective, the use of biodegradable products (e.g., a bicycle made of wood) indirectly generates a carbon footprint. Secondly, the use of any product that can become a part of waste in its production or consumption indirectly generates a carbon footprint. This assumption is premised on research [30] indicating that waste is a major source of greenhouse gases, such as methane. The quantity of greenhouse gases emitted partly depends on the size of a product; larger products that are not biodegradable or cannot be recycled would add more waste to the environment and may, therefore, generate a higher carbon footprint. Biodegradable waste, compared to non-biodegradable waste (e.g., plastics), has a shorter lifespan, so its carbon footprint can be expected to be short-lived. Similarly, recyclable waste would generate a smaller footprint.

Table 1 shows the results of mapping all transport modes onto the three operational scopes. Mapping was based on whether the transport behaviour involves the use of a product that could be harmful to the environment, depends on a utility or energy source that emits greenhouse gases, and whether the product is small, biodegradable, or recyclable. It was also assumed that greenhouse gas emissions across the lifespan of fuel-dependent transport modes (i.e., motorcycle, car, ship, train, and aeroplane) are more than emissions across the lifespan of active transport modes. Only walking, running, and swimming with no or negligible greenhouse gas emissions constitute absolute active transportation. "Walking (PS)" in the table may be associated with a significant emission of greenhouse gases and may, thus, has a carbon footprint. A study [1] has revealed that individuals may drive to convenient destinations before performing sporting activities or active transportation behaviours. Such individuals directly generate a carbon footprint before performing an active transportation behaviour at the chosen destination. Others might use canned energy drinks and other products during active transportation (e.g., walking) which may add up to waste, especially if not properly disposed of. The use of products, especially non-biodegradable ones, in active transportation can have a significant detrimental impact on the environment in the long term.

Figure 1 (based on Table 1) depicts the heuristic of walking as the most environment-friendly active transportation behaviour. The non-active transport modes are at the base of the framework, which signifies that transportation involving the combustion of fossil fuels has the highest carbon footprint. Walking is above running on the pyramid for two reasons. Firstly, research has suggested that walking, compared to running, is more sustainable across the lifespan because it requires less energy expenditure and is part of daily routines [5]. This being so, more people can be expected to perform walking behaviours and impact the environment positively. Secondly, whether people would sustain walking or running as a behaviour depends on their connectedness to nature [36], hereby defined as the amount of time spent observing lawns, forests, gardens, wildlife, rivers, and other natural attributes of the physical environment. People who walk may be better engaged with nature because they can more closely observe and admire nature. In running, people hurriedly observe nature, so their nature-driven motivation to keep fit through running would be low, compared with people who walk. Swimming is set below running in the framework because it is less relaxing and, if conducted in an indoor or artificial facility, provides limited nature connectedness. Worth noting is the idea that all individuals can contribute to environmental sustainability through active transportation, an idea substantiated by the following theoretical analysis of the adoption of this travel behaviour across four generations.

Table 1. The authors' mapping of key active and non-active transport modes onto the three operational scopes or boundaries.

SN	Transport Mode	Operational Boundaries			Attribute(s)	Description
		Scope 1	Scope 2	Scope 3		
	Active modes of transportation					
1	Walking (EF)	No	No	No	Eco-friendly *	Walking without using any supporting product (e.g., canned energy drink or car)
2	Walking (PS)	No	Yes	Yes	Less eco-friendly **	Walking while using a product or driving to a point before starting to walk
3	Running (EF)	No	No	No	Eco-friendly	Running without using any supporting product
4	Running (PS)	No	Yes	Yes	Less eco-friendly	Running while using a product or driving to a point before starting to run
5	Swimming (EF)	No	No	No	Eco-friendly	Swimming without using any supporting product
6	Swimming (PS)	No	Yes	Yes	Less eco-friendly	Using a product while swimming or driving **** to a point before engaging in swimming
7	Skiing/surfing (EF)	No	Yes	Yes	Eco-friendly	Skiing or surfing without any supporting product
8	Skiing/surfing (PS)	No	Yes	Yes	Less eco-friendly	Using a product while surfing or skiing or driving to a point before surfing or skiing
9	Biking (EF)	No	Yes	Yes	Eco-friendly	Using a bicycle that is made of biodegradable or recyclable materials
10	Biking (LEF and PS)	No	Yes	Yes	Less eco-friendly	Using a bicycle that is made of traditional materials ***
11	Skating, skateboarding, roller skating (EF)	No	Yes	Yes	Eco-friendly	Using equipment that is made of biodegradable or recyclable materials
12	Skating, skateboarding, roller skating (LEF and PS)	No	Yes	Yes	Less eco-friendly	Using equipment that is made of traditional materials that are less eco-friendly or can result in non-biodegradable waste
13	Scooter, kick scooter/wheelchair (EF)	No	Yes	Yes	Eco-friendly	Using equipment that is made of biodegradable or recyclable materials
14	Scooter, kick scooter/wheelchair (LEF)	No	Yes	Yes	Less eco-friendly	Using equipment that is made of traditional materials that are less eco-friendly or can result in non-biodegradable waste
15	Rowing (EF and PS)	No	Yes	Yes	Eco-friendly	Using equipment that is eco-friendly and can, therefore, result in less or biodegradable waste
16	Rowing (LEF and PS)	No	Yes	Yes	Less eco-friendly	Using equipment that is made of traditional materials that are less eco-friendly or can result in non-biodegradable waste
	Non-active modes of transportation					
17	Motorbike, car, ship, train, and aeroplane (EF)	Yes	Yes	Yes	Eco-friendly	A motorcycle made of recyclable/biodegradable materials and is 100% electric
18	Motorbike, car, ship, train, and aeroplane (NEF and PS)	Yes	Yes	Yes	Not eco-friendly	A vehicle that uses fossil fuels and is made of materials not biodegradable or recyclable

Note: Active transport modes shown (i.e., 1–16) do not involve the combustion of fossil fuels; the numbers 1–18 do not represent ranks or an order; mapping of transport modes onto the three operational boundaries was based on whether the transport behaviour involves the use of a product or vehicle, depends on a utility or energy source that emits greenhouse gases, and whether the productive involved is small, biodegradable, or recyclable; mapping was also based on the assumption that greenhouse gas emissions across the lifespan of fuel-dependent transport modes are more than emissions across the lifespan of active transport modes; "No" (i.e., colour green) means the boundary or scope does not apply to the corresponding transport type, and this suggests a zero or negligible footprint of the transport type; "Yes" (i.e., colour red) means the boundary applies to the corresponding transport mode; SN—serial number; PS—product-supported; EF—eco-friendly; LEF—less eco-friendly; NEF—not eco-friendly; * biodegradable (e.g., made of wood) or recyclable; ** not biodegradable or recyclable; *** traditional materials are raw or processed materials that are not recyclable or biodegradable; **** driving a vehicle that involves the combustion of a fossil fuel.

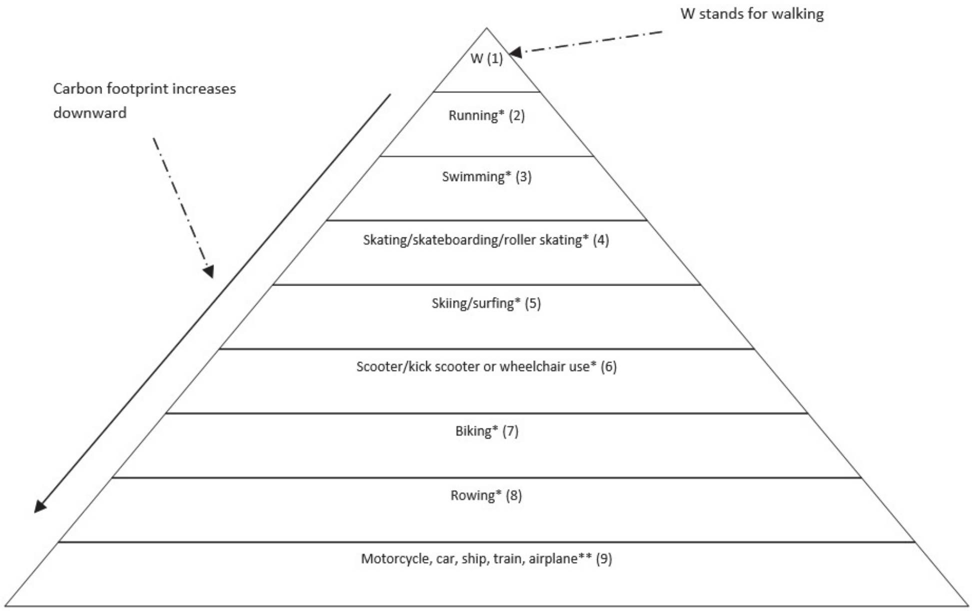

Figure 1. A hierarchy of potential environmental impact of active and non-active transport modes. Note: Active transport modes shown (i.e., 1–8) do not involve the combustion of fossil fuels; the hierarchy was developed based on whether the transport behaviour involves the use of a product or vehicle, depends on a utility or energy source that emits greenhouse gases, and whether the productive involved is small, biodegradable, or recyclable; the hierarchy also assumes that greenhouse gas emissions across the lifespan of fuel-dependent transport modes are more than emissions across the lifespan of active transport modes; size of the vehicle, equipment, or product is assumed to increase down the pyramid; ** Represent non-active or fossil fuel-dependent modes of transportation; * Active modes of transportation.

5. Theoretical Framework

The literature [27,29,31] to date suggests that active transportation behaviour is influenced by three categories of factors, namely, demographic (e.g., age, income, and gender), psychosocial (e.g., neighbourhood trust, safety, and social cohesion), and physical environmental factors (e.g., street connectivity and mixed land use). Income, for example, determines car ownership and whether one will choose driving over walking [28,37]. Neighbourhoods with highly interconnected streets are more likely to encourage walking and bicycling [29,38], and those with psychosocial factors such as safety offer a better contextual advantage for active transportation [29,39]. Yet, the extent to which these factors affect active transportation differs among age groups due to changes in living conditions experienced by the individual in ageing [39]. The Bioecological Systems Theory (BST) developed by Unrie Bronfenbrenner [40,41] implies that the onset of these changes starts in childhood.

The BST is a multi-level framework for understanding the influence of the above categories of factors on active transportation. The primary part of this system is the microsystem where young children begin life by developing relationships with parents and other close relatives. It provides a social climate where family norms and values are transferred by older ones to children in a gradual way, making it possible for younger ones to learn and apply family traditions. Children may grow to appreciate and enjoy biking to school owing to their exposure to a longstanding family tradition of biking to school. Studies have confirmed that children with active parents who travel to work through active transportation are more likely to walk or cycle to school [42,43]. Though the BST suggests that several other factors (e.g., family income) can influence the active travel of children, it implies that children begin to develop behaviours and habits through their subjection to relationships and norms in their immediate family environment. The main disadvantage at this stage is that children may not grow up with healthy behaviours (e.g., walking) if their immediate families do not value these behaviours. If family norms favour driving over walking, children would be influenced to cultivate the habit of using non-active transportation.

Beyond the microsystem, there are the mesosystem and exosystem that encompass a system of external relationships (e.g., teachers, and neighbours) intertwined with the child's immediate family [41]. These systems provide a wider social and physical environment, hereby referred to as the community, where knowledge and habits can diffuse between the family system, neighbours, and service providers, such as the school. From this viewpoint, active transportation among children may be co-influenced by the family, neighbours, and service providers. The wider social environment may support active travel through its qualities of cohesiveness, reciprocity, and safety [39], whereas teachers and social networks (e.g., friends and classmates) can encourage active travel [39,44] depending on norms within the community and their immediate families. As mentioned earlier, children and adolescents who are dependent on their parents are subject to influences from their family and community, so they would not perform active transportation behaviour if it were not a value in these social settings.

Before entering the third generation, children who grow into the second generation may enjoy enhanced autonomy and flexibility in decision-making because their parents may begin to recognise their improving maturity. In the third generation, therefore, parents may allow their adolescent children to make some decisions, including transport decisions. Thus, the second generation is in a stage where there is an onset of opportunities to exercise free will, monitored by mature members of the micro and mesosystems. If the child was well embedded in a family tradition of active transportation, for example, they might exercise free will in ways that translate into active transportation [43,44]. Yet, individuals in this generation may not have absolute autonomy, possibly because their parents are ambivalent about their life experiences.

In adulthood, individuals may have started an independent life, but they can maintain relationships across the three systems through regular communication and commuting with family members, workmates, and business partners. Autonomy and flexibility in decision-making may have reached an optimum level, enabling the individual to decide whether to pursue a lifestyle influenced by the family and other social systems in the first and second generations. Members of this generation are generally a working class who exercise control over their earnings and how to spend them through, for example, car ownership. Adults who grew up in a family or environment where active transportation was a shared hobby are likely to own a bicycle or similar equipment for active transportation. Such individuals, depending on how the three systems including the educational system influenced their pro-environment behaviour [19,27], may own cars but may only use them to travel long distances. The main disadvantage at this stage is that individuals may have new commitments (e.g., work) that may deprive them of social support and time for active transportation behaviour.

Between the first and third generations, the individual can adapt life experiences from social ties spanning the three systems. For instance, those who had left their family and community but were positively influenced to practice walking as a habit may continue to utilise past experiences to maintain walking. The opportunity to draw on the three systems (implicit in social ties and experiences from the previous community) is recognised by the Activity Theory of Ageing (ATA) [45,46]. The ATA asserts that ageing people can adapt their past experiences (e.g., cycling to school) and social networks to maintain physical activity. This process of life course adaptation occurs in a social context where skills and life experiences from social networks (e.g., parents or friends) are acquired through learning, observation, communication, and role modelling.

On the other hand, the Disengagement Theory of Ageing (DTA) argues that the ability to adapt past experiences to maintain physical activity and possibly stick to an acquired active transport behaviour dwindles in the ageing process due to a decline in the individual's resources (e.g., social ties and income) and physical functional ability in later life [46]. The DTA, thus, suggests that resources and physical abilities that may support active transportation may be insufficient in the fourth generation. As such, habits such as walking and cycling learned through the initial life stages may be discouraged by a decline in social networks (e.g., through the death of social ties) and physical functional capacity. Some researchers [39,46] and the ATA suggest, nevertheless, that individuals who maintain physical activity over the life course avoid this decline and maintain physical activity into later life. Individuals may maintain active transportation in the fourth generation if they started an active lifestyle earlier, ideally in the first generation and maintained it through the remaining stages. The ATA also insinuates that people can maintain autonomy in the fourth generation if they adapt past experiences rooted in the three systems of the BST across the lifespan.

Another factor that may influence active transportation across the four generations is a change in life goals necessitated by the ageing process [47]. For example, people in the fourth generation may decide to spend more time with closer social ties such as grandchildren and in-laws and avoid less important activities. This decision stems from older adults' future time perspective [48], which is about awareness of how short their remaining life is and a need to spend time on only activities and people who matter to them. This concept of future time perspective originates with the Socioemotional Selectivity Theory [49], which asserts that older adults may limit their social and physical environment through social disengagement by focusing on only a few valued relations and social activities associated with these relations. This behaviour may terminate the positive influence of demographic, psychosocial, and environmental factors on active transportation in later life. To explain, an older adult may give up social ties and activities in the community to spend more time with grandchildren through childcare at home.

Depending on the lifestyle of their social ties, nevertheless, older adults can maintain engagement with life through active transportation. Older adults who are psychologically and emotionally attached to their valued active grandchildren, in-laws, or surviving spouses may continue to perform physical activity (e.g., walking and cycling) necessitated by social activities. If individuals grew old in a family where active transportation was a tradition, their future time perspective would rather support the maintenance of active transportation [43], especially if this behaviour enhances their longevity, which they need to spend more time with their loved ones. An active family tradition makes it more likely for people in the fourth generation to maintain the willingness and ability to sustain active transportation. The above theoretical deductions suggest that all generations face barriers to active transportation and that even younger adults do not have a perfect chance to adopt active transportation behaviour.

6. Active Transportation Adoption: Are Older Adults Laggards?

Ageism against older adults in environmental activism is partly premised on the notion that older adults perform less pro-environment behaviour (i.e., active transportation) [19,23] and have generated a higher carbon footprint linked to non-active transportation over the life course [9]. As Table 2 suggests, however, every generation has unique barriers and opportunities for active transportation; opportunities for performing active transportation behaviour are uniquely counteracted in each generation, which is why the sustainability of active transportation over the life course is not necessarily higher in generations under 50 years. As the above theoretical framework suggests, the way opportunities and barriers in Table 2 play out in practice depends on context, characterised by the family and wider community from which learning and adaptive behaviour take place. In this section, the authors emphasise empirical evidence supporting this reasoning by reviewing studies on the relationship between age, pro-environmental behaviour, and active transportation.

Table 2. The authors' visualisation of the core characteristics of the four generations within the theoretical framework.

Group	Description	Core Attribute(s)	Possible Barriers	Possible Opportunities	Implications *
Children (generation 1)	Infants and other young children aged 0–12 years who cannot make decisions	Members live with parents or guardians and are subject to parents	(1) Little or no autonomy, and (2) dependence **** on parents that may limit active transportation	(1) Teachableness, and (2) opportunities to start learning from family, networks (e.g., teachers), and community **	Children do not make their own decisions, so their parents and immediate social environment may prevent them from choosing active transportation if they do not value this travel behaviour
Adolescents (generation 2)	Adolescents and teenagers aged 13–17 years who are living with parents or guardians	Members live with parents or guardians and are subject to parents but with improved autonomy vias-a-vis stage 1	(1) Improved but limited autonomy, and (2) insufficient independence from parents, which can prevent active transportation	(1) Youthful vigour or physical strength and (2) learning opportunities through mentoring, formal education, and positive norms (e.g., walking regularly for health)	Adolescents can draw on their physical strength to perform active transportation behaviour if their family and community provide relevant norms and model behaviours
Adults (generation 3)	Individuals aged between 18 and 49 years	Members are likely working, have optimum autonomy, and can make and act on personal decisions	(1) May leave family as well as the community and networks one grew up with, and (2) new commitments (e.g., work) necessitated by independence may prevent active transportation	(1) Independence, (2) income from employment, and (3) optimum autonomy	Adults can make personal decisions, but the pursuit of new goals (e.g., using a car) can prevent them from choosing active transportation, especially in the absence of support *** from previous networks
Older adults (generation 4)	Individuals aged 50 years or higher	Members may have retired; functional ability may decline, and autonomy may reduce due to a disability	May lose supportive social networks, income, or functional abilities due to ageing	(1) Rich life experience, (2) a future time perspective that may support active behaviours, and (3) close ties (e.g., grandchildren) to support engagement with life	Older adults may lose the physical functional ability and resources (e.g., previous social networks) needed to perform active transportation behaviour

* Implications of the barriers and opportunities for the individual's active transportation choices; ** The community represents the multilevel exosystem implicit in the BST that includes institutions (e.g., school and teachers), neighbourhood social environment, and the physical built environment; *** Support refers to positive experiences (e.g., family norms, positive influence from school and teachers, and favourable environmental conditions, such as safety and social support) that encourage or allow the individual to develop and grow with positive behaviours, such as active transportation; **** Dependence on parents is only positive if the family environment provides positive norms and values; otherwise, parents who do not value some behaviours (e.g., active transportation) may prevent their children from choosing it as a travel method.

The empirical literature to date provides mixed evidence regarding the relationship between age and pro-environmental behaviour. A cross-sectional study in Spain found pro-environmental behaviour higher among older adults [21], but two other studies in different countries found this behaviour is higher in younger adults [20]. In China, a cross-sectional study utilising data from 31 countries produced mixed findings, affirming that pro-environmental behaviour is not always higher in younger adults [23]. In a systematic review [20], 31 out of 33 studies reported mixed findings about the association between age and pro-environment behaviour, further affirming that younger adults do not perform higher pro-environment behaviour. This review revealed that older adults can perform higher pro-environment behaviour depending on personal and socio-environmental factors, which is congruent with the foregoing theoretical framework.

A study in the UK [19] found older adults, compared with younger adults, reported less active transportation time, but another study in Germany [26] reported older adults were more likely to perform active transportation behaviours (i.e., walking and cycling), compared with younger adults. In Taiwan, older adults were found to report more active transportation (i.e., cycling) [27] and two other studies [28,29] in Ghana and New Zealand have found older children are more likely to walk or cycle. Thus, the idea that younger people, compared with older people, perform higher active transportation behaviour is also not empirically supported.

Deductively, there is no consistent evidence that active transportation is higher in younger adults because of contextual differences (e.g., some may not grow up in a family or community with opportunities to perform positive behaviours), and differences in people's ability to learn and maintain active transportation over the life course. Because of this, ageing would limit or favour active transportation depending on the context. If so, older adults are not laggards when it comes to the adoption of active transportation, which means ageism against older adults in active transportation and environmental activism has no empirical basis.

7. Discussion

This review aimed to (1) develop a hierarchy for understanding the impacts of active and non-active transport modes on the environment and (2) analyse the adoption of active transportation between older and younger people.

Our analyses suggest that walking, running, and swimming are the only active transport modes with no or negligible carbon footprints. These three modes of transportation are on top of the pyramid or hierarchy, which indicates that they are the most environmentally friendly way to travel. Studies [50,51] recognise these modes of transportation as some of the best ways to travel without adversely impacting the environment, but our review adds to this recognition by proposing the hierarchy and implying that these three transportation methods would produce the least carbon footprint. The hierarchy suggests that active transport modes can generate carbon footprints depending on their size and how they are designed and used. Given this understanding, researchers are encouraged to rather promote active transportation with no or negligible emissions of greenhouse gases and avoid implying that all forms of active transportation behaviour are protective of the environment. Researchers have generally framed active transportation as a pro-environment behaviour [37,50,51], but our analyses reveal a need for them to acknowledge the limitations of active transport modes with a carbon footprint.

The general perception that older adults adopt active transportation less and would, therefore, contribute less to a safer environment is based on mixed and inconclusive evidence. As such, there is no basis for the ageist views reported in the literature [7,9] against older adults in environmental activism. If so, more generalisable empirical evidence is needed on the relationship between active transportation adoption and age, and any future studies assessing this relationship ought to consider the relative carbon footprints of the different modes of active transportation, without which it would be impossible to accurately determine each generation's transportation-related carbon footprint and its impact on the environment. As our review suggests, the adoption of active transportation is not impossible among older adults, though this segment of the population may have the least physical functional ability for performing active transportation behaviour [39,46]. Stakeholders are, therefore, encouraged to include older adults in transportation-related initiatives against climate change. Older adults may contribute unique and complementary experiences for advancing these initiatives.

7.1. Implications for Practice

According to the theoretical framework, communities comprising the family system, service providers (e.g., schools and hospitals), built environment, social networks, and psychosocial factors (e.g., safety and social cohesion) are the embodiment of micro-, meso-, and exosystem factors that enable people to learn and maintain positive behaviours over the life course. Some of the specific factors within these systems that support active transportation across the lifespan are family income, norms favouring healthy behaviours, walkability, and services, such as formal education [27,29,31]. Stakeholders should create inclusive communities and provide services enabling and empowering individuals to overcome barriers to active transportation across their lifespan. Public health education can also be implemented to influence families for developing pro-environment traditions through which their ageing members learn to maintain active transportation behaviour as a habit.

As the ATA suggests, older adults can maintain active transportation in later life if the above measures provide contexts where they can adapt their life experiences across the lifespan. Both the ATA and DTA agree that people become inactive in the ageing process because of a decline in resources and functional ability, but this decline can be avoided through lifelong adaptation of positive experiences acquired through learning in one's family and community. Learning in this vein can be encouraged through public health education or promotion in which individuals are conscientised to practice healthy behaviours, such as walking and cycling [52]. There is, thus, a need for scaling up public health promotion and education programmes intended to create awareness about the role of absolute active transportation in the fight against climate change.

As the hierarchy suggests, people's carbon footprint depends on whether vehicles or products used in their active transportation are biodegradable, recyclable, or large. If possible, manufacturers should prioritise products that are biodegradable, recyclable, and small. They may also consider avoiding the dependence of these products on utilities or energy sources that emit greenhouse gases. If products worn or used during active transportation do not emit any greenhouse gas or eventually become part of environmental waste, most or all active transport modes would generate a zero-carbon footprint. This recalls a need for individuals to properly dispose of waste during active transportation or use environment-friendly products during active transportation.

7.2. Limitations and Future Research

This review included 26 documents from two searches, but an analysis of the relationship between these documents was beyond the scope of our narrative review. Future systematic reviews discussing this relationship are needed. To meet our review goal, we focused on documents exclusively reporting a transportation type and a carbon footprint relating to it. Hence, the number of articles included in this review may be smaller than the number of studies based on active transportation in general. The active transportation types on top of the pyramid (e.g., walking) are not necessarily carbon-free as humans may wear clothes that produce greenhouse gases when walking or running. By referring to them as methods with a "zero-carbon footprint", we meant that they produce the least greenhouse gases and are the most sustainable alternatives for the earth. A more objective way to develop the hierarchy is to rank the transport modes based on their estimated carbon footprints. The literature, however, does not provide standard carbon footprints for transport modes, a shortcoming that future research should remedy. Similarly, this review does not estimate the carbon footprints of the various transport modes due to the non-availability of relevant data. Future researchers are encouraged to provide these estimates, preferably using objectively generated data. Future studies may also assess the validity of the hierarchy by comparing the carbon footprints of transportation types within the hierarchy. The authors' evaluation of product size may not be consistent across contexts and manufacturer niche markets. For instance, a bicycle for adults may be larger than a scooter for young children. Decision-makers should consider these inconsistencies in assessing and using the pyramid.

8. Conclusions

Active transportation can add to atmospheric greenhouse gases and is, therefore, not always environmentally friendly. Active transport modes that may have a zero-carbon footprint are walking, running, and swimming without a product. There are mixed and inconclusive findings regarding the potential effect of age on active transportation and pro-environment behaviour; hence, ageist stereotypes against older adults in environmental activism and active transportation are unwarranted and would weaken the impetus needed to overcome climate change. Younger and older people can avoid a carbon footprint if stakeholders can design the built environment and roll out policies that maximise the diffusion of knowledge and positive active transportation experiences in the family and community. Policies need to be rolled out to encourage families and communities to adopt active transportation behaviour as a culture. Public health education programmes aimed at encouraging individuals to practice active transportation behaviour over the life course are imperative and should be infused into public health policy. Manufacturers are encouraged to prioritise the production of active vehicles (e.g., scooters) that are biodegradable, recyclable, and small.

Author Contributions: Conceptualisation, N.A.; methodology, N.A.; software, N.A. and K.A.-N. validation, K.A.-N., W.N. and E.N.A.; formal analysis, N.A.; investigation, N.A., W.N. and E.N.A.; data curation, N.A. and W.N.; writing—original draft, N.A.; writing—review and editing, N.A., K.A.-N., W.N. and E.N.A.; visualisation, N.A. and K.A.-N.; supervision, N.A.; project administration, N.A. All authors have read and agreed to the published version of the manuscript.

Funding: This research received no external funding.

Institutional Review Board Statement: Not applicable.

Informed Consent Statement: As this study was a review, no informed consent was needed.

Data Availability Statement: Data were not used for this study.

Conflicts of Interest: The authors declare no conflict of interest.

Abbreviations

ATA	Activity Theory of Ageing
BST	Bioecological Systems Theory
DTA	Disengagement Theory of Ageing
MeSH	Medical Subject Headings
PRISMA	Preferred Reporting Items for Systematic Reviews and Meta-Analyses
SPIDER	Sample, Phenomenon of Interest, Design, Evaluation, Research type
UK	United Kingdom

Appendix A

Table A1. The review workplan.

Review title	Active and Non-Active Transportation and Associated Carbon Footprints
Start and end date	1–15 April 2023, (2 searches were performed; the first one was performed on the 1st of April and the second one on the 15th of April).
Research question	What are the potential carbon footprints of active and non-active transport modes?
Condition being studied	Transport modes (i.e., air, land, and sea) and their associated carbon footprints
Search Strategy	
Eligibility criteria (based on SPIDER)	
Sample	All individuals and age groups (to make an intergenerational analysis possible)
Phenomenon of interest	Transport modes accompanying information about their carbon footprints or carbon-dioxide-related emissions
Design	Mixed (qualitative and quantitative)
Evaluation	The relative amount of greenhouse gases produced by each transportation type
Research type	Reviews, primary studies, studies using secondary data, and narratives
Language	English

Table A1. *Cont.*

Date restrictions	No date restriction
Exclusion criteria	Documents published in other languages apart from English, not peer-reviewed, not reporting a transportation type and its carbon footprint, and not published by journals indexed by SCOPUS, Web of Science, or PubMed
Inclusion criteria	Published in English
	Reported transportation type linked to its carbon footprint or greenhouse gas emission
	Peer-reviewed
	Published by journals indexed by Scopus, Web of Science, or PubMed
Geographical scope	Documents from anywhere in the world
Databases	
Essential	PubMed, CINAHL, PsychInfo, ProQuest
As relevant to the subject:	Google Scholar, SCOPUS
Search terms	Transportation, "active transportation", "carbon footprint", "greenhouse gas emissions", association, health, age
Search results	Search 1 = 205; Search 2 = 2

Note: SPIDER—Sample, Phenomenon of Interest, Design, Evaluation, Research type.

Appendix B

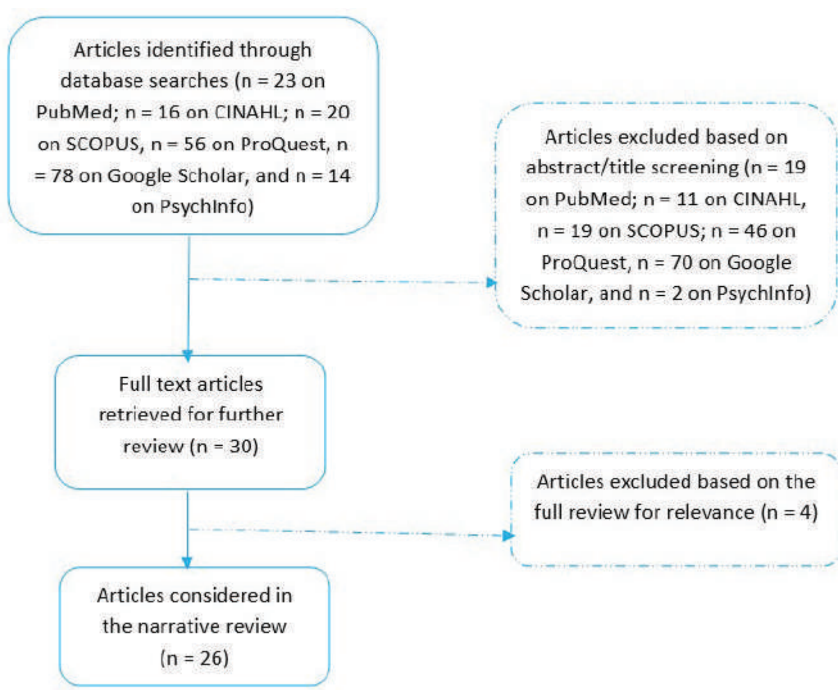

Figure A1. The PRISMA flowchart.

References

1. Wicker, P. The carbon footprint of active sport participants. *Sport Manag. Rev.* **2019**, *22*, 513–526. [CrossRef]
2. Frank, L.D.; Greenwald, M.J.; Winkelman, S.; Chapman, J.; Kavage, S. Carbonless footprints: Promoting health and climate stabilization through active transportation. *Prev. Med.* **2010**, *50*, S99–S105. [CrossRef]

3. Broberg, A.; Salminen, S.; Kyttä, M. Physical environmental characteristics promoting independent and active transport to children's meaningful places. *Appl. Geogr.* **2013**, *38*, 43–52. [CrossRef]
4. Ermagun, A.; Samimi, A. Promoting active transport modes in school trips. *Transp. Policy* **2015**, *37*, 203–211. [CrossRef]
5. Bempong, A.E.; Asiamah, N. Neighbourhood walkability as a moderator of the associations between older Ghanaians' social activity, and the frequency of walking for transportation: A cross-sectional study with sensitivity analyses. *Arch. Gerontol. Geriatr.* **2022**, *100*, 104660. [CrossRef]
6. Goel, R.; Oyebode, O.; Foley, L.; Tatah, L.; Millett, C.; Woodcock, J. Gender differences in active travel in major cities across the world. *Transportation* **2022**, *50*, 733–749. [CrossRef]
7. Ayalon, L.; Roy, S. The Role of Ageism in Climate Change Worries and Willingness to Act. *J. Appl. Gerontol.* **2022**, *42*, 1305–1312. [CrossRef] [PubMed]
8. Ayalon, L.; Ulitsa, N.; AboJabel, H.; Engdau, S. Older Persons' Perceptions concerning Climate Activism and Pro-Environmental Behaviors: Results from a Qualitative Study of Diverse Population Groups of Older Israelis. *Sustainability* **2022**, *14*, 6366. [CrossRef]
9. Ayalon, L.; Roy, S.; Aloni, O.; Keating, N. A Scoping Review of Research on Older People and Intergenerational Relations in the Context of Climate Change. *Gerontologist* **2022**, *63*, 945–958. [CrossRef] [PubMed]
10. Glazener, A.; Sanchez, K.; Ramani, T.; Zietsman, J.; Nieuwenhuijsen, M.J.; Mindell, J.S.; Fox, M.; Khreis, H. Fourteen pathways between urban transportation and health: A conceptual model and literature review. *J. Transp. Health* **2021**, *21*, 101070. [CrossRef]
11. Scheepers, C.E.; Wendel-Vos, G.C.W.; den Broeder, J.M.; van Kempen, E.E.M.M.; van Wesemael, P.J.V.; Schuit, A.J. Shifting from car to active transport: A systematic review of the effectiveness of interventions. *Transp. Res. Part A Policy Pract.* **2014**, *70*, 264–280. [CrossRef]
12. Dixon, A. The United Nations Decade of Healthy Ageing requires concerted global action. *Nat. Aging* **2021**, *1*, 2. [CrossRef] [PubMed]
13. Toner, A.; Lewis, J.S.; Stanhope, J.; Maric, F. Prescribing active transport as a planetary health intervention–benefits, challenges and recommendations. *Phys. Ther. Rev.* **2021**, *26*, 159–167. [CrossRef]
14. Hoj, T.H.; Bramwell, J.J.; Lister, C.; Grant, E.; Crookston, B.T.; Hall, C.; West, J.H. Increasing active transportation through e-bike use: Pilot study comparing the health benefits, attitudes, and beliefs surrounding e-bikes and conventional bikes. *JMIR Public Health Surveill* **2018**, *4*, e10461. [CrossRef]
15. Young, D.R.; Cradock, A.L.; Eyler, A.A.; Fenton, M.; Pedroso, M.; Sallis, J.F.; Whitsel, L.P. Creating Built Environments That Expand Active Transportation and Active Living across the United States: A Policy Statement from the American Heart Association. *Circulation* **2020**, *142*, E167–E183. [CrossRef]
16. Crawford, S.; Garrard, J. A combined impact-process evaluation of a program promoting active transport to school: Understanding the factors that shaped program effectiveness. *J. Environ. Public Health* **2013**, *2013*, 816961. [CrossRef]
17. Silveira-Santos, T.; Manuel Vassallo, J.; Torres, E. Using machine learning models to predict the willingness to carry lightweight goods by bike and kick-scooter. *Transp. Res. Interdiscip. Perspect.* **2022**, *13*, 100568. [CrossRef] [PubMed]
18. Shephard, R.J. Is active commuting the answer to population health? *Sports Med.* **2008**, *38*, 751–758. [CrossRef]
19. Adams, J. Prevalence and socio-demographic correlates of "active transport" in the UK: Analysis of the UK time use survey 2005. *Prev. Med.* **2010**, *50*, 199–203. [CrossRef]
20. Diamantopoulos, A.; Schlegelmilch, B.B.; Sinkovics, R.R.; Bohlen, G.M. Can socio-demographics still play a role in profiling green consumers? A review of the evidence and an empirical investigation. *J. Bus. Res.* **2003**, *56*, 465–480. [CrossRef]
21. Casaló, L.V.; Escario, J.J. Heterogeneity in the association between environmental attitudes and pro-environmental behavior: A multilevel regression approach. *J. Clean. Prod.* **2018**, *175*, 155–163. [CrossRef]
22. Chen, X.; Peterson, M.N.; Hull, V.; Lu, C.; Lee, G.D.; Hong, D.; Liu, J. Effects of attitudinal and sociodemographic factors on pro-environmental behaviour in urban China. *Environ. Conserv.* **2011**, *38*, 45–52. [CrossRef]
23. Wang, Y.; Hao, F.; Liu, Y. Pro-environmental behavior in an aging world: Evidence from 31 countries. *Int. J. Environ. Res. Public Health* **2021**, *18*, 1748. [CrossRef]
24. Sánchez, M.; López-Mosquera, N.; Lera-López, F. Improving Pro-environmental Behaviours in Spain. The Role of Attitudes and Socio-demographic and Political Factors. *J. Environ. Policy Plan.* **2016**, *18*, 47–66. [CrossRef]
25. Patel, J.; Modi, A.; Paul, J. Pro-environmental behavior and socio-demographic factors in an emerging market. *Asian J. Bus. Ethics* **2017**, *6*, 189–214. [CrossRef]
26. Finger, J.D.; Varnaccia, G.; Gabrys, L.; Hoebel, J.; Kroll, L.E.; Krug, S.; Manz, K.; Baumeister, S.E.; Mensink, G.B.M.; Lange, C.; et al. Area-level and individual correlates of active transportation among adults in Germany: A population-based multilevel study. *Sci. Rep.* **2019**, *9*, 16361. [CrossRef] [PubMed]
27. Liao, Y.; Wang, I.T.; Hsu, H.H.; Chang, S.H. Perceived environmental and personal factors associated with walking and cycling for transportation in Taiwanese adults. *Int. J. Environ. Res. Public Health* **2015**, *12*, 2105–2119. [CrossRef]
28. Agyeman, S.; Cheng, L.; Alimo, P.K. Determinants and dynamics of active school travel in Ghanaian children. *J. Transp. Health* **2022**, *24*, 101304. [CrossRef]
29. Ikeda, E.; Stewart, T.; Garrett, N.; Egli, V.; Mandic, S.; Hosking, J.; Witten, K.; Hawley, G.; Tautolo, E.S.; Rodda, J.; et al. Built environment associates of active school travel in New Zealand children and youth: A systematic meta-analysis using individual participant data. *J. Transp. Health* **2018**, *9*, 117–131. [CrossRef]

30. Mohareb, E.A.; Maclean, H.L.; Kennedy, C.A.; Mohareb, E.A.; Maclean, H.L.; Kennedy, C.A.; Mohareb, E.A.; Maclean, H.L.; Kennedy, C.A. Greenhouse Gas Emissions from Waste Management—Assessment of Quantification Methods Greenhouse Gas Emissions from Waste Management—Assessment of Quantification Methods. *J. Air Waste Manag. Assoc.* **2011**, *2247*, 480–493. [CrossRef]
31. Oliver, M.; Badland, H.; Mavoa, S.; Witten, K.; Kearns, R.; Ellaway, A.; Hinckson, E.; Mackay, L.; Schluter, P.J. Environmental and socio-demographic associates of children's active transport to school: A cross-sectional investigation from the URBAN Study. *Int. J. Behav. Nutr. Phys. Act.* **2014**, *11*, 70. [CrossRef] [PubMed]
32. Allin, S.; Masseria, C.; Mossialos, E.; Allin, S.; Masseria, C.; Mossialos, E. Equity in health care use among older people in the UK: An analysis of panel data. *Appl. Econ.* **2011**, *43*, 2229–2239. [CrossRef]
33. Kpessa-Whyte, M. Aging and Demographic Transition in Ghana: State of the Elderly and Emerging Issues. *Gerontologist* **2018**, *58*, 403–408. [CrossRef] [PubMed]
34. Ouchi, Y.; Rakugi, H.; Arai, H.; Akishita, M.; Ito, H.; Toba, K.; Kai, I. Rede fi ning the elderly as aged 75 years and older: Proposal from the Joint Committee of Japan Gerontological Society and the Japan Geriatrics Society. *Geriatr. Gerontol. Int.* **2017**, *17*, 1045–1047. [CrossRef]
35. Dong, Y.; Coleman, M.; Miller, S.A. Greenhouse Gas Emissions from Air Conditioning and Refrigeration Service Expansion in Developing Countries. *Annu. Rev. Environ. Resour.* **2021**, *46*, 59–83. [CrossRef]
36. Rickard, S.C.; White, M.P. Barefoot walking, nature connectedness and psychological restoration: The importance of stimulating the sense of touch for feeling closer to the natural world. *Landsc. Res.* **2021**, *46*, 975–991. [CrossRef]
37. Lee, R.E.; Kim, Y.; Cubbin, C. Residence in unsafe neighborhoods is associated with active transportation among poor women: Geographic Research on Wellbeing (GROW) Study. *J. Transp. Health* **2018**, *9*, 64–72. [CrossRef]
38. Carlson, J.A.; Saelens, B.E.; Kerr, J.; Schipperijn, J.; Conway, T.L.; Frank, L.D.; Chapman, J.E.; Glanz, K.; Cain, K.L.; Sallis, J.F. Association between neighborhood walkability and GPS-measured walking, bicycling and vehicle time in adolescents. *Health Place* **2015**, *32*, 1–7. [CrossRef]
39. Asiamah, N.; Bateman, A.; Hjorth, P.; Khan, H.T.A.; Danquah, E. Socially active neighborhoods: Construct operationalization for aging in place, health promotion and psychometric testing. *Health Promot. Int.* **2023**, *38*, daac191. [CrossRef]
40. Yang, C. Moral education in mainland China today: A bio-ecological systems analysis. *J. Moral Educ.* **2021**, *50*, 529–543. [CrossRef]
41. Oke, A.; Butler, J.E.; O'Neill, C. Identifying Barriers and Solutions to Increase Parent-Practitioner Communication in Early Childhood Care and Educational Services: The Development of an Online Communication Application. *Early Child. Educ. J.* **2021**, *49*, 283–293. [CrossRef]
42. Davison, K.K.; Werder, J.L.; Lawson, C.T. Children's Active Commuting to School: Current Knowledge and Future Directions. *Prev. Chronic Dis.* **2008**, *5*, A100. [PubMed]
43. Henne, H.M.; Tandon, P.S.; Frank, L.D.; Saelens, B.E. Parental factors in children's active transport to school. *Public Health* **2014**, *128*, 643–646. [CrossRef]
44. Rothman, L.; Macpherson, A.K.; Ross, T.; Buliung, R.N. The decline in active school transportation (AST): A systematic review of the factors related to AST and changes in school transport over time in North America. *Prev. Med.* **2018**, *111*, 314–322. [CrossRef] [PubMed]
45. Havighurst, R.J. Successful aging. *Gerontologist* **1961**, *1*, 8–13. [CrossRef]
46. Asiamah, N. Social engagement and physical activity: Commentary on why the activity and disengagement theories of ageing may both be valid. *Cogent Med.* **2017**, *4*, 1289664. [CrossRef]
47. Asiamah, N.; Conduah, A.K.; Eduafo, R. Social network moderators of the association between Ghanaian older adults' neighbourhood walkability and social activity. *Health Promot. Int.* **2021**, *36*, 1357–1367. [CrossRef]
48. Bardach, S.H.; Rhodus, E.K.; Parsons, K.; Gibson, A.K. Older Adults' Adaptations to the Call for Social Distancing and Use of Technology: Insights from Socioemotional Selectivity Theory and Lived Experiences. *J. Appl. Gerontol.* **2021**, *40*, 814–817. [CrossRef]
49. Löckenhoff, C.E.; Carstensen, L.L. Socioemotionol selectivity theory, aging, and health: The increasingly delicate balance between regulating emotions and making tough choices. *J. Pers.* **2004**, *72*, 1395–1424. [CrossRef]
50. Rosa, C.D.; Collado, S. Enhancing Nature Conservation and Health: Changing the Focus to Active Pro-environmental Behaviours. *Psychol. Stud.* **2020**, *65*, 9–15. [CrossRef]
51. Alipour, D.; Dia, H. A Systematic Review of the Role of Land Use, Transport, and Energy-Environment Integration in Shaping Sustainable Cities. *Sustainability* **2023**, *15*, 6447. [CrossRef]
52. Cochrane, T.; Davey, R.C. Increasing uptake of physical activity: A social ecological approach. *Sage J.* **2008**, *128*, 31–40. [CrossRef] [PubMed]

energies

Review

A Review of Current Advances in Ammonia Combustion from the Fundamentals to Applications in Internal Combustion Engines

Fei Ma [1], Lingyan Guo [1], Zhijie Li [1], Xiaoxiao Zeng [1], Zhencao Zheng [2], Wei Li [1,*], Feiyang Zhao [2,*] and Wenbin Yu [2]

1 State Key Laboratory of Engine and Powertrain System, Weichai Power Co., Ltd., Weifang 261061, China
2 School of Energy and Power Engineering, Shandong University, Jinan 250100, China
* Correspondence: liwei09@weichai.com (W.L.); fyzhao@sdu.edu.cn (F.Z.)

Abstract: The energy transition from hydrocarbon-based energy sources to renewable and carbon-free energy sources such as wind, solar and hydrogen is facing increasing demands. The decarbonization of global transportation could come true via applying carbon-free fuel such as ammonia, especially for internal combustion engines (ICEs). Although ammonia has advantages of high hydrogen content, high octane number and safety in storage, it is uninflammable with low laminar burning velocity, thus limiting its direct usage in ICEs. The purpose of this review paper is to provide previous studies and current research on the current technical advances emerging in assisted combustion of ammonia. The limitation of ammonia utilization in ICEs, such as large minimum ignition energy, lower flame speed and more NO_x emission with unburned NH_3, could be solved by oxygen-enriched combustion, ammonia–hydrogen mixed combustion and plasma-assisted combustion (PAC). In dual-fuel or oxygen-enriched NH_3 combustion, accelerated flame propagation speeds are driven by abundant radicals such as H and OH; however, NOx emission should be paid special attention. Furthermore, dissociating NH_3 in situ hydrogen by non-noble metal catalysts or plasma has the potential to replace dual-fuel systems. PAC is able to change classical ignition and extinction S-curves to monotonic stretching, which makes low-temperature ignition possible while leading moderate NO_x emissions. In this review, the underlying fundamental mechanism under these technologies are introduced in detail, providing new insight into overcoming the bottleneck of applying ammonia in ICEs. Finally, the feasibility of ammonia processing as an ICE power source for transport and usage highlights it as an appealing choice for the link between carbon-free energy and power demand.

Keywords: ammonia; internal combustion engines; combustion; emissions

Citation: Ma, F.; Guo, L.; Li, Z.; Zeng, X.; Zheng, Z.; Li, W.; Zhao, F.; Yu, W. A Review of Current Advances in Ammonia Combustion from the Fundamentals to Applications in Internal Combustion Engines. *Energies* **2023**, *16*, 6304. https://doi.org/10.3390/en16176304

Academic Editor: Sergey M. Frolov

Received: 26 July 2023
Revised: 27 August 2023
Accepted: 28 August 2023
Published: 30 August 2023

1. Introduction

Global transition from traditional fossil to renewable resources has been a concern for years to mitigate greenhouse gases. To a large extent, renewable fuels are regarded as promising energy carries particularly adapted for long-distance and high-powered mobility or long-term energy storage. Hydrogen, a carbonless fuel, has been recognized as the most promising fuel and clean energy carrier for automotive, marine and power generation [1]. A global hydrogen-based economy will be a sunrise for the energy issue after solving the bottleneck regarding the transportation and storage of hydrogen with reliable safety and reasonable cost. Therefore, closer attention has been paid to studying H_2-carrier fuel in the form of different chemical substances.

Ammonia (NH_3) is presently receiving a surge of attention as an energy carrier of high gravimetric hydrogen density (17.8% hydrogen content by mass), and is considered a carbon-free fuel that can be directly used in both combustion and fuel cell systems. Ammonia is a colorless gas with a very pungent odor at room temperature and can be dissolved in water. Ammonia has trigonal pyramidal molecule geometry with three hydrogen atoms, as well as an unshared pair of electrons attached to a nitrogen atom, and molecule polar covalent bond formation takes place between nitrogen and hydrogen [2]. Due to the strong hydrogen bonds between ammonia molecules, it is easily liquefied. Liquefaction of ammonia is able to happen at 10 bar at room temperature or −33.4 °C at atmospheric pressure, while hydrogen can only be liquefied under −253 °C. Ammonia is able to be stored in liquid form under suitable pressure conditions, ensuring a comparable energy density with other fuels, and it has competitive lower heating value (LHV) [3]. In terms of energy density in storage conditions, liquid ammonia is more than 40% denser than liquid hydrogen or more than twice that of compressed gas hydrogen.

Ammonia is the second-largest chemical products (after sulfuric acid) in the world (over 200 million tons per annum globally with more than USD $60 billion market value) [4,5]. Approximately 80% of global ammonia is utilized in agriculture as fertilizer, with around 5% for explosives, and the balance for industrial cooler refrigerant and chemical commodities. Currently, little ammonia is utilized for energy carriage, but there is definitely great potential for ammonia to be consumed as a renewable fuel in gas turbines, internal combustion engines or fuel cells without a carbon footprint in the years to come. The industrial production of ammonia (NH_3) from N_2 and H_2 is mainly dominated by the Haber–Bosch (H-B) process in the presence of metal catalyst at high temperature (~700 K) and 10–25 MPa, responsible for 1.2% of the global anthropogenic CO_2 emissions [6]. The energy consumption of green H-B is within the range of 27.4–31.8 GJ ${t_{NH3}}^{-1}$, and improvement in overall energy efficiency up to 65% [7]. Furthermore, ammonia could be manufactured from renewable energy sources such as biomass, wind or solar. Achieving a CO_2-free, energy-efficient, low-capital Haber–Bosch synthesis loop is under investigation by electrically driven [8] or electrochemical [9] power sources. In addition, because the absorption and desorption reactions of ammonia is fully reversible, ammonia is able to be released from a solid complex such as $Mg(NH_3)_6Cl_2$ upon heating and compacted into a dense shape, which makes storage simple and safe [10]. Some of the metal ammine complexes show promising results for storing hydrogen, for example, $Mg(NH_3)_6Cl_2$ can store over 9% hydrogen by weight in its solid form. Therefore, ammonia is considered a superb fuel due to its carbon-free structure, safe storage and transportation and low production cost, but with high hydrogen gravimetric density.

Ammonia has regained a great deal of interest from governments and institutes, since it not only enables the vital delivery of nitrogen needed for crop growth but also serves as a chemical that is capable of producing cooling, heating, power, and propulsion with minimum storage cost [11]. When ammonia is labeled as one of the carbon-free alternative fuels, the interest in deploying ammonia is in fast growth. Herbinet et al. [12] summarized an interesting comparison between the advantages and disadvantages of ammonia when used as power solutions. Gas turbines are the system of choice for large-scale ammonia utilization, while solid oxide fuel cells perform better at small scales (below 10 MW). Ammonia can also be directly used in both spark ignition engines or compression ignition engines [12,13]. Predicted by life cycle analysis, it will reduce greenhouse gas emissions by three times through ammonia-fueled vehicles as an alternative to conventional gasoline [14]. The UK Department for Transport proposed taking action on clean maritime growth by placing "a group of hydrogen or ammonia powered domestic vessels in operation" [15]. Indeed, ammonia has a higher octane number than gasoline and natural gas (Table 1), thus allowing a higher compression ratio applied in engine operation. Even though the energy density of compressed ammonia is comparably less than that of gasoline and diesel, it is still much higher than that of compressed natural gas or liquid hydrogen. Research on ammonia for internal combustion engines (ICEs) is in its early stages. Ammonia has extreme low combustion intensity with difficult flammability, reflected by its narrow flammability limits and low laminar burning velocity (Table 1).

Table 1. The main characteristics of some fuels [16,17].

Properties	Units	Ammonia	Hydrogen	Hydrogen	Natural Gas	Gasoline	Diesel	Methanol	Ethanol
Molecular formula		NH_3	H_2	H_2	CH_4	C_5H_{12}-$C_{12}H_{26}$	C_4H_{100}-$C_{12}H_{26}$	CH_3OH	C_2H_5OH
Density	@NTP (kg/cm^3)	0.73		0.083	0.66	700–780	830–855	791	785
Boiling point	(°C)	−33		−253	−161.5	33–190	180–370	64.7	78
Evaporation latent heat	(kJ/kg)	1370		446	511	305	230–250	1160	840
Low heating value	(MJ/kg)	18.8	120.0	120.0	50.0	44.0	42.6	19.6	26.8
Laminar flame velocity	@NTP (cm/s)	7		100–1000	36.53	50	86.5	50	47
Carbon atomic mass fraction	(wt%)	0	0	0	75	86.5	86.3	37.5	52.1
Hydrogen atomic mass fraction	(wt%)	17.6	100	100	25	13.5	13.1	12.5	13
Storage method		Compressed Liquid	Compressed Liquid	Compressed Gas	Compressed Liquid	Liquid	Liquid		
Storage temperature	(K)	298	20	298	298	298	298		
Energy density under storage	(MJ/L)	11.5	8	4.8	9.7	32.0	35.2		21.3
Autoignition temperature	(K)	924	844/824	844/824	723/885	573	503/499–506	737	696
Minimum ignition energy	(mJ)	8		0.02	0.28	0.2–0.3		0.14	0.28
Octane rating	(RON)	110/≥130	>130/≥130	>130/≥130	107/125	90–98/92–98		109	109

NTP: Normal temperature and pressure condition: P = 1 bar, T = 293.15 K.

2. Method of Ammonia Production

Ammonia production can be classified as brown (or gray) ammonia, blue ammonia and green ammonia based on the carbon emissions from the manufacturing process [18]. Current brown ammonia is massively produced by reforming hydrocarbons such as methane using proven Haber–Bosch industrial technology [19], which requires a high-temperature, high-pressure environment as well as addition of N_2, as shown in Figure 1. Blue ammonia is able to be generated using hydrogen from natural gas in conjunction with CCUS (carbon capture, utilization, and storage), while the most desirable green ammonia can be made using hydrogen from water electrolysis without CO_2 emissions. Overall, the majority of ammonia (around 86% to 96%) is manufactured through the traditional Haber–Bosch process, although it is energy-intensive with low conversion efficiency (25% at 30 MPa) and high carbon emissions [20]. In addition, the remaining commercial ammonia comes from alternative technologies such as electrochemical or thermochemical processes etc. [19,20] powered by low pressure and no catalysts with carbon-free emissions [21]. Moreover, the electrochemical process can be performed over a wide range of temperatures, depending on the electrolyte applied during the process [19].

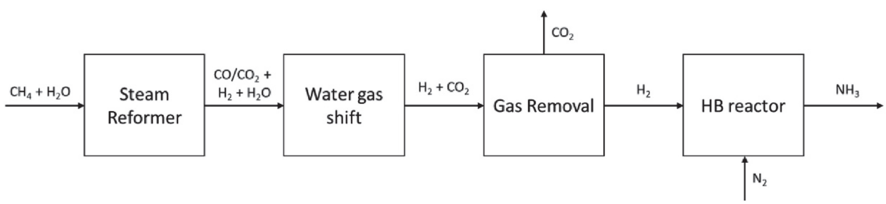

Figure 1. Simplified NH_3 production progress with CH_4 as the main raw material [19].

Plasma-assisted ammonia synthesis is alternative option to produce NH_3 from H_2 and N_2 via the formation of NH radicals. Many studies have concentrated on the application of plasma catalysts at ambient temperature. Li et al. [22] found that the reaction rate of ammonia synthesis was facilitated by the interaction between catalyst and plasma, which was double the pure catalyst load and 30 times that of plasma only. Andersen et al. [23] and Sun et al. [24] used the open-source code ZDPlasKin to numerically figure out the underlying kinetic processes of plasma-assisted ammonia synthesis. They both found surface interactions such as Eley–Rideal (E-R) and Langmuir–Hinshelwood (L-H) reactions contributed to the production of ammonia significantly. The dominant reaction mechanisms of plasma-catalyzed ammonia synthesis are illustrated in Figure 2 and were summarized by Engelmann et al. [25]. Due to electron collisions, a large number of N_2 and H_2 molecules were ionized, excited, adsorbed and dissociated, followed by the adsorption of free radicals (N, H, NH and NH_2) on the surface of the catalyst. After that, these particles in the adsorbed state either underwent E-R reactions with groups in the gas phase or LH reactions on the catalyst surface due to atomic diffusion. Eventually, the resulting NH_3 was released from the catalyst surface. Unlike the traditional H-B process, breakage of the NN triple bond can happen at room temperature and pressure via plasma-assisted ammonia synthesis. However, the efficiency of plasma-assisted ammonia synthesis alone is not high because the strength of the NN bond (NN bond = 946 kJ/mol) is much greater than that of the NH bond (NH bond = 389 kJ/mol) at room temperature. Therefore, the choice of proper catalysts to improve the selectivity of the reaction products is also a hot topic of research.

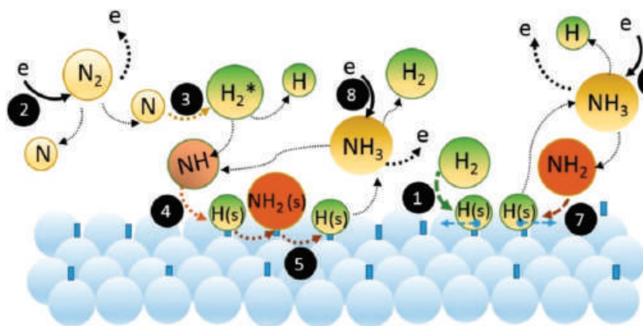

Figure 2. The main reaction process of plasma ammonia synthesis [25].

An efficient catalyst should exhibit not only strong adsorption of reactants but also low dissociation energy of products, which is contradictory to the catalyst itself. However, it is possible to modulate the bonding strength of N_2 and catalyst by elaborate design of alloy catalysts based on the surface bonding energy between metal atoms and N atoms. Xie et al. [26] prepared a high-entropy alloy (HEA) containing five common metallic elements that became saturated at 600 °C (with 100% conversion), and it was much more effective in catalysis than the noble metal Ru (with 73% conversion).

3. Limitations of Ammonia Fuel in ICEs

3.1. Ignition Energy

The minimum ignition energy (MIE) is typically defined as the minimum energy required to ignite the combustible gas [27], and a lower MIE indicates that a stable fire nucleus can be formed more easily in the early stages of combustion. Although ammonia has a high hydrogen content, pure ammonia combustion is inherently difficult to ignite. An ignition energy of 2.8 J is still required in spite of mixing with hydrogen fuel under a modified ignition system, which is two orders of magnitude higher than hydrocarbon fuel and four orders of magnitude higher than hydrogen [28]. Xin et al. [29] performed experimental studies on combustion and emission properties of a hydrogen/ammonia-fueled engine at part-load operating conditions. As illustrated in Figure 3a,b, the addition of ammonia changed the combustion characteristics by prolonging ignition delay times (duration of CA0-10) and flame development periods (duration of CA10-90) due to its higher ignition energy. Meanwhile, the combustion phase was still controllable by modulation of ignition timing for improved indicated thermal efficiency (ITE) and acceptable NOx emission.

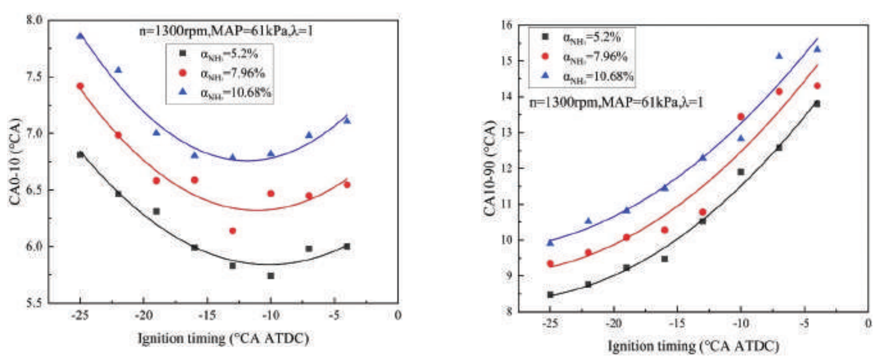

(**a**) (**b**)

Figure 3. Combustion durations versus ignition timing at different ammonia levels [29]. (**a**) duration of CA0-10 for varied addition of ammonia (**b**) duration of CA10-90 for varied addition of ammonia.

3.2. Flame Speed

The primary limitation on the practical usage of ammonia as an engine fuel is the relatively slow flame speeds. The laminar burning velocity (LBV or Su) is an important parameter to characterize the premixed combustion process. Investigations on accelerating NH_3 efficient combustion with fuel additives have attracted the interest of many researchers. Numerical studies on the performance of premixed combustion of NH_3/H_2/air mixtures was conducted by Wang et al. [28] using Cantera open-source code. It was shown that the properties of NH_3/H_2/air mixture combustion could be comparable to that of hydrocarbon fuels under engine-relevant conditions; therefore, a high compression ratio is tolerable because of the excellent knock-resistance ability of the NH_3/H_2 mixture. In addition, the increase in Su with H_2 addition contributes to facilitated diffusion, intensified reactivity, and increased flame temperature. At a compression ratio of 10, Su is observably improved with more H_2 added. However, for the stoichiometric combustion of NH_3/H_2, there still needs to be a 39% hydrogen doping ratio to reach a comparable Su level as CH_4 combustion.

Lhuillier et al. [30] found the same phenomenon when studying ammonia blends under engine-relevant turbulent conditions: enrichment of hydrogen in ammonia leads to an earlier, more intense heat release. To figure out the effects of additives such as H_2, CO and CH_4 on the Su of ammonia blend combustion, Han et al. [31] proposed normalized enhancement parameters for quantitative analysis of the enhancement level. It was concluded that the effects of H_2 enhancement were exponential, while non-monotonic with CO and almost linear with CH_4 at mixing ratios greater than 0.2. Very low Su is constrained with pure CO/air combustion since almost no H or OH radical is accumulated during combustion, as shown in Figure 4, but when blended with moderate CO in NH_3, a rapid increase in Su is achieved by decomposed H and OH radicals. The trends of Su almost coincided with the curves of the maximum H molar fraction, which implied the effect of H radicals on Su was dominant. Similar findings with concentration of H and OH radicals were also reported in the flame combustion of ammonia/methane/air [32].

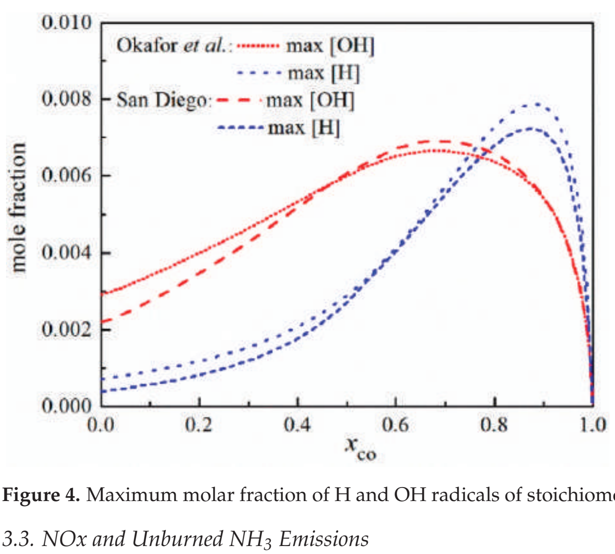

Figure 4. Maximum molar fraction of H and OH radicals of stoichiometric NH_3/CO/air flame [31].

3.3. NOx and Unburned NH_3 Emissions

The use of ammonia fuels is effective in reducing hydrocarbon emissions, but relatively it also increases the content of NOx and unburned NH_3 in exhaust. Representing significant progress in microscopic combustion kinetic reactions, chemical kinetic mechanisms are widely used to understand how quickly or slowly chemical reactions occur in nature. Numerous robust and concise chemical kinetic mechanisms have been proposed for ammonia oxidation under a wide range of conditions after verification of combustion characteristics and NOx emission. Since ammonia chemistry is less complex than that of hydrocarbons, the most recent ammonia oxidation mechanisms in different studies are generally fairly compatible. However, the differences are largely limited to the choice of rate constants or branching ratios for specific elementary reaction groups in varied application circumstances [33]. It is concluded that NO generation in burning lean ammonia depends heavily on OH radicals and HNO relative reactions, but under rich-ammonia combustion, rich H radicals promote formation of NH_x radicals [34]. However, as concluded by Li et al. [35], development of an accurate mechanism to model ammonia-based flame is urgently necessary. Apart from NOx emission, the carbon capture from low-carbon fuel-assisted ammonia flame is still worth studying.

Wang et al. [28] studied the performance of premixed hydrogen–ammonia combustion by simulations. The integrated rate of production (ROP) of NO and the species molar fraction with varied hydrogen molar fraction α are displayed in Figure 5. NO was considered the main source of NOx and two competitive mechanisms of NO production were analyzed: on the one hand, as more H content involved, the flame temperature and concentrations of reactive O/H radical were both increased, leading to a growth in NO generation as well as NH_3 conversion; on the other hand, the decrease in the reactant NH_3 suppressed the NO-related reaction rates in turn. Unlike fuel NO, which was formed with NH_3, the hot NO was more likely to be formed with the increasing of flame temperature caused by O/H radicals. Moreover, NO_2 was rapidly generated by conversion from NO in the flame region, then reconverted back to NO in the post-flame region via $NO_2 + O \rightarrow NO + O_2$, which finally reduced the total amount of NO_2 [36,37]. Jin et al. [38] investigated the effect of different ammonia-to-energy ratios (AER) on the combustion and emission characteristic of an ammonia–diesel dual-fuel engine. Compared to pure diesel engines, the NO emission was decreased instead with increasing AER because of the denitrification of amine, forming more stable N_2 via reduction reaction. However, the incomplete combustion of NH_3 was increased significantly due to the low combustion temperature.

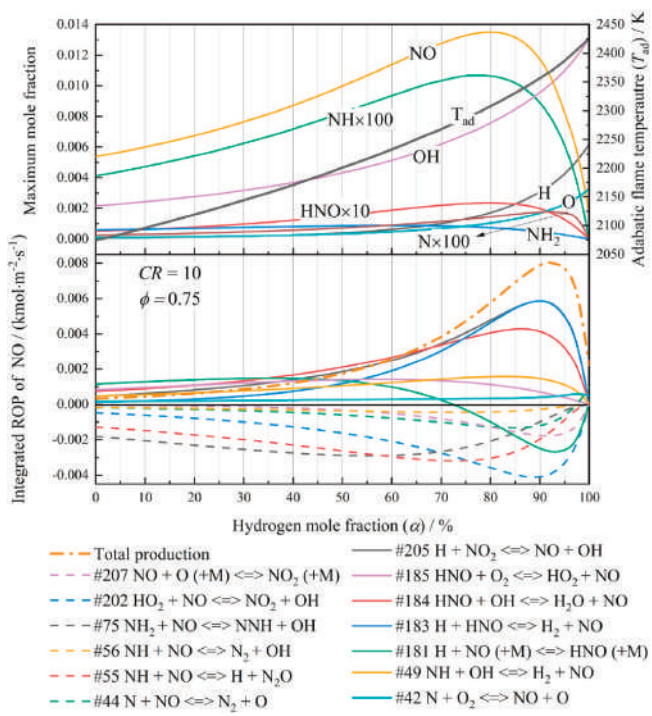

Figure 5. Temperature distribution and integrated production rate such as NO varies with α, φ = 0.75, CR = 10 [28].

As mentioned above, obstacles to the further development of ammonia-fueled engines are large minimum ignition energy, lower flame speed, and more NOx emission with unburned NH_3. However, some new technologies expanded on the next chapter are expected to overcome the difficulties.

4. Current Technologies of Ammonia-Fueled Engines

4.1. Oxygen-Enriched Combustion

It has been confirmed that oxygen-enriched combustion has the ability to lower fuel ignition points, speed up reactions, widen combustion limits and raise flame temperature. Therefore, some scholars studied the combustion characteristics of ammonia under oxygen-enriched conditions. For internal combustion engines, the advantages of oxygen-enriched technology solve the problems of further oxidation of CO and unburned hydrocarbons, but bring higher NOx emissions [39–44]. In order to overcome the shortcomings caused by oxygen enrichment, Liang et al. [45] applied an emulsification technique to diesel, which made the fuel unstable and then disperse throughout the combustion chamber after micro-explosion during the compression stroke in the engine. As a result, the combination of water diesel emulsion and oxygen-enriched combustion reduced the combustion temperature in the cylinder, thus leading to less NOx emission, while the output power of the engine was lower than the normal level. Karimi et al. [46] investigated the effects of oxygen enrichment on the combustion and emission characteristics of a hydrogen–diesel dual fuel (HDDF) engine under low load. Compared with traditional HDDF engines, the oxygen-enriched conditions improved the characteristics of low combustion temperature and laminar flame speed under low load, thus reducing ignition delay. However, more NOx was emitted than a diesel-only engine, but this could be reduced through the EGR technique. Since ammonia engines are not widespread, most of the research on ammonia has been on basic combustion characteristics. An experimental and kinetic modeling investigation on the laminar flame propagation of ammonia was conducted by Mei et al. [47] under oxygen-enrichment conditions. It was found the laminar burning velocity increased with the increasing oxygen content in both experimental and numerical studies, which was driven by the enriched concentrations of key radicals H, OH and NH_2. However, the oxygen enrichment also caused more NOx emissions in turn. Wang [3] investigated the basic characteristics of ammonia fuel in a constant-volume bomb, and the modeling-predicted laminar burning velocities by Cantera code under oxygen enrichment are given in Figure 6. The laminar flame velocity in the ammonia-burning system increased first and then declined as the equivalence ratio changed from 0.6 to 1.5, predicted by varied mechanisms. The greater the oxygen enrichment, the faster the laminar flow flame speed. Meanwhile, there was an interesting phenomenon: the equivalent ratio corresponding to the maximum laminar flame velocity moved towards the lean combustion side with increasing oxygen enrichment Ω. Similar findings were discovered for NOx emissions. As a result, when considering oxygen enrichment to assist ammonia combustion, NOx emissions should be given special attention.

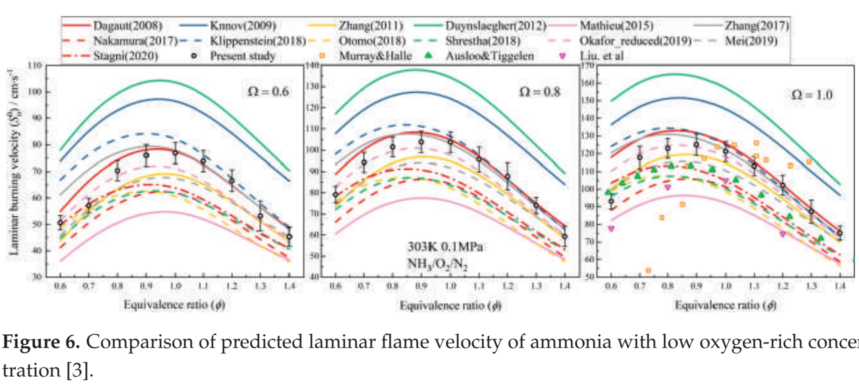

Figure 6. Comparison of predicted laminar flame velocity of ammonia with low oxygen-rich concentration [3].

4.2. Ammonia–Hydrogen Mixed Combustion

To improve the combustion characteristics of ammonia, it is effective to blend hydrogen with ammonia fuel because hydrogen laminar combustion is faster while having a wider combustion limit compared with ammonia. Differently from dual-fuel combustion or oxygen-enriched combustion, addition of hydrogen derived from partially cracked ammonia typically improves the combustion properties under the conditions of high temperature, high pressure and suitable catalyst. A basic investigation on ammonia decomposition was conducted by Ganley et al. [48], who evaluated the activity of metal catalysts: Ru > Ni > Rh > Co > Ir > Fe > Pt > Cr > Pd > Cu >> Te, Se, Pb. Comptti et al. [49] developed a hydrogen generation system (HGS) for ammonia–hydrogen-fueled internal combustion engines using a commercial ruthenium-based catalyst named ACTA 10010. The HGS heated by exhausted combustion gases performed well in hydrogen production, engine brake thermal efficiency and net heat release, but poorly for NOx emissions. Similar results can be found in the work by Ryu et al. [50], and it is emphasized that only a low ammonia flow rate would improve combustion performance.

Apart from dissociating NH_3 in situ from hydrogen, another method of preparing an NH_3/H_2 mixture is to inject hydrogen and ammonia into the intake manifold in the gaseous phase separately [51]. Zhang et al. [52] conducted a numerical investigation on the effects of hydrogen-rich reformate addition on the combustion and emission characteristics of an ammonia engine. It was found that the in-cylinder pressure and heat release rate increased almost linearly with the increasing reformate blending ratio (R_{re}) in stoichiometric cases. This is because more H and OH radicals were generated by the reaction $H_2 + O \rightarrow H + OH$ and the production would promote the consumption of NH_3. The increase in the combustion temperature resulting from greater R_{re} also reduced the emission of unburned NH_3 and N_2O, but too high a reforming ratio would appear undesirable, and thus they recommended a ratio of 7.5–10% near stoichiometry. Li et al. [53] investigated the effects of an ammonia–hydrogen mixture on combustion stability in a single-cylinder, four-value optical SI engine. The results showed that compared with a pure ammonia engine, the misfire phenomenon could be avoided by 5% hydrogen addition, 7.5% was the best thermal efficiency, and more than 20% would lead to unstable combustion. This is because a small amount of hydrogen would increase the combustion temperature in the cylinder and accelerate the ammonia oxidation, while further increasing the hydrogen content would cause heat loss, resulting in a decrease in the indicated thermal efficiency.

To understand the effect of cracking ratio on ammonia combustion, Mei et al. [54] performed both experimental and kinetic numerical investigations on laminar flame propagation of partially cracked NH_3/air mixtures. It was reported the laminar flame speed of the mixture was improved as the cracking ratio increased. The combustion was comparable to methane combustion with a cracking ratio of 40% at atmospheric pressure. Wang [3] investigated the variations in laminar flame speeds with different ammonia oxidation mechanisms at low hydrogen-doping ratios under ambient temperature and pressure conditions. It was found that the laminar flame speed increased significantly with increasing hydrogen-doping ratio α in both simulation and available experiments, since more O/H radicals produced by hydrogen accelerated the oxidation reaction of ammonia. Nevertheless, more NO was formed because NH radicals converted directly to NO without HNO oxidation and the conversion of NO to N_2O would be reduced by higher flame temperature.

Lhuiller et al. [55] investigated the behaviors of an ammonia-fueled engine at different H_2 concentrations, equivalence ratios and boosted pressures. It was found that an engine with high hydrogen concentrations performed well under lean combustion conditions, since the addition of H_2 promoted ignition and combustion stability. Wang et al. [56] studied the combustion characteristics of a NH_3/H_2 mixture with high hydrogen doping ratio (30%) in a medium-speed marine engine. As the equivalence ratio increased, it failed to ignite unless the initial intake temperature and pressure increased, but this limitation could be overcome when moderate proportion of hydrogen doping was added, for example, the peak flame temperature exceeded 2150 K at a 40% hydrogen doping ratio. However, if more hydrogen is required to achieve the assisted-ignition effect [57], it brings new challenges to ensure safe engine operation, since a large amount of additional hydrogen needs to be stored for fuel supply. In general, dual-fuel compression ignition engine operation with ammonia is dependent on the cetane number of pilot fuel and its injection strategies. The concerns of high unburned ammonia and NOx emissions because of the fuel-bound nitrogen are expected to be mitigated by an aftertreatment system. Thus, ammonia can be positively seen as a feasible solution as an alternative fuel for ICEs, without significant engine refit.

5. Plasma-Assisted Combustion Technology

5.1. Principle of Plasma-Assisted Combustion

Plasma is the fourth kind of matter distinguished from solid, liquid and gas, consisting of a large number of charged particles and neutral particles, which are electrically neutral. It can be classified into thermal equilibrium plasma and nonequilibrium plasma. Thermal or equilibrium plasmas are characterized by high energy density and equality between the temperature of heavy particles and electrons, while conversely a nonequilibrium plasma characteristic is a lower-pressure plasma with low ion and neutral temperatures, as shown in Figure 7. Nonequilibrium plasma plays a similar role to a catalyst to activate ambient gas molecules at room temperature and pressure through colliding and dissociating chemical bonding with the help of high-energy electrons [58,59]. Plasma generation methods commonly used are dielectric barrier discharge (DBD), atmospheric pressure plasma jet (APPJ) and sliding arc discharge plasma (GAD), while pulsed power is the most commonly used excitation power source for atmospheric low-temperature plasma [60].

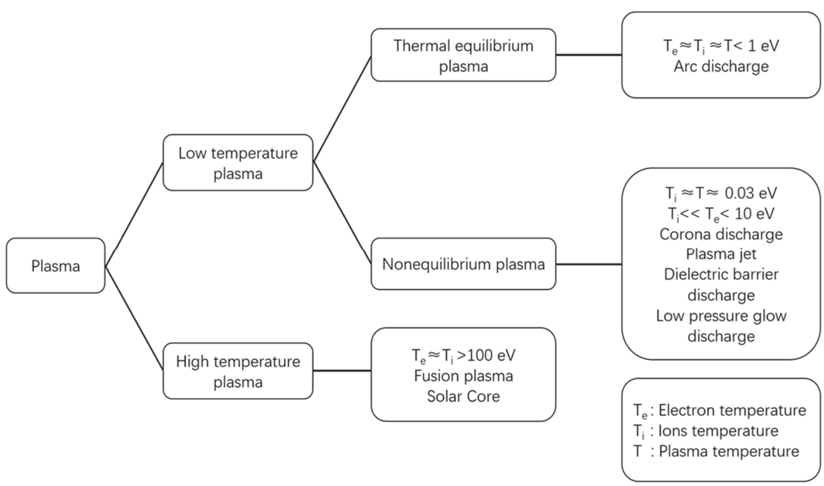

Figure 7. Plasma classification.

The enhancement of plasma-assisted combustion is achieved mainly through three pathways, as illustrated in Figure 8: thermodynamic effects, kinetic effects and transport [61]. Thermodynamically, the increase in overall gas and electron temperatures is ascribed to the energy conversion of the plasma discharge and the exotherm of chemical reactions, thus further accelerating the reactions. Kinetically, a large number of high-energy electrons and active particles involved in plasma not only facilitate chemical reactions due to the reduced activation energy but also introduce new branched reactions in the original system. For transport, plasma discharge will form ionic wind, which can accelerate the mixing process of reaction gases.

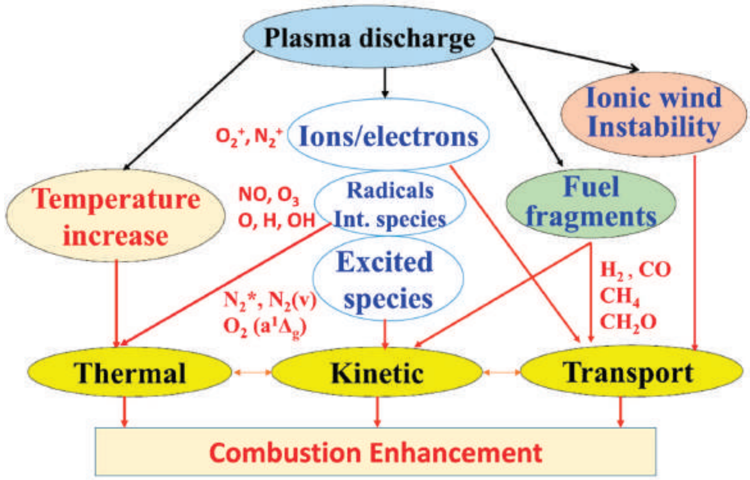

Figure 8. Principle of plasma-assisted combustion [61].

As mentioned, plasma-assisted combustion involves complicated plasma dynamics and combustion kinetics, so it is difficult to decouple the plasma effect and thermal effect from the perspective of conventional experiments due to cross-disciplinary complexity. Although it has been verified that plasma can play a significant role in enhancing combustion, modulating emissions and fuel reforming, the underlying mechanisms are a worthy ongoing topic in different application scenarios.

5.2. PAC Ignition Enhancement

It was found plasma-assisted combustion (PAC) can overcome the flame extinction limit and that PAC ignition enables lower-temperature combustion in contrast to high-temperature ignition, while it must follow the ignition S-curves in conventional ignition process, as shown in Figure 9 [61]. For internal combustion engines, plasma generated by different types of discharge such as microwave [62], radio frequency [63], laser ignition [64] and nanosecond pulses (NRP) [65,66], has been used to assist ignition and combustion. Among these, NRP has a significant advantage applied in low-energy ignition. To clarify the cumulative effect of repetitive NRP pulse number on the PAC, Barleon et al. [67] investigated the ignition of a premixed methane–air mixture by NPR in pin-pin configuration. The conclusion was that there was less total energy required as the pulse frequency increased. Compared with traditional spark ignition, Cathey et al. [65] found that it caused shorter ignition delay, higher peak pressure and greater net heat release in a single-cylinder gasoline engine through NRP. In fact, the expected minimum ignition energy is controlled by the minimum flame radius [61], which has a strong relationship to the Lewis number of the mixture, the fuel reactivity (activation energy) and the flame thickness. Therefore, the reduced ignition delay and lowered ignition energy by PCA were to a great extent due to the increase in the diversity of the reaction system (reduced Lewis number) and the decrease in activation energy.

The reduced electric field E/N is the most significant parameter to control the distribution of energy deposited to the different excitation modes and then generate active particles. Research to figure out the best reduced electric field to minimize the ignition time of CH_4/Air/He mixture was conducted by Mao et al. [68] using a combination of nanosecond pulses and DC discharges. In their study, a DC electric field of 5 Td minimized the time used for ignition, as shown in Figure 10, and it was revealed that the low-DC electric field promoted the excitation of $CH_4(v)$ and $O_2(v)$ effectively, as well as $O_2(a1\Delta g)$, which played a positive role in ignition enhancement through pathway flux analysis.

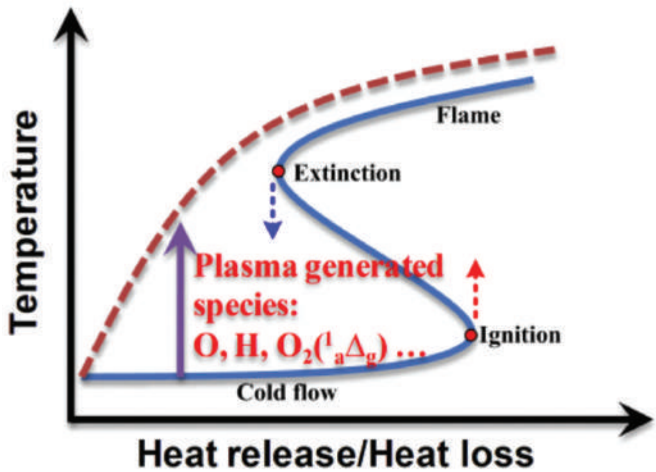

Figure 9. Schematic diagram of the plasma-assisted transition from the classical ignition and extinction S-curve (blue solid line) to the monotonic stretching S-curve (red dashed line) [61].

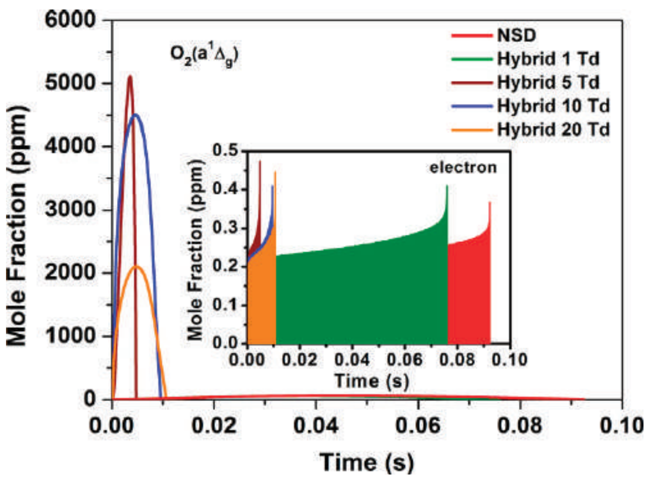

Figure 10. Time evolution of O_2(a1Δg) for NSD and mixed discharges with different DC field strengths at 900 K [68].

Furthermore, the time scale of plasma kinetics is within the order of nanoseconds, while the combustion kinetics fall in ranges from micro- to milliseconds [61], as illustrated in Figure 11. Therefore, the PAC process is the coupling of long-life plasma species with active radicals from fuel pyrolysis via energy transfer and kinetic interaction. From this point of view, the bridge linking fast plasma kinetics and combustion kinetics is critical to fully explore the PAC principles. This motivates the development of an efficient numerical model for multi-timescale PAC. Recently, the zero-dimensional plasma kinetic solver ZDplaskin incorporated with combustion kinetic solver CHEMKIN has been the most widely used numerical tool for PAC. ZDplaskin integrated with Boltzmann equation solver (BOLSIG+) is used to predict time evolution of neural radical and active species. Rate coefficients are formulated based on the incident energy by plasma discharges and collisional cross sections data of electron-associated reaction in LXCat format. Many studies have employed the ZDplaskin-CHEMKIN solver to study flame stability, contemplating the effects of plasma discharges on the flame propagation characteristics and ignition delay times [68,69]. However, there remain challenges in developing plasma kinetic mechanisms accommodating low-temperature and high-pressure conditions. At present, 2-D and 3-D numerical tools are not available for PAC modeling.

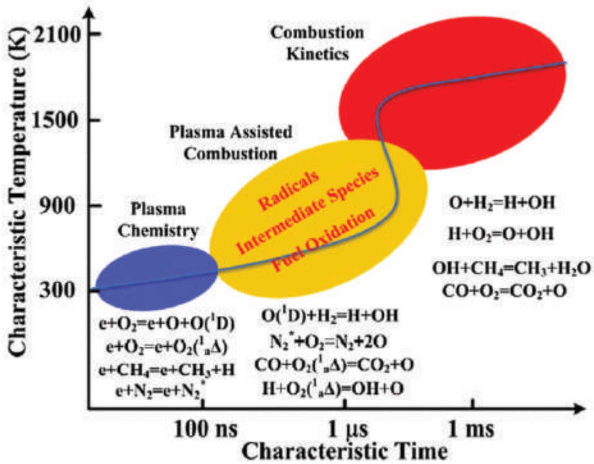

Figure 11. Schematic of timescales for PAC kinetics [61].

The dilution of different types of inert gases also affects electron energy distribution function in plasma, thus influencing the mixture combustion reactivity. A numerical investigation on the effects of methane pyrolysis with different diluents (N_2/Ar/He) was conducted by Mao et al. [70] using the zero-dimensional solver ZDPlasKin coupled with CHEMKIN. The results indicated that the quenching of electronic excited states and relaxation of the vibrational state contributed greatly to the pyrolysis of CH_4, for which the addition of N_2 as diluent performed best. As a result, it is concluded the excited states of equilibrium gases play a dominant role in physicochemical mechanisms and fuel oxidation efficiency through collisional quenching reactions. Similar findings were reported by Snoeckx et al. [71].

The commercial applications of plasma on ICEs are still immature, but many investigations are being carried out. Hwang et al. [72] developed a new microwave-assisted plasma ignition system and applied it to a direct injection gasoline engine. The new ignition system has a shorter ignition delay and a more advanced combustion stage than conventional spark ignition systems. It also broadened the thin combustion limit since it can form a larger fire nucleus by providing abundant reactive radicals over a larger area. A laser-induced plasma (LIP) ignition system has been evaluated to assist the ignition of a diesel–gasoline mixture in a CI engine by José et al. [73]. It was reported that the LIP ignition system can effectively solve the problem of automatic ignition of mixed fuels under different operations, and in addition, the variable height ignition technology improved combustion efficiency and reduced hydrocarbon emissions. L. et al. [74] investigated the ignition behavior of a methane–air mixture in an optically equipped setup consisting of a double chamber under repeated pulse discharge (NRPD). It showed that NRPD has a higher ignition success rate and average flame front propagation compared to standard inductive ignition. It can achieve lean combustion by adjusting the energy and number of pulses, but it did not work after inflammation.

6. Plasma-Assisted Ammonia Ignition

As mentioned above, addition of hydrogen derived from partially cracked ammonia typically improves the combustion properties. Direct decomposition of ammonia to hydrogen is a typical endothermic reaction with an enthalpy change of 91.2 kJ/mol. The decomposition of ammonia is able to be achieved at high temperature in the presence of a classic selective catalyst. Nevertheless, plasma catalysis is a promising approach to decompose ammonia at low temperature (<450 °C), but with a relatively high conversion rate. The synergistic effect of plasma and catalyst refers to the truth that it affects the catalytic process more than the sum of plasma and catalyst alone [75]. Although plasma catalytic ammonia synthesis is well understood, plasma catalytic ammonia decomposition still needs further study, and there is no commercial application available so far. Research on plasma catalytic ammonia decomposition has been centered on experiments, most of which have focused on designing high-efficient catalyst to improve hydrogen conversion. Wang et al. [76] measured the effect of DBD plasma synergism with Fe-based catalysts on ammonia decomposition efficiency through optical diagnostics and isotope scanning techniques. It was revealed the excited-state NH_3* and NH* played an important role in N atoms desorption, thus influencing conversion efficiency as the reaction temperature reduced by 100–140 °C. In their subsequent study [77], it was found the plasma promoted the chemisorption of NH_3*, leading to increased conversion by nearly 40% at 550 °C. The underlying physicochemical mechanisms of plasma catalytic kinetics should be further explored in depth to facilitate its practical usage in on-site hydrogen generation.

A number of simulation studies were carried out by using the kinetic model under wide conditions of temperatures ranging from 600 to 1500 K, and the characteristics of plasma-assisted ammonia combustion were predicted with varying pulsation frequencies and pulse numbers. Faingold and Lefkowitz [78] employed ZDplaskin-CHEMKIN with an assembled kinetic model for the oxidation of ammonia/oxygen/helium to perform pulse repetition frequencies (PRFs) on ignition delay times (IDTs). It was found IDTs could be reduced by 40–60%, as shown in Figure 12, under a moderate number of pulses. Higher PRFs promote an expanding radical pool, whereas lower PRFs favor the radical recombination between pulses.

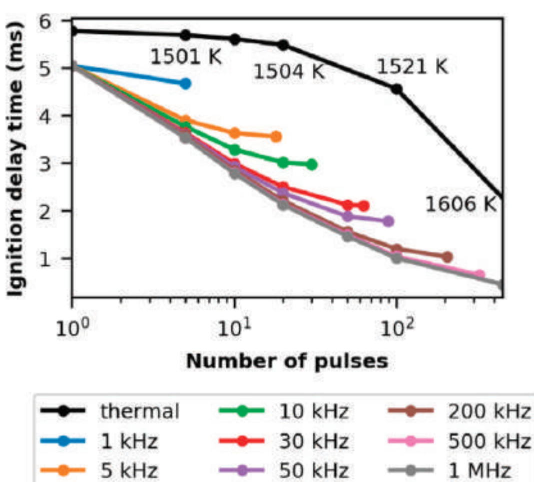

Figure 12. IDTs for different PRFs and number of pulses [78].

A series of experiments on plasma-assisted ammonia combustion were carried out because of the great advantages of plasma-assisted combustion as mentioned before. Lin et al. [79] studied the performance of plasma-assisted combustion via a new gliding arc plasma (GAP) generator combined with a cyclonic burner. The operation map of ammonia combustion flames with the GAP on or off is displayed in Figure 13, in which the ammonia combustion limitation was widened under both air and ammonia GAP. However, if the equivalence ratio exceeded 2.2 under a high air flow rate, the ammonia combustion flame would become unstable. Furthermore, the physicochemical mechanisms of discharged air and ammonia worked differently. The particles (OH*, H* and O*) played a dominant role in the dehydrogenation reaction of ammonia through kinetic mechanisms for the former (air medium) while the latter (ammonia medium) improved the combustion limit by the hydrogen produced from ammonia directly. A similar investigation on ammonia combustion was conducted by Choe et al. [80] using a nanosecond high-pressure pulse generator. It was concluded that plasma was able to extend the lean blowoff limits of ammonia flames and reduce NOx emissions simultaneously, but further research needs to be focused on the interaction between plasma dynamics and combustion kinetics.

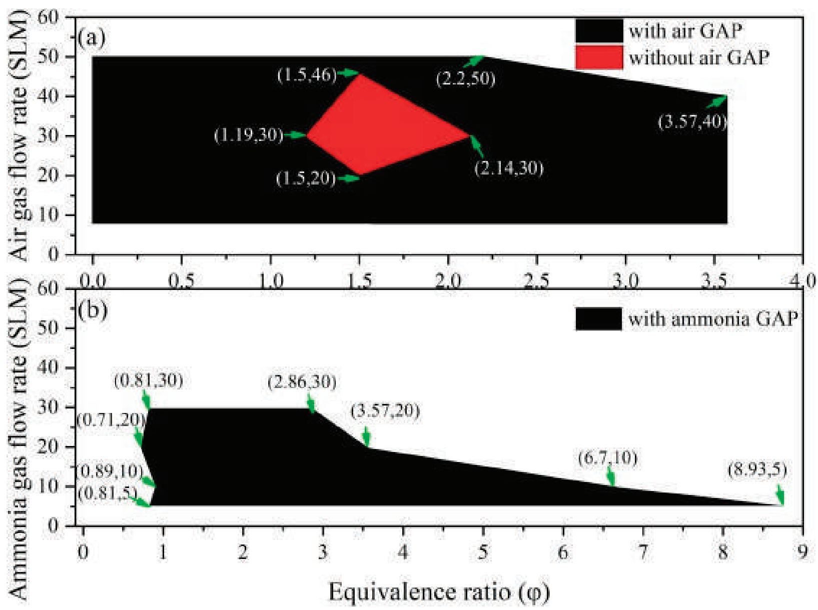

Figure 13. An operation map of ammonia combustion flames under the following conditions: (**a**) air GAP working on/off and (**b**) ammonia GAP working on.

Plasma-assisted ammonia combustion has great capacity for shortening ignition delay timing and extending combustible ranges while reducing NOx emissions. It will definitely promote the use of ammonia in engines. This has attracted lots of attention from scholars dedicated to figuring out the underlying physicochemical mechanisms via theoretical analysis and numerical simulation. Taneja et al. [81] found that PAC achieved the fastest ignition in a lean fuel mixture because of the accumulation of OH radicals through the reactivity-inhibiting reactions between plasma pulses, while an inversely proportional impact on ignition delay times was exhibited on plasma pulse frequency and energy density deposited. Moreover, the reforming of ammonia to nitrogen resulted in lower production of NOx with plasma. Another similar investigation also discovered PAC changed the conventional ignition and extinction characteristics, and the S-shaped curves were replaced by the monotonic and stretched ignition curves, which made low-temperature ignition possible [78]. Shahsavar et al. [82] figured out the most effective range of a reduced electric field on ammonia equivalent ratio combustion: 250–400 Td. This greatly promoted ignition time by increasing the reduced electric field in the early stage. With a more reduced electric field, a large fraction of the energy in the plasma system would be utilized in the ionization reactions of the diluent, thus neutralizing the effective excitations of fuel and oxidizer species, as shown in Figure 14.

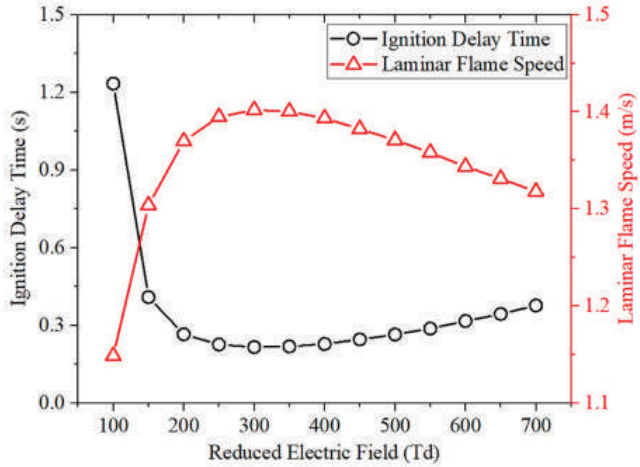

Figure 14. Effects of reduced electric field on ignition delay times and laminar flame velocities for plasma-assisted $NH_3/O_2/N_2$ combustion [82].

Finally, when projecting the adoption of plasma as an encouraging approach to boost ammonia decomposition and ignition, this review summarizes the latest innovations in the field of plasma catalysis and PAC, including progress in both numerical models and experimental studies. Great interest in improving ignition delay timing, increasing flame speed, and extending flammability limits while reducing NOx emissions will promote fast application in practical ICEs.

7. Conclusions

The outlook of independence from conventional fossil fuels is decarbonization in the automotive, marine and power generation sectors. Towards this goal, running with carbon-free fuel such as ammonia in ICEs is drawing more attention in research activities. Currently, ammonia can be ignited with diesel or any other high-reactivity fuel in dual-fuel mode, especially in marine engines and heavy-duty engines. Moreover, the addition of hydrogen is able to be derived from partially cracked ammonia with suitable catalyst in situ. However, the optimal hydrogen ratio in ammonia–hydrogen mixed combustion should not exceed 10%, considering thermal efficiency and combustion stability. A promising technology of plasma-assisted combustion to overcome the bottleneck of ammonia limits has attracted positive interest. The fundamental mechanisms of possible technical advances emerging in assisted combustion of ammonia are reviewed in this study.

(1) The laminar burning velocity of ammonia combustion increased with the increasing oxygen content, driven by the enriched concentrations of key radicals H, OH and NH_2. The maximum laminar flame velocity corresponds to equivalent ratio combustion, but the maximum NOx emissions moved towards lean combustion with increased oxygen enrichment.

(2) Investigations of ammonia-fueled engines have been widely carried out with varied additions of hydrogen, but modulations of inlet temperature and pressure are still necessary, especially for lean combustion. If more hydrogen is needed, it must be a new challenge to ensure operation safety with hydrogen supply.

(3) Plasma-assisted combustion enables lower-temperature combustion and has ability to overcome the flame extinction limit while reducing NOx emissions, due to the increase in diversity via active particles in the reaction system and the decrease in activation energy. The underlying physicochemical mechanisms of plasma-assisted ammonia combustion are rarely reported. The accumulation of OH radicals through reactivity-inhibiting reactions in lean fuel combustion could be stimulated through thermodynamic and kinetic effects via proper plasma generator configuration.

Funding: This research was funded by Open Funds of State Key Laboratory of Engine Reliability grant number [skler-202109], and Shandong Provincial Natural Science Foundation grant number [2022HWYQ-061, ZR2021ME212].

Data Availability Statement: Not applicable.

Conflicts of Interest: The authors declare no conflict of interest.

References

1. Dawood, F.; Anda, M.; Shafiullah, G.M. Hydrogen production for energy: An overview. *Int. J. Hydrogen Energy* **2020**, *45*, 3847–3869. [CrossRef]
2. Gorky, F.; Lucero, J.M.; Crawford, J.M.; Blake, B.A.; Guthrie, S.R.; Carreon, M.A.; Carreon, M.L. Insights on cold plasma ammonia synthesis and decomposition using alkaline earth metal-based perovskites. *Catal. Sci. Technol.* **2021**, *11*, 5109–5118. [CrossRef]
3. Wang, D.; Ji, C.; Wang, Z.; Wang, S.; Zhang, T.; Yang, J. Measurement of oxy-ammonia laminar burning velocity at normal and elevated temperatures. *Fuel* **2020**, *279*, 118425. [CrossRef]
4. Bartels, J.R. A Feasibility Study of Implementing an Ammonia Economy. Master's Thesis, Iowa State University, Ames, IA, USA, 2008.
5. Giddey, S.; Badwal, S.P.S.; Munnings, C.; Dolan, M. Ammonia as a renewable energy transportation media. *ACS Sustain. Chem. Eng.* **2017**, *5*, 10231–10239. [CrossRef]
6. Smith, C.; Hill, A.K.; Torrente-Murciano, L. Current and future role of Haber–Bosch ammonia in a carbon-free energy landscape. *Energy Environ. Sci.* **2020**, *13*, 331–344. [CrossRef]
7. Hasan, M.H.; Mahlia, T.M.I.; Mofijur, M.; Fattah, I.M.R.; Handayani, F.; Ong, H.C.; Silitonga, A.S. A comprehensive review on the recent development of ammonia as a renewable energy carrier. *Energies* **2021**, *14*, 3732. [CrossRef]
8. Schiffer, Z.J.; Manthiram, K. Electrification and decarbonization of the chemical industry. *Joule* **2017**, *1*, 10–14. [CrossRef]
9. Kyriakou, V.; Garagounis, I.; Vourros, A.; Vasileiou, E.; Stoukides, M. An electrochemical Haber-Bosch process. *Joule* **2020**, *4*, 142–158. [CrossRef]
10. Elmøe, T.D.; Sørensen, R.Z.; Quaade, U.; Christensen, C.H.; Nørskov, J.K.; Johannessen, T. A high-density ammonia storage/delivery system based on $Mg(NH_3)_6Cl_2$ for SCR–DeNOx in vehicles. *Chem. Eng. Sci.* **2006**, *61*, 2618–2625. [CrossRef]
11. Rouwenhorst, K.H.R.; Elishav, O.; Mosevitzky Lis, B.; Grader, G.S.; Mounaïm-Rousselle, C.; Roldan, A.; Valera-Medina, A. Future Trends. In *Techno-Economic Challenges of Green Ammonia as an Energy Vector*; Elsevier: Amsterdam, The Netherlands, 2021; pp. 303–319.
12. Herbinet, O.; Bartocci, P.; Dana, A.G. On the use of ammonia as a fuel—A perspective. *Fuel Commun.* **2022**, *11*, 100064. [CrossRef]
13. Dimitriou, P.; Javaid, R. A review of ammonia as a compression ignition engine fuel. *Int. J. Hydrogen Energy* **2020**, *45*, 7098–7118. [CrossRef]
14. Bicer, Y.; Dincer, I. Life cycle assessment of ammonia utilization in city transportation and power generation. *J. Clean. Prod.* **2018**, *170*, 1594–1601. [CrossRef]
15. Brown, T. UK Department of Transport Recommends Launch of Ammonia/Hydrogen Powered Vessels within 5–15 Years [EB/OL]. Ammonia Energy. 2019. Available online: https://www.ammoniaenergy.org/articles/uk-department-of-transport-recommends-launch-of-ammonia-hydrogen-powered-vessels-within-5-15-years/ (accessed on 26 June 2023).
16. Valera-Medina, A.; Amer-Hatem, F.; Azad, A.K.; Dedoussi, I.C.; de Joannon, M.; Fernandes, R.X.; Glarborg, P.; Hashemi, H.; He, X.; Mashruk, S.; et al. Review on ammonia as a potential fuel: From synthesis to economics. *Energy Fuels* **2021**, *35*, 6964–7029. [CrossRef]
17. Dimitriou, P.; Tsujimura, T. A review of hydrogen as a compression ignition engine fuel. *Int. J. Hydrogen Energy* **2017**, *42*, 24470–24486. [CrossRef]
18. Cardoso, J.S.; Silva, V.; Rocha, R.C.; Hall, M.J.; Costa, M.; Eusébio, D. Ammonia as an energy vector: Current and future prospects for low-carbon fuel applications in internal combustion engines. *J. Clean. Prod.* **2021**, *296*, 126562. [CrossRef]
19. Juangsa, F.B.; Irhamna, A.R.; Aziz, M. Production of ammonia as potential hydrogen carrier: Review on thermochemical and electrochemical processes. *Int. J. Hydrogen Energy* **2021**, *46*, 14455–14477. [CrossRef]
20. Berwal, P.; Kumar, S.; Khandelwal, B. A comprehensive review on synthesis, chemical kinetics, and practical application of ammonia as future fuel for combustion. *J. Energy Inst.* **2021**, *99*, 273–298. [CrossRef]
21. Gálvez, M.E.; Frei, A.; Halmann, M.; Steinfeld, A. Ammonia Production via a Two-Step Al_2O_3/AlN Thermochemical Cycle. *Ind. Eng. Chem. Res.* **2007**, *46*, 2047–2053. [CrossRef]
22. Li, K.; Chen, S.; Wang, H.; Wang, F. Plasma-assisted ammonia synthesis over Ni/LaOF: Dual active centers consisting of oxygen vacancies and Ni. *Appl. Catal. A Gen.* **2023**, *650*, 118983. [CrossRef]
23. Andersen, J.A.; Holm, M.C.; van't Veer, K.; Christensen, J.M.; Østberg, M.; Bogaerts, A.; Jensen, A.D. Plasma-catalytic ammonia synthesis in a dielectric barrier discharge reactor: A combined experimental study and kinetic modeling. *Chem. Eng. J.* **2023**, *457*, 141294. [CrossRef]

24. Sun, J.; Chen, Q.; Zhao, X.; Lin, H.; Qin, W. Kinetic investigation of plasma catalytic synthesis of ammonia: Insights into the role of excited states and plasma-enhanced surface chemistry. *Plasma Sources Sci. Technol.* **2022**, *31*, 094009. [CrossRef]
25. Engelmann, Y.; Kevin Yury Gorbanev Neyts, E.C.; Schneider, W.F.; Bogaerts, A. Plasma Catalysis for Ammonia Synthesis: A Microkinetic Modeling Study on the Contributions of Eley–Rideal Reactions. *ACS Publ.* **2021**, *9*, 13151–13163. [CrossRef]
26. Xie, P.; Yao, Y.; Huang, Z.; Liu, Z.; Zhang, J.; Li, T.; Wang, G.; Shahbazian-Yassar, R.; Hu, L.; Wang, C. Highly efficient decomposition of ammonia using high-entropy alloy catalysts. *Nat. Commun.* **2019**, *10*, 4011. [CrossRef] [PubMed]
27. Cui, G.; Zeng, W.; Li, Z.; Fu, Y.; Li, H.; Chen, J. Experimental study of minimum ignition energy of methane/air mixtures at elevated temperatures and pressures. *Fuel* **2016**, *175*, 257–263. [CrossRef]
28. Wang, D.; Ji, C.; Wang, S.; Yang, J.; Wang, Z. Numerical study of the premixed ammonia-hydrogen combustion under engine-relevant conditions. *Int. J. Hydrogen Energy* **2021**, *46*, 2667–2683. [CrossRef]
29. Xin, G.; Ji, C.; Wang, S.; Meng, H.; Chang, K.; Yang, J. Effect of different volume fractions of ammonia on the combustion and emission characteristics of the hydrogen-fueled engine. *Int. J. Hydrogen Energy* **2022**, *47*, 16297–16308. [CrossRef]
30. Lhuillier, C.; Brequigny, P.; Contino, F.; Mounaïm-Rousselle, C. Experimental investigation on ammonia combustion behavior in a spark-ignition engine by means of laminar and turbulent expanding flames. *Proc. Combust. Inst.* **2021**, *38*, 5859–5868. [CrossRef]
31. Han, X.; Wang, Z.; Costa, M.; Sun, Z.; He, Y.; Cen, K. Experimental and kinetic modeling study of laminar burning velocities of NH_3/air, NH_3/H_2/air, NH_3/CO/air and NH_3/CH_4/air premixed flames. *Combust. Flame* **2019**, *206*, 214–226. [CrossRef]
32. Jin, B.; Deng, Y.F.; Li, G.; Li, H. Experimental and numerical study of the laminar burning velocity of NH_3/H_2/air premixed flames at elevated pressure and temperature. *Int. J. Hydrogen Energy* **2022**, *47*, 36046–36057. [CrossRef]
33. Cai, T.; Zhao, D.; Gutmark, E. Overview of fundamental kinetic mechanisms and emission mitigation in ammonia combustion. *Chem. Eng. J.* **2023**, *458*, 141391. [CrossRef]
34. Chai, W.S.; Bao, Y.; Jin, P.; Tang, G.; Zhou, L. A review on ammonia, ammonia-hydrogen and ammonia-methane fuels. *Renew. Sustain. Energy Rev.* **2021**, *147*, 111254. [CrossRef]
35. Li, J.; Lai, S.; Chen, D.; Wu, R.; Kobayashi, N.; Deng, L.; Huang, H. A review on combustion characteristics of ammonia as a carbon-free fuel. *Front. Energy Res.* **2021**, *9*, 760356. [CrossRef]
36. Westlye, F.R.; Ivarsson, A.; Schramm, J. Experimental investigation of nitrogen based emissions from an ammonia fueled SI-engine. *Fuel* **2013**, *111*, 239–247. [CrossRef]
37. Mounaïm-Rousselle, C.; Bréquigny, P.; Dumand, C.; Houillé, S. Operating Limits for Ammonia Fuel Spark-Ignition Engine. *Energies* **2021**, *14*, 4141. [CrossRef]
38. Jin, S.; Wu, B.; Zi, Z.; Yang, P.; Shi, T.; Zhang, J. Effects of fuel injection strategy and ammonia energy ratio on combustion and emissions of ammonia-diesel dual-fuel engine. *Fuel* **2023**, *341*, 127668. [CrossRef]
39. Song, J.; Zello, V.; Boehman, A.L.; Waller, F.J. Comparison of the Impact of Intake Oxygen Enrichment and Fuel Oxygenation on Diesel Combustion and Emissions. *Energy Fuels* **2004**, *18*, 1282–1290. [CrossRef]
40. Maxwell, T.; Setty, V.; Jones, J.; Narayan, R. *The Effect of Oxygen Enriched Air on the Performance and Emissions of an Internal Combustion Engines*; SAE Technical Paper 932804; SAE International: Warrendale, PA, USA, 1993. [CrossRef]
41. Subramanian, K.; Ramesh, A. *Experimental Investigation on the Use of Water Diesel Emulsion with Oxygen Enriched Air in a DI Diesel Engine*; SAE Technical Paper 2001-01-0205; SAE International: Warrendale, PA, USA, 2001. [CrossRef]
42. Salzano, E.; Basco, A.; Cammarota, F.; Di Sarli, V.; Di Benedetto, A. Explosions of Syngas/CO_2 Mixtures in Oxygen-Enriched Air. *Ind. Eng. Chem. Res.* **2011**, *51*, 7671–7678. [CrossRef]
43. Baskar, P.; Senthilkumar, A. Effects of oxygen enriched combustion on pollution and performance characteristics of a diesel engine. *Eng. Sci. Technol. Int. J.* **2016**, *19*, 438–443. [CrossRef]
44. Li, S.-Q.; Guan, Q.; Zhang, W.-H. Test Study on Combustion Process of Oxygen-enriched Gasoline Engine. *J. Highw. Transp. Res. Dev.* **2008**, *3*, 25.
45. Liang, Y.; Shu, G.; Wei, H.; Zhang, W. Effect of oxygen enriched combustion and water–diesel emulsion on the performance and emissions of turbocharged diesel engine. *Energy Convers. Manag.* **2013**, *73*, 69–77. [CrossRef]
46. Karimi, M.; Wang, X.; Hamilton, J.; Negnevitsky, M. Numerical investigation on hydrogen-diesel dual-fuel engine improvements by oxygen enrichment. *Int. J. Hydrogen Energy* **2022**, *47*, 25418–25432. [CrossRef]
47. Mei, B.; Zhang, X.; Ma, S.; Cui, M.; Guo, H.; Cao, Z.; Li, Y. Experimental and kinetic modeling investigation on the laminar flame propagation of ammonia under oxygen enrichment and elevated pressure conditions. *Combust. Flame* **2019**, *210*, 236–246. [CrossRef]
48. Ganley, J.C.; Thomas, F.S.; Seebauer, E.G.; Masel, R.I. A Priori Catalytic Activity Correlations: The Difficult Case of Hydrogen Production from Ammonia. *Catal. Lett.* **2004**, *96*, 117–122. [CrossRef]
49. Comotti, M.; Frigo, S. Hydrogen generation system for ammonia–hydrogen fuelled internal combustion engines. *Int. J. Hydrogen Energy* **2015**, *40*, 10673–10686. [CrossRef]
50. Ryu, K.; Zacharakis-Jutz, G.E.; Kong, S.C. Performance enhancement of ammonia-fueled engine by using dissociation catalyst for hydrogen generation. *Int. J. Hydrogen Energy* **2014**, *39*, 2390–2398. [CrossRef]
51. Frigo, S.; Gentili, R.; Doveri, N. *Ammonia Plus Hydrogen as Fuel in a S.I. Engine: Experimental Results*; SAE Technical Paper 2012-32-0019; SAE International: Warrendale, PA, USA, 2012. [CrossRef]

52. Zhang, H.; Li, G.; Long, Y.; Zhang, Z.; Wei, W.; Zhou, M.; Belal, B.Y. Numerical study on combustion and emission characteristics of a spark-ignition ammonia engine added with hydrogen-rich gas from exhaust-fuel reforming. *Fuel* **2023**, *332*, 125939. [CrossRef]
53. Li, J.; Zhang, R.; Pan, J.; Wei, H.; Shu, G.; Chen, L. Ammonia and hydrogen blending effects on combustion stabilities in optical SI engines. *Energy Convers. Manag.* **2023**, *280*, 116827. [CrossRef]
54. Mei, B.; Zhang, J.; Shi, X.; Xi, Z.; Li, Y. Enhancement of ammonia combustion with partial fuel cracking strategy: Laminar flame propagation and kinetic modeling investigation of $NH_3/H_2/N_2$/air mixtures up to 10 atm. *Combust. Flame* **2021**, *231*, 111472. [CrossRef]
55. Lhuillier, C.; Brequigny, P.; Contino, F.; Mounaïm-Rousselle, C. Experimental study on ammonia/hydrogen/air combustion in spark ignition engine conditions. *Fuel* **2020**, *269*, 117448. [CrossRef]
56. Wang, Y.; Zhou, X.; Liu, L. Theoretical investigation of the combustion performance of ammonia/hydrogen mixtures on a marine diesel engine. *Int. J. Hydrogen Energy* **2021**, *46*, 14805–14812. [CrossRef]
57. Pochet, M.; Dias, V.; Moreau, B.; Foucher, F.; Jeanmart, H.; Contino, F. Experimental and numerical study, under LTC conditions, of ammonia ignition delay with and without hydrogen addition. *Proc. Combust. Inst.* **2019**, *37*, 621–629. [CrossRef]
58. Lin, Q.F.; Jiang, Y.M.; Liu, C.Z.; Chen, L.W.; Zhang, W.J.; Ding, J.; Li, J.G. Instantaneous hydrogen production from ammonia by non-thermal arc plasma combining with catalyst. *Energy Rep.* **2021**, *7*, 4064–4070. [CrossRef]
59. Gu, J.G.; Zhao, P.; Zhang, Y.; Wang, H.Y.; Jiang, W. Discharge Enhancement Phenomenon and Streamer Control in Dielectric Barrier Discharge with Many Pores. *Catalysts* **2020**, *10*, 68. [CrossRef]
60. Mei, D.H.; Fang, C.; Shao, T. Recent Progress on Characteristics and Applications of Atmospheric Pressure Low Temperature Plasmas. *Chin. J. Electr. Eng.* **2020**, *40*, 1339–1358+1425.
61. Ju, Y.; Sun, W. Plasma assisted combustion: Dynamics and chemistry. *Prog. Energy Combust. Sci.* **2015**, *48*, 21–83. [CrossRef]
62. Wolk, B.; DeFilippo, A.; Chen, J.Y.; Dibble, R.; Nishiyama, A.; Ikeda, Y. Enhancement of flame development by microwave-assisted spark ignition in constant volume combustion chamber. *Combust. Flame* **2013**, *160*, 1225–1234. [CrossRef]
63. Mariani, A.; Foucher, F. Radio frequency spark plug: An ignition system for modern internal combustion engines. *Appl. Energy* **2014**, *122*, 151–161. [CrossRef]
64. Morsy, M.H. Review and recent developments of laser ignition for internal combustion engines applications. *Renew. Sustain. Energy Rev.* **2012**, *16*, 4849–4875. [CrossRef]
65. Cathey, C.; Tang, T.; Shiraishi, T.; Urushihara, T.; Kuthi, A.; Gundersen, M.A. Nanosecond Plasma Ignition for Improved Performance of an Internal Combustion Engine. *IEEE Trans. Plasma Sci.* **2007**, *35*, 1664–1668. [CrossRef]
66. Wang, F.; Liu, J.B.; Sinibaldi, J.; Brophy, C.; Kuthi, A.; Jiang, C.; Ronney, P.; Gundersen, M. Transient plasma ignition of quiescent and flowing air/fuel mixtures. *IEEE Trans. Plasma Sci.* **2004**, *33*, 844–849. [CrossRef]
67. Barleon, N.; Cheng, L.; Cuenot, B.; Vermorel, O.; Bourdon, A. Investigation of the impact of NRP discharge frequency on the ignition of a lean methane-air mixture using fully coupled plasma-combustion numerical simulations. *Proc. Combust. Inst.* **2022**, *39*, 5521–5530. [CrossRef]
68. Mao, X.; Rousso, A.; Chen, Q.; Ju, Y. Numerical modeling of ignition enhancement of CH_4/O_2/He mixtures using a hybrid repetitive nanosecond and DC discharge. *Proc. Combust. Inst.* **2019**, *37*, 5545–5552. [CrossRef]
69. Wang, Y.; Guo, P.; Chen, H.; Chen, Z. Numerical modeling of ignition enhancement using repetitive nanosecond discharge in a hydrogen/air mixture I: Calculations assuming homogeneous ignition. *J. Phys. D Appl. Phys.* **2020**, *54*, 065501. [CrossRef]
70. Mao, X.; Chen, Q.; Guo, C. Methane pyrolysis with N_2/Ar/He diluents in a repetitively-pulsed nanosecond discharge: Kinetics development for plasma assisted combustion and fuel reforming. *Energy Convers. Manag.* **2019**, *200*, 112018. [CrossRef]
71. Snoeckx, R.; Cha, M.S. Inevitable chemical effect of balance gas in low temperature plasma assisted combustion. *Combust. Flame* **2021**, *225*, 1–4. [CrossRef]
72. Hwang, J.; Kim, W.; Agarwal, A.K.; Choe, W.; Cha, J.; Woo, S. Application of a novel microwave-assisted plasma ignition system in a direct injection gasoline engine. *Appl. Energy* **2017**, *205*, 562–576. [CrossRef]
73. José Martín Pastor Garcia-Oliver, J.M.; García, A.G.; Micó, C. Combustion improvement and pollutants reduction with diesel-gasoline blends by means of a highly tunable laser plasma induced ignition system. *J. Clean. Prod.* **2020**, *271*, 122499.
74. Merotto, L.; Balmelli, M.; Vera-Tudela, W.; Soltic, P. Comparison of ignition and early flame propagation in methane/air mixtures using nanosecond repetitively pulsed discharge and inductive ignition in a pre-chamber setup under engine relevant conditions. *Combust. Flame* **2022**, *237*, 111851. [CrossRef]
75. Zhang, S.; Oehrlein, G.S. From thermal catalysis to plasma catalysis: A review of surface processes and their characterizations. *J. Phys. D Appl. Phys.* **2021**, *54*, 213001. [CrossRef]
76. Wang, L.; Zhao, Y.; Liu, C.; Gong, W.; Guo, H. Plasma driven ammonia decomposition on a Fe-catalyst: Eliminating surface nitrogen poisoning. *Chem. Commun.* **2013**, *49*, 3787–3789. [CrossRef]
77. Wang, L.; Yi, Y.; Guo, Y.; Zhao, Y.; Zhang, J.; Guo, H. Synergy of DBD plasma and Fe-based catalyst in NH_3 decomposition: Plasma enhancing adsorption step. *Plasma Process. Polym.* **2017**, *14*, 1600111. [CrossRef]
78. Faingold, G.; Lefkowitz, J.K. A numerical investigation of NH_3/O_2/He ignition limits in a non-thermal plasma. *Proc. Combust. Inst.* **2021**, *38*, 6661–6669. [CrossRef]

79. Lin, Q.; Jiang, Y.; Liu, C.; Chen, L.; Zhang, W.; Ding, J.; Li, J. Controllable NO emission and high flame performance of ammonia combustion assisted by non-equilibrium plasma. *Fuel* **2022**, *319*, 123818. [CrossRef]
80. Choe, J.; Sun, W.; Ombrello, T.; Carter, C. Plasma assisted ammonia combustion: Simultaneous NOx reduction and flame enhancement. *Combust. Flame* **2021**, *228*, 430–432. [CrossRef]
81. Taneja, T.S.; Johnson, P.N.; Yang, S. Nanosecond pulsed plasma assisted combustion of ammonia-air mixtures: Effects on ignition delays and NOx emission. *Combust. Flame* **2022**, *245*, 112327. [CrossRef]
82. Shahsavari, M.; Konnov, A.A.; Valera-Medina, A.; Jangi, M. On nanosecond plasma-assisted ammonia combustion: Effects of pulse and mixture properties. *Combust. Flame* **2022**, *245*, 112368. [CrossRef]

sustainability

MDPI

Article

Formulation of a Jet Fuel Surrogate and Its Kinetic Chemical Mechanism by Emulating Physical and Chemical Properties of Real Jet Fuel

Guangze Li [1,2,3], Boxuan Cui [1], Chenglin Zhang [3], Liuyong Chang [1,2,3,*] and Longfei Chen [1,*]

[1] School of Energy and Power Engineering, Beihang University, Beijing 100191, China; liguangze@buaa.edu.cn (G.L.)
[2] Beihang Hangzhou Innovation Institute Yuhang, Hangzhou 310023, China
[3] Zhongfa Aviation Institute of Beihang University, Hangzhou 311115, China
* Correspondence: changliuyong@buaa.edu.cn (L.C.); chenlongfei@buaa.edu.cn (L.C.)

Abstract: The application of jet fuel in gas turbines and diesel engines adheres to the Army's single-fuel forward policy, streamlining supply chains. To ensure precise engine combustion numerical studies, surrogate fuels and mechanisms should faithfully replicate real fuel properties and combustion traits. In this work, a new four-component jet fuel surrogate containing 39.05% n-dodecane/21.79% isocetane/11.49% decalin/27.67% toluene by mole fraction is formulated based on a property optimizer. The new-formulated fuel surrogate can satisfactorily emulate the chemical and physical properties of real jet fuel, including cetane number (CN), threshold sooting index (TSI), molecular weight (MW), lower heating value (LHV), the ratio of hydrogen and carbon (H/C), liquid density, viscosity, and surface tension. Furthermore, a reduced and robust kinetic chemical mechanism (containing 124 species and 590 reactions) that could be directly employed in practical engine combustion simulations has also been developed for the proposed surrogate jet fuel. The mechanism is validated through comprehensive experimental data, including ignition delay time (IDT) determined in shock tubes and rapid compression machines (RCMs), species mole fractions measured in premixed flames and jet stirred reactors (JSRs), and laminar flame speeds. Generally, the property deviations of the jet fuel surrogate are less than 2% except for MW (10.73%), viscosity (5.88%), and surface tension (8.71%). The comparison results between the predictions and measurements are in good agreement, indicating that the current kinetic mechanism is capable of reflecting the oxidation process of real jet fuel. The current mechanism can accurately capture variations in the ignition delay time in the negative temperature coefficient (NTC) region as well. In the future, the proposed surrogate jet fuel could be applied in practical engine computational fluid dynamic (CFD) simulations.

Keywords: fuel property; ignition delay time; species profile; laminar flame speed; reduced chemical mechanism

Citation: Li, G.; Cui, B.; Zhang, C.; Chang, L.; Chen, L. Formulation of a Jet Fuel Surrogate and Its Kinetic Chemical Mechanism by Emulating Physical and Chemical Properties of Real Jet Fuel. *Sustainability* **2023**, *15*, 13792. https://doi.org/10.3390/su151813792

Academic Editor: Talal Yusaf

Received: 7 July 2023
Revised: 4 September 2023
Accepted: 12 September 2023
Published: 15 September 2023

1. Introduction

Jet fuel has been widely adopted as a general fuel for aircraft and ground vehicles in battlefields under the auspices of the U.S. army single-fuel policy [1], which aims to significantly reduce the costs of fuel supply. Furthermore, jet fuel is expected to reduce NOx and particle matter emissions in diesel engines, and thus it would be beneficial to investigate the effects of using jet fuel on the combustion and emission characteristics of diesel engines. However, due to the limitation of current computational capacity, the real jet fuel, which comprises hundreds of compounds, was unable to be directly employed in a practical engine simulation [2,3]. Therefore, surrogate jet fuels, which normally consist of several well-characterized compounds, were proposed [4–6]. The research on surrogate jet fuels is expected to achieve sustainability in the aviation fuel industry.

Previous research studies have been conducted on the development of jet fuel surrogate and their chemical mechanisms. In order to reproduce real fuels as well as possible, surrogates are required to closely emulate the thermo-physical properties and combustion characteristics of target jet fuels. Violi et al. [7] developed a JP-8 surrogate that contained six hydrocarbons and could emulate the distillation curve and thermo-physical properties of the target fuel. A detailed chemical mechanism of the surrogate was also presented in their work and validated by experimental data. Vasu et al. [8] evaluated the aforementioned chemical mechanism by comparing the measured and simulated IDT in a shock tube, and they reported that the mechanism could provide accurate IDT predictions above a temperature of 1000 K while predicting IDT poorly at low temperatures. Dagaut et al. [9] compared the kinetic modelling results of four jet fuel surrogates (one- and three-component mixtures of n-decane, n-propylbenzene, and n-propylcyclohexane) with JSR experimental data. The comparison results showed that the three-component surrogate was the most reliable substitute for the target fuel among all the test fuel surrogates. Gokulakrishnan et al. [10] developed a detailed kinetic model for the four-component kerosene fuel surrogate (n-decane/n-propylcyclohexane/n-propylbenzene/decene), which exhibited good performance in predicting the measured species concentrations. However, the IDT validations were not comprehensively conducted by them. Eddings et al. [11] proposed two six-component jet fuel surrogates named Hex-11 and Hex-12 to emulate a Jet-8 pool fire. The comparison results indicated that the surrogates could accurately capture the burning rate, emissive power, flame height, and puffing frequency of the steady-state pool fire. Dooley et al. [12] formulated a three-component jet fuel surrogate, 'MURI1′ (n-decane/iso-octane/toluene), based on chemical group theory. The CN and H/C of the target fuel were regarded as the target properties of MURI1. Several devices, including a flow reactor and shock tube, were employed to validate the combustion properties of the proposed surrogate. They further developed an improved jet fuel surrogate named MURI2 comprising n-dodecane, iso-octane, n-propylbenzen, and 1,3,5-trimethylbenzene [13]. Apart from CN and H/C, TSI and MW were also selected as the emulating metrics. According to the ignition characteristic study conducted by Malewicki et al. [14], MURI2 exhibited a satisfactory performance on predicting the species profiles of small molecules including oxygen, carbon monoxide, carbon dioxide, and C1-C3 hydrocarbons. Kim et al. [15] proposed two four-component aviation fuel surrogates named UM1 and UM2 based on a model-based optimizer. The physical and chemical properties of the target fuel were reproduced by the two surrogates to some extent.

Despite the extensive research efforts directed towards the creation of various jet fuel surrogates and their accompanying kinetic mechanisms, notable limitations remain apparent in this scientific domain: (1) A recurring challenge is the inability of these surrogates to comprehensively replicate the intricate amalgamation of the physical and chemical properties characteristic of the target fuel. Achieving a harmonious equilibrium between these multifaceted attributes remains an elusive goal. (2) Furthermore, the chemical kinetic mechanisms developed for these surrogates have often exhibited tendencies towards impracticality. They tend to be excessively voluminous or overly intricate, thus impeding their direct application within the confines of practical engine combustion simulations. (3) In addition, the validation of these proposed surrogate mechanisms has not been exhaustive, especially when it comes to crucial parameters such as ignition delay time (IDT), species mole fractions, and flame speeds. The inadequacy of rigorous validation procedures raises pertinent concerns about the reliability and robustness of these surrogates in real-world applications. Addressing these limitations represents an imperative for the advancement of this field.

With the aim of addressing the mentioned issues, a four-component fuel surrogate incorporating the physical and chemical properties of real jet fuel was developed using a property optimizer. Eight properties, including CN, TSI, MW, LHV, H/C, liquid density, viscosity, and surface tension, were selected as the target physical and chemical properties. A reduced kinetic mechanism, comprising 124 species and 590 reactions, for the surrogate was created which can prove advantageous in practical engine combustion simulations. Massive amounts of experimental data, including IDT, species concentration, and laminar flame speed, were collected to validate the mechanism from two aspects: the surrogate mixture and its components.

2. Formulation of Jet Fuel Surrogate

2.1. Target Fuel and Its Properties

The fuel combustion process inside an engine is very complex and always involves intricate physical and chemical processes. As shown in Figure 1, the fuel jet is injected into the cylinder via an injector, breaks down to small liquid droplets under the action of air shear force, and then evaporates and mixes with air to form a combustible fuel–air mixture. The processes are heavily affected by fuel physical properties such as viscosity, liquid density, and surface tension [16,17]. After that, the spontaneous ignition and combustion processes of the mixed fuel/air occur, where the chemical properties of the fuel have a significant influence on the events. Herein, CN dominates fuel ignitability, and MW plays a critical role in the diffusive transport process between liquid and the vaporized fuel. H/C influences the local ratio of fuel/air and adiabatic flame temperature, while LHV represents the energy generated from the fuel oxidation. Considering the above processes, eight properties, including CN, TSI, MW, LHV, H/C, liquid density, viscosity, and surface tension, were chosen as target properties for the surrogate in order to comprehensively reproduce the chemical and physical characteristics of real fuel in engine.

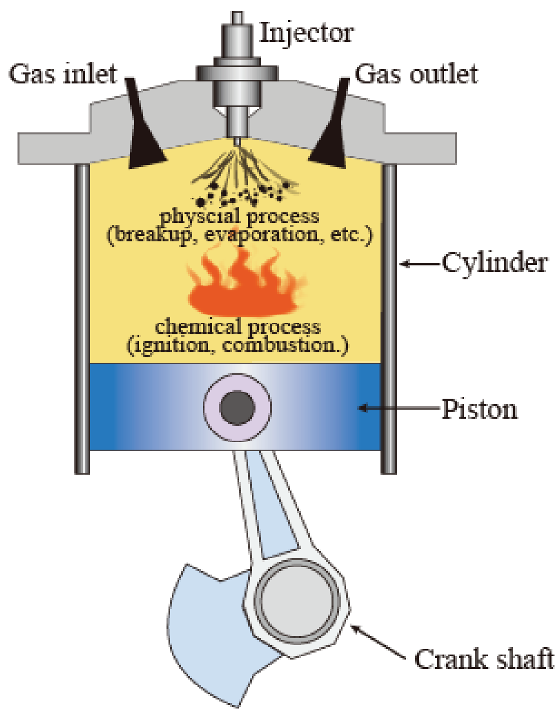

Figure 1. The physical and chemical processes in compression ignition engine.

In this work, Jet-A POSF-4658 (supplied by Edwards, AFRL-WP, Wright, OH, USA) was selected as the target real fuel for two reasons: First, it is a representative jet fuel comprising different jet-A batches, and its components and various properties have been extensively studied. Second, the experimental data on the IDT, laminar flame speed, and species concentration profiles of the fuel are available in the literature, so comparisons can be more readily conducted. However, since the data for LHV and surface tension of POSF-4658 are not available, the LHV of JP-8 fuel and surface tension of Jet-A were used instead as references in this study, similar to the previous studies [15,18]. The relevant properties of POSF-4658 were listed in Table 1.

Table 1. The properties of the target jet fuel [18].

Target Properties	Jet-A (POSF-4658)
CN *	47.1
MW	142 kg/kmol
H/C	1.957
LHV	43.23 MJ/kg
TSI	21.4
Liquid density	Temperature-dependent (See Figure 2)
Viscosity	Temperature-dependent (See Figure 2)
Surface tension	Temperature-dependent (See Figure 2)

* Derived cetane number (DCN).

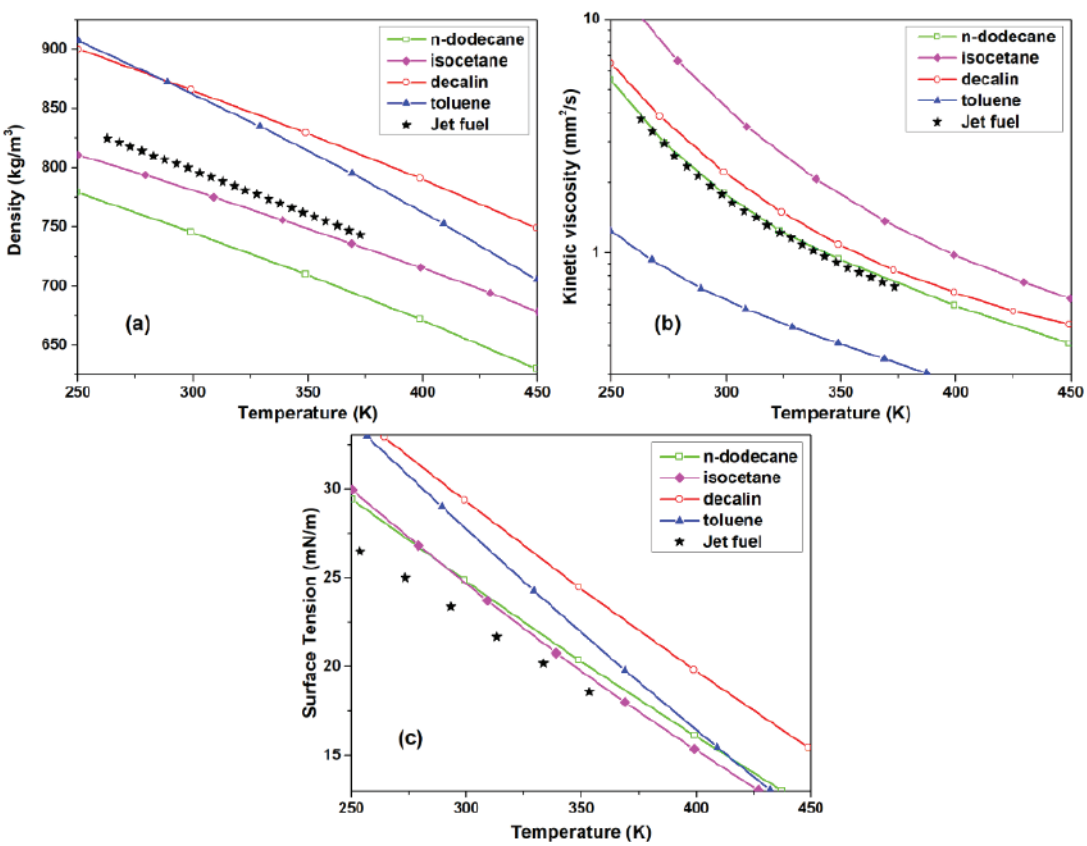

Figure 2. The temperature-dependent properties of the components: (**a**) density, (**b**) kinematic viscosity, and (**c**) surface tension.

2.2. Surrogate Fuel Components

Although real jet fuels contain a large number of compounds, according to Ref. [19], conventional jet fuels normally comprise 60% chain paraffins, 20% cycloalkanes, and 20% aromatics. Hence, it is reasonable to adopt the well-characterized compounds recognized in real jet fuels as the main surrogate components. Moreover, the components of jet fuel mainly belonged to C9–C16 hydrocarbons, which indicates that HC class and molecule size are also important criteria for surrogate components. The components whose chemical kinetic mechanisms have been well established are more preferred in our study. Based on these considerations, four components, including n-dodecane, isocetane, decalin, and toluene, were finally selected. The properties (CN, TSI, MW, LHV, and H/C) and formulae of the four components are listed in Table 2. The temperature-dependent properties, density, viscosity, and surface tension, are plotted in Figure 2. It can be easily seen that a single component is unable to represent real jet fuel because of the significant property differences between the single component and real fuel.

Table 2. The properties of the surrogate components.

Hydrocarbon Class Name	N-Alkane n-Dodecane	Iso-Alkane Isocetane	Cycloalkane Decalin	Aromatic Toluene
Formula	$C_{12}H_{26}$	$C_{16}H_{34}$	$C_{10}H_{18}$	C_7H_8
CN [20]	82.5	15	46.5	7.4
MW (g/mol)	170.33	226.44	138.25	92.14
LHV [21] (MJ/kg)	44.11	44.85	42.58	40.53
TSI [22]	7.0	22	22	40
H/C	2.17	2.13	1.8	1.1

2.3. Formation of Jet Fuel Surrogate

In this work, we improved the optimization algorithm from our previous study [18] to obtain the optimum component proportions of a jet fuel surrogate. The calculations for the target properties are showed in Table 3.

As reported in [20], the CN of the mixture can be calculated using the volume fraction average of the component CNs. The TSI of a mixture is obtained by calculating the mole fraction average of the pure component's TSI [23], while the LHV is estimated using the mass fraction average of the LHV. H/C and MW were directly determined by the component formula. The mixture density is also computed by the volume fraction average of component density. The viscosity is obtained using the Grunberg–Nissan equation [24,25], whereas surface tension is derived from the parachor correlation [26]. Finally, the equations proposed by Kim et al. [15] were employed as the merit functions:

$$MeritFunc = \sum_{i=1}^{Num_{target}} V_i \tag{1}$$

$$V_i = \frac{\sum_{j=1}^{Num_{data,i}} \left(\frac{Q_{i,j,cal} - Q_{i,j,exp}}{Q_{i,j,exp}} \right)^2}{Num_{data,\ i}} \tag{2}$$

where i and j represent the numbers of properties and experimental data points, respectively. $Num_{data,i}$ refers to the total number of measurements of the ith property, and Num_{target} represents the total number of target properties. $Q_{i,j,cal}$ and $Q_{i,j,exp}$ are the computed and measured properties, respectively.

Table 3. The estimation methods [18] of the properties of fuel surrogate.

Properties	Estimation Approaches
MW	Average of mole fraction: $\sum MW_{mix} = \sum X_i MW_i$ X_i is mole fraction of component i,
H/C	$\frac{H}{C_{mix}} = \sum X_i \frac{H_i}{\sum X_i} C_i$ C_i is the number of carbon atoms of component i
TSI	Average of mole fraction: $TSI_{mix} = \sum X_i TSI_i$
LHV	Average of mass fraction: $LHV_{mix} = \sum Y_i LHV_i$
CN	Average of volume fraction: $\sum CN_{mix} = \sum V_i CN_i$ V_i is volume fraction of component i
Density	Average of volume fraction: $\rho(T)_{mix} = \sum V(T)_i \rho(T)_i$
MW	Average of mole fraction: $\sum MW_{mix} = \sum X_i MW_i$
H/C	$\frac{H}{C_{mix}} = \sum X_i \frac{H_i}{\sum X_i} C_i$ H_i is the number of hydrogen atoms of component i;
Viscosity	Grunberg–Nissan equation [24]: $In(\mu(T)_{mix}) = \sum X_i In(\mu(T)_i) + 0.5 \sum\sum X_i X_j G_{ij}$ G_{ij} is the binary interaction parameter
Surface tension	Parachor correlation: $\sigma(T)_{mix} = \left(P_{L,mix} \rho(T)_{L,mix,molar}\right)^4$ $P_{L,mix} = 0.5 \sum\sum X_i X_j \left(P_i + P_j\right)$ $\sigma(T)_{mix}$ is liquid surface tension, P is parachor, $\rho(T)_{L,mix,molar}$ is liquid mixture molar density

A flowchart of the whole optimization process is given in Figure 3. It should be noted that the component will be removed when its mole fraction is less than 0.3% during the optimization process, the same as in our previous study [18]. Based on the above calculations, the optimum jet fuel surrogate was achieved, and it comprised 39.05% n-dodecane, 21.79% isocetane, 11.49% decalin, and 27.67% toluene by mole fraction and was abbreviated as JFS.

Table 4 shows the comparison results among the JFS surrogate and other jet fuel surrogates, including UM1, UM2, MURI2, S5 [27], and HEX12 [11]. In general, the property deviations of the surrogate JFS are less than 2% except for MW (10.73%), viscosity (5.88%), and surface tension (8.71%). The high deviations of MW and surface tension can be regarded as acceptable compared to other surrogates. As shown in Table 4, the deviation of the MW of S5 is 12.11%, and the averaged deviations of surface tension of UM2, Hex12, and S5 are larger than 15%, which are all larger than the corresponding property deviations of the surrogate JFS. It is also observed that the CN, MW, H/C and, LHV of the surrogate UM1 show good agreement with the target fuel; however, the deviations of TSI (−21.52%) and viscosity (−21.2%) are too large. The surface tension of UM2 deviates from the target property by 15.8%, even though CN, LHV, and density are well captured by the surrogate UM2. The LHV, MW, CN, and H/C are well emulated by MURI2; however, the deviation of viscosity (34.608%) is too large. As for the properties of HEX12 and S5, the majority of them greatly deviate from the target properties. Overall, the surrogate JFS performs better than other surrogates at reproducing the chemical and physical properties of real jet fuel; hence, it is more likely to be adopted for practical engine combustion simulation.

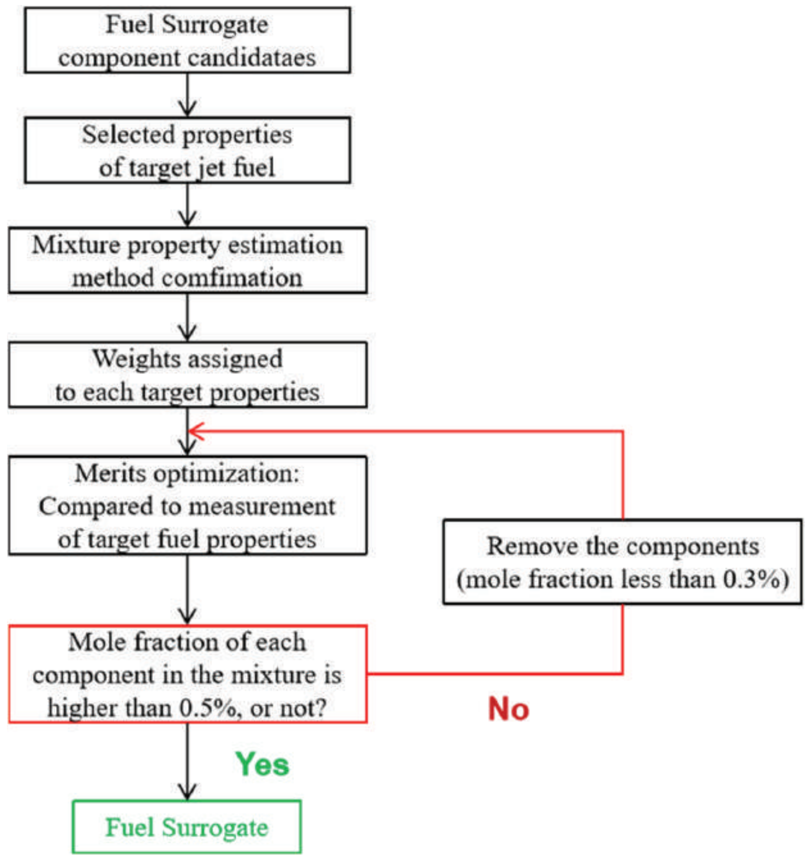

Figure 3. The flow chart of optimization process for the jet fuel surrogate.

Table 4. The comparison results among JFS and other jet fuel surrogates.

Jet Fuel	Surrogate	JFS	UM1	UM2	MURI2	S5	HEX12
CN 47.1	Val	46.93	46.8	46.7	48.5	32.1	60.5
	Dev (%)	−0.35	−0.64	−0.85	2.97	−31.8	28.45
H/C 1.957	Val	1.94	1.967	1.881	1.950	1.807	1.856
	Dev (%)	−0.86	0.51	−3.88	−0.36	−7.66	−5.16
MW 142	Val	157.23	143.5	148.6	138.7	159.2	152.2
	Dev (%)	10.73	1.06	4.65	2.32	12.11	7.18
LHV	Val	43.61	43.62	43.36	43.55	43.02	44.6
	Dev (%)	0.87	0.90	0.30	0.74	−0.49	3.17
TSI 21.4	Val	21.12	16.79	22.14	20.4	34.61	25.0
	Dev (%)	−1.29	−21.52	3.45	−4.67	61.72	16.84
Density	Average dev (%)	1.84	−3.4	0.6	−5.518	2.392	1.423
Viscosity	Average dev (%)	5.88	−21.2	−3.6	−34.608	18.167	5.077
Surface tension	Average dev (%)	8.71	9.1	15.8	3.131	19.1	18.774

3. Kinetic Modelling

3.1. Methodology

In this study, to facilitate the simulation of a practical engine combustion, a so-called decoupling methodology [5,18] was adopted for developing the JFS chemical mechanisms. The chemical kinetic mechanism was established through a systematic formation process, starting from C16 reactions and progressing towards $H_2/O_2/C1$ reactions. The subsequent steps involved incorporating a NOx sub-mechanism and polycyclic aromatic hydrocarbon (PAH). The reduction and optimization procedures employed in this process are briefly outlined as follows:

(1) The initial stage of the reduction and optimization process involves conducting a reaction pathway analysis to identify the key reactions. Subsequently, unimportant species and reactions are eliminated from the initial kinetic model. Simultaneously, the rate of production (ROP) and sensitivity analyses are performed to evaluate the remaining species and reactions. This allows for a clear understanding of the impact of each reaction on the oxidation process.

(2) Subsequently, the reaction rate constants were optimized to improve the agreement between the simulated and experimental data of fuel ignition delay time (IDT).

(3) Afterward, the concentrations of species and laminar flame speeds predicted by the reduced mechanism were compared to the corresponding measurements. This allowed for references to fine-tune the reaction rate constants further.

(4) Steps 1 to 3 were iteratively repeated until the desired size and accuracy of the mechanism were attained.

3.2. Toluene Sub-Mechanism

The current chemical kinetic model mainly comprises four sub-mechanisms, including the toluene sub-mechanism, decalin sub-mechanism, n-dodecane sub-mechanism, and isocetane sub-mechanism (Figure 4).

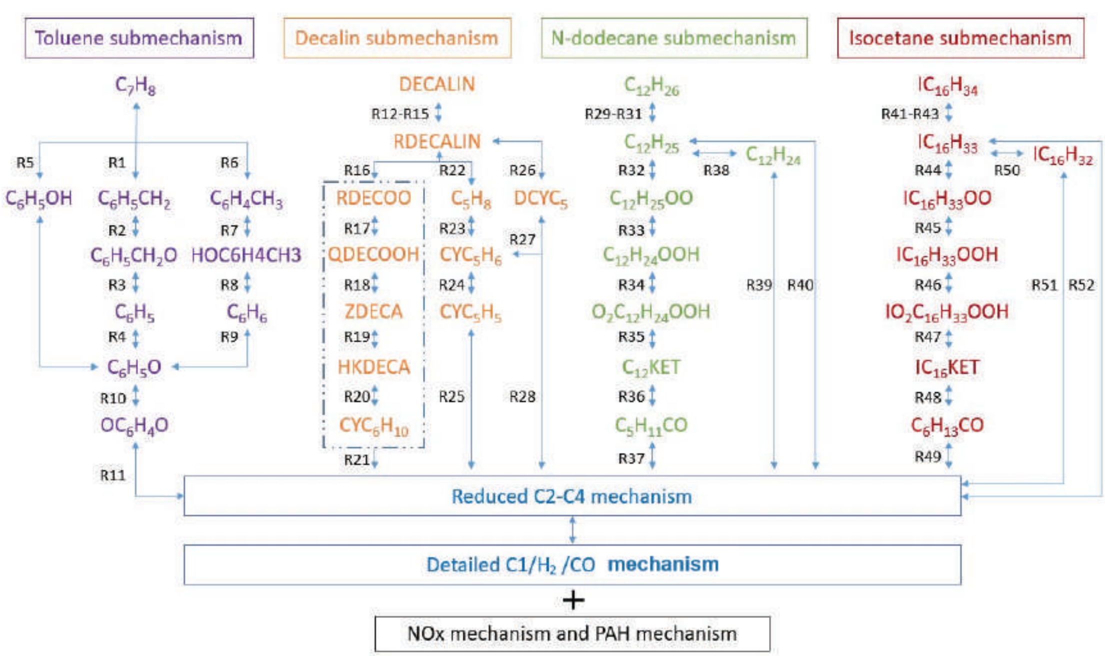

Figure 4. The major reaction pathways for the JFS kinetic mechanism.